System Identification Approach for Determining Flight Dynamical Characteristics of an Airship from Flight Data

Von der Fakultät Luft- und Raumfahrttechnik und Geodäsie der Universität Stuttgart zur Erlangung der Würde eines Doktor-Ingenieurs (Dr.-Ing.) genehmigte Abhandlung

Vorgelegt von

Andrei Kornienko

aus Sankt-Petersburg

Hauptberichter:	**Prof. Klaus H. Well, Ph.D.**
Mitberichter:	**Prof. Dr.-Ing. habil. Jörg Wagner**
Tag der mündlichen Prüfung:	**3. August 2006**

Institut für Flugmechanik und Flugregelung
Universität Stuttgart

2006

Abstract

The knowledge of dynamical characteristics of a flight vehicle is necessary for the control system design and realization of high fidelity flight simulators. The development of a flight mechanical model and determination of its basic components, as for example mass properties and the major aerodynamic terms, addresses a complex process involving various analytical, numerical and experimental techniques.

The objective of this dissertation is a determination of the basic dynamical characteristics of a research airship from the flight data. In order to achieve this objective a system identification approach is used. As the modern identification methodology requires a coordinated treatment of tasks from multidisciplinary areas, such as modelling, parameter estimation methods, instrumentation and flight maneuver definition, within this research framework these topics are studied and extended with regard to the airship example.

The dynamic modelling consists of two parts. The first part is devoted to derivation of the nonlinear flight mechanical model of the airship. It incorporates the classical laws of newtonian mechanics used for derivation of equations of motion. In addition, the airship specific properties, like buoyancy force and the unsteady aerodynamic effects, are included in the equations of motion. In the second part, the linearized longitudinal and lateral-directional models are introduced. Investigations of stability and controllability under different flight and configuration conditions are performed. The important parameters of the linearized models are then utilized in the parameter estimation.

For determining the model parameters statistical estimation methods are considered. Their choice is motivated by airship operational properties and limitations posed by the used instrumentation system. A particular emphasis is made on the algorithm that incorporates the Kalman filter to obtain parameter estimates in the presence of process and measurement noise. The process noise is used to model the uncommanded forcing function, mainly caused by atmospheric disturbances. The measurement noise is caused by the distortions of measured channels.

A valuable effort in this research framework is devoted to the design of experiments. This includes a realization of the onboard data acquisition system and definition of flight maneuvers. The conventional methods used in the aircraft field are accommodated for the experiment design.

Application of the used methodology to the flight data has shown a very good trajectory matching between the model and the real airship responses. It verifies the adequacy of the selected identification methodology for determining the dynamical characteristics of the airship from the flight data.

Identifizierung der flugdynamischen Eigenschaften eines Luftschiffes aus Flugmessdaten

Die Kenntnis der flugdynamischen Eigenschaften von Fluggeräten ist notwendig für den Entwurf von Systemen zur Flugregelung und zur Realisierung von Flugsimulatoren. Die Erstellung eines flugmechanischen Modells und die Bestimmung von Modellkenngrößen, wie z.B. Masse, Trägheitsmomente und aerodynamische Parameter, erfordern umfangreiche analytische, numerische sowie experimentelle Arbeiten.

Das Ziel der vorliegenden Dissertation ist die Bestimmung von flugdynamischen Eigenschaften eines Luftschiffes aus Flugmessdaten durch Verfahren zur Systemidentifikation. Die Vorgehensweise bei modernen Verfahren zur Systemidentifikation erfordert die Formulierung und Lösung von multidisziplinären Aufgaben. Dazu gehört die Erstellung eines flugmechanischen Modells, die Wahl der geeigneten Parameteridentifikationsalgorithmen, die Entwicklung des Onboard-Messsystems und die Definition von Flugmanövern. In dieser Arbeit wird diese Vorgehensweise auf ein Forschungsluftschiff angewendet.

Die Modellbildung besteht im wesentlichen aus zwei Teilen. Im ersten Teil wird das nichtlineare flugmechanische Modell des Luftschiffes entwickelt. Zur Bestimmung der Bewegungsgleichungen werden die physikalische Zusammenhänge der klassischen Mechanik und die spezifischen Eigenschaften von Luftschiffen, wie z. B. die aerostatische Verdrängungskraft und Effekte aus der instationären Aerodynamik wie scheinbare Massen, verwendet. Der zweite Teil konzentriert sich auf die lineare Approximation der Luftschiffdynamik. Dazu werden die Bewegungsgleichungen linearisiert und die Längs- und Seitenbewegung entkoppelt. Dann werden die klassischen Stabilitäts- und Steuerbarkeitseigenschaften bei verschiedenen Flug- und Konfigurationszuständen untersucht. Die wichtigsten Derivativa des linearen Modells werden in der folgenden Parameteridentifizierung bestimmt.

Die Identifizierung der Derivativa basiert auf statistischen Verfahren, deren Auswahl anhand der Flugeigenschaften des Luftschiffes und des verwendeten Onboard-Messsystems getroffen werden. Ein Schwerpunkt dieser Arbeit ist die Implementierung und Anwendung eines kalmanfilterbasierten Algorithmus, dessen wesentlicher Vorteil die Möglichkeit der Parameterschätzung mit Prozeß- und Messrauschen ist. Dem Prozessrauschen entsprechen die unkommandierten Bewegungen des Luftschiffs aufgrund atmosphärischer Störungen, dem Messrauschen Störungen in den Sensorsignalen.

Ein wichtiger Teil der Arbeit betrifft die Erstellung der experimentellen Testumgebung. Dazu gehören die Hardware des entwickelten Onboard-Messsystem und die Auswahl von geeigneten Flugmanövern. Die bekannten Flugmanöver zur Identifizierung der Dynamik von Starrflüglern werden für die Anwendung am Luftschiff angepasst.

Die Vorgehensweise für die Identifizierung der linearen Luftschiffmodelle zeigt eine sehr gute Übereinstimmung zwischen dem realen Flugverhalten und dem Modellverhalten des Luftschiffes. Der gewählte Ansatz zur Systemidentifizierung eignet sich somit gut für die Bestimmung der flugdynamischen Eigenschaften des Luftschiffs aus Flugmessdaten.

Acknowledgment

This work was carried out during my time as a research engineer at the Institute of Flight Mechanics and Control (IFR) at the University of Stuttgart. Many people have contributed in a variety of ways to make this work successful.

Foremost I would especially like to thank my advisor and director of IFR, Professor Klaus H. Well for giving me the opportunity to perform this research under his leadership and for giving me great freedom in my endeavours. His technical experience, encouragement and support were very helpful for me throughout my time in Stuttgart.

I am very grateful to Professor Jörg Wagner for his participation in the reading committee and for valuable discussion about the identification methodology.

Several discussions with Dr. Ravindra Jategaonkar from the German Airspace Center (DLR) have strongly influenced the guidelines of my work. I thank him for sharing his expertise on the area of aircraft identification with me.

Acquisition of flight data was not that easy as one may think. I appreciate the efforts of Dirk-Alexander Wimmer and Peter Kungl, who contributed greatly in providing the experimental data applicable for analysis.

I want to extend my thanks to all my former colleagues from IFR, in particular to Tanja Stäbler, Daniel Reber and Wassef Ayadi, for their support, many technical discussions and a warm working atmosphere. I am also grateful to Karen Buchholz, our secretary, for helping me with many organizational matters.

To Robert Taylor I am greatly indebted for his review of the manuscript. Moreover, many friends in Stuttgart, Regensburg and St.-Petersburg have supported me in different phases of this work, I want to thank all of them.

Finally, special thanks go to my wife Valérie and my parents, whose love and ever-lasting support make me possible to complete this work.

Regensburg, October 2006

Andrei Kornienko

Table of Contents

Nomenclature

Scalars

ax, ay, az	components of linear acceleration
c	aerodynamic coefficient (with subscript)
L, M, N	moment components (with subscript)
N	number of measurement instants
p, q, r	components of rotational velocity
p	probability density function
P	pressure
R	gas constant
t	time
T	temperature
T	time constant (with subscript)
u, v, w	components of linear velocity
x, y, z	reference coordinates (with subscript)
X, Y, Z	force components
α	angle of attack
β	sideslip angle
γ	flight path angle
δ	perturbed quantity
ρ	air density
ζ, η, ξ	aerodynamic control variables
τ	integration variable
ϕ, θ, ψ	Euler angles
ω	cyclic frequency

Vectors and matrices

$\boldsymbol{a}$	linear acceleration
$\boldsymbol{A}$	dynamic matrix
$\boldsymbol{b}$	bias vector
$\boldsymbol{B}$	control matrix
$\boldsymbol{C}$	observation matrix
$\boldsymbol{D}$	feedthrough matrix
$\boldsymbol{E}$	identity matrix
$\boldsymbol{f}$	vector of nonlinear state equations
$\boldsymbol{F}$	force vector (with superscript)
$\boldsymbol{F}$	process noise intensity matrix
$\boldsymbol{g}$	vector of nonlinear measurement equations
$\boldsymbol{H}$	Measurement noise intensity matrix
$\boldsymbol{I}$	inertia matrix
$\boldsymbol{J}$	linear flow momentum
$\boldsymbol{K}$	Kalman gain matrix
$\boldsymbol{K}$	dynamics vector
$\boldsymbol{L}$	rotation matrix (with superscript)
$\boldsymbol{L}$	Fisher information matrix
$\boldsymbol{M}$	mass matrix
$\boldsymbol{n}$	procss noise vector
$\boldsymbol{P}$	covariance matrix of state estimation error
$\boldsymbol{Q}$	moment vector
$\boldsymbol{r}$	coordinate vector
$\boldsymbol{R}$	covariance matrix of residuals
$\boldsymbol{S}$	eigenvector matrix
$\boldsymbol{T}$	direction cosine matrix
$\boldsymbol{u}$	input vector
$\boldsymbol{v}$	measurement noise vector
$\boldsymbol{V}$	velocity vector
$\boldsymbol{x}$	state vector
$\boldsymbol{y}$	system output vector
$\boldsymbol{z}$	measurement vector
$\boldsymbol{Z}$	vector of observable variables

Γ	discrete state noise intensity matrix
Θ	vector of estimated parameters
ρ	correlation matrix
Φ	state transition matrix
Ψ	control transition matrix
Ω	angular rate vector

Subscripts and superscripts

A	aerodynamic quantity
B	buoyancy quantity
G	gravity quantity
T	propulsion quantity
T	transpose of a matrix or vector
f	reference in body frame
g	reference in geodatic frame
i	measurement instance index
lon	longitudinal
lat	lateral
red	reduced
det	determinant of a matrix
$diag$	diagonal
0	initial (trim) value

Chapter 1

Introduction

1.1 Motivation

The beginning of the twentieth century has started the era of airships. The airship is a flight vehicle that gets its buoyancy from the presence of a Lighter-Than-Air gas. One of the greatest contributions to the airship's history was made by a german inventor Ferdinand Graf von Zeppelin (1838-1917). He proposed a rigid structure dirigible that became known as the zeppelin. Zeppelins had transported people worldwide at velocities which could not be achieved by other transportation means. However, as the technology of other types of transportation developed, airships became too slow. The era of airships ended in the year 1921 as the "Hindenburg" dramatically crashed.

Nowadays, the interest in Lighter Than Air systems revives as the technology has reached its new level in safety and reliability. Currently, there are many activities worldwide, engaged with designing and building modern technology helium airships. There are also new demands on transportation which cannot be satisfied by conventional aircraft. The static buoyancy property of the Lighter Than Air vehicles has generated a number of concepts to utilize these systems as a flying crane or as a semi-stationary station for communication and observation services. However, this raises a question: has the current level of technological achievements reached a point where the utilization of modern airships are economically feasible? The answer to this question should be given with time by trying out different application areas where the airships can be helpful.

Germany is probably the most airship inspired country, where the spirit of Zeppelins is still very strong. At the University of Stuttgart at the Institute of Static and Dynamics of Aerospace Constructions, a research team has built a solar powered airship "Lotte" [35]. Its construction was required for two reasons. First, it was necessary to prove that an airship can be driven by solar energy only. Second, a prototype airship would be a perfect object for verifying theoretical investigations made by researchers in this field. Hence, the fifteen meter long airship "Lotte" illustrated in Figure 1.1 is an object of study for several research groups from different institutes at the University. Among them, the Institute of Flight Mechanics and Control plays one of the key roles. Its major goal is to perform an autonomous flight operation of "Lotte".

Figure 1.1: Research airship “Lotte” during test flight

In order to carry out the autonomous flight mission of the airship, the development of a flight management and control system is obligatory. A vision for this approach was in utilizing a classical flight control system methodology and synthesis techniques to the control system design of the “Lotte” airship. In this approach, several prerequisites should be fulfilled.

The baseline requirement for designing the flight control system is an extensive knowledge of the flight dynamics of the vehicle. It incorporates a development of an appropriate flight mechanical model, which represents a set of input-output relations.

An important step in developing the flight mechanical model is the model verification. The model should adequately describe the airship dynamics, and if not, it should be adapted in terms of its structure and internal parameters to obtain it. Several systematic approaches can be utilized for the model verification. Among them, the aerodynamic verification is of the primary importance, since the aerodynamic uncertainties are the most dominant. The aerodynamic verification is usually performed using numerical computations of the fluid dynamics (CFD) and a variety of wind tunnel experiments. However, performing only aerodynamic verification of the model, one can not guarantee that the complete model will be adequate to the dynamics of the flight vehicle.

Apart from the aerodynamic verification, there are other methods available, which allow the model adjustments to be obtained directly from flight experiments. These methods are based on system identification theory and extensively utilized in practice. This dissertation examines an application of the system identification for the determination of the dynamic characteristics of the “Lotte” airship from flight experiments. Throughout this thesis, a better insight into the system identification problem and its application to the real practical problem will be introduced.

1.2 System Identification: An Overview

The system identification is commonly referred to as the inverse problem and postulated as *"given the answer, what was the question"* [45]. From the basic diagram illustrated in Figure 1.2, one observes that system identification is the field of modelling of physical processes based on experimental data.

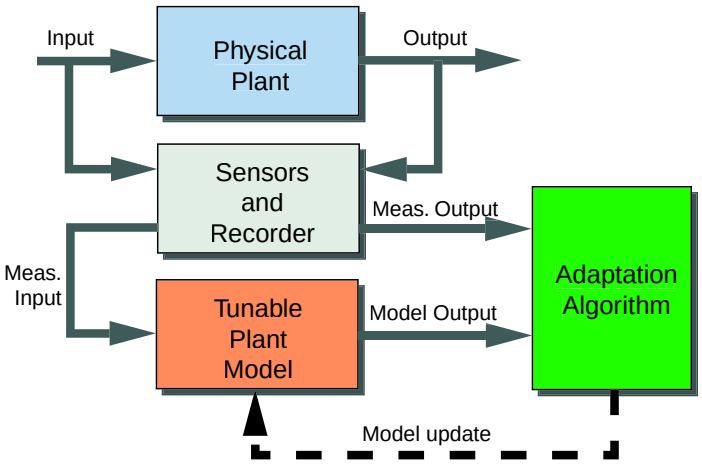

Figure 1.2: Fundamental concept of system identification

The system identification has grown to a separate topic of the control theory and the examples of its successful utilization can be found in many areas of practical applications. These are the cases, where a verification of some mathematically described phenomena from the experimentally derived data is required. A more expanded formulation of the identification problem is given in [65]:

> *"Identification is the determination of the basis of input and output, of a system within a specified class of systems, to which the system under test is equivalent*".

From this definition it follows that several items contribute to the identification process: the *input-output data*, a *model* or *set* of models and a *rule* or *criteria* for model estimation.

- The input-output data is usually collected during an identification experiment, which is designed to produce measured data with maximal information content about the involved process. Hence, for acquiring the input-output data, the measurement instrumentation is required. The measurements should indicate the reaction of the system to input signals.
- The model is the key item in the identification process. Within extensive theoretical explorations, an *a priori* knowledge should be extensively applied and a number of compromises made, so that the model is simple and distinct from one side, and to be able to adequately describe the behavior of the physical plant from the other. The model may be presented as a set of candidate models. Among them, there are several families of models: the *black-box* models, the *grey-box* models, and the models with a

predefined internal structure [39]. The black-box models do not use any prior knowledge of physical relationship between input and output. The grey-box model is some extension of the black-box class, where some a priori relations are involved in the process, but physical interpretation of the problem is still missing. Both the black-box and grey-box models are commonly utilized in cases where the "curve-fitting" is important and not the physical interpretation. Apart from the two previously mentioned models, those with a predefined internal structure are of primary interest in engineering applications. They require a physical insight about the process to be modelled and are, therefore, more preferable in general. The models with a defined structure determine a family of *parametric models*, where adjustable parameters specify the essential characteristics of the physical process. If the parametric model is specified, the original system identification problem narrows to the parameter identification problem.

- When the input-output data is available and the model has been selected, a rule according to which the model fits the data should be defined. In the parameter identification, where parametric models are utilized, a criteria is used for *parameter estimation*. Parameter estimation, being an integral part of system identification can be easily formulated as a classical optimization problem.

All above described items are basic elements, which appear in any identification problem. In many cases, where the need exists to model the physical phenomena of the process, the problem of parameter identification is of major interest.

1.3 System Identification in Flight Mechanics

The problem of system identification has been extensively utilized in flight mechanics. Flight mechanics, being a field of aerospace engineering, is focused on the motion of a flight vehicle. The main objectives of flight mechanics are based on specification and modelling of dynamic characteristics of the vehicle. The dynamic characteristics are mainly derived from the Newtonian laws of mechanics, which suppose the motion of the vehicle (rigid body) caused by action of externally applied forces. A classification of the external forces and moments is typical for any flight vehicle. These are aerodynamic, propulsive, gravity forces and, if the vehicle belongs to a class of Lighter Than Air (LTA) systems, also the static buoyancy forces. In derivation of the flight mechanical model, the system identification procedure is used as a tool for updating the aerodynamic database [12], [44].

1.3.1 Historical Overview and Current State of the Art

The first attempt to apply parameter estimation principle to a flight vehicle was performed by Norton and Warner in 1919 [63]. The scope of their investigation was the determination of aerodynamic parameters from various flight maneuvers, flown at certain airspeeds. They utilized a basic idea of equating the lift force to the weight of the test aircraft and drag to the thrust force, assuming that weight and thrust were known for the test aircraft.

The evolution of system identification applied to flight vehicles has been continuously expanding. The following sections distinguish some research groups that have contributed greatly to the application of system identification on flight vehicles. In addition, a current state of airship system identification will be presented.

Experience at NASA

The experience gained at NASA has the strongest influence on today's methodology of the flight vehicle system identification. Scientific potential governed at NASA by studying various types of flight vehicles is very high. Evaluations made at Aimes and Dryden Flight Research Centers have considered a whole spectrum of flight vehicles starting from remotely controlled scaled models up to estimation of hypersonic dynamics of reentry space vehicles [16]. With evolution of aircraft and other flight vehicles, the new requirements on system identification have been posed. For example, the estimation of aircraft aerodynamic parameters at high angles of attack has been performed by implementation of the extended Kalman filter into the parameter estimation algorithm [17]. Additionally, estimation of aircraft dynamics in presence of turbulence is performed [15]. These, and many other system identification problems have been examined and successfully solved at NASA.

Experience at DLR

The "Deutsches Zentrum für Luft und Raumfahrt" (DLR) has been extensively utilizing system identification as a tool for validating flight mechanical and aerodynamic models for a variety of flight vehicles since 1960. Many research activities have been devoted to the problem of system identification. Today's identification efforts are made on estimating the dynamics of an aircraft at stall regimes and extracting aerodynamic coefficients at high angles of attack. Additional focus is concentrated on identifying nonlinear models of aircraft [21].

Other Research Activities on Aircraft System Identification

Today many researchers utilize the system identification approach for validating different types of models. Recent developments have considered different modifications on existing identification algorithms, applying them to special problems where common identification methods fail. There are, for example, a number of evaluations that concern identification of different aircraft models using neural networks [13], [56]. Others devote their efforts to solving problems, where numerical computation problems are dominant, e.g. singular and sparse matrices, discontinuity in the process dynamics, difficulties in evaluating numerical gradients [3], [22], [30].

Articles Related to the Airship Identification

Although a number of references exist devoted to dynamic response models for the LTA vehicles, there are few examples where a comparison of the analytical models versus actual flight data is performed. Some results on this area are reported in [23], where the stability derivatives of the Skyship-500 are determined from the flight data using the frequency

domain fitting. However, until now no common approach for identifying airships is available and therefore it is an attractive area for research activities.

1.3.2 Unified Approach to Flight Vehicle System Identification

In recent years the problem of flight vehicle system identification led to a consolidated methodology (Quad-**M**), which has been proposed by a research group from the German Aerospace Center (DLR) and illustrated in Figure 1.3. The topology of the Quad-**M** methodology is tightly related to the basic definition of the system identification problem as pointed out in section 1.2 and contains four basic elements, namely: **M**aneuvers, **M**easurements, **M**odels and **M**ethods.

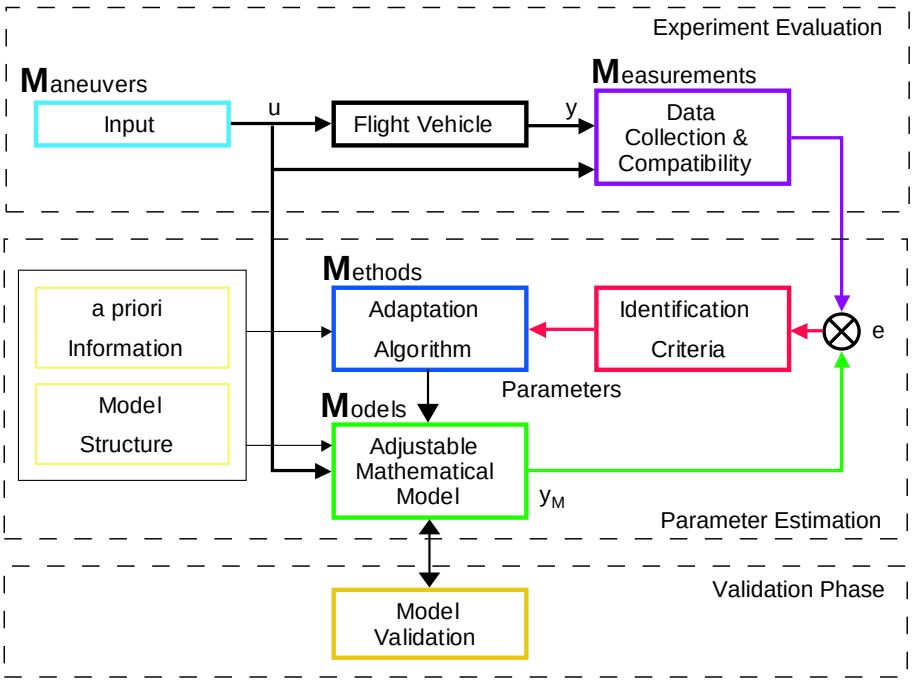

Figure 1.3: Unified Quad-M approach of flight vehicle system identification [18].

Maneuvers

The maneuvers are related to the selected flight vehicle maneuvering procedure. The control inputs should be designed to provide maximum sensitivities of the vehicle reactions on the unknown parameters.

Measurements

The measurement part of the Quad-**M** diagram is responsible for instrumentation used in the identification process. Measurements, delivered by variety of measurement units should track both the input controls and the vehicle's reaction on the given input. The quality of the overall identification process is strongly influenced by the accuracy of the measurement

equipment. The flight data, collected during experiments are further evaluated in order to provide consistency of measured quantities from various sensors [25].

Model

Similarly to the general definition of the system identification problem, the model part plays a central role in the flight vehicle system identification. As pointed out, the basic equations are derived from the Newtonian laws of mechanics. Structural interconnection of the model is usually predefined and some a priori information extensively used as indicated in Figure 1.3 as external inputs to the model. The a priori information contains for example databases derived from wind tunnel experiments or upper-lower bounds on the parameters according to their physical interpretation. The flight vehicle system identification utilize linearized as well as nonlinear model realizations for parameter determination.

Methods

There are many approaches for estimating the parameters of dynamic systems that are presently available in flight vehicle system identification. Their application is based on analysis of input-output behavior in both time and frequency domains. In the past decade however, with the increased computation capability of modern computers, the focus has changed from frequency domain to time domain analysis [12]. The time domain analysis addresses more preferable advantages on the parameter estimation problem. They follow from the ability to apply an optimal state estimation using optimal (e.g. Kalman) filters. Additional benefit is acquired from the recent possibilities of estimating moderate nonlinear models from experimental data [21]. On the other hand, the frequency domain methods work well in determining parameters of unstable linear systems and in estimation of a time periodic (helicopter) dynamics [22]. There are also a number of realizations that are capable of performing parameter estimation in real time scale (online identification) [61]. Every estimation method has particular advantages and disadvantages over the others. There is no direct answer to the best method, its choice is dictated by the engineering anticipation of the problem. This knowledge should be governed by an assumption made on the functionality of the flight vehicle under test and the ability and accuracy of the measurement instrumentation.

Validation Phase

An additional important issue in the identification methodology is the model validation (see the bottom of the Quad-M diagram). Model validation is the process of testing whether the estimated model is sufficiently accurate for the intended purposes of its use. Here, several answers should be given [51]. First of all, it is necessary to specify if the estimated model is in agreement with the adopted a priori knowledge of the flight vehicle (*internal verification*). The next question to answer is whether the model can provide an acceptable fit in experiments, where input-output data sequences have not been used in model estimation (*external validation* or *cross-validation*). Some indirect aid to the validation process can be taken directly from the statistical characteristics of estimated parameters (Cramer-Rao bounds). Altogether, the internal verification, cross-validation and the statistical characteristics of estimated parameters provide the final confidence about the quality of the estimated model.

1.4 Objectives of the Work

This thesis considers a problem of the “Lotte” airship system identification, as a tool for determining its dynamics from the flight data. The unified approach described in section 1.3 is used as a basis for this work, which could be further utilized for designing the flight control system.

The modern identification problem poses several objectives from different multidisciplinary areas. Therefore, the consequent treatment of the problems is considered in the current workframe:

- **Study of airship dynamics and derivation of identification models:** The study of airship dynamics should be based on previous work, where a closed form of a generic airship flight mechanical model is introduced [26]. Then, derivation of simplified models, which are applicable for estimation purposes should be performed and arguments for their selection should be made.
- **Parameter estimation methods:** The choice of appropriate parameter estimation algorithms should be motivated by airship operation properties and tightly connected with available instrumentation used in the project.
- **Measurement hardware realization:** Since the system identification approach is based on the measured data, the availability of a measurement hardware is obligatory. For this reason the development of an appropriate measurement system is an additional objective of the work.
- **Input design:** This objective implies a selection of the control input type and shape for providing maximum sensitivities of the airship reactions on the unknown parameters.
- **Flight tests, data analysis:** The availability of the Lotte airship makes it possible to carry out the flight tests with onboard instrumentation system. The issues, associated with the flight data postprocessing as well as estimation of the model parameters from the flight data should be examined. Finally, the reliability of the considered identification approach should be proved through validation tests.

1.5 Structure of the Thesis

The structure of current thesis is organized in compliance with the objectives defined for the work. Primary, the derivation of the airship flight mechanical model is performed in Chapter 2. There the input, state and the output quantities of the model are defined and their relation to the complete airship dynamics are concluded. After the major properties of the model are studied, Chapter 3 discusses a subclass of linear models, based on linearization of the nonlinear flight mechanical model. The corresponding analysis of stability of the linearized model is performed. With the a priori knowledge, gained about the airship dynamics, a variety of estimation methods are considered in Chapter 4. There, the analysis of advantages and disadvantages of particular estimation methods is performed. Chapter 5 is devoted to the problems

of experiment design. It involves a discussion of the experimental part of the airship identification project, including design of control inputs and hardware realization. Chapter 6 summarizes the estimation and validation results, obtained from flight experiments performed using “Lotte” airship. Finally, Chapter 7 summarizes the achieved results and gives directions for future research.

Chapter 2

Airship Flight Mechanical Model

2.1 Generalized Approach to Airship Modeling

The airship dynamical model used in this work originates from that developed in [26]. It is based on the classical flight mechanical methodology for building a flight mechanical model [6]. The modelling of the airship dynamics is constrained on a single rigid body. This incorporates an utilization of principles of the Newtonian mechanics for a dynamic description of the body motion.

There are two significant additions to the classical equations of motion of a flight vehicle that should be accounted for, when considering the dynamics of the lighter than air vehicle. They are characterized by:

- The buoyancy force
- Aerodynamically induced *virtual mass* and *virtual moment of inertia* effects

The buoyancy force is based on the well known principle of aerostatics. The virtual mass and moment of inertia effects are known from the potential flow theory and arise due to the fact that the mass of the airship is being of the same order of magnitude as the mass of the displaced air [62].

2.2 Definition of Reference Frames, Motion Variables and Controls

2.2.1 Flight Mechanical Variables

It is common in flight mechanics to define some typical variables for describing the motion of a flight vehicle. For this purpose several vectors that determine position, velocity, and

rotation are introduced. The vectors are naturally described through their components as projections on the axes of a predefined frame of reference:

Position	**Velocity**	**Angular rate**	**Force**	**Moment**

$$\boldsymbol{r} = \begin{bmatrix} x \\ y \\ z \end{bmatrix}, \quad \boldsymbol{V} = \begin{bmatrix} u \\ v \\ w \end{bmatrix}, \quad \Omega = \begin{bmatrix} p \\ q \\ r \end{bmatrix}, \quad \boldsymbol{F} = \begin{bmatrix} X \\ Y \\ Z \end{bmatrix}, \quad \boldsymbol{Q} = \begin{bmatrix} L \\ M \\ N \end{bmatrix}.$$

For indicating the relative orientation of the flight vehicle with respect to a stationary frame the Euler angles: ϕ-Bank, θ-Pitch and ψ-Yaw are defined.

If the airship moves in non-steady atmosphere with wind velocity $\boldsymbol{V}_W$, it is necessary to distinguish between the flight path velocity $\boldsymbol{V}_K$ and the airstream velocity $\boldsymbol{V}_A$. The airstream velocity represents a relative motion of the airship with respect to the surrounding air. The velocities $\boldsymbol{V}_K$, $\boldsymbol{V}_A$ and $\boldsymbol{V}_W$ are distinguished using relation:

$$\boldsymbol{V}_A = \boldsymbol{V}_K - \boldsymbol{V}_W. \tag{2.1}$$

The introduced flight path, wind and airstream velocities will further appear in determination of external forces and moments acting on the airship. The motion variables described here, as well as forces and moments are sufficient for describing the complete motion of an airship.

2.2.2 Basic Frames of Reference

For describing the airship motion, two main frames of reference are defined. These are geodetic and body-fixed frames. The geodetic frame of reference is a right-handed orthogonal frame with index g that coincides with the geodetic coordinate system. The origin of the frame is located near the vehicle and the x-axis is aligned with the north direction and the z-axis points toward the center of the Earth. The Earth is assumed to be plain and non-rotating.

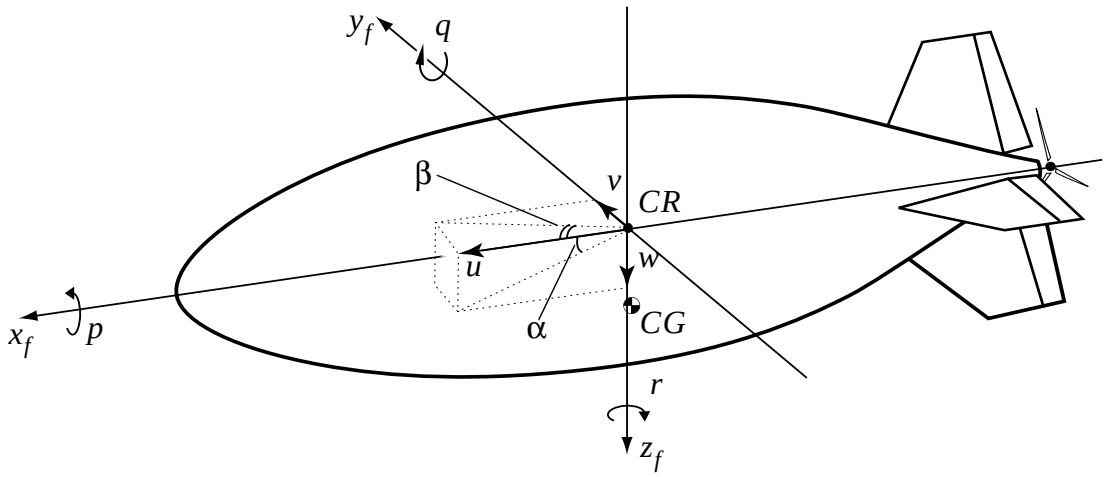

Figure 2.1: Body axis system of an lighter than air vehicle

The other frame, the natural frame of reference for most vehicle-borne description, is regarded to be fixed with the airship as illustrated in Figure 2.1. In the body frame of reference, all motion variables and equations of motion will be treated with index f. In contrast to aircraft models, where the body fixed reference frame is traditionally placed at the center of mass point CG, the airship center of reference CR coincides with the center of geometrical symmetry of the hull. The location is chosen for two reasons. First, to simplify the computation of aerodynamic forces and moments, acting on the airship. Second, the center of mass may significantly change its location during the flight (see 2.4.1). If the body axes were fixed to the CG point, its movement would cause the change of the body axes with respect to the airship body and consequent change of all geometrical locations.

It is common practice to describe the motion of a flight vehicle in the flight path axes, i.e. using the true speed U, angle of attack α, and the sideslip angle β instead of the linear velocity components u, v and w. In the current development however, the motion description was restricted by considering the body linear velocities only. Because the equations of motion expressed in U and α variables introduce numerical singularity at the operation condition at the hover mode, it is advantageous to formulate the equations using velocity components of the body reference.

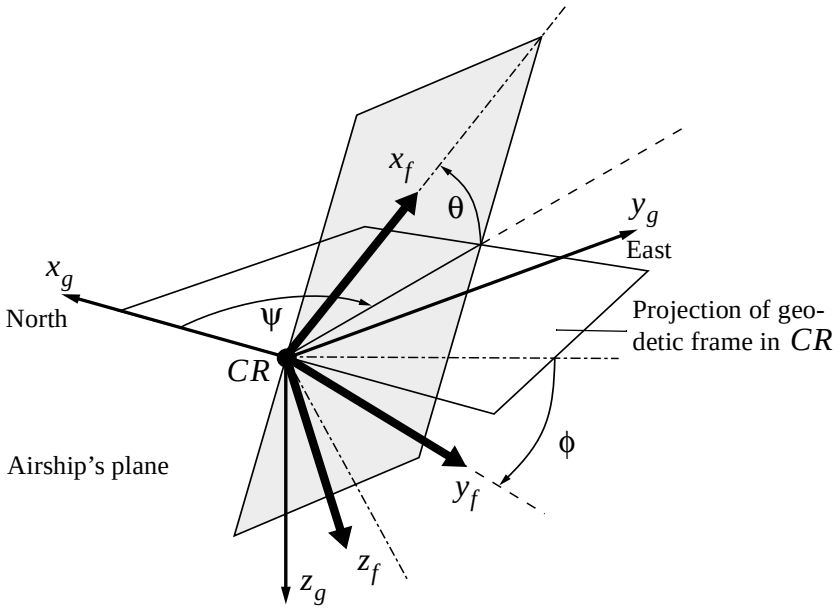

Figure 2.2: Relationship between geodetic and body fixed frames

The angular orientation of the body axis system with respect to the geodetic frame depends on the orientation sequence, which is derived by rotating the geodetic axes around azimuthal-ψ, elevation-θ and bank-ϕ angles respectively, as illustrated in Figure 2.2.

This transformation can be analytically represented by a direction cosine matrix $\boldsymbol{T}_{fg}$:

$$\begin{bmatrix} x \\ y \\ z \end{bmatrix}_f = \boldsymbol{T}_{fg} \begin{bmatrix} x \\ y \\ z \end{bmatrix}_g , \tag{2.2}$$

where the matrix $\boldsymbol{T}_{fg}$ is the direction cosine matrix, which is obtained by the consolidated multiplication of rotation matrices

$$T_{fg} = \boldsymbol{L}_{\phi}^{(I)} \boldsymbol{L}_{\theta}^{(II)} \boldsymbol{L}_{\psi}^{(III)}, \tag{2.3}$$

with

$$\boldsymbol{L}_{\phi}^{(I)} = \begin{bmatrix} 1 & 0 & 0 \\ 0 & \cos\phi & \sin\phi \\ 0 & -\sin\phi & \cos\phi \end{bmatrix}, \boldsymbol{L}_{\theta}^{(II)} = \begin{bmatrix} \cos\theta & 0 & -\sin\theta \\ 0 & 1 & 0 \\ \sin\theta & 0 & \cos\theta \end{bmatrix}, \boldsymbol{L}_{\psi}^{(III)} = \begin{bmatrix} \cos\psi & \sin\psi & 0 \\ -\sin\psi & \cos\psi & 0 \\ 0 & 0 & 1 \end{bmatrix}. \tag{2.4}$$

Using equation (2.2), the transformation of a vector quantity from geodetic into body fixed axes is possible. For this transformation also valid:

$$\boldsymbol{T}_{fg} = \boldsymbol{T}_{gf}^{T} = \boldsymbol{T}_{gf}^{-1}. \tag{2.5}$$

2.2.3 Airship Controls

The principal control of a pilot on the examined airship is achieved by two main sources. These are aerodynamic control and propulsion control.

The aerodynamic control is performed through the change of the effective local flow angles made by control surfaces. The control surfaces are the attached horizontal and vertical fins as illustrated in Figure 2.3 and can act as elevator-η, rudder-ζ and aileron-ξ.

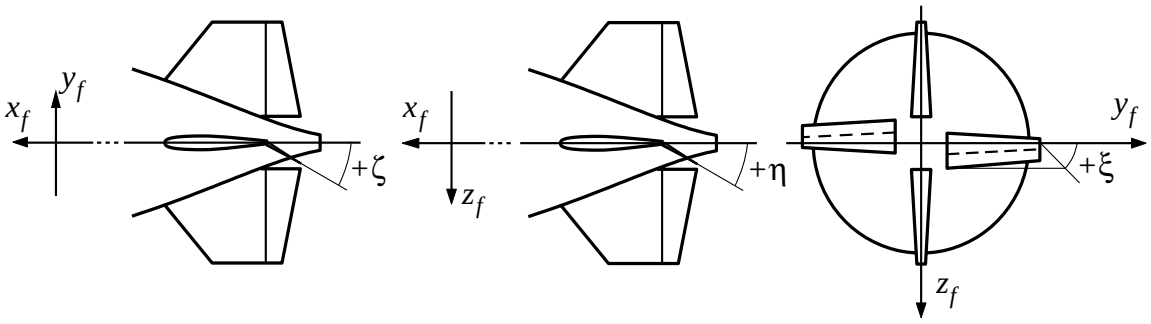

Figure 2.3: Aerodynamic control surfaces of the airship “Lotte”

The propulsion control is achieved by variation of the rotation rate of the propeller. In the hardware configuration of airship “Lotte” the propeller is located at the rear part of its body. The axis of propeller’s rotation might be changed with respect to the airship body, changing therefore the vector of applied thrust force (thrust vectoring). The thrust vectoring is commonly used for maneuvering and occurs during the starting and landing phases of the flight.

2.3 Rigid Body Dynamics

2.3.1 Equations of Motion in the Body Reference Frame

From the statement of treating the airship as a rigid body given in 2.1, the classical laws of Newtonian mechanics can be utilized. Thus, the motion of a rigid body is characterized by the action of external forces. By applying Newton’s Second Law, the equations of motion can be established in terms of translational and angular accelerations as a consequence of the external forces and moments applied to the center of mass CG

$$\frac{d}{dt}\{m\boldsymbol{V}_{K|CG}\}_f^g = \{\boldsymbol{F}^{\Sigma}{}_{CG}\}_f \tag{2.6}$$

and

$$\frac{d}{dt}\{\boldsymbol{I}_{CG}\Omega_{CG}\}_f^g = \{\boldsymbol{Q}^{\Sigma}{}_{CG}\}_f\,, \tag{2.7}$$

where the operator $\frac{d}{dt}\{\ \}_f^g$ denotes the time derivative of a vector taken in the g-geodetic frame and expressed in the body reference frame f. The vectors $\boldsymbol{F}$ and $\boldsymbol{Q}$ in the right hand side of equations (2.6) and (2.7) represent resulting vectors of all externally applied forces and moments respectively. As the equations describe the motion of the mass center of the airship, all its variables - the velocity $\boldsymbol{V}_{K|CG}$, the inertia matrix $\boldsymbol{I}_{CG}$, and the summary of external forces and moments - are determined with respect to the CG point.

From similar transformations, outlined in B.1, the equations of motion (2.6), (2.7) can be expressed in the body reference coordinates:

$$m(\dot{\boldsymbol{V}}_K + \dot{\Omega}\times \boldsymbol{r}_{CG} + \Omega\times (\boldsymbol{V}_K + \Omega\times \boldsymbol{r}_{CG})) = \boldsymbol{F}^{\Sigma}, \tag{2.8}$$

$$\boldsymbol{I}\dot{\Omega} + \Omega\times (\boldsymbol{I}\Omega) + m\boldsymbol{r}_{CG}\times (\dot{\boldsymbol{V}}_K + \Omega\times \boldsymbol{V}_K) = \boldsymbol{Q}^{\Sigma}, \tag{2.9}$$

with all terms expressed with respect to the center of body reference CR:

$$\dot{\boldsymbol{V}}_K = \frac{d}{dt}\{\boldsymbol{V}_{K|CR}\}_f \quad , \quad \dot{\Omega} = \frac{d}{dt}\{\Omega_{CR}\}_f \quad ,$$

$$\boldsymbol{I} = \boldsymbol{I}_{CR}, \tag{2.10}$$

$$\boldsymbol{F}^{\Sigma} = \{\boldsymbol{F}^{\Sigma}{}_{CR}\}_f \quad , \quad \boldsymbol{Q}^{\Sigma} = \{\boldsymbol{Q}^{\Sigma}{}_{CR}\}_f \quad .$$

In order to combine the force (2.8) and the moment (2.9) equations together, they can be transformed into a compact block matrix form. For this purpose the vector product terms, where the linear $\dot{\boldsymbol{V}}_K$ and the rotational $\dot{\Omega}$ accelerations appear, can be equivalently expressed by a scalar multiplication involving a skewing matrix and a vector

$$\begin{aligned} \boldsymbol{r}_{CG} \times \dot{\boldsymbol{V}}_K &= \boldsymbol{r}^X_{CG} \cdot \dot{\boldsymbol{V}}_K \quad , \\ \dot{\Omega} \times \boldsymbol{r}_{CG} &= -\boldsymbol{r}_{CG} \times \dot{\Omega} = -\boldsymbol{r}^X_{CG} \cdot \dot{\Omega} \quad , \end{aligned} \tag{2.11}$$

where the $\boldsymbol{r}^X_{CG}$ multiplier denotes the skewing matrix. Applying these substitutions into equations (2.8) and (2.9) and rearranging terms, the general equation of motion yields:

$$\underbrace{\begin{bmatrix} m\boldsymbol{E} & -m\boldsymbol{r}^X_{CG} \\ m\boldsymbol{r}^X_{CG} & \boldsymbol{I} \end{bmatrix}}_{\text{Mass Matrix}} \begin{bmatrix} \dot{\boldsymbol{V}}_K \\ \dot{\Omega} \end{bmatrix} = \underbrace{\begin{bmatrix} -\Omega \times (\boldsymbol{V}_K + \Omega \times \boldsymbol{r}_{CG}) m \\ -\Omega \times (\boldsymbol{I}\Omega) - (m \cdot \boldsymbol{r}_{CG} \times (\Omega \times \boldsymbol{V}_K)) \end{bmatrix}}_{\text{Dynamics Vector}} + \underbrace{\begin{bmatrix} \boldsymbol{F}^{\Sigma} \\ \boldsymbol{Q}^{\Sigma} \end{bmatrix}}_{\substack{\text{External Forces} \\ \text{and Moments}}} . \tag{2.12}$$

The form of the equation (2.12) represents a state space realization of the nonlinear differential equation. Its state vector is comprised of the motion variables, i.e the linear $\boldsymbol{V}_K$ and the rotational Ω velocities. The state space form of (2.12) can be suitably applied for simulation purposes. The general equation of motion has three major components: the mass matrix, the dynamics vector and the vector of net forces and moments.

The mass matrix is a symmetrical matrix, where the mass, tensor of moments of inertia and off-diagonal coupling terms are placed. Its expanded form is outlined in B.2. The dynamics vector appears due to kinematic transformations and translation from mass center to the body reference center (see also B.3).

The resulting vectors of external force $\boldsymbol{F}^{\Sigma}$ and moment $\boldsymbol{Q}^{\Sigma}$ can now be closer examined. They can be separated by terms, which are classified by their physical nature. These are

gravitational, aerostatic, aerodynamic and propulsive terms. All external forces and moments are considered as a sum of nonlinear functions

$$\begin{aligned} \boldsymbol{F}^{\Sigma} &= \boldsymbol{F}^{A} + \boldsymbol{F}^{B} + \boldsymbol{F}^{G} + \boldsymbol{F}^{T} \\ \boldsymbol{Q}^{\Sigma} &= \boldsymbol{Q}^{A} + \boldsymbol{Q}^{B} + \boldsymbol{Q}^{G} + \boldsymbol{Q}^{T}, \end{aligned} \tag{2.13}$$

where the superscript A corresponds to the aerodynamic component, B-buoyancy, G-gravity and T indicates the thrust term.

The formulation of equations of motion derived until now, does not adopt the common aerodynamic properties of airships. For the sake of simplicity in formulation, all major components that appear in the equation (2.12) will be individually examined later in section 2.4.

2.3.2 Orientation and Position Equations

The equations of motion have been derived for an axis system fixed to the airship. However, the position and orientation of the airship cannot be described relative to the moving body axis frame, rather than related to the stationary (geodetic) frame. The orientation of the airship can be defined in terms of rotational variables:

$$\begin{bmatrix} \dot{\phi} \\ \dot{\theta} \\ \dot{\psi} \end{bmatrix} = \begin{bmatrix} 1 & \sin\phi\tan\theta & \cos\phi\tan\theta \\ 0 & \cos\phi & -\sin\phi \\ 0 & \dfrac{\sin\phi}{\cos\theta} & \dfrac{\cos\phi}{\cos\theta} \end{bmatrix} \begin{bmatrix} p \\ q \\ r \end{bmatrix}. \tag{2.14}$$

In this relation the transformation matrix becomes singular for the pitch angle at values $\theta = \pm 90^{\circ}$. However, under normal airship operation, this singularity does not occur.

In order to determine the position of the origin of body reference CR with respect to the inertial reference frame, the following differential equation should be solved:

$$\begin{bmatrix} \dot{x} \\ \dot{y} \\ \dot{z} \end{bmatrix}_{g} = \boldsymbol{T}_{gf} \begin{bmatrix} u_K \\ v_K \\ w_K \end{bmatrix}_{f}. \tag{2.15}$$

2.4 Airship Mass and External Forces and Moments

2.4.1 Mass Characteristics

Significant difference of a buoyant-like vehicle from a typical aircraft is that its mass characteristics strongly depends on environmental conditions, i.e. the change of altitude H:

$$m = m(H),\ \boldsymbol{I} = \boldsymbol{I}(H),\ \boldsymbol{r}_{CG} = \boldsymbol{r}_{CG}(H). \tag{2.16}$$

It follows from the fact that due to construction requirements, the pressure difference between the surrounding atmosphere and the inner gas (Helium) should be kept as constant as possible at each altitude level:

$$\Delta P(H) = P_G(H) - P_A(H) \approx \text{ constant}. \tag{2.17}$$

This permanent pressure difference is required for maintaining the aerodynamic shape of the envelope under most operational conditions. As the atmospheric pressure $P_A(H)$ changes with the height H (see Figure 2.4), it should be compensated by the internal gas pressure. For this purpose the envelope is equipped with two air-filled-ballonets, namely the *fore*- and the *aft*-ballonets located inside the hull. The volume occupied by the inner gas and the ballonets, represent the inner volume of the airship's hull envelope and is nearly constant.

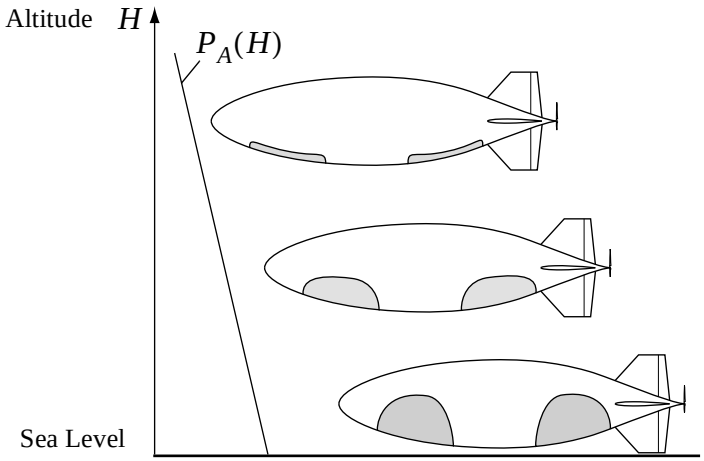

Figure 2.4: Ballonet filling on variation of altitude H

By filling the ballonets with the air, they displace the volume of the inner gas, increasing the total pressure of the gas in the envelope. In general, the total mass of the airship can be expressed by

$$m(H) = m_G + m_B(H) + m_R, \tag{2.18}$$

where m_G is mass of the inner gas, $m_B(H)$ is the total mass of air ballonets and m_R represents the mass of all internal components (skin, structure, energy sources, etc.). The mass of the Helium m_G can be considered as constant if leakage through the hull's skin is insignificant. The mass of all internal components m_R can be derived by accounting all elements of the airship as a consolidation of point and distributed masses. The total sum of the internal components m_R is assumed to be constant during the flight operation, since the "Lotte" airship is electrically powered.

The volume of the ballonets depends on change of the atmospheric pressure gradient, as denoted in Figure 2.4. At sea level where the atmospheric pressure is high, the ballonet volume has its maximum level and reduces with the increased altitude. The atmospheric variation can be approximated by common laws of ideal gas. For determining the values of the air pressure $P_A(H)$ and the air density $\rho_A(H)$, a model based on International Standard Atmosphere (ISA) can be applied [10].

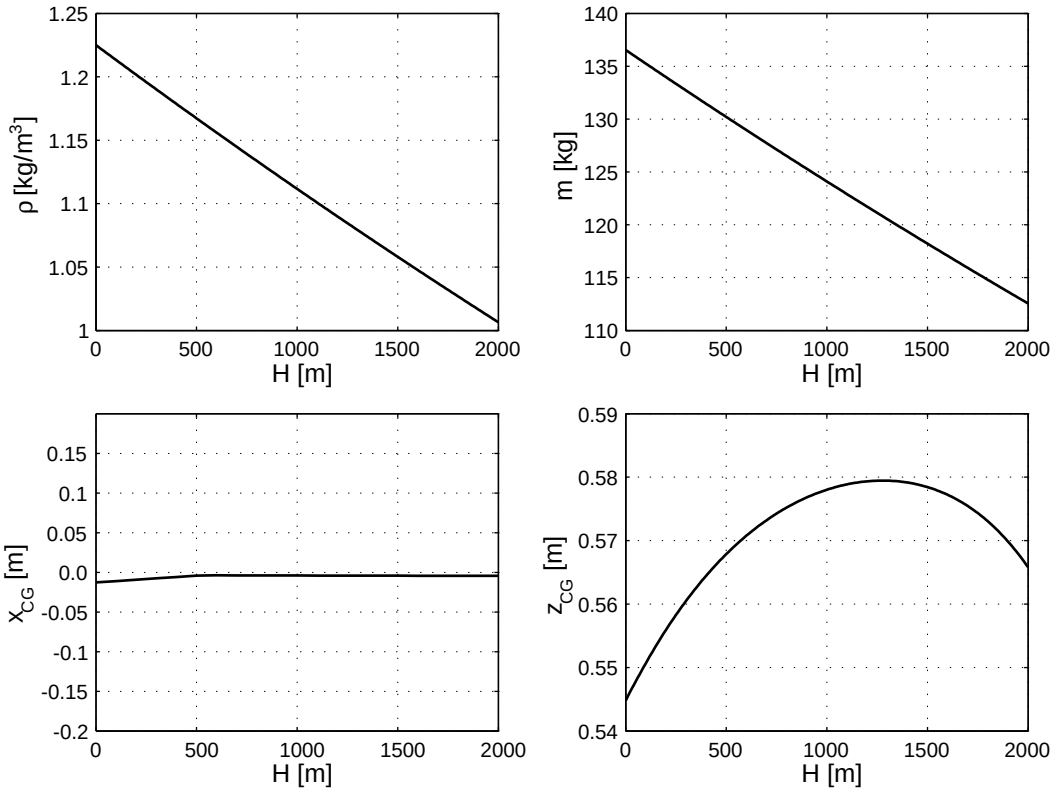

Figure 2.5: Variation of atmospheric density-ρ_A, the total mass-m and CG position against the altitude-H change. Simulation case with ISA atmospheric model

Variation of mass of ballonets also results in a change of the center of gravity CG position with respect to the body reference frame. Some results of the modelling of the mass variation against the altitude are presented in Figure 2.5. The ballonets play an additional role in the airship operation. By filling the ballonets unequally, the variation of position of the center mass CG is obtained. Utilization of the unequal filling of the ballonets is commonly used for airship trimming.

Determination of the tensor of moments and products of inertia is performed analogously to derivation of the mass characteristics and requires the analysis of point and distributed elements. In general, the tensor of inertia is expressed with respect to the mass center of the airship CG. With the altitude variation the change of the inertia tensor should be also considered as the mass characteristics of the airship change.

2.4.2 Gravity Terms

The external gravity force component exerts a force along the earth geodetic z_g axis and is proportional to the total mass of the airship. Because the center of mass coincides with the center of gravity CG and is different to the center of the body reference CR, the gravity force produces external moments about the body reference point. If the gravity force is to be defined as

$$\boldsymbol{F}_g^G = \begin{bmatrix} 0 \\ 0 \\ mg \end{bmatrix}_g , \tag{2.19}$$

then transformation from geodetic into body fixed reference frame is performed using equation (2.2):

$$\begin{aligned} \boldsymbol{F}^G &= \boldsymbol{T}_{fg}\boldsymbol{F}_g^G \\ \boldsymbol{Q}^G &= \boldsymbol{r}_{CG} \times \boldsymbol{F}^G. \end{aligned} \tag{2.20}$$

The total mass of the airship and its center CG should be computed under considerations given in subsection 2.4.1 due to variations of the ballonets.

2.4.3 Static Buoyancy Effects

The static buoyancy terms are derived from a well known principle of aerostatics. The upward buoyancy force of a body immersed into a media is equal to the weight of the displaced media:

$$\boldsymbol{F}_g^B = \begin{bmatrix} 0 \\ 0 \\ -\rho_A g V \end{bmatrix}_g . \tag{2.21}$$

Transforming the buoyancy force into body fixed coordinates, as with the case of gravity force, the components of the buoyancy are derived:

$$\boldsymbol{F}^B = \boldsymbol{T}_{fg}\boldsymbol{F}_g^B. \tag{2.22}$$

As the shape of airship's body remains unchanged, its displaced volume V and the center of buoyancy CB are regarded as constant. The point of the applied buoyancy force can be determined by taking an integral of the volume distribution along the airship body axes. The induced moment with respect to the center of reference is regarded as:

$$\boldsymbol{Q}^B = \boldsymbol{r}_{CB} \times \boldsymbol{F}^B. \tag{2.23}$$

It is fair to assume that for conventional airships the center of buoyancy CB coincides with the volumetric center of the hull $CV = CR$. Hence, the offset $\boldsymbol{r}_{CB}$ can be neglected and the buoyancy moment results in a zero length vector $\boldsymbol{Q}^B = \boldsymbol{0}$.

2.4.4 Thrust Terms

The thrust force is generated from the reaction force of the air on the rotating propeller. During normal flight operation, vector thrusting is not applied. For simplicity, we can conclude that the thrust force is attached only to the x-axis of the body reference

$$\boldsymbol{F}^T = \begin{bmatrix} X^T \\ 0 \\ 0 \end{bmatrix}. \tag{2.24}$$

Due to the relatively small rotational rates of the main thrust engine, any effects of spinning rotors can be neglected. Moreover, it is assumed that the aerodynamically induced rolling moment of the stern propeller is small enough to not induce a significant aerodynamic rolling moment around the body x-axis [6]. Therefore, the induced thrust moment is a vector of zero length, i.e.

$$\boldsymbol{Q}^T = \boldsymbol{r}_{CT} \times \boldsymbol{F}^T = \begin{bmatrix} 0 \\ 0 \\ 0 \end{bmatrix}. \tag{2.25}$$

2.4.5 Airship Aerodynamics

An accurate modelling of aerodynamic phenomena that appears due to relative motion between the flight vehicle and the atmosphere, is of primary importance in building of the flight mechanical model. Throughout the motion of an airship, a complicated flow distribu-

tion occurs along its body. There are number of existing studies that examine the aerodynamic properties of airships [10], [24], [52].

Reference [26] is devoted to theoretical investigation of airship aerodynamics. As an outcome, a closed form analytical aerodynamic model is derived. It is based on geometrical characteristics of a conventional airship and a set of semi-empirical parameters. The model covers a modelling of flow phenomena for steady linear and curvilinear flight, accelerated motion, steady and unsteady winds. Important modelling issues are recapitulated in Appendix B.4.

Accounting for Unsteady Aerodynamics

According to formulations derived in B.4, the aerodynamic description of an airship can be divided onto two main terms. The first term accounts for a steady aerodynamics together with unsteady wind influence, whereas the second term is used to describe the unsteady motion:

$$\begin{aligned} \boldsymbol{F}^A &= \boldsymbol{F}^A(\boldsymbol{V}_A,\ \Omega,\ \dot{\boldsymbol{V}}_W) + \boldsymbol{F}^A(\dot{\boldsymbol{V}}_K,\ \dot{\Omega}) \\ \boldsymbol{Q}^A &= \boldsymbol{Q}^A(\boldsymbol{V}_A,\ \Omega,\ \dot{\boldsymbol{V}}_W) + \boldsymbol{Q}^A(\dot{\boldsymbol{V}}_K,\ \dot{\Omega}). \end{aligned} \tag{2.26}$$

The terms containing unsteady motion $\boldsymbol{F}^A(\dot{\boldsymbol{V}}_K,\ \dot{\Omega})$ and $\boldsymbol{Q}^A(\dot{\boldsymbol{V}}_K,\ \dot{\Omega})$ represent the apparent mass effects. They can be further rearranged to a linear form, describing translational and rotational accelerations respectively

$$\begin{aligned} \boldsymbol{F}^A(\dot{\boldsymbol{V}}_K,\ \dot{\Omega}) &= -\rho \boldsymbol{F}_{11}\dot{\boldsymbol{V}}_K - \rho \boldsymbol{F}_{12}\dot{\Omega} \\ \boldsymbol{Q}^A(\dot{\boldsymbol{V}}_K,\ \dot{\Omega}) &= -\rho \boldsymbol{F}_{21}\dot{\boldsymbol{V}}_K - \rho \boldsymbol{F}_{22}\dot{\Omega}, \end{aligned} \tag{2.27}$$

where the matrices $\boldsymbol{F}_{11}$, $\boldsymbol{F}_{12}$, $\boldsymbol{F}_{21}$, $\boldsymbol{F}_{22}$ are derived from modelling the accelerated flow around a rotation-symmetric ellipsoidal body using potential flow theory [36]. The common representation of the apparent mass terms is

$$\begin{aligned} F_{11} &= V\begin{bmatrix} k_1 & 0 & 0 \\ 0 & k_2 & 0 \\ 0 & 0 & k_3 \end{bmatrix}, & F_{12} &= \mathbf{0}, \\ F_{21} &= \mathbf{0}, & F_{22} &= \begin{bmatrix} 0 & 0 & 0 \\ 0 & k'I_{yy} & 0 \\ 0 & 0 & k'I_{zz} \end{bmatrix}, \end{aligned} \tag{2.28}$$

where k_1, k_2, k_3 and k' are the hull's geometry dependent coefficients- Munk factors and V denotes the volume of the airship's hull [60].

Modification of Equations of Motion

Without a great effort, the derived aerodynamic part of the flight mechanical model can be incorporated in the equations of motion. By substituting equations (2.26) and (2.27) into (2.12) and rearranging the instationary aerodynamics terms (due to body acceleration) onto left hand side, the original equation of motion yields

$$\begin{bmatrix} m\boldsymbol{E} + \rho \boldsymbol{F}_{11} & -m\boldsymbol{r}_{CG}^{X} \\ m\boldsymbol{r}_{CG}^{X} & \boldsymbol{I} + \rho \boldsymbol{F}_{22} \end{bmatrix} \begin{bmatrix} \dot{\boldsymbol{V}}_K \\ \dot{\Omega} \end{bmatrix} = \begin{bmatrix} -\Omega \times (\boldsymbol{V}_K + \Omega \times \boldsymbol{r}_{CG}) m \\ -\Omega \times (\boldsymbol{I}\Omega) - (m \cdot \boldsymbol{r}_{CG} \times (\Omega \times \boldsymbol{V}_K)) \end{bmatrix} + \\ + \begin{bmatrix} \boldsymbol{F}^B + \boldsymbol{F}^G + \boldsymbol{F}^T + \boldsymbol{F}^A(\boldsymbol{V}_A,\ \Omega,\ \dot{\boldsymbol{V}}_W) \\ \boldsymbol{Q}^B + \boldsymbol{Q}^G + \boldsymbol{Q}^T + \boldsymbol{Q}^A(\boldsymbol{V}_A,\ \Omega,\ \dot{\boldsymbol{V}}_W) \end{bmatrix}. \tag{2.29}$$

The apparent mass and inertia effects are regarded now as additional mass and inertia terms and not as a part of the aerodynamic description of the model. The presented formulation of the instationary aerodynamics as a part of the generalized mass matrix has become, meanwhile, a standard form for describing airship dynamics, as also reported in other studies [10], [52].

Experimental Database from Wind Tunnel Tests

Together with the theoretical investigations on airship aerodynamics, the knowledge from various experiments is also of a great importance. Therefore a group of researches from the Institute of Aerodynamics and Gas Dynamics (IAG) of the University of Stuttgart have been involved in determining the airship aerodynamics from wind tunnel experiments. The experiments have been carried out with a scaled model of the “Lotte” airship.

The aerodynamic database was obtained as a result of wind tunnel tests and delivers a set of stationary aerodynamic coefficients of forces

$$c_D(\alpha,\ \beta,\ \eta),\ c_L(\alpha,\ \beta,\ \eta)$$

and moments

$$c_m(\alpha,\ \beta,\ \eta),\ c_n(\alpha,\ \beta,\ \zeta),$$

measured at different angles of attack α, sideslip angles β and at different levels of the control surfaces η, ζ. The main objectives were the determination of the main aerodynamic coefficients, a detailed study of the three-dimensional boundary layer development, and especially, the study of the flow behavior at the tail area of the model. Some results of these experiments are illustrated in Figure 2.6. A detailed overview of the obtained results is given

in [8] and [38]. One remarkable property of the airship aerodynamics is the positive gradient of the pitching moment (see Figure 2.6(c)):

$$\frac{d}{d\alpha}c_m(\alpha,\ \beta,\ \eta=0)>0 \qquad \text{at} \qquad |\alpha|\le 10°,$$

and hence the aerodynamic instability of the static pitching moment c_m. Due to geometrical symmetry of the airship Lotte in the horizontal-XY and the vertical-XZ plains, the aerodynamic instability appears also for the static yawing moment c_n at $|\beta|\le 10°$.

The obtained aerodynamic database has been also utilized in [26] for fitting the analytically derived aerodynamic model with the experimental data at different levels of flow angles, as illustrated in Figure 2.6.

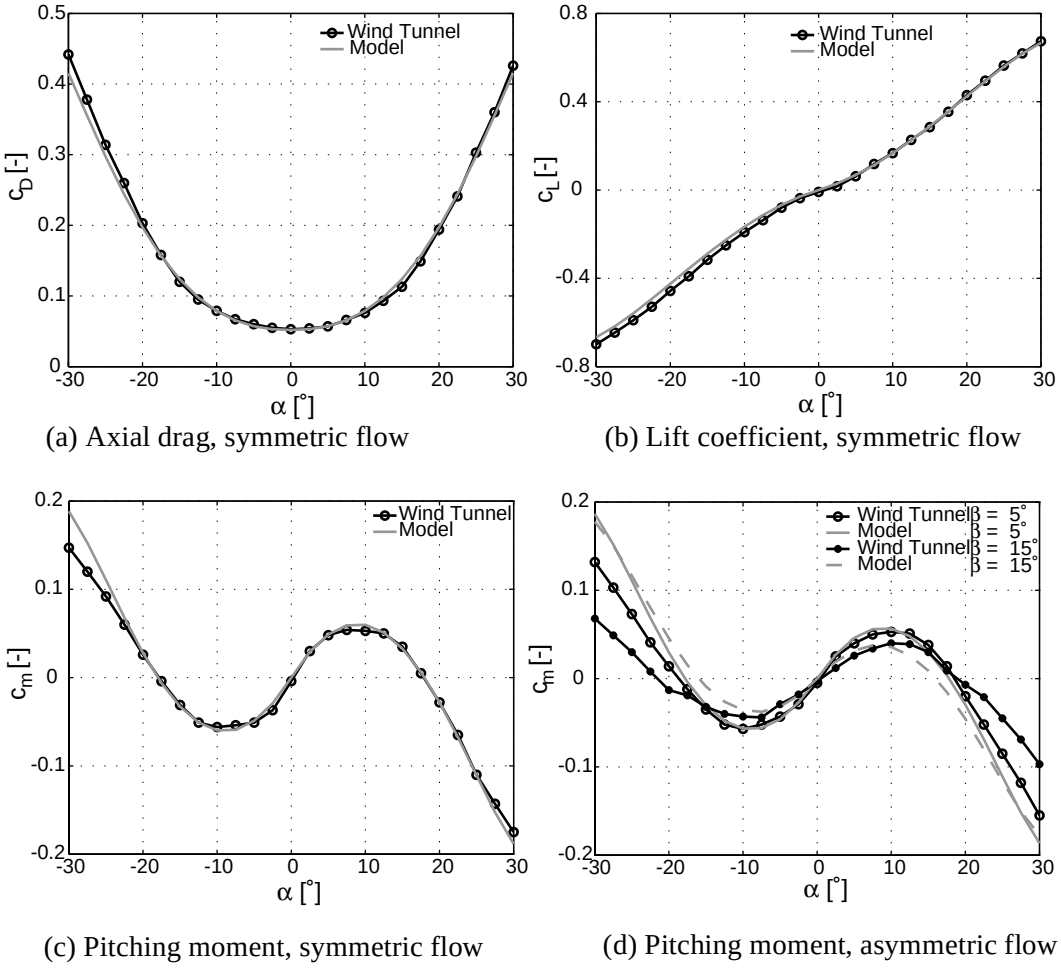

(a) Axial drag, symmetric flow

(b) Lift coefficient, symmetric flow

(c) Pitching moment, symmetric flow

(d) Pitching moment, asymmetric flow

Figure 2.6: Results of wind tunnel measurements and predictions of analytical aerodynamic model [26].

2.5 Nonlinear Observation Equations

2.5.1 Requirements and Limitations

The basic requirement for selecting the measurement quantities is to get sufficient information about the processes involved in the system dynamics. On the other hand, to provide extensive information about the dynamics of the airship, all measurement quantities should be classified by:

- Inertial measurements
- Relative airstream measurements
- Measurements of control variables
- Auxiliary measurements

All these items will be individually discussed in the following subsections.

It should be pointed out that availability and configuration of sensors pose additional constraints on the measurement equipment. Requirements of the payload, power consumption and sensor placement are the key issues that should be accepted for any flight vehicle. Therefore, under given constraints, this section will be mainly focused on the “Lotte” specific measurement setup. The practical realization of the measurement equipment is provided in Chapter 5. Figure 2.7 provides a schematic overview of main locations of measurement instrumentation. Their geometric offsets from the reference center are given in Appendix A.

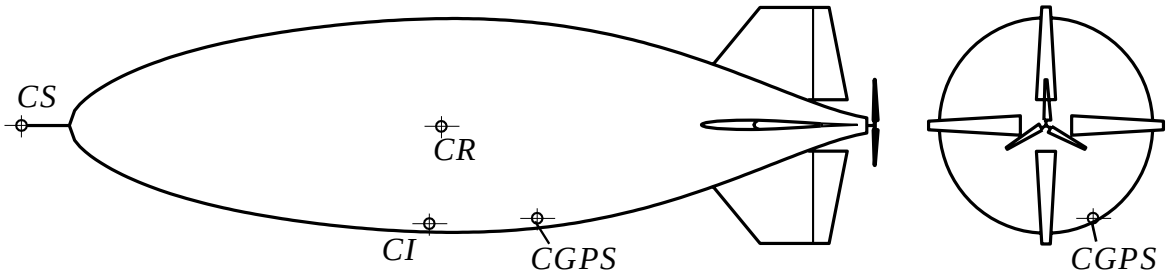

Figure 2.7: Main instrumentation locations of “Lotte” airship

2.5.2 Inertial Measurements

For measuring the inertial variables, accelerometers and rotational gyros are commonly utilized. The relations describing acceleration with motion variables are similar to that used for determination of dynamics in body reference frame and consist of the pure kinematic dependencies

$$\boldsymbol{a}_{CI} = \dot{\boldsymbol{V}}_K + \dot{\Omega}\times \boldsymbol{r}_{CI} + \Omega\times \boldsymbol{V}_K + \Omega\times (\Omega\times \boldsymbol{r}_{CI}) \,, \tag{2.30}$$

where CI reference indicates the position of the inertial measurements.

Under assumption of the rigid body, the measured values of rotation rates and Euler angles are the same at any point of airship:

$$\Omega_{CI} = \Omega, \tag{2.31}$$

$$\phi_{CI} = \phi, \theta_{CI} = \theta, \psi_{CI} = \psi. \tag{2.32}$$

Recent developments in satellite navigation have tremendously improved estimation quality of 3D position and velocity for civil users. Due to this fact, the Lotte airship is additionally equipped with the GPS receiver for acquiring the inertial velocity measurements. As the measurements are performed in geodetic frame, a transformation into body frame is required:

$$\{\boldsymbol{V}_{K|CGPS}\}_g = \boldsymbol{T}_{gf} \cdot (\boldsymbol{V}_K + \Omega \times \boldsymbol{r}_{CGPS}) . \tag{2.33}$$

2.5.3 Airstream Measurements

The aerodynamic forces and moments are proportional to the relative airstream distribution along the airship body. Hence, the availability of the airstream measurements is necessary for determination of the aerodynamic part of the flight mechanical model.

The airstream velocity sensor should provide information about current flow velocity and its direction at the measurement point CS. For aerodynamic purposes, it is preferable to locate the airstream sensor at places where the free-stream velocities could be measured avoiding interaction from the vehicle's body. In the hardware setup of the Lotte airship, the sensor is located at the end of the nose-boom CS (see Figure 2.7)

$$\boldsymbol{V}_{A|CS} = \boldsymbol{V}_{K|CS} - \boldsymbol{V}_{W|CS} , \tag{2.34}$$

where $\boldsymbol{V}_{K|CS}$ is the flight path velocity at the nose boom location

$$\boldsymbol{V}_{K|CS} = \boldsymbol{V}_K + \Omega \times \boldsymbol{r}_{CS} . \tag{2.35}$$

2.5.4 Measurements of Control Variables

The control of the airship is obtained by variation of the control surfaces on the fins or by variation of the thrust. Therefore, one of the important issues is the provision of measurements of the controls during flight experiments. As defined in 2.2.3, the airship is controlled by the surface deflections of fins and by the stern propeller.

In the up-to-date hardware realization there are no measurement devices installed, which directly indicate the state of the control surfaces and the thrust force. Pilot only commanded inputs could be stored by the flight recorder.

For handling the flap deflections it was possible to derive a model which accurately approximates the dynamics of the flaps as a function of the pilot commands:

$$\zeta = \zeta(\delta_{\zeta,\text{Pilot}})$$
$$\eta = \eta(\delta_{\eta,\text{Pilot}})$$
$$\xi = \xi(\delta_{\xi,\text{Pilot}}).$$

The actuator model is based on common servo actuator dynamics [4] and calibrated accurately during ground base tests. Some testing results are illustrated in Figure 2.8, where the model response has been compared with measured flap angles under different loads. Small modelling errors of the fin actuators have a minor influence in the overall identification process and hence have been ignored here.

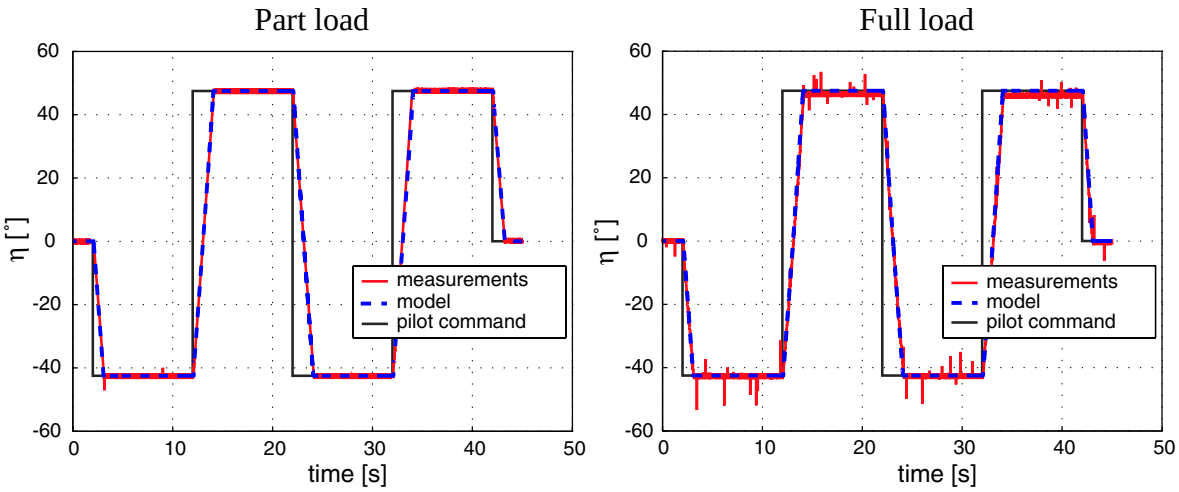

Figure 2.8: Comparison of flap model responses with measured flap deflections at different loads

Modelling the thrust dynamics is a much more elaborate process in comparison to that of the fin dynamics. The complex dynamics of thrust force depends not only on the rotational velocity of the stern propeller, but also on the airstream velocity distribution at the rear part of the airship. Therefore, verification of the thrust model using ground tests is impossible. In such a case the thrust measurement is achieved through measurement of strain between the airship body and mounting points of the thrust engine. However, this possibility was not available in the current measurement setup of the Lotte airship and, therefore, no thrust measurements were available.

2.5.5 Auxiliary Measurements

The purpose of the auxiliary measurement sources is not to deliver a direct measure of motion and control variables. They are mainly intended to measure the thermodynamic properties of the surrounding (Air) and the inner (Helium) gases.

For determining the atmospheric density ρ_A, the airship "Lotte" is equipped with the barometric P_A and temperature T_A sensors. At any flight condition, the density can be calculated/approximated with formula:

$$\rho_A = \frac{P_A}{R_A T_A},$$

where R_A is the gas constant $R_A = 287$ [J/(kgK)].

Variations of the total mass m, location of CG and inertia tensor $\boldsymbol{I}$ are mainly influenced by the change of atmospheric pressure. Their characteristics could be estimated during the flight, if additional pressure and temperature measurements of the Helium are available. For this purpose, the "Lotte" airship is equipped with inner temperature and pressure sensors.

Chapter 3

Model Simplification for Identification Purposes

3.1 General Remarks

3.1.1 Requirements on Identification Model

The flight mechanical model of the airship “Lotte” presented in Chapter 2 represents a very complicated structure. The equations of motion are strongly nonlinear in terms of the model variables. Especially the aerodynamic part of the model poses significant uncertainties in describing the aerodynamically induced forces and moments.

Approaches for analyzing the dynamic behavior of the derived nonlinear model are very restricted. From the other side, the goal of the system identification is determination of the model parameters from the experimental data, and this implies a determination of the model structure that meets two basic objectives. The first objective addresses the model structure definition that combines the essential physics of the plant (the conformity of the flight mechanical model to the physical processes, which appear during the flight, was established in the previous chapter). The second requirement demands the model description, its structure and parameterization in a simple and distinct way (as acceptable e.g. for the control design) and will be briefly explained in the following.

The integral part of the system identification problem is the parameter optimization procedure. During the optimization, the model parameters are adjusted in a way to provide a trajectory fit between the model response and the experimental data. The identification problem turns at this stage into a classical optimization problem. The optimization problem is a field of its own and is not the major topic of this thesis. However, one important extraction from the optimization theory should be mentioned. It is well known, that along with the chosen optimization method, the result also strongly depends upon formulation of the optimization problem [7]. This means the choice of the model structure and the number of the optimized parameters that are relevant to the chosen cost function (Figure 3.1). Otherwise, a poorly formulated problem can not be efficiently optimized. A careful choice of the model structure and its parametrization is one of the central problems of the system identification.

There is no transparent theory available that helps to maintain good model integrity whilst allowing unnecessary complications to be discarded. Regardless of its complexity, the mathematically described model will be still not reflect the real dynamics of the plant accurately. One of the most important factors in selecting a suitable model structure and its parametrization is based on “engineering judgement” [18]. This assessment is mainly deduced from the a priori knowledge about the physical plant. How this judgement is related to the airship identification problem, will be discussed within the following subsection.

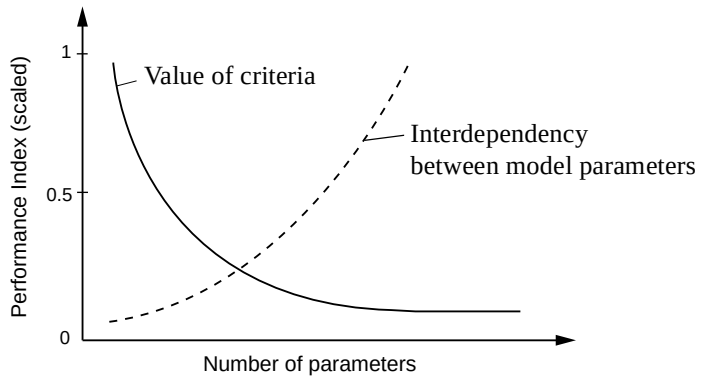

Figure 3.1: Optimization criteria and parameter interdependency versus number of model parameters [59]

3.1.2 Linear Identification of Airship Dynamics: Motivation

The emphasis of this work is on estimating the airship dynamics using linear time invariant models. The linear system identification was dictated by the fact that many physically meaningful parameters of the nonlinear flight mechanical model could not be clearly determined. These deficits arose from:

- Uncertain mass model including the mass m, the moment of inertia $\boldsymbol{I}$, and the center mass position $\boldsymbol{r}_{CG}$
- Availability of only static aerodynamical database in terms of c_L, c_D, c_m
- Inability to provide the thrust measurements $\boldsymbol{F}^T$

Although the mass can be well described in terms of internal components and a change of the environmental conditions (see Section 2.4.1), its accurate determination in practice was not possible. This difficulty was mainly caused by inability to derive the complete configuration database with the weight and position information for the whole set of internal elements. For instance, in order to determine some internal parts that constitute the nominal mass m_R in equation (2.18), only a subjective estimation of weight parts was used [27]. Additional uncertainties have been caused by limited information about the pre-launch state of the air ballonets.

Experience gained in the aircraft identification field shows that estimation of uncertain aerodynamic characteristics presumes a correct knowledge of the mass model [45]. A simul-

taneous determination of the mass and aerodynamic terms of the model from flight data leads, usually, to very poor results, mainly caused by a linear dependency between the mass and aerodynamic coefficients (using symbolic processing tools, e.g. Mathematica, it is easy to observe the linear dependence between mass and aerodynamic parameters). A similar problem occurs when the thrust force of the main engine is estimated along with the aerodynamic axial drag force.

A possibility to avoid identification of the mass and aerodynamic parts explicitly is to estimate dimensional stability and control derivatives, i.e. the parameters of a linearized model. This approach is justified if care of the approximation validity is taken. In this case, small perturbations about some steady operational condition are allowed. Several advantages benefit the linear identification of a flight vehicle:

- Using this approach, the direct methods of control system design can be utilized
- Elimination of coupling effects by considering the longitudinal and lateral-directional motion separately reduces the model complexity and the number of its parameters
- A linear representation of the model makes the identification problem more plausible than for a nonlinear model; in some cases the model parameters can be determined in a single batch operation
- The linear identification is more appropriate when large amounts of the flight data need to be evaluated, which is common in flight testing
- Additional benefit is acquired, if the system is being disturbed by signals of a stochastic nature; this fact allows for a direct application of optimal (e.g. Kalman) filters to account for such disturbances

Along with the above given advantages, several drawbacks exist which must be taken into account when the linear identification is performed. The most general can be distinguished by:

- Single point identification: as mentioned this approach is valid only at steady conditions and small deviations from them
- Due to linearization procedure, the derived linear system often looses a physically meaningful interpretation of its parameters; if a constrained optimization of the model parameters is utilized, it is difficult to assign the bounds properly
- Necessity to achieve sufficient steady conditions of the flight envelope is a very time consuming task for the test pilot and the ground crew

3.2 Linearized Dynamic and Observation Equations

Many classical references are devoted to linearization techniques of nonlinear equations of motion of a convenient aircraft [6], [47]. The linearization of the dynamic equations of an airship is performed in a similar manner by taking the first order derivatives of the Taylor series expansion about the equilibrium condition.

If an airship operates within small perturbations about some steady rectilinear motion, then its complete dynamic behavior can be approximated by two independent sets of dynamic equations, i.e. the well known *longitudinal* and the *lateral-directional* equations of motion [29]. The longitudinal and the lateral-directional dynamics can be studied separately, without accounting for the cross-coupling effects, assuming them negligible.

3.2.1 Assumptions on Flight Condition, Environmental and Configuration Properties

For getting a simplified form of the airship dynamics an assumption of the steady atmosphere can be adopted at the first stage. In this case all flight path variables are identical to their relative quantities $\boldsymbol{V}_K = \boldsymbol{V}_A$ and the effects due to an accelerated wind (see B.4.1) do not appear.

The baseline of the model reduction concerns a consideration of a steady flight condition. For this kind of motion all linear and rotational accelerations in the equation (2.12) have zero values:

$$\begin{bmatrix} \dot{u}_K \\ \dot{v}_K \\ \dot{w}_K \end{bmatrix} = \begin{bmatrix} \dot{p} \\ \dot{q} \\ \dot{r} \end{bmatrix} = \begin{bmatrix} 0 \\ 0 \\ 0 \end{bmatrix}. \tag{3.1}$$

Steady flight requires an equilibrium between the kinematic coupling terms (Equation (2.12)) and the vector that represents the net external force $\boldsymbol{F}^{\Sigma}$ and moments $\boldsymbol{Q}^{\Sigma}$. Such a balance holds for two basic flight conditions: the steady rectilinear flight and steady turning flight. Both are valid and produce stationary motion.

Similarly to the classical flight mechanics of airplanes, the steady rectilinear motion is of major interest because of the ability to separate the total dynamics into two independent sets of equations using linearization technique [6]. For further examination of the system dynamics the steady turning motion of the airship will be excluded. The steady rectilinear flight gives a rotation-free motion and zero side velocity

$$p_0 = q_0 = r_0 = 0, \quad v_0 = 0. \tag{3.2}$$

The subscript 0 denotes a condition where equilibrium is achieved. Because of the vertical symmetry in the mass and the aerodynamics, the following simplifications are valid:

$$\phi_0 = 0, \quad \zeta_0 = \xi_0 = 0. \tag{3.3}$$

The conditions of the equations (3.2) and (3.3) result to zero side force as well as the roll and yaw moments respectively

$$Y^{\Sigma} = 0\,,\; L^{\Sigma} = 0\,,\; N^{\Sigma} = 0\,. \tag{3.4}$$

Another assumption can be made if the airship operates at nearly constant altitude. At this operation condition, variations of the air density, the airship mass, moment of inertia and the position of the center of gravity CG can be neglected:

$$\rho_A \approx \text{const}\,,\; m \approx \text{const}\,,\; \boldsymbol{I} \approx \text{const},$$

$$x_{CG} \approx \text{const}\,,\; z_{CG} \approx \text{const}\,. \tag{3.5}$$

Moreover, the axial offset of the center mass from the center of reference can be assumed to have an infinitely small value

$$|x_{CG}| \ll 1\,.$$

It follows from this fact that the test pilot always performs an obligatory ground trimming procedure before the flight takes place. Its aim is to minimize the static pitching moment at zero pitch angles

$$|M(\theta)|\big|_{\theta = 0} \Rightarrow \min.$$

In this configuration the x_{CG} position does not change greatly with variation of height, as concluded in section 2.4.1, and therefore, can be neglected for all altitude changes $x_{CG} \approx 0$.

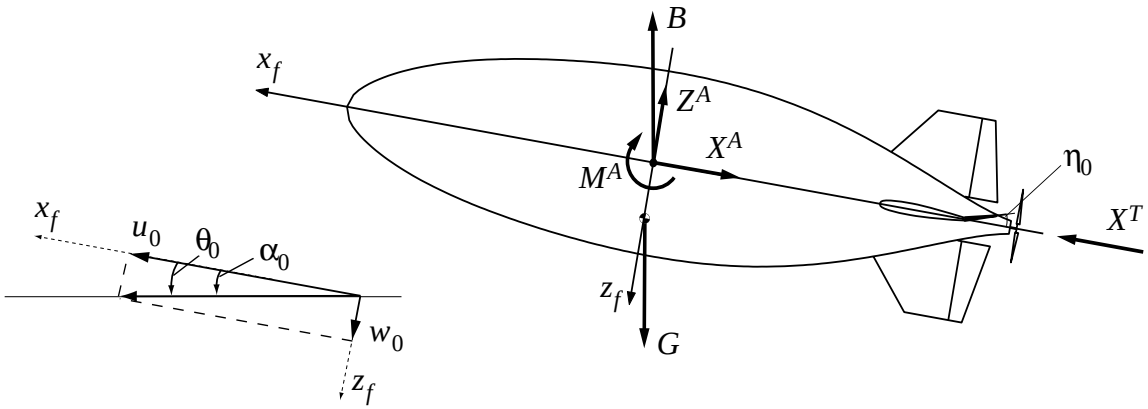

Figure 3.2: Steady-state equilibrium condition in rectilinear flight

Under given conditions, the steady rectilinear motion can now be described as a projection to the vertical plane. Figure 3.2 highlights the respective forces acting on airship in steady rectilinear flight. The remaining nonzero motion variables are now expressed by the

corresponding axial and vertical velocities u_0 and w_0, the pitch attitude θ_0, the elevator deflection angle η_0 and the throttle T_0.

The equilibrium condition in the vertical plane yields

$$\begin{aligned} X^{\Sigma} &= 0 = X^{A}(u_0,\ w_0,\ \eta_0) + X^{T}(u_0,\ T_0) + (B-G)\sin\theta_0 \\ Z^{\Sigma} &= 0 = Z^{A}(u_0,\ w_0,\ \eta_0) - (B-G)\cos\theta_0 \\ M^{\Sigma} &= 0 = M^{A}(u_0,\ w_0,\ \eta_0) - z_{CG}G\sin\theta_0\ . \end{aligned} \tag{3.6}$$

3.2.2 Linearized Longitudinal Dynamic Equations

Assuming a steady condition of the rectilinear flight at the constant altitude, the perturbed longitudinal motion involves small perturbations of motion u, w, q, θ and control η, T variables respectively about their trimmed values. The linearized longitudinal dynamic equations are derived by linearizing the nonlinear equations of motion (2.29) and taking the parts (motion/control terms and force/moment derivatives) which are related to the longitudinal motion. It can be established as

$$\begin{aligned} (m - X_{,\dot{u}})\delta\dot{u} + mz_{CG}\delta\dot{q} &= -mw_0\delta q + X_{,u}\delta u + X_{,q}\delta q + X_{,\theta}\delta\theta + X_{,T}\delta T \\ (m - Z_{,\dot{w}})\delta\dot{w} &= mu_0\delta q + Z_{,w}\delta w + Z_{,q}\delta q + Z_{,\theta}\delta\theta + Z_{,\eta}\delta\eta \\ mz_{CG}\delta\dot{u} + (I_{yy} - M_{,\dot{q}})\delta\dot{q} &= -mz_{CG}w_0\delta q + M_{,u}\delta u + M_{,w}\delta w + M_{,q}\delta q + M_{,\theta}\delta\theta + M_{,\eta}\delta\eta \\ \delta\dot{\theta} &= \delta q, \end{aligned} \tag{3.7}$$

where the state and control variables are interpreted as small deviations from the reference flight condition ($\delta u = u - u_0$, …). The analytical derivation of the force and moment derivatives is outlined in B.5.

In examining particular force and moment derivatives, it was found that for a nominal rectilinear flight, some of derivatives in equation (3.7)(3.7) can be neglected [26]. The classification of their dominance is summarized in Table 3.1.

Table 3.1: Classification of derivatives for longitudinal motion [26]

Quantity	**Dominant derivatives**	**Insignificant derivatives**
Axial force X	$X_{,\dot{u}}$, $X_{,u}$, $X_{,\theta}$, $X_{,T}$	$X_{,w}$, $X_{,q}$, $X_{,\eta}$
Vertical force Z	$Z_{,\dot{w}}$, $Z_{,w}$, $Z_{,q}$, $Z_{,\eta}$	$Z_{,u}$, $Z_{,\theta}$ $Z_{,\delta}$
Pitching moment M	$M_{,\dot{q}}$, $M_{,w}$, $M_{,q}$, $M_{,\theta}$, $M_{,\eta}$	$M_{,u}$, $M_{,\delta}$

Because of the apparent mass effects are independent of trimmed velocity, they begin to influence the dynamic response of the airship at already low velocities. These effects are

appropriately modelled by the $X_{,\dot{u}}$, $Z_{,\dot{w}}$, and $M_{,\dot{q}}$ terms at the left hand side in equation (3.7).

Two differences can be observed when comparing equation (3.7) with the aircraft's classical linearized equations [6]. First, due to the fact that the center of gravity CG does not coincide with the center of reference CR, the perturbation of pitch rate δq and the perturbed forward velocity δu are coupled. Second, from the offset of the mass center from the center of reference, the gravitational force exerts a nonzero static pitching moment and is expressed through the $M_{,\theta}\delta\theta$ term in the moment equation.

In order to derive a conventional state space representation of the longitudinal dynamics, equation (3.7) should be slightly transformed by multiplying both sides with the inverse mass matrix

$$\dot{\boldsymbol{x}}_{lon} = (\boldsymbol{M}'_{lon})^{-1}\boldsymbol{A}'_{lon}\boldsymbol{x}_{lon} + (\boldsymbol{M}'_{lon})^{-1}\boldsymbol{B}'_{lon}\boldsymbol{u}_{lon} = \boldsymbol{A}_{lon}\boldsymbol{x}_{lon} + \boldsymbol{B}_{lon}\boldsymbol{u}_{lon}\,, \tag{3.8}$$

with the respective state and control vectors

$$\boldsymbol{x}_{lon} = \left[\delta u \;\; \delta w \;\; \delta q \;\; \delta\theta\right]^T,\; \boldsymbol{u}_{lon} = \left[\delta\eta \;\; \delta T\right]^T, \tag{3.9}$$

and the system matrices, omitting small derivatives, can be expressed by

$$\begin{aligned}
\boldsymbol{M}'_{lon} &= \begin{bmatrix} m - X_{,\dot{u}} & 0 & mz_{CG} & 0 \\ 0 & m - Z_{,\dot{w}} & \sim 0 & 0 \\ mz_{CG} & \sim 0 & I_{yy} - M_{,\dot{q}} & 0 \\ 0 & 0 & 0 & 1 \end{bmatrix}, \\
\boldsymbol{A}'_{lon} &= \begin{bmatrix} X_{,u} & \sim 0 & -mw_0 & X_{,\theta} \\ \sim 0 & Z_{,w} & Z_{,q} + mu_0 & \sim 0 \\ \sim 0 & M_{,w} & M_{,\dot{q}} - mz_{CG}w_0 & M_{,\theta} \\ 0 & 0 & 1 & 0 \end{bmatrix}, \qquad \boldsymbol{B}'_{lon} = \begin{bmatrix} \sim 0 & X_{,T} \\ Z_{,\eta} & \sim 0 \\ M_{,\eta} & \sim 0 \\ 0 & 0 \end{bmatrix}.
\end{aligned} \tag{3.10}$$

The obtained matrices $\boldsymbol{A}_{lon} = (\boldsymbol{M}'_{lon})^{-1}\boldsymbol{A}'_{lon}$ and $\boldsymbol{B}_{lon} = (\boldsymbol{M}'_{lon})^{-1}\boldsymbol{B}'_{lon}$ contain typical flight mechanical stability and control derivatives respectively

$$\boldsymbol{A}_{lon} = \boldsymbol{M}'^{-1}_{lon}\boldsymbol{A}'_{lon} = \begin{bmatrix} X_u & X_w & X_q & X_\theta \\ \sim 0 & Z_w & Z_q & \sim 0 \\ M_u & M_w & M_q & M_\theta \\ 0 & 0 & 1 & 0 \end{bmatrix}, \; \boldsymbol{B}_{lon} = \boldsymbol{M}'^{-1}_{lon}\boldsymbol{B}'_{lon} = \begin{bmatrix} X_\eta & X_\delta \\ Z_\eta & 0 \\ M_\eta & M_\delta \\ 0 & 0 \end{bmatrix}. \tag{3.11}$$

Because of the kinematic coupling effect between the u and q states (induced by the inverted mass matrix $\boldsymbol{M}'^{-1}_{lon}$), some stability and control derivatives result in nonzero values. The airship stability and control derivatives are similar to the conventional aircraft derivatives, but they are more complex and can not be simply interpreted. The analytical form of the stability and control derivatives can be found in reference [26] and are outlined in B.5.

3.2.3 Linearized Lateral-Directional Dynamic Equations

The linearized lateral-directional equation of motion can be derived in a similar manner as for the longitudinal dynamics. It involves small perturbations of motion v, p, r, ϕ, ψ and control ζ, ξ variables respectively. In general, the yaw angle ψ does not exert any influence on the dynamics, and therefore can be disregarded in lateral-directional dynamic equations. Assuming the cross coupling effects with the longitudinal variables as negligible, the common form of the linearized lateral-directional perturbed motion of airship yields

$$\begin{aligned}
(m - Y_{,\dot{v}})\delta\dot{v} - mz_{CG}\delta\dot{p} &= -mw_0\delta p + mu_0\delta r + Y_{,v}\delta v + Y_{,p}\delta p + Y_{,r}\delta r + Y_{,\phi}\delta\phi + Y_{,\zeta}\delta\zeta \\
-mz_{CG}\delta\dot{v} + I_{xx}\delta\dot{p} + I_{xz}\delta\dot{r} &= -mz_{CG}w_0\delta p + mz_{CG}u_0\delta r + L_{,v}\delta v + L_{,p}\delta p + \ldots \\
&\quad + L_{,r}\delta r + L_{,\phi}\delta\phi + L_{,\xi}\,\delta\xi \\
I_{xz}\delta\dot{p} + (I_{zz} - N_{,\dot{r}})\delta\dot{r} &= N_{,v}\delta v + N_{,p}\delta p + N_{,r}\delta r + N_{,\phi}\delta\phi + N_{,\zeta}\delta\zeta \\
\delta\dot{\phi} &= \delta p + \tan\theta_0\delta r,
\end{aligned} \tag{3.12}$$

where all perturbations occur around zero trim values of the lateral-directional variables ($v_0 = 0$, …).

In the lateral-directional perturbed motion, only dominant force and moment derivatives, as given in Table 3.2, are important [26].

Table 3.2: Classification of derivatives for lateral-directional motion [26]

Quantity	Dominant derivatives	Insignificant derivatives
Side force Y	$Y_{,\dot{v}}$, $Y_{,v}$, $Y_{,r}$, $Y_{,\zeta}$	$Y_{,p}$, $Y_{,\xi}$
Rolling moment L	$L_{,p}$, $L_{,\phi}$, $L_{,\xi}$	$L_{,v}$, $L_{,r}$
Pitching moment M	$N_{,v}$, $N_{,r}$, $N_{,\zeta}$	$N_{,p}$, $N_{,\phi}$

Analogously to derivation of the longitudinal model, the lateral-directional dynamic equations can be represented using the state-space form

$$\dot{\boldsymbol{x}}_{lat} = (\boldsymbol{M}'_{lat})^{-1}\boldsymbol{A}'_{lat}\boldsymbol{x}_{lat} + (\boldsymbol{M}'_{lat})^{-1}\boldsymbol{B}'_{lat}\boldsymbol{u}_{lat} = \boldsymbol{A}_{lat}\boldsymbol{x}_{lat} + \boldsymbol{B}_{lat}\boldsymbol{u}_{lat}\,, \tag{3.13}$$

with the respective state and control vectors

$$\boldsymbol{x}_{lat} = \left[\delta v \;\; \delta p \;\; \delta r \;\; \delta\phi\right]^T, \; \boldsymbol{u}_{lat} = \left[\delta\zeta \;\; \delta\xi\right]^T. \tag{3.14}$$

The system matrices without small terms, can be expressed by

$$\begin{aligned}
\boldsymbol{M}'_{lat} &= \begin{bmatrix} m - Y_{,\dot{v}} & -mz_{CG} & \sim 0 & 0 \\ -mz_{CG} & I_{xx} & I_{xz} & 0 \\ \sim 0 & I_{xz} & I_{zz} - N_{,\dot{r}} & 0 \\ 0 & 0 & 0 & 1 \end{bmatrix}, \\
\boldsymbol{A}'_{lat} &= \begin{bmatrix} Y_{,v} & mw_0 & Y_{,r} - mu_0 & \sim 0 \\ \sim 0 & L_{,p} - mz_{CG}w_0 & L_{,r} + mz_{CG}u_0 & L_{,\phi} \\ N_{,v} & \sim 0 & N_{,r} & \sim 0 \\ 0 & 1 & \sim 0 & 0 \end{bmatrix}, \qquad \boldsymbol{B}'_{lat} = \begin{bmatrix} Y_{,\zeta} & 0 \\ 0 & L_{,\xi} \\ N_{,\zeta} & \sim 0 \\ 0 & 0 \end{bmatrix}.
\end{aligned} \tag{3.15}$$

The matrices $\boldsymbol{A}_{lat} = (\boldsymbol{M}'_{lat})^{-1}\boldsymbol{A}'_{lat}$ and $\boldsymbol{B}_{lat} = (\boldsymbol{M}'_{lat})^{-1}\boldsymbol{B}'_{lat}$ contain typical lateral stability and control derivatives:

$$\boldsymbol{A}_{lat} = \boldsymbol{M}'^{-1}_{lat}\boldsymbol{A}'_{lat} = \begin{bmatrix} Y_v & Y_p & Y_r & Y_\phi \\ L_v & L_p & L_r & L_\phi \\ N_v & N_p & N_r & N_\phi \\ 0 & 1 & \sim 0 & 0 \end{bmatrix}, \; \boldsymbol{B}_{lat} = \boldsymbol{M}'^{-1}_{lat}\boldsymbol{B}'_{lat} = \begin{bmatrix} Y_\zeta & 0 \\ 0 & L_\xi \\ N_\zeta & 0 \\ 0 & 0 \end{bmatrix}. \tag{3.16}$$

3.2.4 Linearized Measurement Equations

In section 2.5 the nonlinear relations between the state and the measured variables have been derived. For representation of system dynamics in the state space form, the observation relations should be also established in the linear form. The linearization of measurement equations is performed similarly to that made for nonlinear dynamic model by taking the first order terms of the Taylor series. The measurements of airstream velocity, Euler angles, body rotational rates and accelerations are of the primary importance.

It is common practice to transform all measured variables from the sensor locations to the center of reference CR point [18]. This can be performed using kinematic equations and information derived from the measured velocity and rotational rates. From one side, this transformation simplifies the model structure compared to that which accounts for the measurement offsets. From the other side, the transformation of measured variables into CR point, in particular for the linear accelerations ax_{CI}, ay_{CI}, az_{CI}, requires a component of the angular acceleration as follows from equation (2.30). In general, the numerical differentia-

tion of a noisy measurement results in a signal with a low signal to noise ratio [44]. For this reason it is advantageous to account for the sensor offsets within the observation model.

Longitudinal Observation Model

For the longitudinal motion the observable variables are

$$\boldsymbol{y}_{lon} = \left[\delta u_{A|CS}\ \delta w_{A|CS}\ \delta q\ \delta\theta\ ax_{CI}\ az_{CI}\right]^T. \tag{3.17}$$

To model the offset of the center of airstream measurements CS from the center of the airship reference CR, the necessary rotation about the body y-axis is included. Therefore, linearizing equation (2.34), for the longitudinal motion

$$\begin{aligned} \delta u_{A|CS} &= \delta u + z_{CS}\delta q \\ \delta w_{A|CS} &= \delta w - x_{CS}\delta q, \end{aligned} \tag{3.18}$$

where $\delta u_{A|CS} = u_{A|CS} - u_0$ and $\delta w_{A|CS} = w_{A|CS} - w_0$.

The axial and vertical accelerations are linearized with respect to the longitudinal state variables and expressed by

$$\begin{aligned} ax_{CI} &= \delta\dot{u} + w_0\delta q + z_{CI}\delta\dot{q} \\ az_{CI} &= \delta\dot{w} - u_0\delta q - x_{CI}\delta\dot{q}. \end{aligned} \tag{3.19}$$

The terms of linear body accelerations $\delta\dot{u}$ and $\delta\dot{w}$, and the angular pitch acceleration $\delta\dot{q}$ can be substituted from the linearized system dynamics from equation (3.2). Expanding terms, the linearized form of the acceleration measurements is derived

$$\begin{aligned} ax_{CI} &= X_u\delta u + (X_w + z_{CI}M_w)\delta w + (X_q + z_{CI}M_q + w_0)\delta q + (X_\theta + z_{CI}M_\theta)\delta\theta + \ldots \\ &\qquad + (X_\eta + z_{CI}M_\eta)\delta\eta + (X_\delta)\delta T \\ az_{CI} &= (Z_w - x_{CI}M_w)\delta w + (Z_q - x_{CI}M_q - u_0)\delta q - x_{CI}M_\theta\delta\theta + (Z_\eta - x_{CI}M_\eta)\delta\eta. \end{aligned} \tag{3.20}$$

Transferring the observation model in general state-space form yields

$$\boldsymbol{y}_{lon} = \boldsymbol{C}_{lon}\boldsymbol{x}_{lon} + \boldsymbol{D}_{lon}\boldsymbol{u}_{lon}, \tag{3.21}$$

where the observation-$\boldsymbol{C}_{lon}$ and the feedthrough-$\boldsymbol{D}_{lon}$ matrices are defined respectively:

$$\boldsymbol{C}_{lon} = \begin{bmatrix} 1 & 0 & z_{CS} & 0 \\ 0 & 1 & -x_{CS} & 0 \\ 0 & 0 & 1 & 0 \\ 0 & 0 & 0 & 1 \\ c_{51} & c_{52} & c_{53} & c_{54} \\ c_{61} & c_{62} & c_{63} & c_{64} \end{bmatrix}, \quad \boldsymbol{D}_{lon} = \begin{bmatrix} 0 & 0 \\ 0 & 0 \\ 0 & 0 \\ 0 & 0 \\ X_\delta & z_{CI}M_\eta \\ \sim 0 & Z_\eta - x_{CI}M_\eta \end{bmatrix}, \tag{3.22}$$

$$\begin{aligned} c_{51} &= X_u + z_{CI}M_u, & c_{61} &= -x_{CI}M_u, \\ c_{52} &= X_w + z_{CI}M_w, & c_{62} &= Z_w - x_{CI}M_w, \\ c_{53} &= X_q + z_{CI}M_q + w_0, & c_{63} &= Z_q - x_{CI}M_q - u_0, \\ c_{54} &= X_\theta + z_{CI}M_\theta, & c_{64} &= -x_{CI}M_\theta. \end{aligned} \tag{3.23}$$

Lateral-Directional Observation Model

The linearized lateral-directional measurement model can be derived similarly as for the longitudinal motion. For the lateral-directional motion the observation vector consists of

$$\boldsymbol{y}_{lat} = \begin{bmatrix} \delta v_{A|CS} & \delta p & \delta r & \delta\phi & a y_{CI} \end{bmatrix}^T. \tag{3.24}$$

The observation model in the state space form

$$\boldsymbol{y}_{lat} = \boldsymbol{C}_{lat}\boldsymbol{x}_{lat} + \boldsymbol{D}_{lat}\boldsymbol{u}_{lat}, \tag{3.25}$$

where the observation-$\boldsymbol{C}_{lat}$ and the feedthrough-$\boldsymbol{D}_{lat}$ matrices are defined respectively:

$$\boldsymbol{C}_{lat} = \begin{bmatrix} 1 & -z_{CS} & x_{CS} & 0 \\ 0 & 1 & 0 & 0 \\ 0 & 0 & 1 & 0 \\ 0 & 0 & 0 & 1 \\ c_{51} & c_{52} & c_{53} & c_{54} \end{bmatrix}, \quad \boldsymbol{D}_{lat} = \begin{bmatrix} 0 & 0 \\ 0 & 0 \\ 0 & 0 \\ 0 & 0 \\ (Y_\zeta - z_{CI}L_\zeta + x_{CI}N_\zeta) & (z_{CI}M_\eta) \end{bmatrix}, \tag{3.26}$$

$$\begin{aligned} c_{51} &= Y_v - z_{CI}L_v + x_{CI}N_v, \\ c_{52} &= Y_p - z_{CI}L_p + x_{CI}N_p - w_0, \\ c_{53} &= Y_r - z_{CI}L_r + x_{CI}N_r + u_0, \\ c_{54} &= Y_\phi - z_{CI}L_\phi + x_{CI}N_\phi. \end{aligned} \tag{3.27}$$

3.3 Analysis of Stability and Controllability

Using stability and controllability analysis, it is possible to determine the eigen dynamic characteristics of the airship and its expected responses to the applied control inputs. This information is of considerable interest not only for the controller design purposes, but also for system identification, because it represents the a priori knowledge of the dynamics involved.

The characteristics of stability (or instability) play an important role in selecting an appropriate estimation algorithm [22]. Moreover, from the eigenvalues/eigenvector analysis, one can assess a contribution of a physical state to a particular eigenmode of the system, and therefore, the significance of the corresponding stability derivative. The information about the mode decoupling can be utilized for reducing the order of the estimation model and, consequently, reduction of the parameter space.

Finally, based on knowledge of stability and controllability, it is possible to provide an adequate design of the identification experiments [50], as will be additionally discussed in Chapter 5.

3.3.1 Characteristic Eigenmodes of a Conventional Airship

The stability of a linear system is characterized by eigenvalues (poles) of the dynamic $\boldsymbol{A}$ matrix, determined as the roots of a characteristic polynomial

$$det(s\boldsymbol{E} - \boldsymbol{A}) = 0 \,. \tag{3.28}$$

The stability analysis for a number of conventional airships has resulted in a common pole distribution (shown in Figure 3.3) of the linearized longitudinal and lateral-directional models [10], [23], [26], [52].

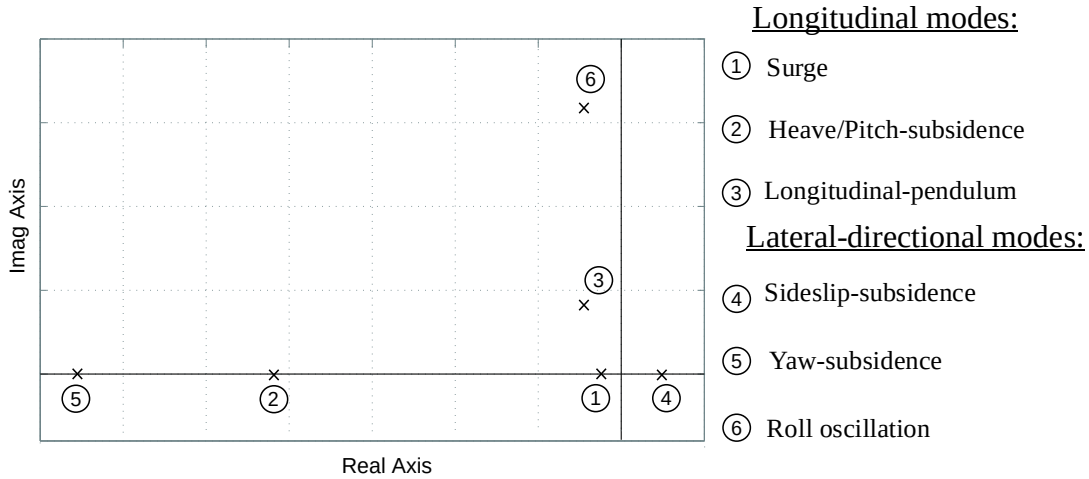

Figure 3.3: Characteristic pole locations of longitudinal and lateral-directional dynamics[26]

In the longitudinal dynamics they are distinguished by two real eigenvalues- for the *surge* and *heave* modes, and one conjugate pair- for the *longitudinal-pendulum* mode.

In the lateral-directional motion the typical eigendynamics is associated with two aperiodic modes, known as *sideslip-subsidence* and *yaw-subsidence* modes, and one oscillatory motion, recognized as *roll-oscillation* mode.

3.3.2 Characterization of Eigenmodes at Different Flight Velocities

For studying the eigendynamic properties of the Lotte airship at specific flight regimes, the nominal flight mechanical model has been utilized for trimming and linearization facilities. Although it is possible to express the characteristic modes in analytical form using stability derivatives, its form is too complicated to perform a comprehensive analysis. Therefore, the stability derivatives were determined numerically.

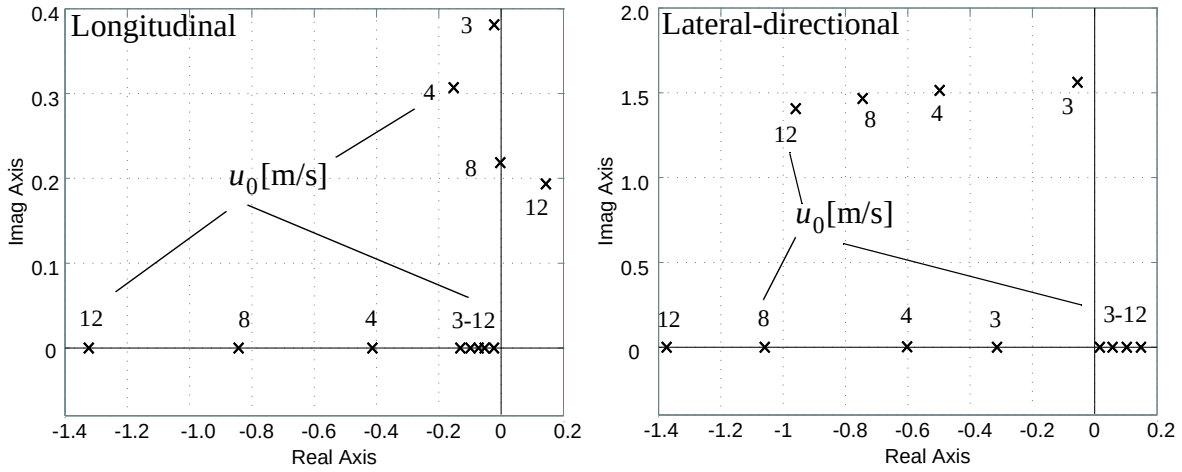

Figure 3.4: Root locus of longitudinal dynamics at different trim velocity u_0

Figure 3.4 shows the pole distribution at different flight speeds, with the forward trim velocity ranging from $4\,[\mathrm{m/s}]$ to the maximal $12\,[\mathrm{m/s}]$. For numerical evaluation, the nominal flight mechanical model was assigned to a realistic buoyancy to gravity ratio $B/G = 0.98$. This ratio represents the static heaviness of the airship and can be alternatively expressed by $B/G = (\rho V)/m$. Usually the static heaviness varies from the "nearly neutral" $B/G \approx 1$ to the "heavy" configurations $B/G = 0.85$.

In order to expand the analysis of the system dynamics, a contribution of a physical state to a particular eigenmode of the system using modal analysis will be performed. This involves a definition of a state space system in the modal state basis

$$\dot{\tilde{\boldsymbol{x}}} = \underbrace{\boldsymbol{S}^{-1}\boldsymbol{A}\boldsymbol{S}}_{\tilde{\boldsymbol{A}}}\tilde{\boldsymbol{x}} + \underbrace{\boldsymbol{S}^{-1}\boldsymbol{B}}_{\tilde{\boldsymbol{B}}}\boldsymbol{u}, \tag{3.29}$$

where $\tilde{\boldsymbol{x}} = \boldsymbol{S}^{-1}\boldsymbol{x}$ is the modal state vector, $\tilde{\boldsymbol{A}} = \boldsymbol{S}\boldsymbol{A}\boldsymbol{S}^{-1} = diag(\lambda_1, \lambda_2, \ldots, \lambda_n)$ is the modal system matrix. By using the eigenvector matrix $\boldsymbol{S} = [\boldsymbol{v}_1, \boldsymbol{v}_2, \ldots, \boldsymbol{v}_n]$, the transformation of the original system into the decoupled modal system is performed. Note, because the modal analysis is very sensitive on selection of the basis of the state vector, it is preferable to perform the analysis of a pre-scaled system (in the current case the analysis was performed in the following units, δu, δv, δw in [m/s], δp, δq, δr in [°/s], $\delta\phi$, $\delta\theta$, $\delta\zeta$, $\delta\eta$, $\delta\xi$ in [°], δT in [%] of $T_{\max}$).

Longitudinal Dynamics

- **Surge Mode:** The surge mode is distinguished by a stable aperiodic dynamics with a large time constant. Its physical interpretation corresponds to the forward velocity damping and can be explained as a reminder of a well known phugoid mode, when the part due to potential energy is missing, which is a common property of lighter than air vehicles. This mode is always stable. Studying the eigenvector diagram, shown in Figure 3.5, one also concludes that the surge mode is slightly coupled with perturbations of the pitch angle-$\delta\theta$ and almost decoupled with the δq and δw states. This is mainly because of insignificant values of stability derivatives X_w and X_q.
- **Heave Mode:** The heave eigendynamic corresponds to a well dampened aperiodic motion with a comparatively small time constant. It is characterized by the vertical motion of the airship, incorporating the cross-flow aerodynamic effects. At low airship velocities u_0, the coupling with the vertical velocity δw is dominant (see Figure 3.5). This can be interpreted by the aerodynamic phenomena that acts in the vertical direction, where the cross flow effects are dominant. As the forward trim velocity u_0 increases, the influence of the fins becomes stronger. This results in a stabilizing pitching moment and, therefore, the coupling with the δq and consequently with $\delta\theta$ becomes apparent. At high trim velocities this mode is also referenced as *pitch-subsidence mode* [29]. From the pole map diagram given in Figure 3.4, it can be seen that the damping of the heave mode increases with increased trim velocity u_0. The contribution of the forward velocity δu perturbation is negligibly small.
- **Longitudinal-Pendulum Mode:** The longitudinal pendulum mode is the most critical eigenmode in the longitudinal dynamics. At very low velocities, where aerodynamic effects are negligible, the longitudinal pendulum mode appears as a slightly dampened low frequency oscillation in pitch. Physically this can be interpreted as a pendulum motion of the center of gravity CG "suspended" at the center of buoyancy CB [26]. As can be concluded from the eigenvector diagram (Figure 3.5), the states δq and $\delta\theta$ are dominant. With increased trim velocity u_0, the mode starts to interact with the heave mode throughout the δw variable. The stabilizing moment of the fins increases the damping ratio of the mode, as seen on the pole map at velocities of about $4\,[\mathrm{m/s}]$. If the velocity is further increased, the unstable aerodynamic moment M^A begins to dominate over the stabilizing moment produced by fins. At a certain velocity, the destabilizing aerodynamic moment becomes greater than the stabilizing moment due to gravity force, and the longitudinal pendulum mode becomes unstable (see Figure 3.4).

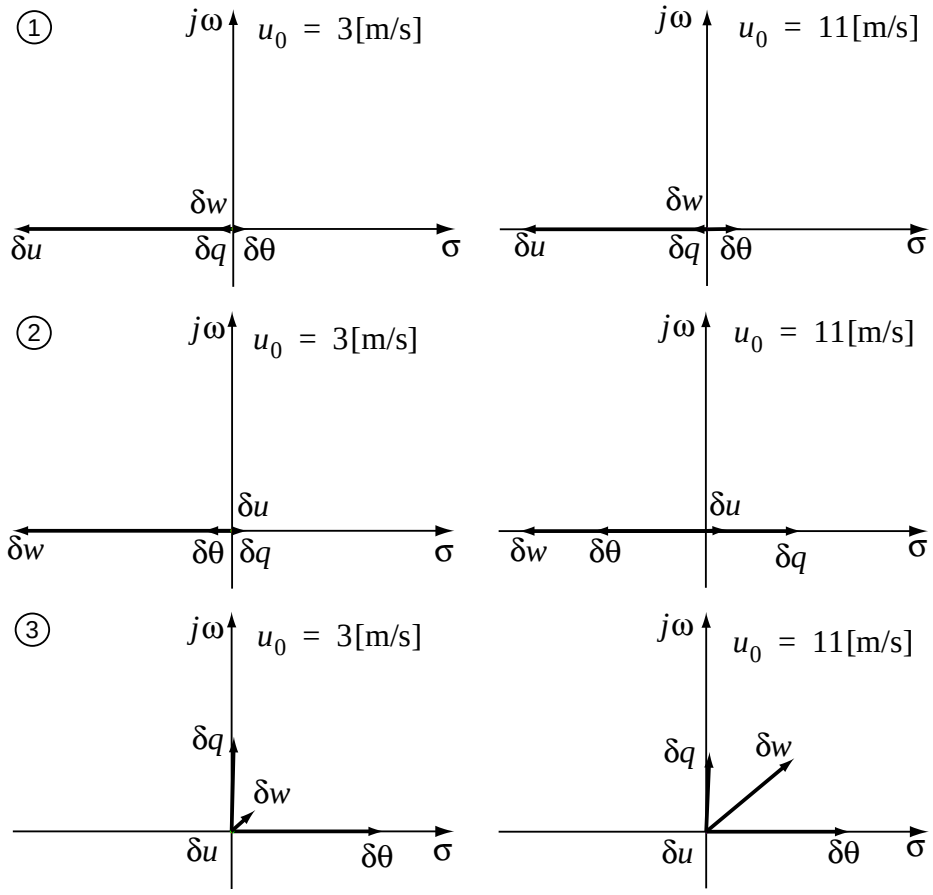

Figure 3.5: Eigenvector diagrams of longitudinal modes

Lateral-Directional Dynamics

- **Sideslip-Subsidence Mode:** In the studied configuration, the sideslip-subsidence mode resulted in unstable real pole on the complex plane. This instability arises from the static destabilizing aerodynamic yawing moment N^A, which can be approximated by M^A at small angles of attack. The states δv and δr play a dominant role in this unstable dynamics (see Figure 3.6). At higher trim velocities u_0, this mode is also slightly coupled with perturbations of the roll angle $\delta\phi$ due to centrifugal effects, which appear in the yaw motion due to low CG location. The time constant of the sideslip-subsidence mode is very sensitive to variations of the trim velocity u_0. The terms Y_p and Y_ϕ are negligibly small.
- **Yaw-Subsidence Mode:** This mode can be explained by similar physical phenomena, as was observed for the heave mode. Due to the dominant presence of the δv, δr perturbations, concluded from Figure 3.6, the yaw-subsidence mode is strongly coupled with the unstable sideslip-subsidence mode. With increased speed u_0, the mode increases its damping.

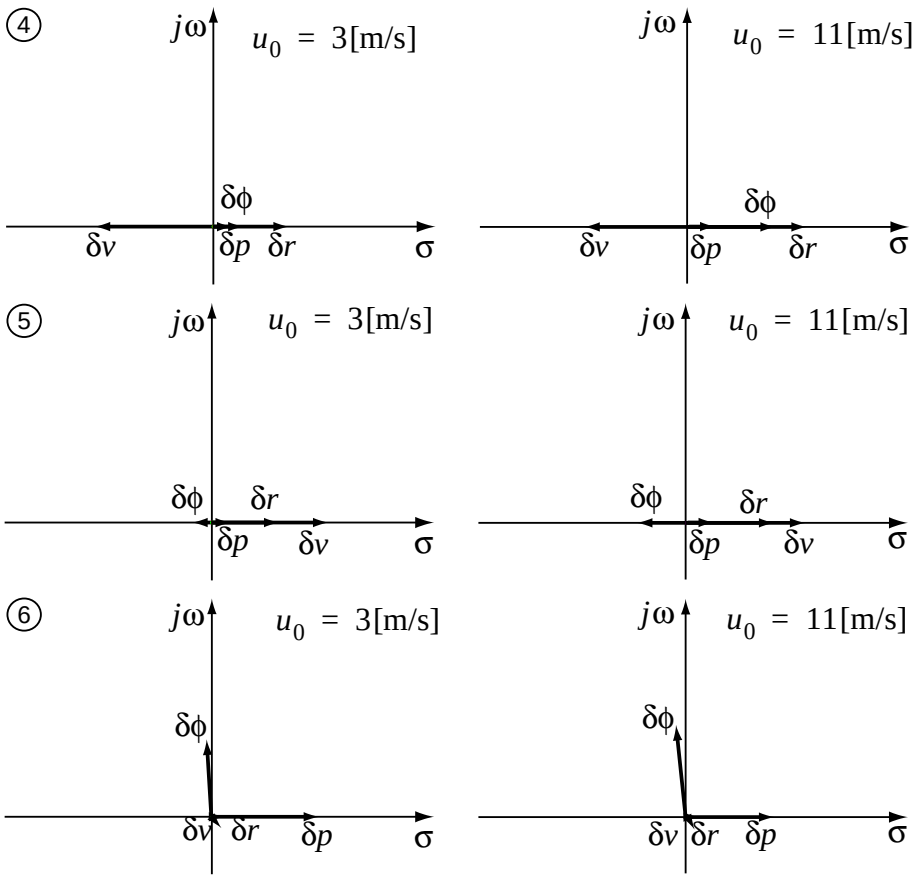

Figure 3.6: Eigenvector diagrams of lateral-directional modes

- **Roll-Oscillation Mode:** The roll oscillation mode describes a lightly dampened pendulum motion around the x axis of airship. Both, the aerodynamic and gravity phenomena contribute to this eigenmotion. The mode is mainly composed of the δp and $\delta\phi$ states (see Figure 3.6). With increasing velocity u_0, the rolling motion is better dampened due to aerodynamic roll damping produced by the fins.

3.3.3 Influence of Configuration Changes on System Dynamics

The eigendynamic characteristics of an airship do not only depend on aerodynamic phenomena, but are also strongly influenced by the change of configuration properties. Variation of static heaviness, as well as change of position of the mass center CG contribute greatly in the system dynamics of the lighter than air vehicle. For this reason, the nominal flight mechanical model has been linearized at different configurations, including different levels of static weight and variations of the center mass location. The linearization has been performed at a reasonable trim velocity $u_0 = 8[\text{m/s}]$.

Figure 3.7 shows results of a numerical investigation, where eigenvalues were calculated at different buoyancy to gravity levels. The mass of airship is varied from the “neutral” $B/G = 1$ to the “heavy” buoyancy configurations $B/G = 0.85$.

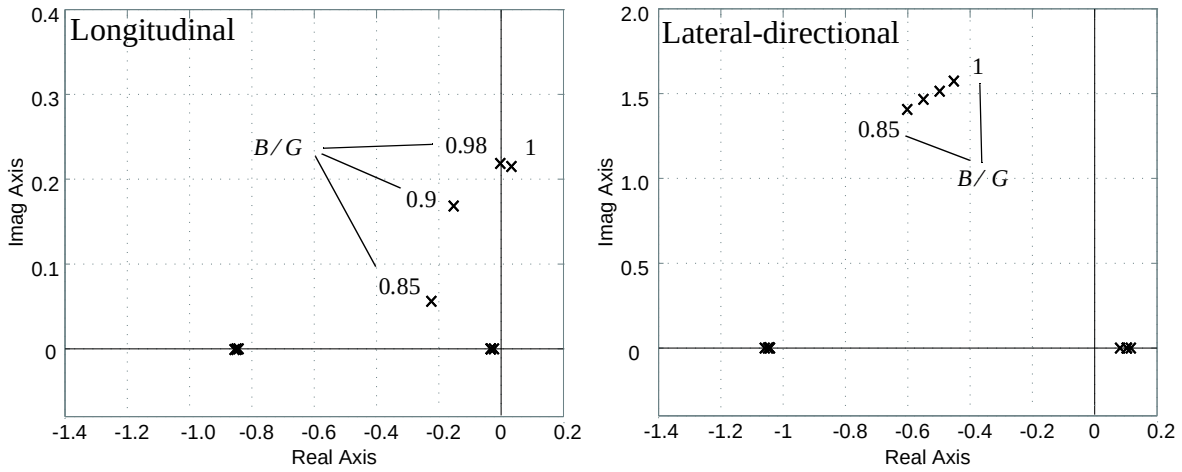

Figure 3.7: Root locus of longitudinal dynamics at different heaviness conditions

Figure 3.8 shows the pole locations on variation of the vertical position of center mass CG. In the numerically evaluated case, the CG position of a $B/G = 0.98$ heavy airship has been moved in the vertical direction at limits $z_{CG} \in [0.2d_{max},\ 0.5d_{max}]$, with d_{max} denoting the maximal thickness of the Lotte airship.

From the practical considerations described earlier, variations of the x_{CG} component assumed to be negligibly small over the whole flight and are therefore, not considered here. A more detailed analysis of the sensitivity of the pole locations on configuration changes can be found in reference [26].

In the following, the common longitudinal and lateral-directional modes will be analyzed individually. Because the dominance of particular states in eigendynamics does not change significantly, the eigenvector diagrams will be omitted.

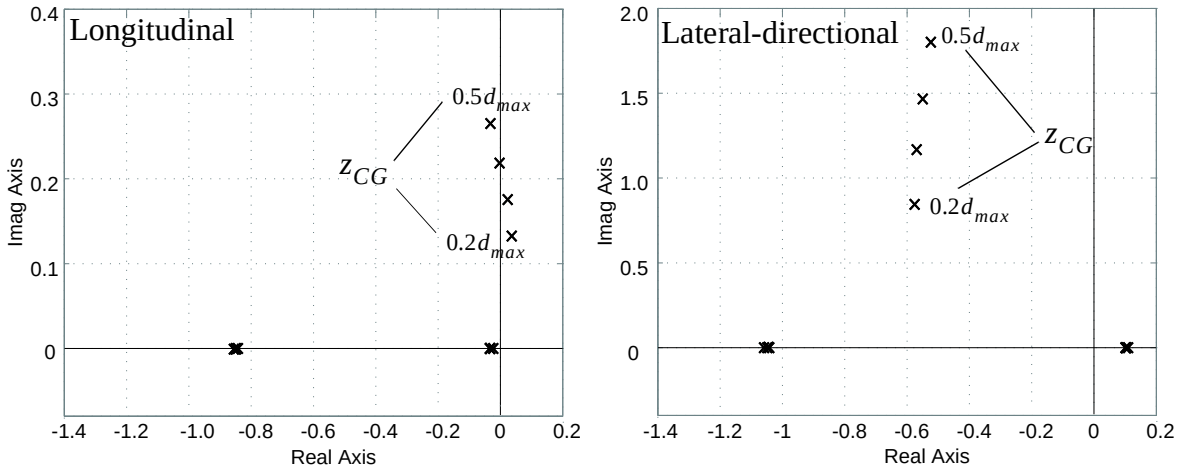

Figure 3.8: Root locus of longitudinal dynamics at different heights of center of gravity

Longitudinal Dynamics

- **Surge Mode:** Due to mainly aerodynamic phenomena of the surge mode, its pole location is relatively insensitive to variations of static heaviness and center of mass position. The perturbations of the axial velocity δu remain the dominant component in this mode.
- **Heave Mode:** The pole location of this mode shows that changes of the static heaviness and the center of mass have very little influence on the damping properties. Only small variations can be observed when the center mass is changed in vertical direction.
- **Longitudinal-Pendulum Mode:** The longitudinal-pendulum mode is mostly affected by the static heaviness variation. In the studied configurations, the Lotte airship acquires unstable oscillating response when the static heaviness approaches unity. Only at heavier configurations with $B/G < 0.95$ does the pole migrate to the left half-plane with increased damping ratio. Such a behavior is similar to that described for the velocity variations, where the destabilizing aerodynamic moment is compensated by increased gravity moment. Because the z_{CG} characterizes the metacentric height of the CB point above the center mass CG, its variation influences the frequency of the pitch oscillation and, therefore, directly impacts the longitudinal-pendulum mode. As shown in Figure 3.8, in the configurations with high CG locations, there is not enough static gravity moment to compensate the destabilizing aerodynamic pitching moment. Therefore, the mode becomes unstable. Only at lower CG positions $z_{CG} > 0.2 d_{max}$ is stability achieved.

Lateral-Directional Dynamics

- **Sideslip-Subsidence Mode:** The unstable sideslip subsidence eigenmode slightly changes on variations of the static heaviness. A small migration towards the imaginary axis at heavier configurations can be explained by the increased moment of inertia of the airship. Variations due to center mass position change are negligibly small.
- **Yaw-Subsidence Mode:** Similarly to the longitudinal heave mode, the yaw subsidence mode does not appear to be much affected by configuration changes of the airship.
- **Roll-Oscillation Mode:** The roll-oscillation mode behaves in a similar matter as the changes observed for the longitudinal pendulum mode. The increase of the static heaviness leads to a small increase of the damping ratio, whereas the eigenfrequency remains nearly unchanged. With increase of the metacentric height z_{CG}, the frequency of the roll oscillation becomes larger.

3.3.4 Analysis of Control Efficiency

The control efficiency of a linear system can be studied using various analysis methods, such as Bode-plots, modal analysis or evaluating the controllability Grammians [6], [53]. From the other hand, the analysis can be performed in a simple way, examining the eigenvector diagrams and interpreting the physical control variables.

Longitudinal Control

From the stability analysis it may be concluded that the axial velocity dominates upon other states in the surge eigenmode. A substantial contribution to the change of the forward velocity can be achieved by the thrust control. Therefore, it is likely to expect that variations of the throttle input δT will mainly excite the surge eigenmode. Figure 3.9(a) illustrates numerical values of the modal control matrix $\tilde{\boldsymbol{B}}$ introduced in equation (3.29). As can be seen, the first (surge) eigenmode is best excited by the throttle perturbations δT.

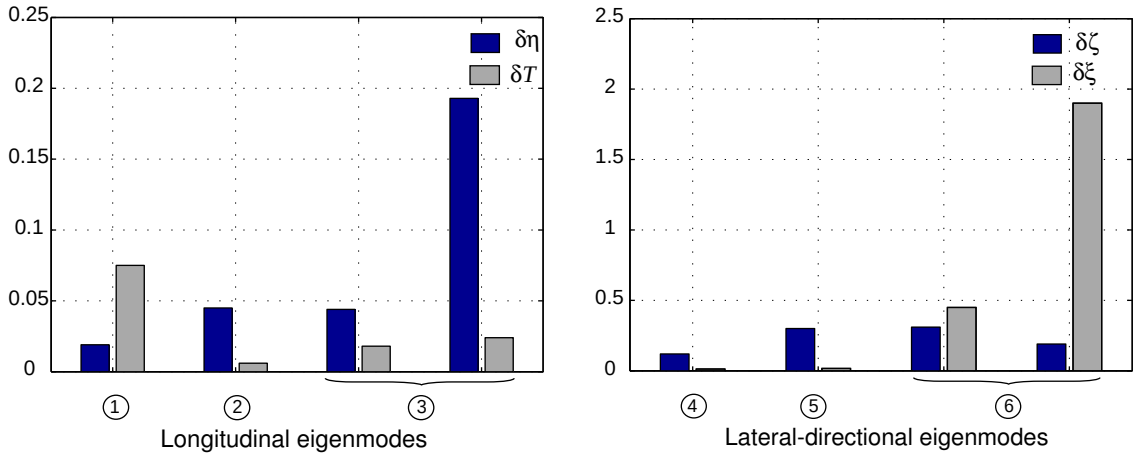

(a) (b)

Figure 3.9: Excitation of the airship eigendynamics

The eigenvector diagrams shown in Figure 3.5 illustrate that the heave and longitudinal-pendulum eigenmodes are strongly coupled with perturbed states δw, δq and $\delta\theta$. As it is assumed that the thrust force mainly acts along the axial direction of airship, its influence on these states can be regarded as insignificant. On the other side, the elevator perturbations of fins $\delta\eta$ produces additional vertical force and exerts aerodynamical pitching moment with respect to the center of reference. The results shown in Figure 3.9(a) (modes (2) and (3)) verify these propositions.

Lateral Control

A similar argument can be extended to the lateral-directional dynamics. From the fact that the sideslip and yaw subsidence modes (modes (4) and (5) in Figure 3.9(b)) are predominantly composed of the δv and δr states, the best controlling effect is expected when applying the rudder perturbations $\delta\zeta$. From the other side, the roll oscillation mode, defined mainly by the δp and $\delta\phi$ states, is well exited if the aileron input $\delta\xi$ is applied.

3.3.5 Approximated Models

Having examined the dynamic stability of the longitudinal and lateral-directional motions, several preliminary conclusions can be drawn:

- The surge mode is largely decoupled with the rest of longitudinal system modes. This eigenmotion can be approximated by the *forward-velocity* motion

$$\delta\dot{u} = X_u \delta u + X_{\delta_T} \delta T \tag{3.30}$$

- The heave and the longitudinal-pendulum eigenmodes are strongly coupled. They can be approximated by *angle-of-attack-pitch* equation

$$\begin{bmatrix} \delta\dot{w} \\ \delta\dot{q} \\ \delta\dot{\theta} \end{bmatrix} = \begin{bmatrix} Z_w & Z_q & \sim 0 \\ M_w & M_q & M_\theta \\ 0 & 1 & 0 \end{bmatrix} \begin{bmatrix} \delta w \\ \delta q \\ \delta\theta \end{bmatrix} + \begin{bmatrix} Z_\eta \\ M_\eta \\ 0 \end{bmatrix} \delta\eta \tag{3.31}$$

- The sideslip-subsidence and yaw-subsidence eigenmodes are strongly coupled through the δv, δr states and slightly through $\delta\phi$ state due to centrifugal force. This leads to the following approximation possibility

$$\begin{bmatrix} \delta\dot{v} \\ \delta\dot{r} \end{bmatrix} = \begin{bmatrix} Y_v & Y_r \\ N_v & N_r \end{bmatrix} \begin{bmatrix} \delta v \\ \delta r \end{bmatrix} + \begin{bmatrix} Y_\zeta \\ N_\zeta \end{bmatrix} \delta\zeta \tag{3.32}$$

- The roll-pendulum eigenmotion can be well approximated by

$$\begin{bmatrix} \delta\dot{p} \\ \delta\dot{\phi} \end{bmatrix} = \begin{bmatrix} L_p & L_\phi \\ 1 & 0 \end{bmatrix} \begin{bmatrix} \delta p \\ \delta\phi \end{bmatrix} + \begin{bmatrix} L_\xi \\ 0 \end{bmatrix} \delta\xi \ . \tag{3.33}$$

The introduction of the approximated models can be desirable for the identification purposes for two basic reasons. First, fewer unknown parameters should be estimated if the approximated models are studied separately. Second, the identification experiments (flight maneuvers) for the coupled modes excitations can be planned individually.

The results of the stability analysis presented above are only of a preliminary basis. They are based on the theoretical investigations of the flight mechanical model and verified against the results obtained in other references. How these predictions are relevant to the “real world” operation of the Lotte airship, can be only evaluated when the flight data are available and analyzed.

3.4 Stochastic Disturbances of the Model

An airship is subjected to various disturbances that contribute to its response as uncontrolled (i.e. not by means of the airship controls) motion. These disturbances have different physical origins and are typically of a random nature. Additionally, the measured responses are inevi-

tably accompanied with the measurement noise. These facts considerably complicate the identification problem. The following discussion is devoted to the analysis of possible disturbance sources, and suggestions, which adequately accommodate the estimation model to these discomposes.

3.4.1 Wind and Turbulence

A description of flight vehicle motion in the unsteady atmosphere poses a very complicated and analytically unsolvable problem, where interactions between the vehicle and the atmosphere should be accounted for. Only some restricted turbulence models, empirically determined from numerous flight experimental data, are applicable in classical flight mechanics [54].

Although the turbulence models, such as Dryden or von Kármán are extensively utilized in the lifting body applications, their “frozen windfield” assumption [14]

$$\frac{D}{Dt}(\boldsymbol{V}_W(\boldsymbol{r},\ t)) = \underbrace{\frac{\partial}{\partial t}\boldsymbol{V}_W(\boldsymbol{r},\ t)}_{\approx\ 0\,|_{\boldsymbol{V}_K \gg \boldsymbol{V}_W}} + (\nabla_{\boldsymbol{r}}\ \boldsymbol{V}_W(\boldsymbol{r},\ t))^T\boldsymbol{V}_K \cong (\nabla_{\boldsymbol{r}}\ \boldsymbol{V}_W(\boldsymbol{r},\ t))^T\boldsymbol{V}_K \tag{3.34}$$

is, in general, not valid for airships because of very low flight velocities.

It should be noticed that even with the well determined turbulence models, in the aircraft identification field few examples exist where the dynamical model is coupled together with a turbulence model. The turbulence is commonly attributed as a stochastic disturbance or process noise with colored or white noise properties [19], [40]. This is done in order to reduce the complexity of the estimation model and to account properly for the model deficiencies (see discussion in section 3.1).

From the aspects described above, it was purposed to treat the wind disturbances and possible modelling errors as an additive process in the process dynamics

$$\dot{\boldsymbol{x}} = \boldsymbol{A}\boldsymbol{x} + \boldsymbol{B}\boldsymbol{u} + \boldsymbol{F}\boldsymbol{n}\ , \tag{3.35}$$

having zero mean $E\{\boldsymbol{n}\} = \boldsymbol{0}$ and unity white spectral density function [9]. The $\boldsymbol{F}$ matrix represents the state noise intensity.

The main requirement to the process noise disturbances is that their influence should be apparently small to be accepted. This can be quantified by performing the compatibility analysis of flight data (discussed later in Chapter 6) and applying parameter estimation algorithms that neglect the presence of the state noise (discussed in Chapter 4).

3.4.2 Measurement Noise

The measurements delivered by hardware are subjected to measurement errors. The plant, whose parameters are to be estimated, is assumed to be described by the state space system with the additive measurement $\boldsymbol{v}$ disturbances

$$\begin{aligned} \boldsymbol{y} &= \boldsymbol{C}\boldsymbol{x} + \boldsymbol{D}\boldsymbol{u} + \boldsymbol{H}\boldsymbol{v} \\ \boldsymbol{z}_i &= \boldsymbol{y}(\boldsymbol{t}_i), \end{aligned} \tag{3.36}$$

where $\boldsymbol{v}$ is assumed to be white Gaussian signals, with zero mean and identity power spectral density matrices.

3.5 Model Parametrization

3.5.1 Accounting for Nontrim Condition and Systematic Sensor Offsets

The treatment of the linearized estimation model leads to additional complications when it is applied to fit the flight data. The equilibrium condition, defined in section 3.2.1 is very rigorous. It is practically impossible to achieve a condition where the linear and angular accelerations have exactly zero values. For this reason, the state equations are commonly accompanied with an additional *state bias* unknown [55]:

$$\dot{\boldsymbol{x}} = \boldsymbol{A}\boldsymbol{x} + \boldsymbol{B}\boldsymbol{u} + \boldsymbol{b}_x \,. \tag{3.37}$$

In the presence of trim errors the state bias $\boldsymbol{b}_x$ balances the state equation and accurately determines the trim state. Without the state bias, the equations would integrate a small error over the measurement interval. The state bias term is very important for long identification maneuvers. For the longitudinal and lateral-directional models, the state bias vectors are correspondingly:

$$\boldsymbol{b}_{x,\ lon} = \left[b_{\dot{u}} \ b_{\dot{w}} \ b_{\dot{q}} \ b_{\dot{\theta}} \right]^T, \qquad \boldsymbol{b}_{x,\ lat} = \left[b_{\dot{v}} \ b_{\dot{p}} \ b_{\dot{r}} \ b_{\dot{\phi}} \right]^T . \tag{3.38}$$

In addition to the state bias parameter, the *observation bias* vector $\boldsymbol{b}_y$ is applied to the measurement equations in order to account for systematic offsets of the measured data

$$\boldsymbol{y} = \boldsymbol{C}\boldsymbol{x} + \boldsymbol{D}\boldsymbol{u} + \boldsymbol{b}_y \,, \tag{3.39}$$

with:

$$\boldsymbol{b}_{y,\ lon} = \left[b_u \ b_w \ b_q \ b_\theta \ b_{ax} \ b_{az} \right]^T, \qquad \boldsymbol{b}_{y,\ lat} = \left[b_v \ b_p \ b_r \ b_\phi \ b_{ay} \right]^T . \tag{3.40}$$

The elements of vectors $\boldsymbol{b}_x$ and $\boldsymbol{b}_y$ should be estimated together with the unknown stability and control derivatives [55]. Introducing the state and observation bias parameters, it is also possible to utilize directly measured input and output variables (i.e. not their perturbations) in the estimation algorithm.

3.5.2 Initial Parametrization

So far, the dynamic models used for estimation has been derived and analyzed. The unknown model parameters can be now summarized in a generalized parameter vector Θ defined for the longitudinal model by

$$\begin{aligned}\Theta_{lon} = [&\underline{X_u}\ X_w\ X_q\ X_\theta\ Z_u\ \underline{Z_w}\ \underline{Z_q}\ Z_\theta\ M_u\ \underline{M_w}\ \underline{M_q}\ \underline{M_\theta}\ \underline{X_{\delta T}}\ X_\eta\ \underline{Z_\eta}\ \underline{M_\eta}\ \dots \\ &\dots b_{\dot{u}}\ b_{\dot{w}}\ b_{\dot{q}}\ b_{\dot{\theta}}\ b_u\ b_w\ b_q\ b_{ax}\ b_{az}\ u_0\ w_0]^T\ ,\end{aligned} \tag{3.41}$$

and for the lateral-directional model

$$\begin{aligned}\Theta_{lat} = [&\underline{Y_v}\ Y_p\ \underline{Y_r}\ Y_\phi\ L_v\ \underline{L_p}\ L_r\ \underline{L_\phi}\ \underline{N_v}\ N_p\ \underline{N_r}\ N_\phi\ \underline{Y_\zeta}\ Y_\xi\ L_\zeta\ \underline{L_\xi}\ \underline{N_\zeta}\ N_\xi\ \dots \\ &\dots b_{\dot{v}}\ b_{\dot{p}}\ b_{\dot{r}}\ b_{\dot{\phi}}\ b_v\ b_p\ b_r\ b_\phi\ b_{ay}\ u_0\ w_0]^T\ .\end{aligned} \tag{3.42}$$

For identification purposes, it is preferable to choose only the derivatives that contribute significantly to the dynamics of airship. Based on stability and controllability analysis performed in section 3.3, the influence of some derivatives in stability-$\boldsymbol{A}$ and control-$\boldsymbol{B}$ matrices is found to be insignificant. The important derivatives in Equations (3.41) and (3.42) are underlined. However, these assumptions should be additionally verified by closer examination of the flight data.

Chapter 4

Estimation Algorithms

4.1 Overview and Discussion

4.1.1 General Estimation Methods

The introductory part of the thesis set out some common approaches for estimating parameters of flight vehicles from experimental data. It was pointed out that treating the input-output signals has shifted from frequency domain into time domain analysis, and therefore, the time domain methods were considered in the airship identification project.

From the theoretical point of view, all estimation algorithms can be separated into two major classes: *deterministic* methods and *stochastic* methods or estimators [11]. The deterministic estimators do, in general, solve the problem of the “best-fit” between the model and the real system. In that sense, the fit is treated according to a deterministic measure of error between model output and observed system output, as for example the integral of squared errors do. Opposite to the deterministic methods, the stochastic estimators utilize a statistical approach in interpreting the error. They do not only estimate parameters in the statistical matter, but also provide a quantitative information about the efficiency of estimation [53].

In the field of time domain flight vehicle parameter estimation, both the deterministic and stochastic estimators are widely utilized. According to reference [12], the most common methods are recognized as *equation error, output error, filter error* and *filtering* methods. In the following discussion, a short description of the approaches will be presented and their applicability to the airship identification problem is discussed.

Equation Error Method

The equation error (EE) method represents a broad class of methods that are applicable to linear time invariant dynamic systems and based on the least squares regression method [53]. The regression approach requires a direct measurement of all state variables. It constitutes the dynamic equations linear in terms of unknown parameters

$$y(t_i) = \Theta_1 x_1(t_i) + \Theta_2 x_2(t_i) + \ldots + \Theta_n x_n(t_i) + e(t_i), \tag{4.1}$$

where t_i denoting the time instance t_i, $i = 1 \ldots N$, y is the *independent* variable, the x_k, $k = 1 \ldots n$ is the *dependant* variable (state), Θ is the n dimensional vector of parameters and $\boldsymbol{e}$ is the stochastic equation error. Having all independent $\boldsymbol{y}$ and all dependant $\boldsymbol{x}$ variables measured in N discrete points, the equation error $\boldsymbol{e}$ can be minimized in one batch iteration using the least squares method:

$$\hat{\Theta} = (\boldsymbol{x}^T\boldsymbol{x})^{-1}\boldsymbol{x}^T\boldsymbol{y} \quad . \tag{4.2}$$

This method does not require any initial parameter values and is widely utilized for obtaining primary start-up parameters for other estimation algorithms [55]. An additional benefit of using the equation error method is that it does not require any temporal relation between the measured data points. It is therefore possible to concatenate several data segments in one record. This approach, regarded as *data partitioning*, is utilized in estimating large amplitude maneuvers by dividing the maneuver into several smaller portions of the flight data [1].

Within simplicity of its realization, the equation error method provides biased estimates, if the measurements of the dependant (state) variables are contaminated with the measurement noise [66]. Therefore, this method is advisable only if high-quality sensors are used for measuring the system responses.

Output Error Method

The output-error (OE) method has been successfully approved for a variety of flight vehicles using flight test data. The goodness criteria, that is usually employed with this approach is based on the maximum likelihood criteria. The criteria uses a statistical treatment of the error between the model and the system and provides efficient[1] parameter estimations.

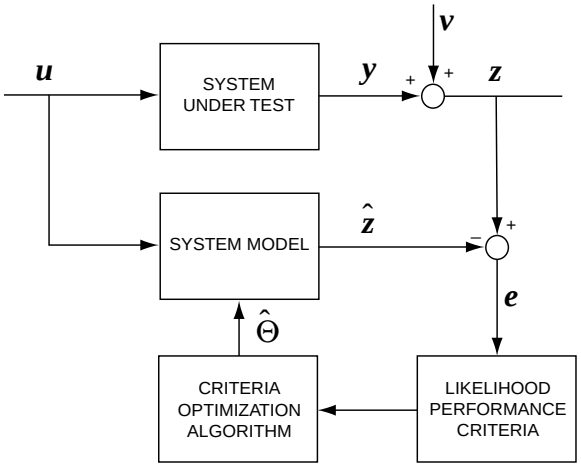

Figure 4.1: Output error estimation principle.

1. Asymptotically unbiased, minimum covariance of estimations [53].

The experience obtained by applying the maximum-likelihood identification shows the great adequateness of the models to the real systems, despite the poor initial knowledge of the physical plant during experiments [12]. Furthermore, the output-error method successfully works on estimation of parameters of nonlinear models [20].

Filter Error Method

This approach is some extension of the output error method. Based on Kalman filter for providing the state estimations of the identified system, the filter error (FE) method has a significant advantage in providing parameter estimates in presence of the process noise. There are several studies available, that utilize the filter error method for estimating aircraft parameters from the flight data in presence of turbulence [15], [19], [64]. The diagram in Figure 4.2 illustrates the principle of the filter error approach, including model dynamics, the presence of additive random process noise and random disturbances corrupting the measurements.

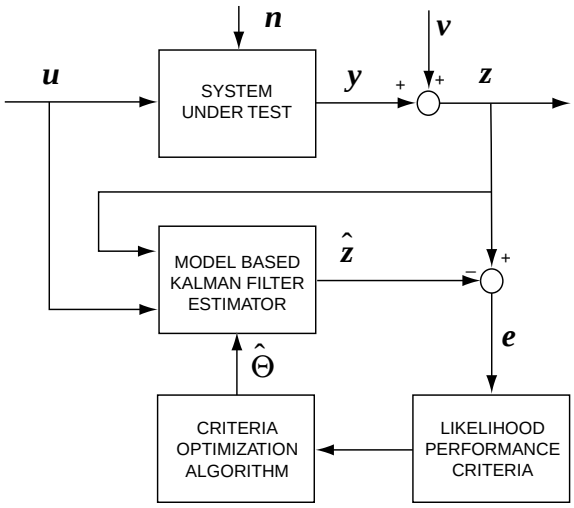

Figure 4.2: Diagram of the filter error algorithm

Filtering Method

In the filter error approach the Kalman filter is dedicated to the state estimation only. However, it is possible to use the filter as a set up for the simultaneous estimation of the state and the unknown parameters. This problem is successfully solved if the unknown parameters augmented with the model state vector and Kalman filter estimates in this combination both the state vector and parameters simultaneously. The parameters and states are combined into a composite state vector

$$\tilde{\boldsymbol{x}} = \left[\boldsymbol{x}\ \Theta\right]^T, \tag{4.3}$$

with $\dot{\Theta} = 0$ for the time invariant model parameters.

This method is widely used in the real time parameter estimation applications [2], [61]. However, this approach poses some additional computation difficulties. Even if the system dynamics is approximated by a linear model, the multiplicative nonlinearity appears due to relation $\boldsymbol{A}(\Theta)\cdot\boldsymbol{x}$. This nonlinearity requires an implementation of the extended Kalman filter, where the system equations are linearized at each successive integration step.

4.1.2 Applicable Algorithms for Estimation of Airship Derivatives

The properties of the common estimation methods can be summarized in Table 4.1 (based on reference publications [16], [22], [53]). Although all methods are being successfully utilized in practical applications, only the output error and the filter error methods favor the estimation of the airship dynamics.

As pointed out, the equation error method requires high accuracy measurements of the motion variables. The actual measurement hardware realization (discussed later in section 5.3) and the high structural flexibility leave little hope that the measurements would be accurate enough to produce satisfactory results in applying the equation error approach. Therefore, in the workframe of this thesis, this method was not considered as a main parameter estimation technique. Nevertheless, since the equation-error algorithm does not require initial parameter values, its utilization is useful for generating a startup parameterization for other estimation methods.

Table 4.1 Advantages (+) and drawbacks (-) of common parameter estimation methods

Equation Error Method	**Output Error Method**	**Filter Error Method**	**Filtering Method**
+ Numerically stable	+ Optimal bias free estimators		
+ No a priori parameter values needed	+ Possibility of nonlinear identification		
- Linear models only	+ Estimation of systematic sensor errors		+ Real-time identification
- Biased parameter estimation	- Measurement noise only	+ Estimation with process and measurement noise sources	
- Precise sensors required	- Sensitive to unstable models	+ Numerically stable	
		- Computational complexity	

The complexity of the filtering approach is unwanted in our case, since there is no requirement of online identification and the model parameters are assumed to be time invariant.

The output error and filter error methods are both maximum likelihood estimators and their implementation is very similar. It will be further illustrated, that the filter error method under certain conditions appears as a pure output error method. The power of the filter error method is in its ability to account altogether the uncontrolled motion due to external distur-

bances, the modelling errors and the measurement noise during parameter estimation. Moreover, a feedback proportional to the fit error (discussed later in equation (4.13))

$$\hat{\boldsymbol{x}}_i = \tilde{\boldsymbol{x}}_i + \boldsymbol{K}(\boldsymbol{z}_i - \tilde{\boldsymbol{z}}_i),$$

which is used to update the state estimates, also improves the numerical stability of the algorithm. This property is favorable for estimation of the unstable lateral-directional dynamics of airship [22].

It is, nevertheless, desirable to utilize the output error method along with the filter-error algorithm. In the output error realization, the response of the model is integrated in the open loop mode, i.e. where only the system input is used as a control variable. In this case it is possible to provide a rough estimation of the acting process noise disturbances (atmospheric turbulence and nonlinearity of the airship dynamics, see the discussion given in 3.4.1).

4.2 Maximum Likelihood Principle

4.2.1 Definition

The maximum likelihood estimation arose from the statistical estimation problem and utilizes the probabilistic treatment of stochastic signals. The principle of the maximum likelihood approach is to choose the values of parameters, which maximize the conditional probability density function [11]

$$\hat{\Theta}(\boldsymbol{Z}) = \arg max_{\Theta} p(\boldsymbol{Z}|\Theta), \tag{4.4}$$

where $\arg max_{\Theta}$ notation indicates that $\hat{\Theta}$ is the value of Θ that maximizes the conditional probability density function $p(\boldsymbol{Z}|\Theta)$ of observable variables $\boldsymbol{Z}$, given Θ. The parameters are chosen in a way that the observations caused by these parameters are most likely to occur.

The probability density function is of especial interest for the maximum-likelihood estimation. If $\boldsymbol{Z}$ represents a set of independent measurement samples, then the function can be expanded as product of conditional probabilities [53]

$$\begin{aligned} p(\boldsymbol{Z}|\Theta) &= p(z_1, z_2, \ldots, z_N|\Theta) \\ &= \prod_{i=1}^{N} p(z_i|\Theta), \end{aligned} \tag{4.5}$$

where N is the number of taken measurements.

As the logarithmic function has monotonic properties, the log-likelihood function is then:

$$\begin{aligned}\hat{\Theta}(Z) &= \arg max_{\Theta} \ln p(\boldsymbol{Z}|\Theta) \\ &= \arg max_{\Theta} \sum_{i=1}^{N} \ln p(\boldsymbol{z}_i|\Theta).\end{aligned} \tag{4.6}$$

The above given probabilistic approach can be easily applied to the estimation of parameters of the dynamic system. If the measured responses are contaminated with an additive measurement noise $\boldsymbol{v}$ and the process noise is absent (no modelling errors), then the output error is defined by

$$\boldsymbol{v}_i = \boldsymbol{z}_i - \hat{\boldsymbol{z}}_i \ . \tag{4.7}$$

It is common practice to associate the measurement error with a random process having the Gaussian distribution [39]. In this case, the statistical analysis simplifies greatly and the likelihood function becomes [55]:

$$\begin{aligned}L(\boldsymbol{Z}, \Theta) &= \ln p(\boldsymbol{Z}|\Theta) \\ &= -\frac{1}{2}\sum_{i=1}^{N}[(\boldsymbol{z}_i - \hat{\boldsymbol{z}}_i)^T(\boldsymbol{H}\boldsymbol{H}^T)^{-1}(\boldsymbol{z}_i - \hat{\boldsymbol{z}}_i)] - \frac{N}{2}\ln|\boldsymbol{H}\boldsymbol{H}^T| - \frac{N}{2}m\ln 2\pi,\end{aligned} \tag{4.8}$$

where m denotes the length of the observation vector and $\boldsymbol{H}\boldsymbol{H}^T$ represents the covariance matrix of the measurement noise vector. The maximization of given likelihood functional against the unknown parameters is equivalent to minimization of its negative value, which is a typical optimization task.

4.2.2 Limitations

The form and property of the maximum likelihood estimator strongly depends on the type of the noise distribution, adopted for the analysis. As stated, the Gaussian distribution of the output error is assumed. In this configuration, the efficiency of the maximum likelihood estimator is obtained. If the system operates when both state and measurement disturbances exist, the efficiency of the output error realization degrades [59].

4.3 Filter Error Method

4.3.1 Kalman Filter State Estimation

The Kalman filter produces optimal state estimates in the presence of the process and measurement noise. The objective of the Kalman filter is the minimization of process state error covariance matrix. It is assumed that a set of unknown parameters constitute the matrices $\boldsymbol{A}$, $\boldsymbol{B}$, $\boldsymbol{C}$ and $\boldsymbol{D}$ of the state space model. The matrices $\boldsymbol{F}$ and $\boldsymbol{H}$ indicate a level of intensity of the process and measurement noises respectively and are usually unknown.

The Kalman filter can be described in both continuos and discrete forms with respect to time. The principle of its functioning lays in performing state predictions of the system dynamics on the model basis, and corrections using measured quantities [9]. As the observations have discrete nature, it is favorable to use the discrete form of the Kalman filter. However, the individual parameters of the continuous state space formulation have more physical meaning, than those expressed in discrete form. Therefore, an implementation of mixed continuous/discrete form was adopted according to [41], where the initial system dynamics is continuous and the realization of the Kalman filter is discrete (see Figure 4.3).

The discrete form of the state equation yields

$$\tilde{\boldsymbol{x}}_i \cong \Phi\hat{\boldsymbol{x}}_{i-1} + \Psi\boldsymbol{B}\frac{1}{2}(\boldsymbol{u}_i + \boldsymbol{u}_{i-1}), \tag{4.9}$$

where vector $\tilde{\boldsymbol{x}}_i$ represents the state prediction for the time stamp i, $\hat{\boldsymbol{x}}_{i-1}$ is the estimated state for the time stamp $i-1$. The discrete transition Φ and control Ψ matrices for small sampling interval Δt can be approximated as

$$\Phi = e^{\boldsymbol{A}\Delta t} \cong \boldsymbol{E} + \boldsymbol{A}\Delta t + \boldsymbol{A}^2\frac{\Delta t^2}{2!} + \ldots, \tag{4.10}$$

$$\Psi = \int_0^{\Delta t} e^{\boldsymbol{A}\tau}\, d\tau \;\cong \boldsymbol{E}\Delta t + \boldsymbol{A}\frac{\Delta t^2}{2!} + \ldots. \tag{4.11}$$

The predicted system output is computed as

$$\tilde{\boldsymbol{z}}_i = \boldsymbol{C}\tilde{\boldsymbol{x}}_i + \boldsymbol{D}\boldsymbol{u}_i. \tag{4.12}$$

As the measurement for the time stamp i has taken place, a correction to the predicted state estimate is performed by adding weighted residuals or *innovations* $(\boldsymbol{z}_i - \tilde{\boldsymbol{z}}_i)$

$$\hat{\boldsymbol{x}}_i = \tilde{\boldsymbol{x}}_i + \boldsymbol{K}(\boldsymbol{z}_i - \tilde{\boldsymbol{z}}_i), \tag{4.13}$$

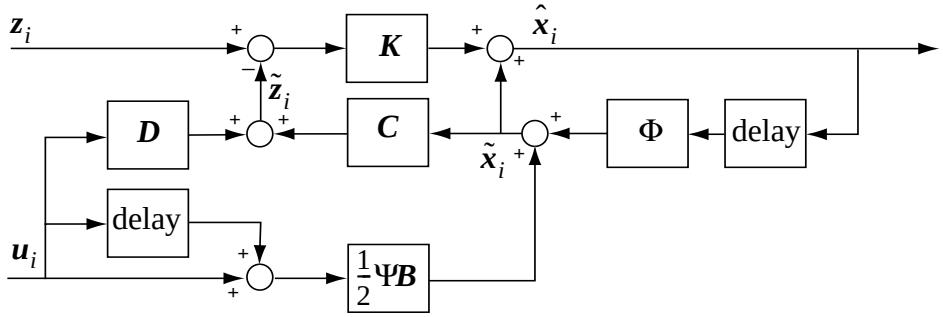

Figure 4.3: Structure of the discrete Kalman filter

where the weighting matrix $\boldsymbol{K}$ is the Kalman gain matrix. The $\boldsymbol{K}$ matrix is found by minimizing the covariance of the state estimation error [9]

$$\begin{aligned} \boldsymbol{P} &= E\{(\boldsymbol{x}-\hat{\boldsymbol{x}})(\boldsymbol{x}-\hat{\boldsymbol{x}})^T\} \\ \boldsymbol{K} &= \min(\text{trace}(\boldsymbol{P})). \end{aligned} \tag{4.14}$$

Computation of the state error covariance is a dual problem with the standard linear quadratic regulators and requires a solution of the time varying Riccati equation [11]. Rather than calculating the time varying form of the equation, which is elaborate and requires a definition of the initial $\boldsymbol{P}_0$ matrix, it is sometimes advantageous to consider a steady form of the Riccati equation, there the time varying term vanishes $\lim_{t\to\infty}\dot{\boldsymbol{P}} = 0$. The steady discrete-time Riccati equation then appears as [41]:

$$\Phi(\boldsymbol{P}-\boldsymbol{P}\boldsymbol{C}^T(\boldsymbol{H}\boldsymbol{H}^T+\boldsymbol{C}\boldsymbol{P}\boldsymbol{C}^T)^{-1}\boldsymbol{C}\boldsymbol{P}+\Gamma)\Phi^T = \boldsymbol{0}\ , \tag{4.15}$$

where Γ is the discrete form of the process noise covariance matrix [9]:

$$\Gamma = E\{\boldsymbol{n}_i\boldsymbol{n}_i^T\} = E\left\{\left(\int_0^{\Delta t}\Phi\boldsymbol{F}\boldsymbol{n}(\tau)d\tau\right)\left(\int_0^{\Delta t}\Phi\boldsymbol{F}\boldsymbol{n}(\gamma)d\gamma\right)^T\right\} \approx \Delta t\cdot\boldsymbol{F}\boldsymbol{F}^T. \tag{4.16}$$

Alternatively, the discrete-time realization of Riccati equation (4.15) can be effectively approximated by the continuous time form of the Riccati equation obtained as [19]:

$$\boldsymbol{A}\boldsymbol{P}+\boldsymbol{P}\boldsymbol{A}^T-\frac{1}{\Delta t}\boldsymbol{P}\boldsymbol{C}^T(\boldsymbol{H}\boldsymbol{H}^T+\boldsymbol{C}\boldsymbol{P}\boldsymbol{C}^T)^{-1}\boldsymbol{C}\boldsymbol{P}+\boldsymbol{F}\boldsymbol{F}^T = \boldsymbol{0} \tag{4.17}$$

The equation (4.17) is more preferable for numerical solution techniques then equation (4.15). Solving equation for $\boldsymbol{P}$, one obtains the Kalman gain matrix $\boldsymbol{K}$:

$$\boldsymbol{K} = \boldsymbol{P}\boldsymbol{C}^T(\boldsymbol{H}\boldsymbol{H}^T+\boldsymbol{C}\boldsymbol{P}\boldsymbol{C}^T). \tag{4.18}$$

If the Kalman filter based model response is computed, and if the process and measurement noises are Gaussian white, then the innovations $(\boldsymbol{z}_i - \tilde{\boldsymbol{z}}_i)$ have also Gaussian distribution. The Kalman filter is sometimes referenced as the whitening filter because it creates white innovation samples [45]. The proof of this statement is left beyond the scope of this work and can be found in reference [47]. This makes the likelihood criteria also tractable for the cases where the process noise is apparent. Although the appropriate likelihood function is similar to that formulated for the pure output error method, it has nevertheless two differences. First, the residuals require innovations provided by applying the Kalman filter state estimation. The second difference of the derived maximum likelihood is in introducing the weighting matrix $\boldsymbol{R}$. This matrix represents the covariance of the residuals and can be evaluated using the following transformation:

$$E\{(\boldsymbol{z}_i - \tilde{\boldsymbol{z}}_i)(\boldsymbol{z}_i - \tilde{\boldsymbol{z}}_i)^T\} = \boldsymbol{CPC}^T + \boldsymbol{HH}^T = \boldsymbol{R} \quad . \tag{4.19}$$

The likelihood function in this case is evaluated as

$$L(\boldsymbol{Z},\ \Theta) = -\frac{1}{2}\sum_{i=1}^{N}[(\boldsymbol{z}_i - \tilde{\boldsymbol{z}}_i)^T\boldsymbol{R}^{-1}(\boldsymbol{z}_i - \tilde{\boldsymbol{z}}_i)] - \frac{N}{2}\ln|\boldsymbol{R}| - \frac{N}{2}m\ln 2\pi \quad . \tag{4.20}$$

It is now easy to observe an interrelation between the filter error and the output error method. If the process noise is disregarded, the $\boldsymbol{F}$ matrix is respectively zero and the solution of the Riccati equation also results in zero $\boldsymbol{P}$ matrix. In the absence of the process noise, the Kalman gain matrix $\boldsymbol{K}$ has zero elements and the algorithm appears as the pure output error method.

4.4 Computational Aspects of Optimization

Let us now formulate the optimization objectives for the filter error method. As in the modelling chapter, the unknown parameter vector contains the system state space model ($\boldsymbol{A}$, $\boldsymbol{B}$, $\boldsymbol{C}$ and $\boldsymbol{D}$ matrices), statistical characteristics of noise sources (intensity of the process $\boldsymbol{F}$ and measurement $\boldsymbol{H}$ noise sources), and the bias parameters due to the unknown initial trim condition of the system. This optimization setup is commonly regarded as *original formulation* [41]. The goodness criteria is expressed by the negated likelihood function in equation (4.20):

$$J(\Theta) = -L(\boldsymbol{Z},\ \Theta) = \frac{1}{2}\sum_{i=1}^{N}[(\boldsymbol{z}_i - \tilde{\boldsymbol{z}}_i)^T\boldsymbol{R}^{-1}(\boldsymbol{z}_i - \tilde{\boldsymbol{z}}_i)] + \frac{N}{2}\ln|\boldsymbol{R}| + \frac{N}{2}m\ln 2\pi. \tag{4.21}$$

Attempts to estimate the parameters of the original formulation led to enormous numerical problems during optimization, as reported in [41]. The poor convergence of the originally formulated optimization setup motivated the development of a number of meth-

ods, which were able to speed up the convergence property. The emphasis of one is made on inclusion of additional unknowns into the parameter vector and setting the optimization constraints [59]. Others use indirect computations of unknowns, as for example a direct estimation of parameters of the Kalman gain matrix $\boldsymbol{K}$ (Equation (4.18)) [64], [39].

Early in 1980s an algorithm called MMLE3 (Marginal Maximum Likelihood Estimation) was developed at NASA Dryden Flight Research Center [40]. Compilation of many related works [59], [64] devoted to the problem of parameter estimation in the presence of the process and measurement noise, has indicated that this algorithm can be suitably applied to the airship identification problem. It has proven its efficiency in the variety of applications. It requires slight modifications to the original formulation. Details of its functioning can be found in reference [41] and are shortly recapitulated in the next section.

4.5 MMLE3 Algorithm

The MMLE3 algorithm is designed to minimize a risk of divergence during minimization of the cost function. The major idea behind this is to transform the original formulation to a more convenient form for optimization. For this purpose, instead of direct estimation of the measurement noise characteristics (covariance matrix $\boldsymbol{HH}^T$), the covariance of innovations $\boldsymbol{R}$ is estimated. However, due to the functional dependency of the system parameters Θ (included in $\boldsymbol{A}$, $\boldsymbol{B}$, $\boldsymbol{C}$, $\boldsymbol{D}$ matrices) on the covariance of innovations $\boldsymbol{R}$ from equation (4.19), a strong correlation between estimated variables exists. This fact slows down the convergence performance of optimization. To overcome this problem, a so called *relaxation strategy* is utilized [11].

4.5.1 Relaxation Strategy

The idea of the relaxation strategy lays in partitioning the entire vector of parameters into two sets. The first set of estimated parameters $\hat{\Theta}$ contains the system parameters along with the $\boldsymbol{F}$ matrix, whereas the second set is regarded to the elements of the $\boldsymbol{R}$ matrix. Relaxation strategy of optimization involves a two step iteration. At the first step the estimations of Θ and $\boldsymbol{F}$ are obtained, while the covariance matrix of residuals is held fixed. In the second step, the closed form solution of the $\boldsymbol{R}$ matrix is performed.

4.5.2 Gauss-Newton Optimization

From the variety of optimization methods the most commonly used are the Newton-like methods [7]. They require a computation of first and second gradients of the cost function. As the likelihood functional is strongly nonlinear in estimation parameters, the optimization

is performed recursively. So, if there is a first phase of relaxation method, the $\hat{\boldsymbol{R}}$ matrix is constant. Hence, the first gradient of the cost function (Equation (4.21)) is computed:

$$\nabla_{\Theta} J(\hat{\Theta},\ \hat{\boldsymbol{R}}) = \sum_{i=1}^{N} (\boldsymbol{z}_i - \hat{\boldsymbol{z}}_i)^T (\hat{\boldsymbol{R}})^{-1} \nabla_{\Theta} \hat{\boldsymbol{z}}_i \ . \tag{4.22}$$

The numerical advantage of the Gauss-Newton method upon the pure Newton method is that it does not require a computation of the second gradient of the cost function, rather utilizes the approximation using first gradients of the model output:

$$\nabla_{\Theta}^2 J(\hat{\Theta},\ \hat{\boldsymbol{R}}) \cong \sum_{i=1}^{N} \nabla_{\Theta} \hat{\boldsymbol{z}}_i^T (\hat{\boldsymbol{R}})^{-1} \nabla_{\Theta} \hat{\boldsymbol{z}}_i \quad . \tag{4.23}$$

We can further expand the gradients $\nabla_{\Theta} \hat{\boldsymbol{z}}_i$ and write them in a pure analytic form. However, this expansion does not accelerate greatly the computation of the second gradient. It is therefore favorable to use a numerical differentiation to obtain the gradient of the model output $\nabla_{\Theta} \hat{\boldsymbol{z}}_i$. Using (4.22) and (4.23) one can compute the update to the estimated parameter:

$$\hat{\Theta}_{k+1} = \hat{\Theta}_k + \Delta\hat{\Theta}, \tag{4.24}$$

with

$$\Delta\hat{\Theta} = -(\nabla_{\Theta}^2 J(\hat{\Theta},\ \hat{\boldsymbol{R}}))^{-1} (\nabla_{\Theta} J(\hat{\Theta},\ \hat{\boldsymbol{R}})) . \tag{4.25}$$

Evaluations of equations (4.22) through (4.25) were computed for the system parameters, whereas $\hat{\boldsymbol{R}}$ matrix were held fixed. After each step of optimization, a revision to the covariance matrix of residuals is performed, where the optimized system parameters are used. Estimating $\boldsymbol{R}$ instead of $\boldsymbol{H}$ allows the explicit computation from the evaluated innovations [40]

$$\hat{\boldsymbol{R}} = \frac{1}{N} \sum_{i=1}^{N} (\boldsymbol{z}_i - \hat{\boldsymbol{z}}_i)(\boldsymbol{z} - \hat{\boldsymbol{z}}_i)^T \ . \tag{4.26}$$

4.5.3 Optimization Constraints

The successive evaluation of the MMLE3 algorithm poses several computational constraints. Although the estimation of the $\boldsymbol{H}$ matrix is not directly performed, its values should be nevertheless physically meaningful. The physical interpretation should satisfy an assumption that the diagonal elements of $\boldsymbol{H}$ represent the standard deviations of the measurement of random disturbances.

Using equation 4.19 we can express the $\boldsymbol{HH}^T$ matrix through the estimated $\hat{\boldsymbol{R}}$ matrix and other matrices where system parameters appear. Hence, to be physically meaningful, the $\boldsymbol{HH}^T$ matrix should be positive definitive

$$\boldsymbol{HH}^T = \hat{\boldsymbol{R}} - \boldsymbol{CPC}^T \geq 0 \ . \tag{4.27}$$

As it is shown in [41], the nonlinear constraint equation (4.27) can be accurately approximated by constraining the diagonal elements of the $\boldsymbol{KC}$ matrix to be less than 1. Minimization of the nonlinear cost functional subject to a nonlinear inequality constraint is a problem in nonlinear programming [7]. The most common solution for such problems is to solve a series of quadratic programming problems that locally approximate the nonlinear problem and converge to a solution. A quadratic programming problem is a minimization of a quadratic functional subject to a linear inequality constraint.

To perform the constrained optimization, we have to obtain the local linear approximations to constraints

$$(\boldsymbol{KC})_{ii} + \nabla_\Theta [(\boldsymbol{KC})_{ii}](\Theta - \Theta_k) \leq 1 \, , \tag{4.28}$$

where subscript ii indicates, that only diagonal elements of $\boldsymbol{KC}$ matrix are taken. Expanding the gradient of equation (4.28) yields

$$\nabla_\Theta (\boldsymbol{KC}) = (\nabla_\Theta \boldsymbol{K})\boldsymbol{C} + \boldsymbol{K}(\nabla_\Theta \boldsymbol{C}) \ . \tag{4.29}$$

The gradients of the equation (4.29) are three dimensional tensors and can be also found from numerical differentiation. To solve the quadratic programming problem, first find the unconstrained minimum, using equation (4.25):

$$\tilde{\Theta}_{k+1} = \Theta_k - (\nabla^2_\Theta J(\hat{\Theta}, \ \hat{\boldsymbol{R}}))^{-1}(\nabla_\Theta J(\hat{\Theta}, \ \hat{\boldsymbol{R}})) \ , \tag{4.30}$$

where $\tilde{\Theta}$ is the unconstrained solution of the Gauss-Newton algorithm and k stays for indication of the optimization iteration. With new obtained parameters check if any constraints of (4.28) are violated. If none is violated, the quadratic programming problem is solved and the iteration is complete. If, however, any diagonal elements of $\boldsymbol{KC}$ is greater than 1 then additional vector μ and matrix Ξ should be formed as

$$\mu_i = 1 - (\boldsymbol{KC})_{ii}, \qquad \Xi \, (i, \ .) = \nabla_\Theta [(\boldsymbol{KC})_{ii}] . \tag{4.31}$$

The elements of μ and Ξ corresponding to constraints which are not violated should be deleted. The constrained solution is then

$$\begin{aligned}\hat{\Theta}_{k+1} &= \tilde{\Theta}_{k+1} - \dots \\ &\dots - (\nabla^2_{\Theta} J(\hat{\Theta}, \hat{\boldsymbol{R}}))^{-1} \Xi^T [\Xi (\nabla^2_{\Theta} J(\hat{\Theta}, \hat{\boldsymbol{R}}))^{-1} \Xi^T]^{-1} (\Xi \tilde{\Theta}_{k+1} - \mu).\end{aligned} \tag{4.32}$$

Equation (4.32) should be reevaluated with the revised constraints until the correct set of active constraints is obtained.

4.5.4 Two-Step Iteration

The above given relaxation algorithm works well for the cases where correlation of the estimates within two steps is low. However, in the adopted MMLE3 algorithm, the optimal estimates of the process noise matrix $\boldsymbol{F}$ and covariance $\boldsymbol{R}$ are strongly correlated. Therefore a heuristic weighting operation is performed to minimize the correlation between the $\boldsymbol{F}$ and $\boldsymbol{R}$ matrices. This weighting operation is based on the fact, that after a certain number of optimization iterations, the Kalman gain is mostly induced by the change of only the $\boldsymbol{F}$ and $\boldsymbol{R}$ matrices and insensitive to the other system matrices. This fact is utilized to provide new estimates of the process noise matrix $\boldsymbol{F}$, after the revision of $\boldsymbol{R}$ has succeeded. The main idea of this operation is to find such values of the $\boldsymbol{F}$ matrix, that change of the Kalman gain matrix would be minimal before and after the revision procedure. In [41], the following heuristically determined update procedure is suggested

$$\boldsymbol{F}_{ii}^{new} = \boldsymbol{F}_{ii}^{old} \left(\frac{\sum_k c_{ki}^2 g_k^{old} \sqrt{g_k^{old} / \; g_k^{new}}}{\sum_k c_{ki}^2 g_k^{old}} \right), \tag{4.33}$$

where g_k is the k-th diagonal element of the $\boldsymbol{R}$ matrix. Since the process noise is assumed as white gaussian noise, the $\boldsymbol{F}$ matrix reduces to diagonal form.

To summarize the functioning of the MMLE3 algorithm, the iteration steps are given according to the computation sequences:

1. Choose an a priori Θ and $\boldsymbol{R}$.
2. Perform one iteration of the Gauss-Newton optimization algorithm (minimize negative likelihood functional (4.20) w.r.t. Θ, except for the $\boldsymbol{R}$) using equations (4.22) through (4.30).
3. Revise the estimate $\boldsymbol{R}$ using parameters Θ from step (2) using equation (4.26).
4. Evaluate the update process noise matrix $\boldsymbol{F}$ using (4.33).
5. Return to step (2), if an exit condition is not fulfilled.

The algorithm loop is terminated on step (5) if the condition for optimality has been reached, i.e. no more tries were successful to minimize the negative likelihood functional.

The MMLE3 algorithm utilizes not only rigorous mathematical relations, it includes some discrete approximations and several “numerical tricks” to speed up its convergence. The algorithm was implemented in the Matlab™ simulation environment and some basic tests have been carried out for its verification, as outlined in [32], [33].

4.5.5 Initial Values of Estimates

The MMLE3 algorithm is based on the Gauss-Newton optimization method. The convergence speed of this method is strongly dependent on selection of the initial values of the parameters. They should be chosen as close as possible to the optimal solution. In order to achieve this, a startup evaluation of the model parameters can be utilized [55]. Based on the regression method, this procedure produces initial estimates in one batch iteration, without a need of a priori values. The necessary requirement for the startup procedure is a set of independent measurements of all state variables. The system equations can be transformed as

$$\begin{aligned} \dot{\boldsymbol{x}} &= \boldsymbol{A}_0\boldsymbol{x} + \begin{bmatrix}\boldsymbol{B} & \boldsymbol{A}_1\end{bmatrix}\begin{bmatrix}\boldsymbol{u}\\ \boldsymbol{x}_m\end{bmatrix} + \boldsymbol{b}_x \\ \boldsymbol{y} &= \boldsymbol{C}_0\boldsymbol{x} + \begin{bmatrix}\boldsymbol{D} & \boldsymbol{C}_1\end{bmatrix}\begin{bmatrix}\boldsymbol{u}\\ \boldsymbol{x}_m\end{bmatrix} + \boldsymbol{b}_y, \end{aligned} \tag{4.34}$$

with $\boldsymbol{x}_m$ denoting the measured state, the matrices $\boldsymbol{A}_1$, $\boldsymbol{C}_1$, $\boldsymbol{B}$, $\boldsymbol{D}$ and vectors $\boldsymbol{b}_x$, $\boldsymbol{b}_y$ containing the parameters to be estimated, and the matrices $\boldsymbol{A}_0$ and $\boldsymbol{B}_0$ containing constant (a priori known) coefficients. Because in the transformed system the state $\boldsymbol{x}_m$ and thereby the observation $\boldsymbol{y}$ vectors are linear with the unknown parameters, their values can be determined in one iteration.

Initial values for covariance matrix of innovations $\boldsymbol{R}$ can be found by applying equation (4.26), where estimated responses of the model are based on parameters obtained from equation (4.34).

4.6 Assessment of Estimation Quality

The maximum likelihood estimation method, being a class of the statistical estimators, obtains not only the estimations of parameters itself, but also a level of confidence about their accuracy and their interdependency (correlation). This information helps to get a confidence of estimation for a particular parameter [43]. It also gives a direct indication if the chosen model structure is overparameterized. Finally, the information of the confidence of parameters is an additional aid in designing the future identification experiments. In this sec-

tion, several factors are recognized, which can be obtained by applying the maximum-likelihood estimator.

4.6.1 Theil's Inequality Coefficient

One of the simplest judgements of the results of the estimation is to compare the system response with the model output. The agreement between the model and the real system can be well described by Theil's Inequality Coefficient (TIC) [51]:

$$\mathrm{TIC} = \frac{\sqrt{\sum_{i=1}^{N}(\boldsymbol{z}_i - \hat{\boldsymbol{z}}_i)^2}}{\sqrt{\sum_{i=1}^{N}\boldsymbol{z}_i^2} + \sqrt{\sum_{i=1}^{N}\hat{\boldsymbol{z}}_i^2}} \ . \tag{4.35}$$

The TIC inequality should be calculated for each measurement and corresponding model channel and represents a normalized measure of fit between the system and the model. A value of TIC close to zero indicates a good agreement of the measured and estimated quantity, whereas a value close to unity reflects a poor estimation fit. In many cases of the flight vehicle system identification, values of the TIC measure that lay in interval between 0 and 0.3 are acceptable [18].

4.6.2 Cramer-Rao Bounds

The confidence of estimated parameters is typically regarded in Cramer-Rao bounds. This measure characterizes the lower bound of the covariance of the obtained estimates. That means that subject to some conditions, the covariance of the estimates $\hat{\Theta}$ cannot be less than the Cramer-Rao bound

$$cov(\hat{\Theta}_i) \geq (\boldsymbol{L}^{-1})_{ii} \ , \tag{4.36}$$

where $\boldsymbol{L}$ is the Fisher information matrix. It can be derived from approximation of the Hesse matrix:

$$\boldsymbol{L} = \nabla^2_{\Theta} J(\hat{\Theta}) \approx \sum_{i=1}^{N} \nabla_{\Theta}\hat{\boldsymbol{z}}_i^T \boldsymbol{R}^{-1} \nabla_{\Theta}\hat{\boldsymbol{z}}_i \ . \tag{4.37}$$

Studying the latter equation the following conclusion can be made. In a narrow sense, the Fisher information matrix gives a measure of the information content of the data. Qualitatively, it can be well interpreted by the sensitivity of the particular parameter to the system

output, as the $\nabla_{\Theta}\ddot{\boldsymbol{z}}_i$ terms do. If the sensitivity is large, then the information content of the parameter is also large. This should lead to a smaller Cramer-Rao bound due to inversion of the Fisher (sensitivity) matrix. Therefore, large confidence is obtained about the estimated parameter. Moreover, the quality of the parameter estimates are influenced by the form of the input signal.

Because the Cramer-Rao bounds are defined under assumption of the Gaussian white noise statistics of the state and measurement disturbances, evaluating them with a real flight data provides normally too optimistic results [18]. This is because colored residuals exist between the measured and simulated responses. For this reason, the estimated Cramer-Rao bounds are commonly multiplied by fudge values 5 to 10 or scaled by a factor

$$k = \frac{1}{2f_c\Delta t}\,, \tag{4.38}$$

where f_c is the cut-off frequency of the applied pre-filter [43] (the measured flight data is typically filtered before evaluating in the estimation algorithm, as discussed in section 6.1).

4.6.3 Correlation Between Parameters

The Fisher information matrix delivers an additional measure about the estimation quality. It is attributed to the fact of interdependence of the estimated parameters in the statistical sense, or alternatively referenced as *correlation* [45]. The approximation for the correlation between two parameters Θ_i and Θ_j can be computed as follows

$$\rho_{ij} = \frac{(\boldsymbol{L}^{-1})_{ij}}{\sqrt{(\boldsymbol{L}^{-1})_{ii}(\boldsymbol{L}^{-1})_{jj}}}\,, \tag{4.39}$$

where ρ_{ij} denotes the correlation coefficient between the parameters. The ρ_{ij} has values between 0 (no correlation) and 1 (linear dependency). A consolidated treatment of all correlations results in a correlation map. In the ideal case, one attempts to eliminate the correlation between parameters, so that the estimation problem becomes orthogonal in parameter space (diagonal form of the correlation map).

In practical applications, however, the ideal case can be reached only for a few simple types of systems. For typical multivariable systems it is not the case. As reported in [37], the correlation between parameters in values $\rho_{ij} \leq 0.9$ can be treated as acceptable in flight vehicle system identification. Therefore, this value will be regarded as a maximum allowable for estimation parameters of the postulated airship model.

There are two practical ways to reduce the high correlation between parameters of the estimation model:

- Analyzing the parameter correlation map, one can modify the structure and parametrization of the entire model to minimize the correlation effects
- Some reduction of the interdependency between the parameters can be achieved by selecting an appropriate control input. In the latter case, the control input is designed to affect only one portion of dependant parameters, holding the other parameters unchanged [18]

4.6.4 Cross-Validation Tests

One of the most efficient way to assert the quality of the estimated model is to perform a *cross-validation* check [66]. In this test the estimated model is used to predict the system response for the data records, which were not used in the estimation (the Theil's inequality coefficient is an effective measure of the predictive qualities of the identified model [51]). For critical applications the boundaries of unnoticeable dynamics are defined [12]. In general, a successful cross-validation test is the ultimate goal of the system identification.

Chapter 5

Experiment Design

5.1 Introduction

The experimental part of the “Quad-M” diagram presented in Figure 5.1 recognizes three main items: the flight vehicle (airship), the maneuvers and the measurements. In this chapter, the discussion will be constrained to the issues applicable to the design of the identification experiments. The emphasis will be given on the appropriate choice of the flight maneuvers and the data acquisition system used in the airship identification project.

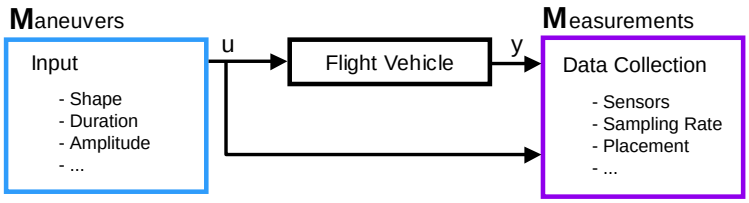

Figure 5.1: Experimental setup in flight vehicle system identification

The design of the maneuvers and setup of the appropriate data acquisition system, are alone sufficiently complicated and very time consuming procedures. They should strongly incorporate the initial knowledge about the flight vehicle dynamics and take into account the restrictions posed by practical utilization of the flight vehicle.

5.2 Design of Control Inputs

5.2.1 General Requirements on Control Input Design

It is well known that the accuracy of parameter estimations is very “input” dependant [39]. The maneuver design commonly used in the flight vehicle system identification, can be summarized as a cyclic process as shown in Figure 5.2. Going through one iteration of the whole design cycle can easily take months or even years in practice [49].

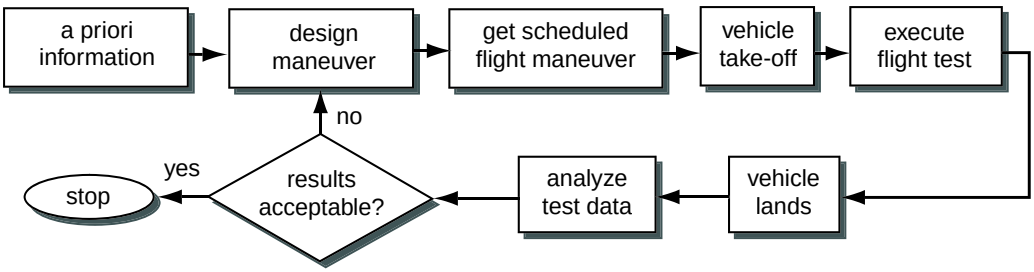

Figure 5.2: Conventional input design cycle [49]

By designing the control inputs for aircraft identification purposes, some general requirements are defined [59]:

1. The frequency band of actuators and the pilot commands should be greater than the eigenfrequencies of the system.
2. Large excitations of the physical plant from the nominal point should be avoided, if possible.
3. The identification inputs of the multi input plant should be applied sequentially.
4. The frequency band of the input signal should cover the frequency band of the plant or alternatively the *persistency to excitation* requirement [53].

The first requirement poses no additional problem in practical application of an airship because of very slow dynamics.

For fulfilling the second requirement, it is generally true that the amplitude and duration of the control input should not deviate the plant too much from its nominal trim condition in order to keep the validity assumptions of the linear model. From the other hand, too small perturbations of the motion variables have, in general, very low signal to noise ratio of measured signals. Typically, these problems can be detected first after post-processing of the flight data, requiring additional flight tests.

The third requirement is attributed mainly to safety critical applications. A typical example is a highly unstable combat aircraft, which can not be flown without incorporating a flight control system. In this case, the control surface deflections can not be applied individually [18]. There are no apparent constraints in fulfilling this requirement for airships.

One major factor in designing the control input for estimating the linear models is the persistency to excitation objective. Through the design of the input shape and its duration, it is desirable to stimulate possibly all eigenmodes of the linear system by the control input. The “well excited” system provides high sensitivities of the model outputs to the parameters and consequently increased accuracy of the parameter estimates (see calculation of the Cramer-Rao bounds in section 4.6.2). This property is closely related to the eigendynamic characteristics of the plant. The a priori knowledge of the plant dynamics is used as a starting point for designing appropriate shapes of input signals.

5.2.2 Typical Input Shapes

Among a variety of identification inputs, in flight mechanics the most common are: the *step, frequency sweep, doublet* and the *multistep 3-2-1-1* inputs [58]. Their time domain realizations are shown in Figure 5.3.

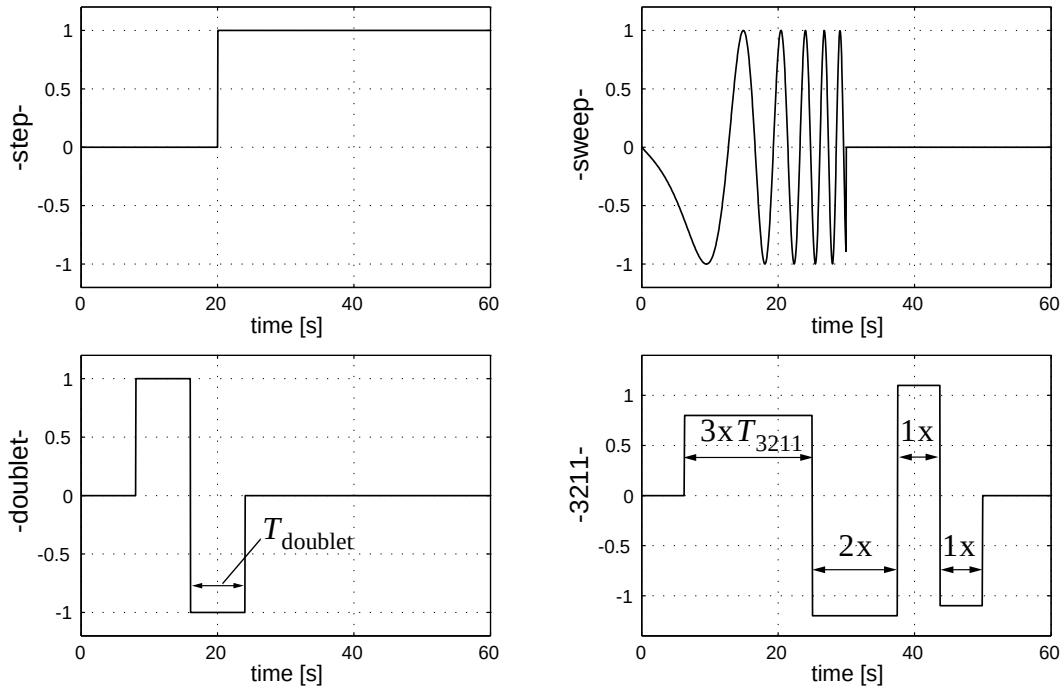

Figure 5.3: Realization of common inputs utilized in aircraft system identification [58]

The step input signal is used to excite very low eigenfrequencies of the plant (see Figure 5.4). Application of this input leads to a stationary system deviation from its nominal (trim) point. For this reason, the step input signal is inadvisable for identification of the linear systems.

The frequency sweep shape of the input signal has the widest frequency band (Figure 5.4) and usually accomplishes the persistency to excitation requirement. However, practical utilization of this input shape is restricted by two limitations. First, generation of the sweep shape poses for the human pilot a considerable difficulty. Second, this input requires a relatively long duration for sweeping the required frequency band [50].

The multistep doublet and the 3-2-1-1 input shape maneuvers are the most widely flown for the aircraft identification purposes. Their advantages are attributed by easy implementation in flight and a simple (re)-design phase based on the current best known modal frequencies of the flight vehicle. To design the multistep input its step duration is selected in such a way, that the natural frequency of the system (i.e. the frequency of undamped system) corresponds to half the frequency band of the input (see Figure 5.4). In this case the maximum power of the input signal is concentrated at the desired system eigenfrequency and

thereby the maximum excitation of the eigendynamics is achieved. For the doublet and 3-2-1-1 inputs it is defined respectively [46]

$$T_{\text{doublet}} = \frac{\pi}{\omega_0}, \qquad T_{3211} = \frac{\pi}{2\omega_0}, \tag{5.1}$$

where ω_0 is the natural eigenfrequency of the vehicle.

From the spectral characteristics, shown in Figure 5.4, the 3-2-1-1 shape is preferable upon the doublet input, as it provides a broader frequency band (1:10 versus 1:3 taken at half of the maximum amplitude) [46]. As a consequence, the 3-2-1-1 input is more robust to errors of the a priori knowledge of the system dynamics then the doublet input.

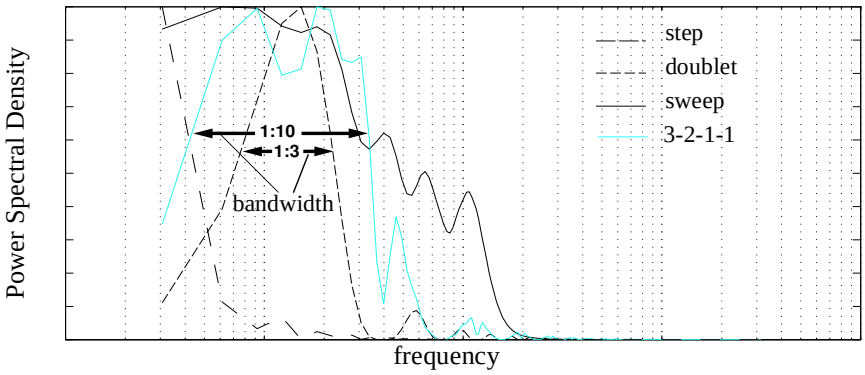

Figure 5.4: Power spectral density function of different input shapes [58]

Several studies utilize the property of the Cramer-Rao bounds as a criteria for designing the optimal input [48], [50], [59]. These techniques use a sequential input design process, in which the inputs are based on the current best knowledge of the system dynamics. However, these “fine tuning” approaches can be only applicable, if sufficient knowledge of the system dynamics is known.

5.2.3 Designing Flight Maneuvers for Airship Identification Purposes

Longitudinal Maneuvers

Investigations of longitudinal dynamics performed in section 3.3 are summarized in Table 5.1. It was shown that the surge mode is largely decoupled with other longitudinal modes. It is therefore advantageous to consider two independent identification maneuvers, where the surge motion is assumed to be determined from the throttle input maneuver, whereas the parameters of the coupled heave and longitudinal-pendulum modes are assumed to be determined from the elevator perturbation maneuvers.

In the longitudinal dynamics, the most important eigenmotion is characterized by the longitudinal-pendulum mode. Because the eigenfrequency and damping of the pendulum

oscillation are strongly dependant on aerodynamic and configuration properties (in the examined case the predicted eigenfrequency ranges from approximately $\omega_{0,\mathrm{LP}} = 0.15[\mathrm{rad/s}]$ to $\omega_{0,\mathrm{LP}} = 0.35[\mathrm{rad/s}]$), it is necessary to design the shape of the control input, which has a possibly wide bandwidth to cover the frequencies of interest.

Table 5.1: Excitation possibility of the longitudinal eigenmodes

Longitudinal Modes	**Physical Interpretation**	**Excitation possibility**
Surge	Axial velocity damping axial drag	Thrust input δT
Heave	Cross-flow/Weatherwaning	Elevator η
Longitudinal-Pendulum	Aerodynamic/Gravity-Buoyancy interactions	Elevator η

From the frequency bandwidth characteristics (Figure 5.4), the most attractive input signals are of the sweep and the multistep 3-2-1-1 shapes. Having the most relevant configuration of a "slightly heavy" airship $B/G = 0.98$ with a trim velocity of about $8[\mathrm{m/s}]$, the eigenfrequency of the pendulum mode is $\omega_{0,\mathrm{LP}} = 0.23[\mathrm{rad/s}]$. The optimal step duration (3-2-1-1) for exciting this frequency can be computed using equation (5.1) which result in the duration of one step sequence $T_{3\text{-}2\text{-}1\text{-}1} \approx 7[\mathrm{s}]$.

Because of relatively small time constant of the aperiodic heave mode, it is possible to excite this eigendynamics within the 3-2-1-1 input applied for exciting the longitudinal-pendulum mode.

A specific scenario for conducting the flight with the thrust perturbations can be developed in order to excite the surge eigendynamics. A simple doublet maneuver with a period of $T_{\mathrm{doublet}} > 2T_{\mathrm{SU}}$, where $T_{\mathrm{SU}} \approx 10[\mathrm{s}]$, indicating the time constant of the surge mode, can be applied to the throttle input.

Lateral-Directional Maneuvers

Table 5.2 summarizes the dynamic analysis of the airship lateral-directional motion. The predicted instability of the sideslip-subsidence mode poses an additional challenge in estimating the lateral-directional dynamics. In order to keep the perturbations at small values, the airship should be flown only with the aid of a flight controller, i.e. in a closed loop operation, which, as well known, suppresses the essential dynamics of the plant [39].

Table 5.2: Excitation possibility of the lateral-directional eigenmodes

Lateral-directional Modes	**Physical Interpretation**	**Excitation possibility**
Sideslip-subsidence	Sideslip-β divergence due to unsteady aerodynamic yawing moment	Rudder ζ
Yaw-subsidence	Cross-flow/Weatherwaning	Rudder ζ
Roll-Pendulum	Aerodynamic-Gravity-Buoyancy interactions	Ailerons ξ

From the other side, the basic dynamic characteristics itself, i.e. the open loop reactions are of primary interest. It can be expected that the marginal instability (depending on flight velocity the time constant ranges $T_{SS} = 7..20[s]$) can be efficiently corrected manually by the pilot, without incorporating the closed-loop control.

5.2.4 Experienced Practical Limitations

The critical issues in designing the flight maneuvers are often settled by practical limitations, which can be first discovered during the flight test. The following discussion is devoted to several constraints revealed while carrying out the test flights with the Lotte airship.

As was determined for the nominal longitudinal model, the duration of the optimally designed 3-2-1-1 input signal with $T_{3\text{-}2\text{-}1\text{-}1} \approx 7[s]$ is 49 seconds. With additional time required for acquisition of the trim condition and subsequent transient motion, the identification maneuver would have resulted in practically unacceptable endurance. This follows from the fact that the Lotte airship, being a remotely controlled vehicle, can be flown only if the line of sight between the test pilot and the airship is clear (which in our case constituted approximately 850 meters). Figure 5.5 illustrates different flight instances of the real flight interval, which was reconstructed from GPS data.

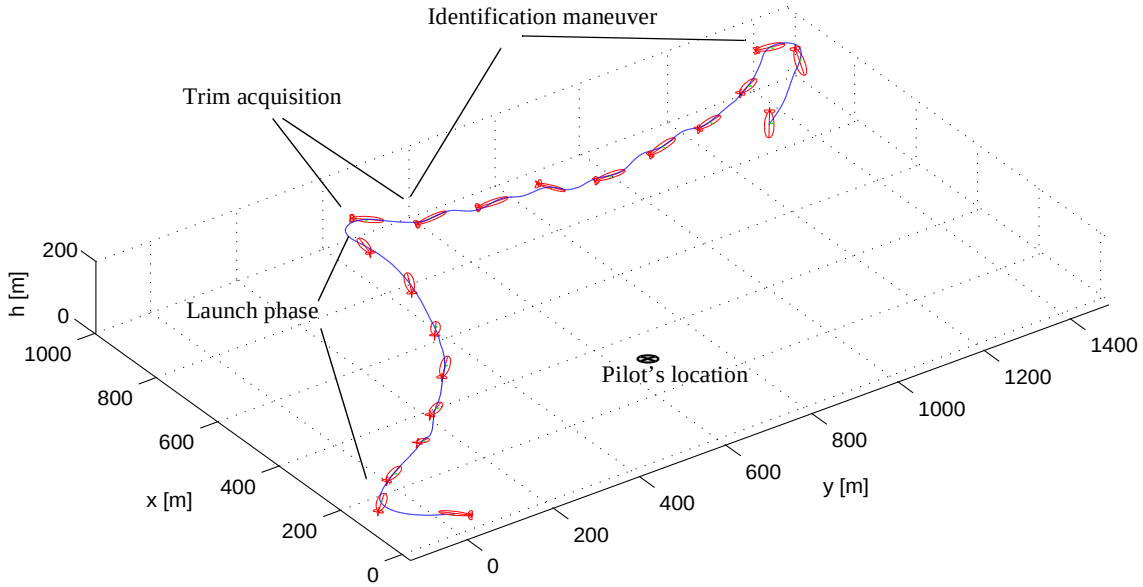

Figure 5.5: Reconstruction of flown trajectory of the Lotte airship

Fortunately, during preliminary identification flights, the test pilot experienced the transient responses of the Lotte on the elevator inputs much shorter than it was predicted by modelling. Due to this fact, the step length of the 3-2-1-1 input has been reduced to $T_{3\text{-}2\text{-}1\text{-}1} \approx 4[s]$. Note, the applied input was not optimal with respect to the initial model knowledge, but became apparent from the flight testing and the pilot's opinion. In addition to the 3-2-1-1 input shape, the test signals of different shapes (doublet and sweep) have been also applied during the subsequent flight tests.

Another examination of the measured data from the trial flights has resulted in additional limitations. In the remotely controlled operation of Lotte, the test pilot was neither able to acquire some desired trim condition with a predetermined states u_0, w_0, θ_0, nor repeat it in the subsequent maneuvers. This drawback could not be eliminated during the whole testing program and has significantly constrained the availability of the data at different flight regimes.

In order to assure the validity of the assumed linear model, the initially commanded flap deviations from the trimmed condition were limited at $|\delta\eta| \leq 5°$. However, in this case the low signal to noise measurements made the flight data practically intractable for the identification task. For overcoming the low signal to noise problem, it was decided to carry out all subsequent flight maneuvers at maximal amplitudes of the control surfaces, which constitute $|\delta\eta|_{max} = 41°$.

In conducting the lateral-directional identification maneuvers, a complete authority of the pilot was required in order to keep the airship near its rectilinear trajectory.

Of course, the most critical limitation in the flight testing program was posed by the atmospheric conditions. If the flight tests were performed in the highly turbulent atmosphere, even optimally designed inputs and sophisticated identification algorithms could do nothing for improving the identification results.

5.3 Data Collection System

Realization of an appropriate flight recording system takes, in general, even more time than the design of the flight maneuvers. During the airship identification project it was not possible to skip this elaborate process, and therefore it became necessary to deal with problems associated with instrumentation setup and analysis of the measured data. This section will be devoted accordingly to issues related to hardware realization.

5.3.1 Realization of Measurement Hardware

The discussion in Chapter 2 was briefly devoted to the problems of choice of measurement quantities for the identification problem. In the airship identification project it was necessary to develop measurement hardware which could perform required measurements in the real-time scale. One of the most important objectives of the measurement hardware was the accomplishment of the weight constraints and power consumption. Inasmuch as time and financial funds were restricted, the utilization of commercially available products was concluded in the project.

An appropriate solution in choosing the measurement hardware was the use of a combined device as illustrated in Figure 5.6. The unit is integrated with several elements: the 3D accelerometer, the rate gyros, the GPS receiver and the evaluation unit. The computer evaluation unit has several functional duties, such as evaluation and storage of the flight data in real-time mode, the generation of preprogrammed identification inputs for use during flight

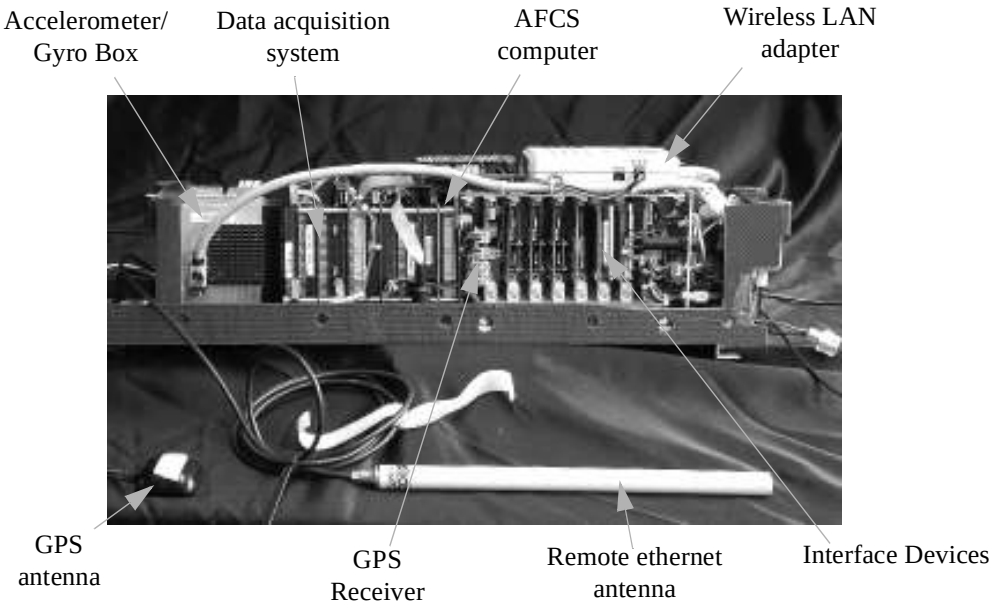

Figure 5.6: Realization of a combined measurement platform

tests, and the automatic flight control system (AFCS). In addition, the combined measurement unit is equipped with several communication interfaces for collecting and exchanging data with different measurement and actuating units, and for the online telemetry to the ground based observation station.

The working prototype has been continuously modernized in both hardware and software modules. The general characteristics of the recent setup of the measurement platform are presented in Table 5.3.

Table 5.3: Accuracy characteristics of sensors integrated in the measurement platform

Measurement	**RMS**	**Units**
Accelerations ax, ay, az	0.003	$[m/s^2]$
Rotation rates p, q, r	0.003	[deg/s]
Euler angles ϕ, θ, ψ	0.2	[deg/h][a]
GPS velocity 3D[b] u_K, v_K, w_K	0.2	[m/s]

a. Specified drift rate of the measured Euler angles

b. For a stationary user

Following the discussion from section 2.5, the aerodynamic measurements of airstream velocity, air density and temperature should be available for tracking the flow properties. These measurements should be made at the nose part of the airship to avoid the interference effects of the airship's body. As it is in principle difficult to combine the aerodynamic sensors together with the inertial measurement sensors, the measurement configuration led to a distributed network.

Figure 5.7: Realization of ultrasonic anemometer for airstream velocity measurements

At early stages of the identification project, the measurements of the airstream velocity were based on a conventional multiple hole probe device. However, low operation velocities induced a relatively small dynamic pressure and this device produced high noisy measurements. It was therefore decided to replace the hole probe sensor with an ultra sonic anemometer. The ultra sonic anemometer, shown in Figure 5.7 has a significant benefit in providing accurate 3D airstream velocity measurements (see Table 5.4) at low velocities up to 30 [m/s]. The anemometer delivers the airstream measurements to the main measurement platform via a CAN (Controller Area Network) data interface. The top-level overview of the communication network of the Lotte airship is shown in Figure 5.8.

Table 5.4: Accuracy of airstream velocities provided by ultrasonic anemometer

Measurements	**RMS**	**Units**
Airstream velocities u_A, v_A, w_A	0.4	[m/s]

Along with measurements of the output variables, it was also necessary to store the pilot commands and the control variables respectively. As pointed out, the “Lotte” airship is normally controlled by a pilot in the remote operating mode. The pilot initiates the command signals and distributes them onboard via remote datalink. The onboard receiver transforms commanded signals into digital messages and distributes them via the onboard local network. These messages are used to drive the actuators and are therefore available for recording them. In addition, the option was included to employ preprogrammed commands to drive the actuators.

5.3.2 Sampling Strategy

In a computer-based acquisition system, it is unavoidable that sampling of measurements leads to information losses. Therefore it is important to select the sampling frequency so that these losses are insignificant for the estimation process. As with the design of the input sig-

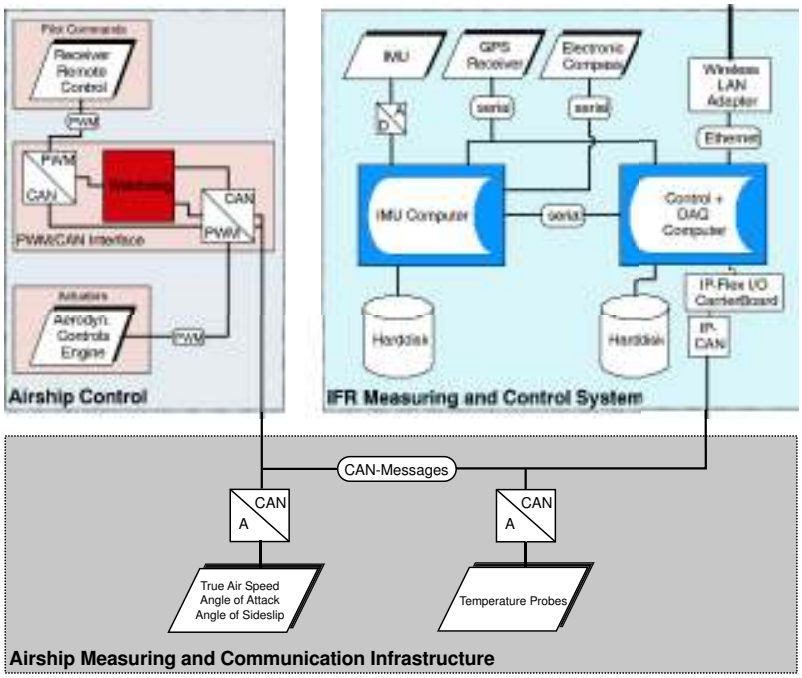

Figure 5.8: Basic communication network of “Lotte” airship

nals, the sampling strategy is directly related to a priori information about the system dynamics. Here, the following factors are taken into account by selecting the sampling frequency:

- According to Shannon’s theorem [11], the sampling frequency should be at least two times higher than the system highest eigenfrequency

$$\omega_{0,\max} < \frac{\omega_s}{2},\ \omega_s = 2\pi f_s = \frac{2\pi}{\Delta t}. \tag{5.2}$$

  It is in general true that a higher sampling frequency will cause less loss of information. However, building the discrete-time models with a very small sampling time Δt may also lead to numerical evaluation problems. According to Equation (4.10) the state transition matrix Φ at high sampling rates will converge to the identity matrix

$$\Phi = e^{\boldsymbol{A}\Delta t} \cong \boldsymbol{E} + \boldsymbol{A}\Delta t + \boldsymbol{A}^2\frac{\Delta t^2}{2!} + \ldots \approx \boldsymbol{E}\ , \tag{5.3}$$

  which leads to the pole distribution of the discrete system around the point $(1{,}0\mathrm{i})$ on the complex plane, i.e. at the border of the stability region [9].

- The real-time operation mode of the data acquisition system also poses strong requirements on the data storage frequency. It depends on the evaluation capacity of the onboard digital computer.

From the above given constraints, the last one was the dominant in our case. With relatively slow dynamics of the airship the sampling frequency of measurement signals of 20[Hz] was found to be sufficient for acquiring the system response.

Chapter 6

Results and Analysis

6.1 Details of Flight Maneuvers and Postflight Analysis

6.1.1 Carrying Out the Flight Tests

In August 2002, favorable weather conditions allowed several identification flights with the “Lotte” airship to be carried out. Altogether, 15 identification maneuvers of a duration of approximately 60 seconds each, have been flown. Most of the flight maneuvers, were conducted for the longitudinal character of motion. Some preliminary identification results were reported in [34]. A complete overview of the flown identification maneuvers is outlined in Appendix C.

6.1.2 Postflight Data Analysis

It is common practice to perform a number of preliminary analysis of the raw measurements, before the flight data is accepted for parameter estimation. Their intention is to reduce unwanted effects in the measured data and to conclude whether the flight data is relevant for further analysis. In the current identification project the postflight data analysis consisted of:

- prefiltering
- air data correction
- data compatibility checking.

A limited choice of mounting places for the measurement equipment poses a common vibration problem [42]. The measurements were heavily contaminated with high frequency structural vibrations caused by the thrust propeller. For minimizing the high frequency content in the flight data, filtering is applied. This procedure is outlined in C.2.1.

The airstream measurements were corrected for the free-stream conditions in order to eliminate the interference effects caused by the hull of the airship. These results are presented in C.2.2.

Utilization of the data compatibility checking procedure had two basic goals in the postflight data analysis [18]. First, the determination of typical instrumentation errors before the parameter estimation. Second, using this approach, a plausibility check of the flight data, which provides a systematic judgement about the applicability of the postulated estimation model to the flown maneuvers can be gained. The details of this procedure and the achieved results are presented in section C.2.3.

6.2 Longitudinal Derivatives from Elevator Perturbation Flight

Estimation of parameters of the longitudinal model introduced in section 3.2, aims to determine the longitudinal stability and control derivatives. Because the output-error and the filter-error estimation algorithms are based on the Gauss-Newton optimization method, to speed up their convergence, the initial values of parameters have been determined using the equation-error based start up algorithm, as described in section 4.5.5.

6.2.1 Application of Output-Error Method

Just a simple visual analysis of the measured trajectories can give an initial confidence about the dynamic behavior of the airship. Studying the measured trajectories (Figure 6.1), one observes that the forward velocity remains nearly unchanged during the whole measurement interval. This behavior agrees with the conclusions made in subsection 3.3.4, where the nominal simulation model was considered. The elevator control input effectively excites only vertical and rotational (pitch) variables and has almost no effect on perturbations of the axial velocity. For this reason, the forward velocity damping derivative X_u will be hardly determined from this maneuver.

An additional, but less evident conclusion can be drawn when variations of the axial velocity are analyzed at different pitch angles. Even at large values of θ there is no apparent change in the $u_{A|CS}$ trajectory. This behavior indicates that the airship operates at nearly neutral buoyancy-gravity condition, i.e. the gravity force is almost compensated by the buoyancy force. In this case, the contribution of the X_θ and Z_θ derivatives should be negligibly small.

In order to ensure that these conclusions are valid, a verification test was performed, were the fully parametrized longitudinal model, having 24 unknowns

$$\Theta = \left[\begin{array}{l} X_u\ X_w\ X_q\ X_\theta\ Z_w\ Z_q\ Z_\theta\ M_u\ M_w\ M_q\ M_\theta\ X_\eta\ Z_\eta\ M_\eta \ldots \\ \ldots b_{\dot{u}}\ b_{\dot{w}}\ b_{\dot{q}}\ b_{\dot{\theta}}\ b_u\ b_w\ b_q\ b_\theta\ b_{ax}\ b_{az} \end{array} \right]^T \tag{6.1}$$

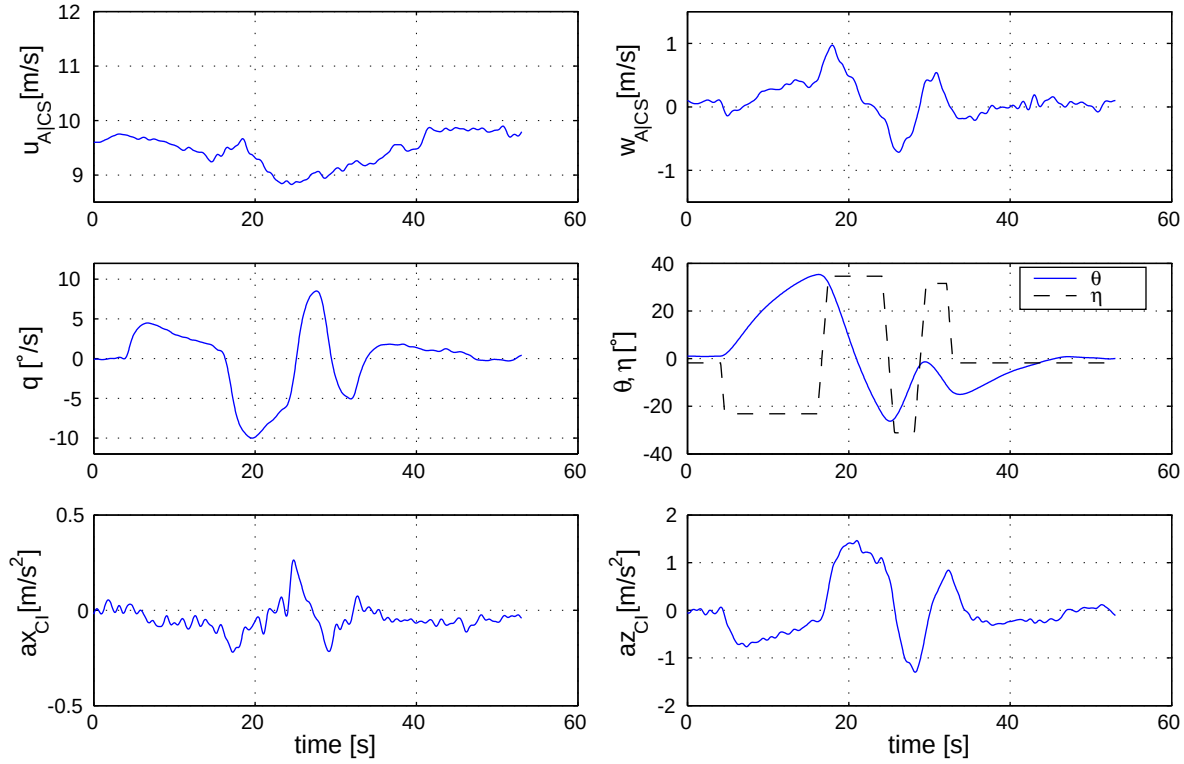

Figure 6.1: Filtered time history data of longitudinal F4S1e flight maneuver

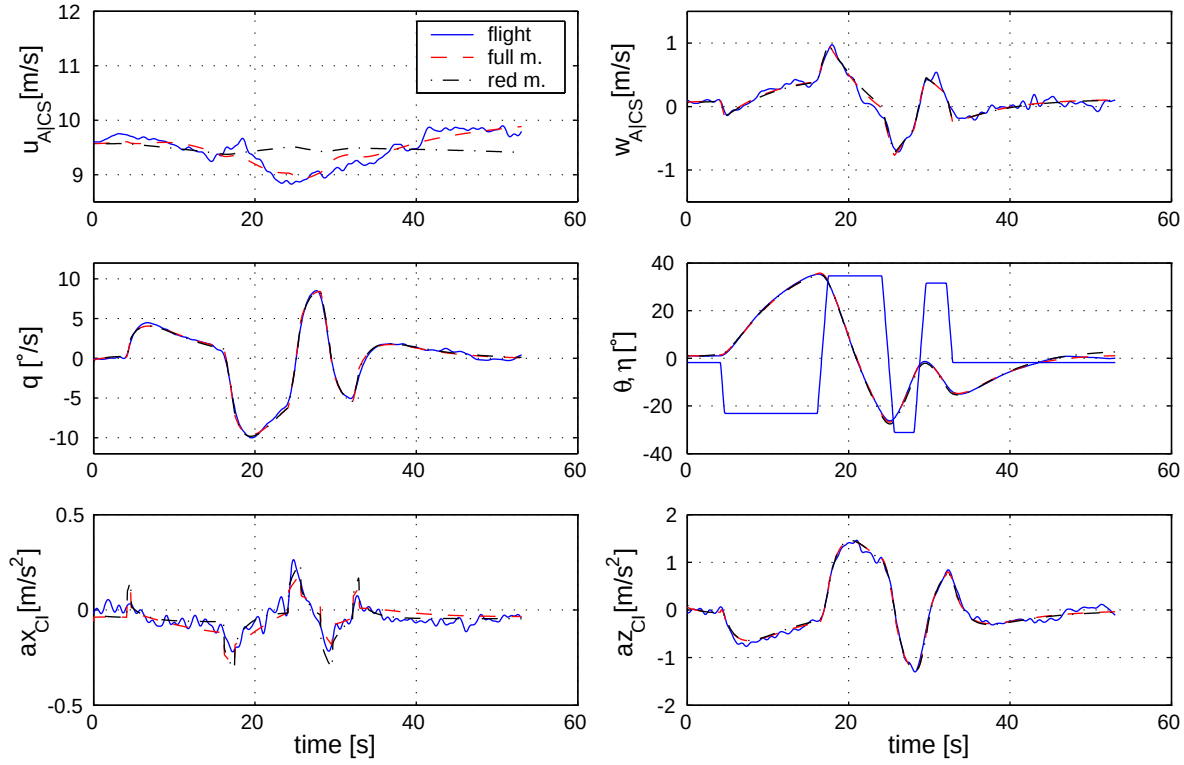

Figure 6.2: Time histories of measured and estimated (Output-Error) responses, of the full state longitudinal models

and a model with a reduced set of parameters, are estimated. The reduced model neglects the X_w, X_q, X_θ, Z_u, Z_θ and M_u derivatives in the dynamic matrix

$$\boldsymbol{A}_{\text{red}} = \begin{bmatrix} X_u & 0 & 0 & 0 \\ 0 & Z_w & Z_q & 0 \\ 0 & M_w & M_q & M_\theta \\ 0 & 0 & 1 & 0 \end{bmatrix}. \tag{6.2}$$

The time responses of both models, estimated using the output error algorithm, are illustrated in Figure 6.2. As can be observed, there is a quite small difference between the two models in estimating the forward velocity $u_{A|CS}$ and no apparent differences in other response variables. Numerical values of the estimated parameters and the supplementary information (Cramer-Rao bounds, TIC coefficients, Eigenvalues) are provided in Table C.2.

Another important indication of the parameter estimation procedure is characterized by the algorithm convergence property. The model with the reduced number of estimation parameters has required 29 iterations to converge, whereas the convergence of the fully parameterized model could not be reached and has been broken after 100 iterations. As will be shown later, this improvement arise due to reduced correlation between estimates and, therefore, a better conditioning of the Hessian matrix (Equation (4.37)).

From this simple verification trial, one concludes that the forward velocity perturbation state δu, corresponding to the surge mode, can be regarded as decoupled with the remaining states. It follows from the structure of the dynamic matrix $\boldsymbol{A}_{\text{red}}$ (6.2) of the simplified model. With this knowledge, it is now possible to concentrate efforts on estimating the reduced order model without the δu state. It should be noticed, that fairly similar flight phenomena was observed not only for this particular flight record, but in all subsequent longitudinal maneuvers perturbed by elevator deflections. These trajectories are outlined in section C.3.

Low Order Estimation Model

The reduced plant model involves the state-space formulation as described in equation (3.31). Altogether, there are 14 estimation parameters, including 5 stability, 2 control derivatives and 7 bias unknowns respectively:

$$\Theta = \begin{bmatrix} Z_w & Z_q & M_w & M_q & M_\theta & Z_\eta & M_\eta & b_{\dot{w}} & b_{\dot{q}} & b_{\dot{\theta}} & b_w & b_q & b_\theta & b_{az} & u_0 \end{bmatrix}^T. \tag{6.3}$$

As can be concluded from Figure 6.3, in spite of the state reduction, the agreement between the measured and the computed responses is still very good.

So far, only the fit between the measured and the model responses was used as a basic goodness criteria. The trajectory fit does not, however, guarantee the fact that the estimated parameters are reliable. This can be evident when analyzing the correlations between esti-

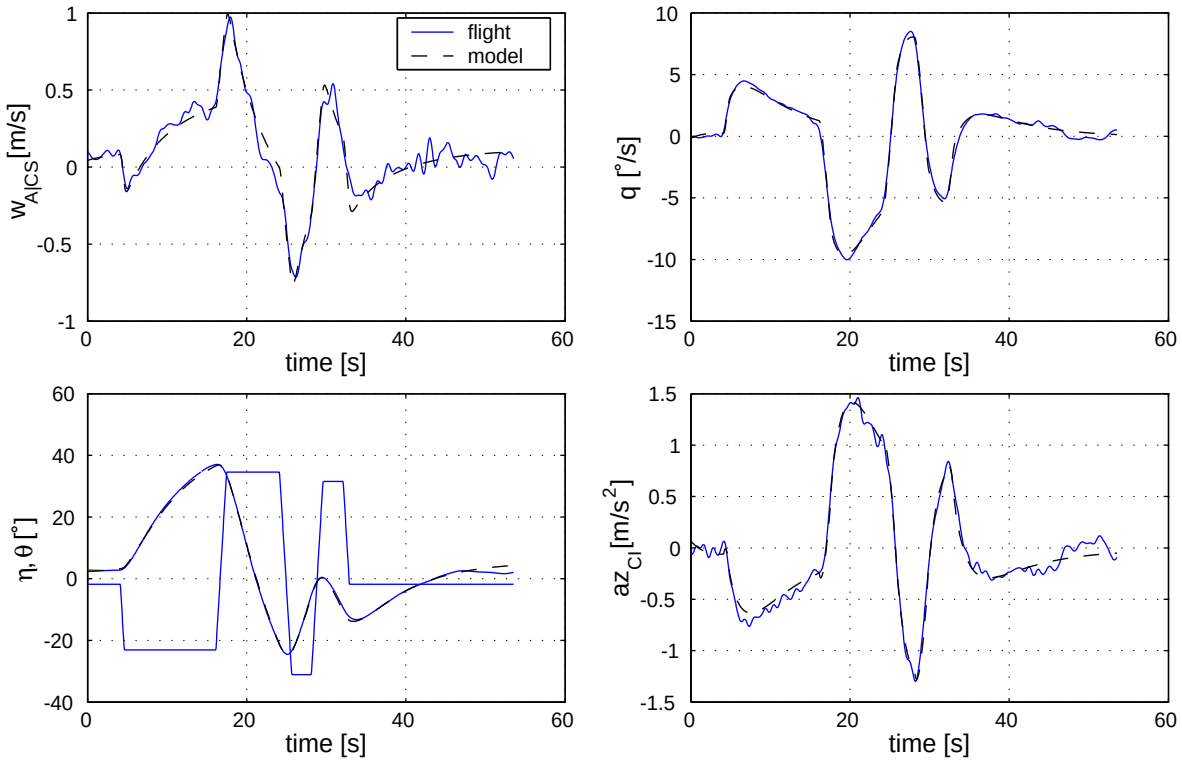

Figure 6.3: Time histories of measured and estimated (Output-Error) response, of the reduced order longitudinal models

mated parameters, presented in Figure 6.4(a). In spite of a good trajectory agreement, a nearly linear dependency ($\rho_{ij} > 0.98$) exists for several pairs of estimated parameters.

The adopted estimation model with highly correlated parameters should be possibly re-parametrized in order to reduce this interdependence. The reduction of the parameter space of the model can be done based on the following propositions:

- Because the parameters comprising the bias vectors $\boldsymbol{b}_x$ and $\boldsymbol{b}_y$ have only minor importance (e.g. for accounting for the initial condition and the sensor errors), a high correlation between them can be allowed unless this does not affect the stability and control estimation or the optimization convergence.
- If a strong dependence between any derivative and the bias parameter exists, the latter should be fixed at some (nominal or zero) value during estimation.

These steps should be regarded as a trade off between the performance of the model and estimation confidence of important derivatives.

A serious difficulty arises from the fact that the estimated derivatives M_w, M_q and M_θ are highly correlated. Neglecting one of these parameters is undesired, because otherwise it will change the essential properties of the model (such as removing of the second order dynamics of the longitudinal pendulum motion). One advisable solution is to fix the static pitch stability coefficient M_θ at some nominal value during estimation. Fixing the M_θ has a particular advantage, because its value basically characterizes the metacentric position z_{CG}

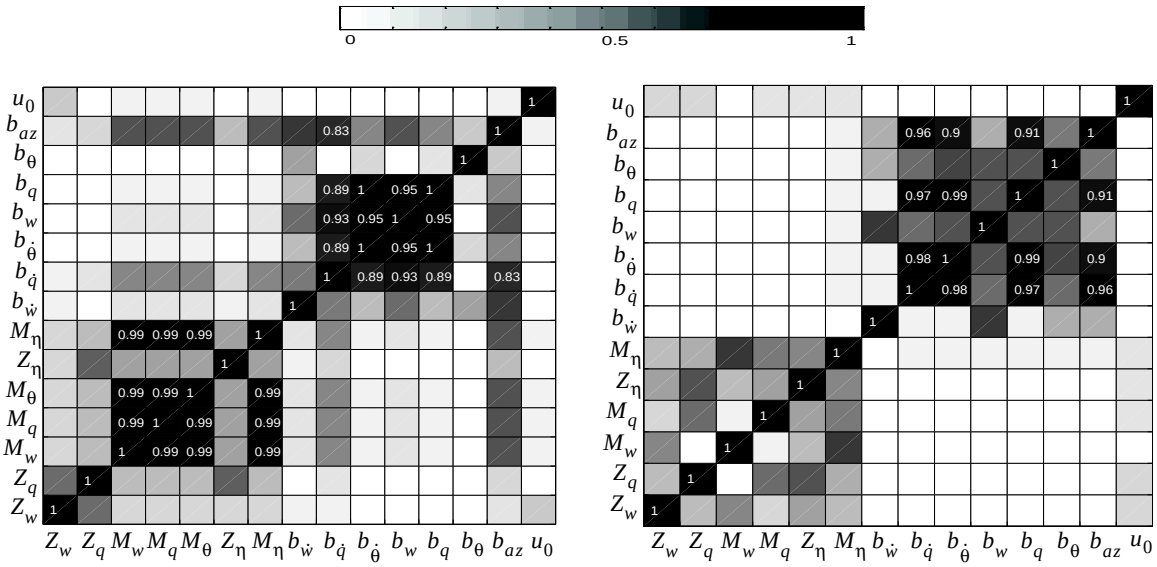

(a) M_θ included (b) M_θ excluded

Figure 6.4: Correlation map of estimated parameters (numerical values provided for $\rho_{ij} > 0.8$)

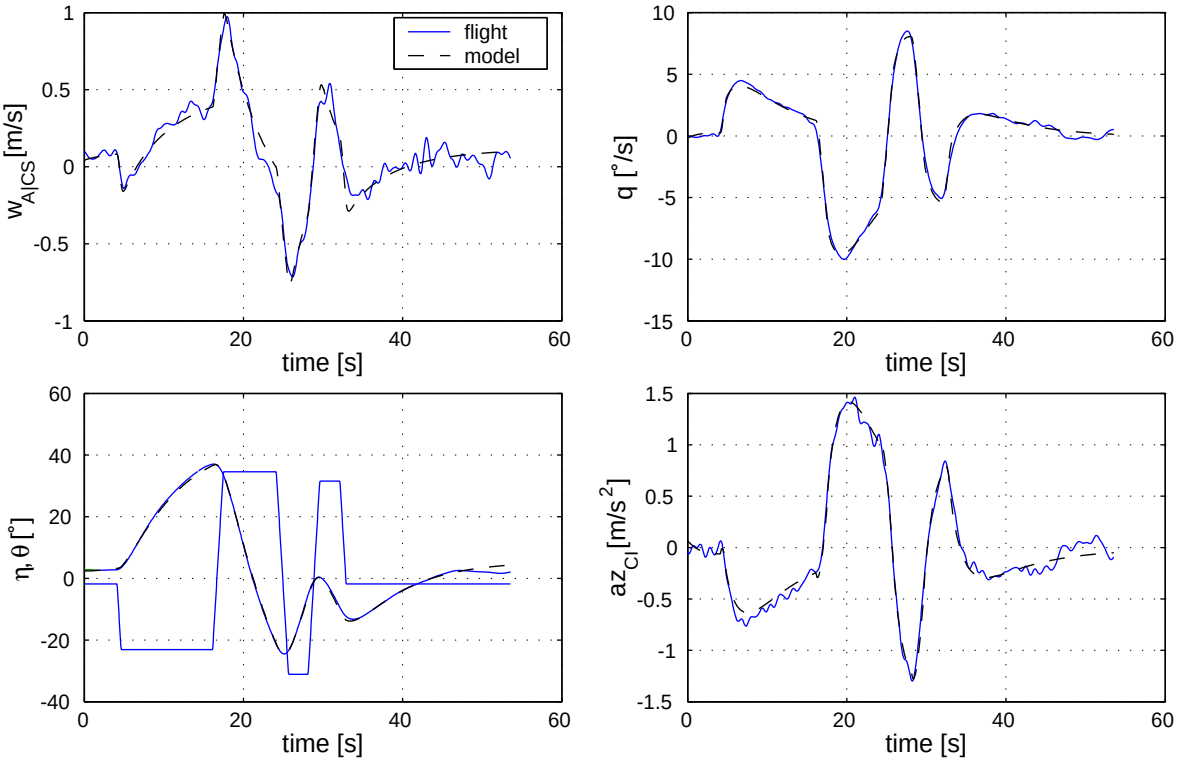

Figure 6.5: Time histories of measured and estimated (Output-Error) responses with fixed M_θ derivatie

and is quite insensitive to variations of the trimmed velocity. This derivative can be alternatively calculated using approximation [23]:

$$M_\theta \approx -\frac{mgz_{CG}}{(I_{yy} - M_{,\dot{q}})}. \tag{6.4}$$

Therefore, the same value of M_θ can be used for several flight segments, under supposition that environmental conditions and configuration of the airship remain unchanged. Because the static pitch stability derivative was not known exactly, was initially decided to use an averaged value of the M_θ estimations from several maneuvers.

The model with the reduced parameter space has been evaluated and compared with the response of the model that uses the estimated M_θ derivative for the same flight maneuver. Because the bias parameters show (Figure 6.4(a)) a little correlation with important derivatives, they have not been discarded. Figure 6.5 shows that there is almost no qualitative difference in the time plots provided by the nominal model and the model with fixed M_θ. Fixing this parameter also results in reduction of interdependency between M_w and M_q, as illustrated by the correlation map in Figure 6.4(b). As a consequence, estimation of the Cramer-Rao bounds of these two derivatives M_w, M_q has been significantly reduced (see Table C.3).

Accounting for Large Pitch Deviations

One interesting result is that the purely linear model fits the measurements even at the cases, where nonlinear effects are evident. For example, examining the system responses shown in Figure 6.6, one observes that the pitch angle reaches very large values $\theta_{\max} > 35^\circ$. The trigonometric nonlinearities, associated with these large deviations, invalidate the modelling assumptions, given in section 3.2.1. On the other hand, even at large pitch deviations, the aerodynamic linearity assumption is acceptable due to relatively small perturbations of the angle of attack $|\alpha| < 8^\circ$.

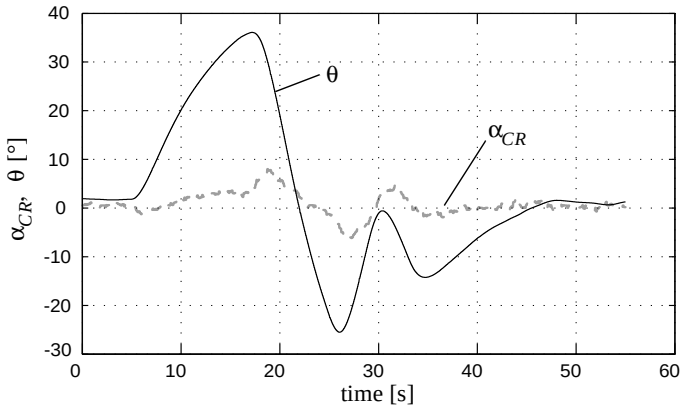

Figure 6.6: Measured pitch deviations and angle of attack during 3-2-1-1 identification maneuver

In order to keep the physical validity of the estimation model, its basic structure established in equation (3.31) has been slightly changed. Because the measured Euler angles are normally subjected to a relatively small sensor noise, a directly measured value of θ can be taken for precomputing the trigonometric nonlinearity. The resulted signal is then applied to the model as a deterministic pseudo-input. In the state-space representation, the enhanced dynamic model yields

$$\begin{bmatrix} \delta\dot{w} \\ \delta\dot{q} \end{bmatrix} = \begin{bmatrix} Z_w & Z_q \\ M_w & M_q \end{bmatrix} \begin{bmatrix} \delta w \\ \delta q \end{bmatrix} + \begin{bmatrix} Z_\eta & 0 & b_{\dot{w}} \\ M_\eta & M_\theta & b_{\dot{q}} \end{bmatrix} \begin{bmatrix} \eta \\ \sin\theta \\ 1 \end{bmatrix}. \tag{6.5}$$

Because the measured pitch angle was used as the pseudo control variable, the system output was reduced to

$$\boldsymbol{y} = \begin{bmatrix} w_{A|CS} & q & az_{CI} \end{bmatrix}^T.$$

In this case the observation model appears as:

$$\begin{bmatrix} w_{A|CS} \\ q \\ az_{CI} \end{bmatrix} = \begin{bmatrix} 1 & -x_{CS} \\ 0 & 1 \\ Z_w - x_{CI}M_w & Z_q - x_{CI}M_q - u_0 \end{bmatrix} \begin{bmatrix} \delta w \\ \delta q \end{bmatrix} + \begin{bmatrix} 0 & 0 & b_w \\ 0 & 0 & b_q \\ Z_\eta - x_{CI}M_\eta & -x_{CI}M_\theta & b_{az} \end{bmatrix} \begin{bmatrix} \eta \\ \sin\theta \\ 1 \end{bmatrix}. \tag{6.6}$$

In this formulation, the model has been estimated using the output error method. The estimated time histories are presented in Figure 6.7.

In addition to the proposed parametrization, Figure 6.8 illustrates the trajectory estimations of the model that assumes the zero static pitching moment $M_\theta = 0$. This "worst-case" parametrization, corresponding to the case when $x_{CG} = 0$, $z_{CG} = 0$, is used here to ensure the significance of the M_θ derivative in the system dynamics.

The estimated response of the enhanced model provides no visible improvement in trajectory. However, the overall performance of the extended model is more confident with regard to the performance of the pure linear model. The responses of the model that discards the static pitching moment M_θ, has lead to inacceptable large model deviations from the flight trajectories.

Application of the enhanced model, however, did not reduce the problem of a high correlation between estimates. A nearly linear dependency (not shown) between the derivatives M_w, M_q and M_θ remains unchanged. Therefore, the demand on fixing the M_θ is actual for this model formulation as well.

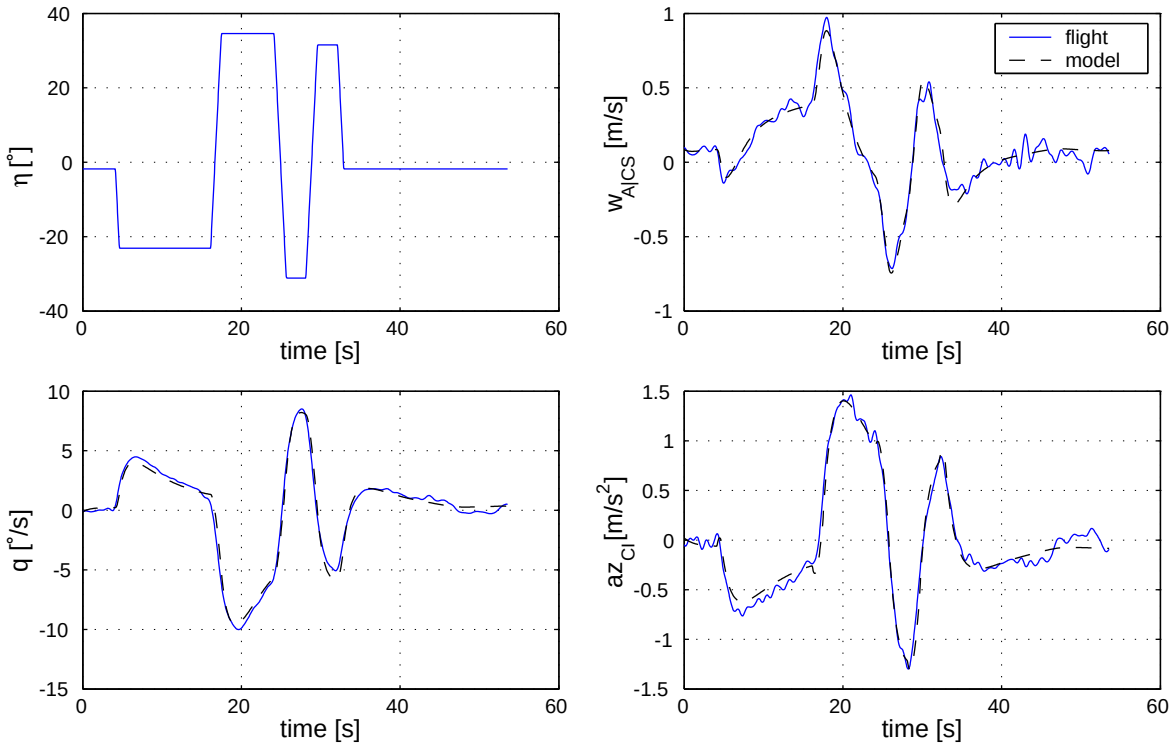

Figure 6.7: Estimated trajectories of the enhanced model for estimating the large pitch deviations

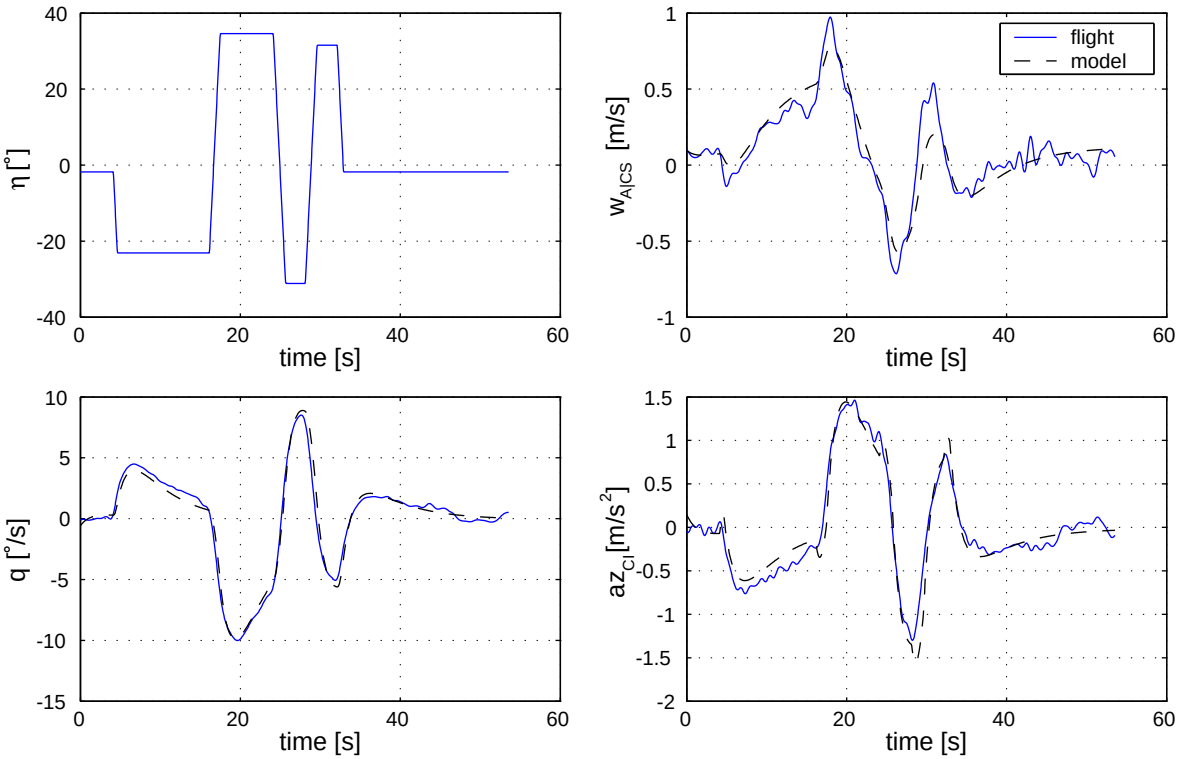

Figure 6.8: Estimated trajectories of the model with $M_\theta = 0$.

6.2.2 Application of the Filter Error Method

Estimation results, obtained by using the output error algorithm, can be treated as a basis for selecting a reliable parametrization of the longitudinal model and for acquiring the intermediate estimation results. Although the trajectory and parameter estimations are very encouraging, still some discrepancies in particular in the vertical velocity (Figure 6.7) between the measured and estimated trajectories. These discrepancies can be classified by a presence of a slightly turbulent atmosphere.

The filter error algorithm is applied to the measured data, in order to minimize the negative effect of this uncontrolled motion on parameter estimations. The model has been used which accounts for the large pitch variations. To minimize the risk of numerical instability during optimization, the unknown disturbances are regarded as two uncorrelated white gaussian processes that affect the q and w states

$$\boldsymbol{F} = \begin{bmatrix} \sigma_{\dot{w}} & 0 \\ 0 & \sigma_{\dot{q}} \end{bmatrix}. \tag{6.7}$$

The filter error algorithm incorporates these two parameters additionally to estimate the intensity of the process noise. The parameter vector is then defined by

$$\Theta = \begin{bmatrix} Z_w & Z_q & M_w & M_q & Z_\eta & M_\eta & b_{\dot{w}} & b_{\dot{q}} & b_w & b_q & b_{az} & \sigma_{\dot{w}} & \sigma_{\dot{q}} \end{bmatrix}^T \quad . \tag{6.8}$$

Estimation results using the filter error method are presented in Table C.4 and the time plots are shown in Figure 6.9. The agreement between the measured and estimated trajectories is now nearly perfect. This improvement of the trajectory fit also affects the confidence of the estimated parameters. Most of them were estimated with reduced Cramer-Rao bounds, comparing to estimations derived by the output-error method. Estimating the process noise parameters $\sigma_{\dot{w}}$, $\sigma_{\dot{q}}$, along with other model unknowns, did not lead to a critical interdependencies between parameters.

The performance of the filter-error algorithm is more efficient, when the model parameters are estimated from maneuvers conducted at a higher turbulence level. Figure 6.10 illustrates the time histories of the model estimated with both algorithms, i.e. the output-error and the filter-error methods. Not only large residuals in trajectories, but also inadequate numerical values of some estimated parameters have been obtained, when the output-error method was used. Although the evaluation time was not the central factor in the current analysis, the slow convergence speed has indicated serious numerical difficulties during optimization.

A better performance has been observed when the filter error method was applied. In almost all performance characteristics, i.e. the trajectory fit, the plausibility of parameter estimates, Cramer-Rao bounds and convergence properties, a significant improvement has been achieved. The numerical values of estimated derivatives are close to those, obtained for records at very calm atmospheric conditions.

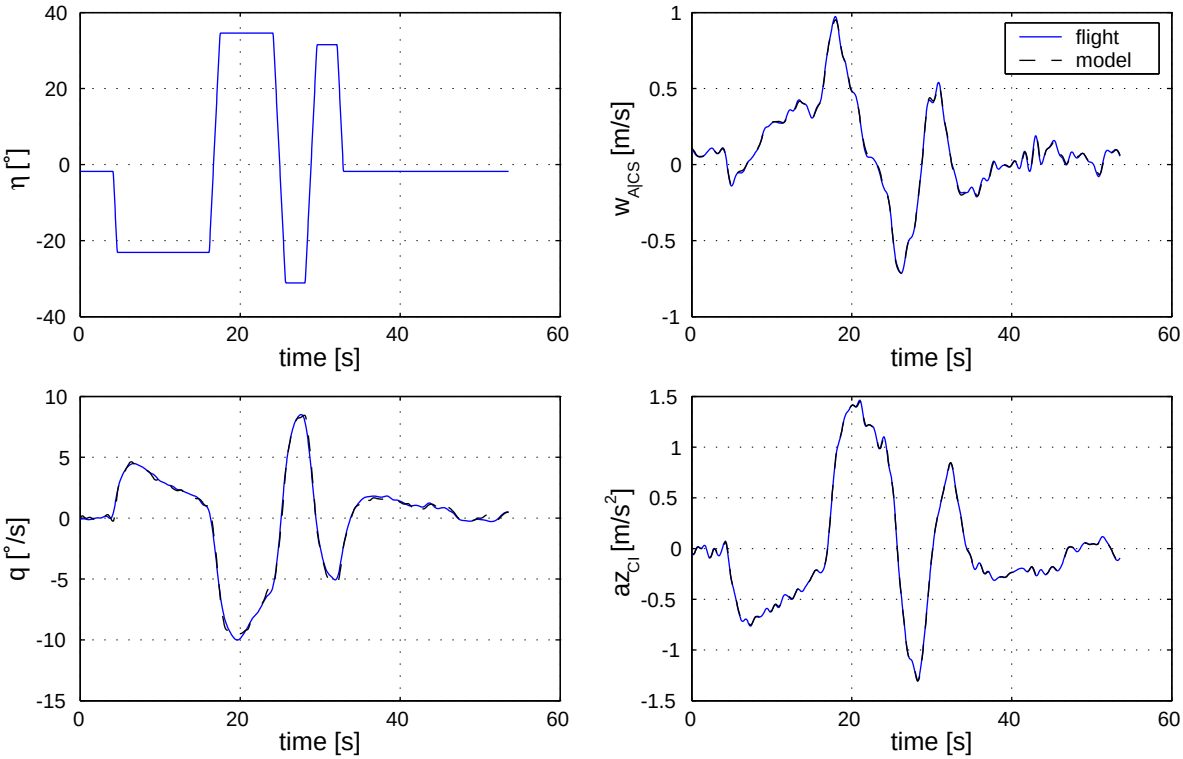

Figure 6.9: Filter error method applied for estimation of the F4S1 longitudinal maneuver

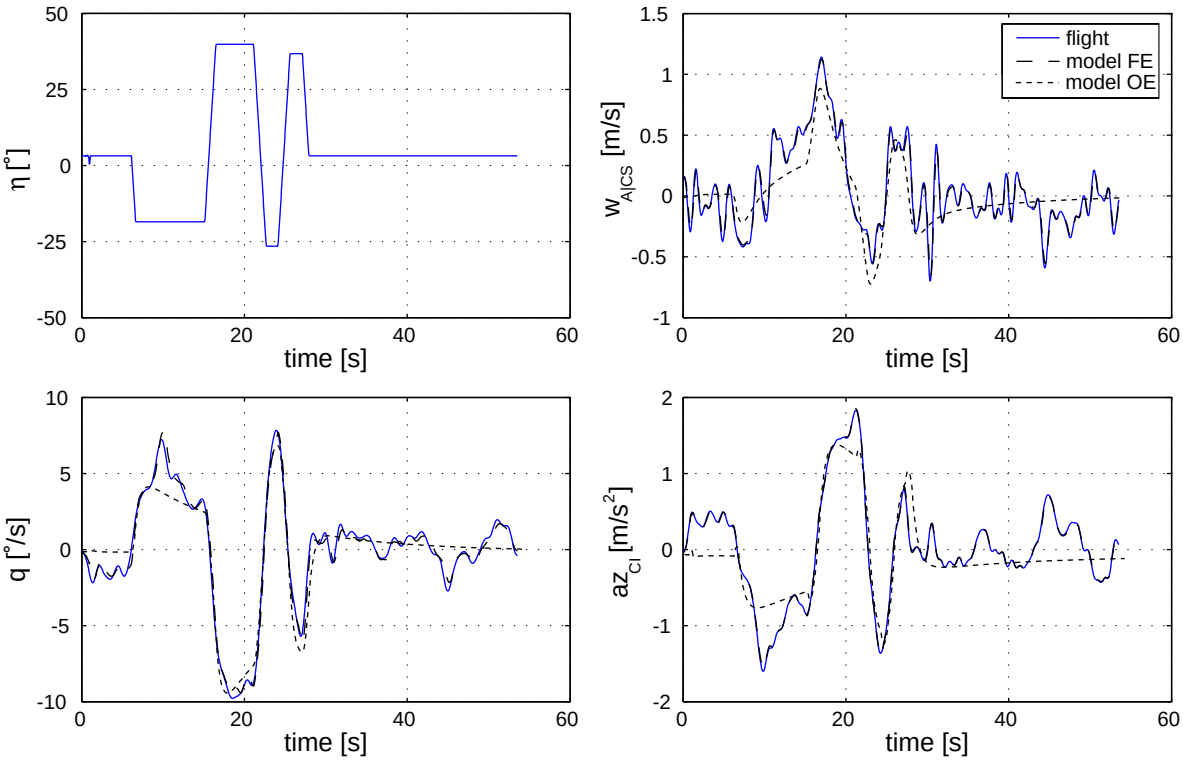

Figure 6.10: Filter error (FE) and output error (OE) methods applied for estimation of the F3S2 longitudinal maneuver flown at high turbulence level

Even though the maneuvers flown in severe turbulence, in general, did not pass the data compatibility check (see results in C.2.3), a better performance of the filter-error algorithm is apparent over the output error method. For this reason, more plausible estimation results are expected also for “calm air” maneuvers.

6.3 Estimation of Lateral Derivatives

Unfortunately, having focused on the examination of the longitudinal dynamics, there were almost no flight maneuvers carried out in order to determine the lateral-directional dynamics. Figure 6.11 shows the time histories of a single lateral maneuver, where two multistep perturbation sequences were applied to the rudder controls.

From the analysis of the flight trajectories it becomes apparent that the roll oscillations are tightly coupled with the yawing motion, excited by rudder perturbations $\delta\zeta$. This character of motion implies the use of the full state lateral-directional model (Equations (3.16), (3.26)) for parameter estimation.

As in the case of the longitudinal estimations, the fully parameterized lateral-directional model has also lead to very poor estimation results due to highly dependant parameters. The initial anticipation of the importance of a particular stability/control derivative was acquired by studying the components of the nominal model (discussed in Chapter 3). From the analysis of magnitude of the dynamic $\boldsymbol{A}$ and control $\boldsymbol{B}$ matrix terms (Equation (3.16)) follows, that the derivatives Y_p, Y_ϕ, L_v, L_r, N_p, N_ϕ and L_ζ could be replaced by zeros in the state and control matrices without significantly affecting the dynamics of the linearized model.

Inspection of magnitudes of the flight determined parameters (stability/control derivative multiplied with a corresponding recovered state/control trajectory) has confirmed the insignificance of Y_p, Y_ϕ, L_v, N_p derivatives. However, as pointed out previously, the rudder perturbations effectively excite the rolling oscillations. It turns out to be reasonable to estimate also the L_r and L_ζ derivatives. In this parametrization, the model has produced the best fit to the flight data without encountering convergence problems. The final parametrization of the lateral-directional model yields

$$\begin{aligned}\Theta_{lat} = \; & [Y_v \; Y_r \; L_p \; L_r \; L_\phi \; N_v \; N_r \; Y_\zeta \; L_\zeta \; N_\zeta \; \ldots \\ & \ldots b_{\dot{v}} \; b_{\dot{p}} \; b_{\dot{r}} \; b_{\dot{\phi}} \; b_v \; b_p \; b_r \; b_\phi \; b_{ay} \; u_0 \; w_0]^T.\end{aligned} \tag{6.9}$$

The evaluated trajectories of the new parametrized model against the flight data are shown in Figure 6.12. The correlation map of the estimated parameters is shown in Figure 6.13. Numerical values of estimated parameters are given in Table C.14.

Although the correlation among the parameters contributing to the pendulum motion appears to be not as critical as in the longitudinal maneuvers, a high correlation among many other stability derivatives exist. Because the high correlation exist for almost all parameters that constitute the model’s state equations, resolving for it would require a fixing of several

important derivatives, which is unwanted in this case. Therefore, the high correlation among parameters was accepted here.

During the lateral-directional maneuver, small discerpancies of the side velocity $v_{A|CS}$ exist, which could not be followed by the model. The objective of the filter error algorithm was to perform an efficient maximum likelihood estimations in spite of these discrepancies. The process noise matrix incorporates the estimation of three state noise components

$$\boldsymbol{F}_{lat} = \begin{bmatrix} \sigma_{\dot{v}} & 0 & 0 & 0 \\ 0 & \sigma_{\dot{p}} & 0 & 0 \\ 0 & 0 & \sigma_{\dot{r}} & 0 \\ 0 & 0 & 0 & 0 \end{bmatrix} . \tag{6.10}$$

The updated set of parameter vector consists of 24 unknowns:

$$\begin{aligned} \Theta = \; & [Y_v \; Y_r \; L_p \; L_r \; L_\phi \; N_v \; N_r \; Y_\zeta \; L_\zeta \; N_\zeta \; \ldots \\ & \ldots b_{\dot{v}} \; b_{\dot{p}} \; b_{\dot{r}} \; b_{\dot{\phi}} \; b_v \; b_p \; b_r \; b_\phi \; b_{ay} \; u_0 \; w_0 \; \sigma_{\dot{v}} \; \sigma_{\dot{p}} \; \sigma_{\dot{r}}]^T . \end{aligned} \tag{6.11}$$

The time histories of the model estimated by the filter error method are shown in Figure 6.14. As expected, the filter error algorithm provides a better estimation trajectories. The numerical values of the estimated parameters are given in Table C.14.

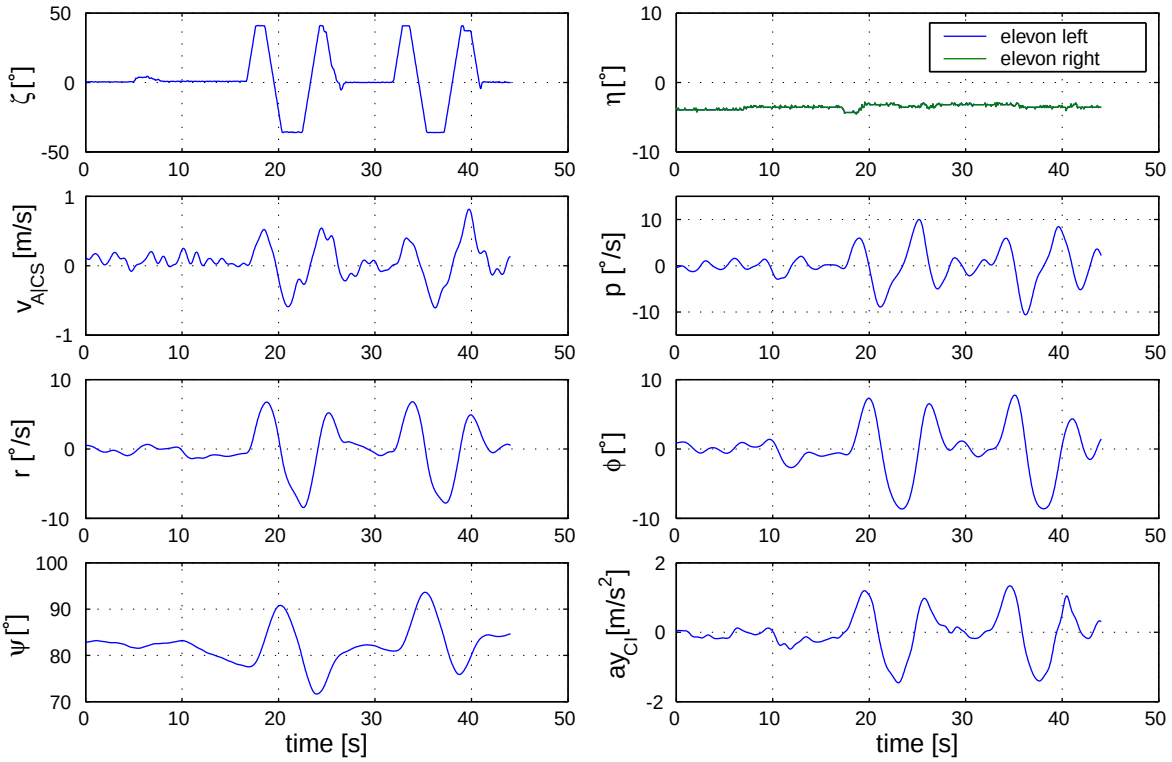

Figure 6.11: Lateral-directional maneuver with rudder perturbations

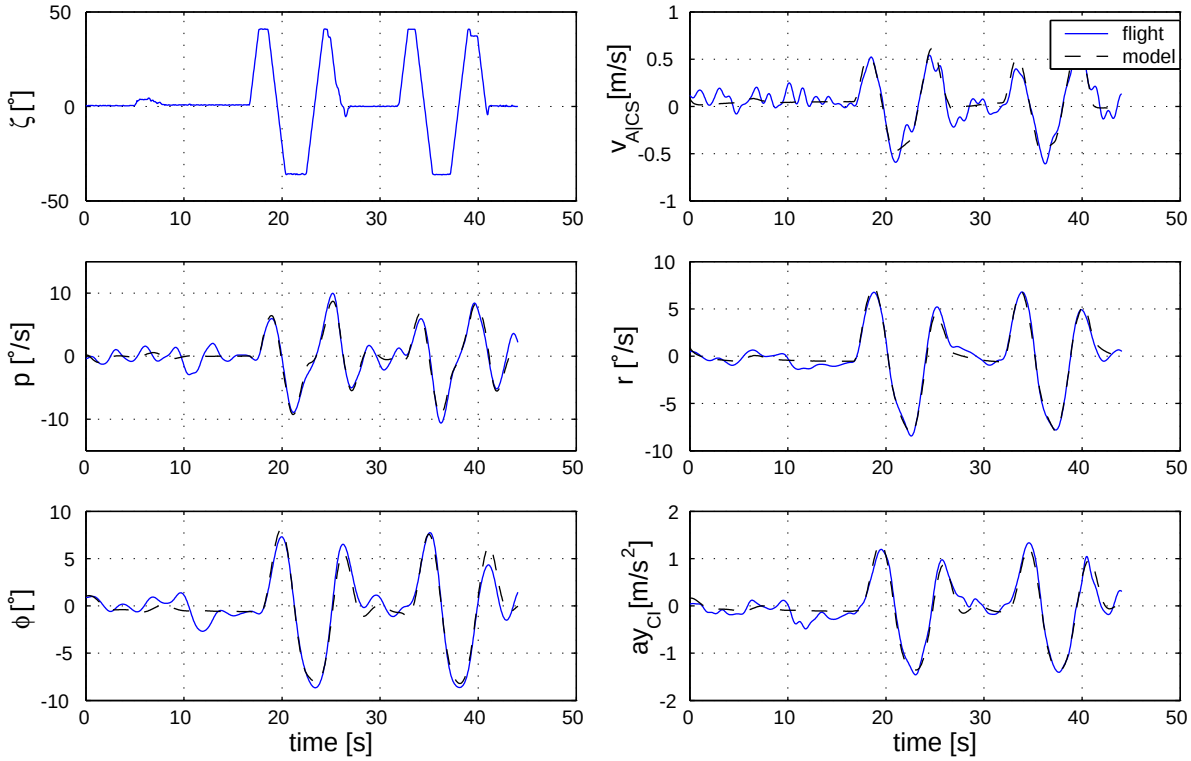

Figure 6.12: Estimations of lateral-directional maneuver using Output-Error method

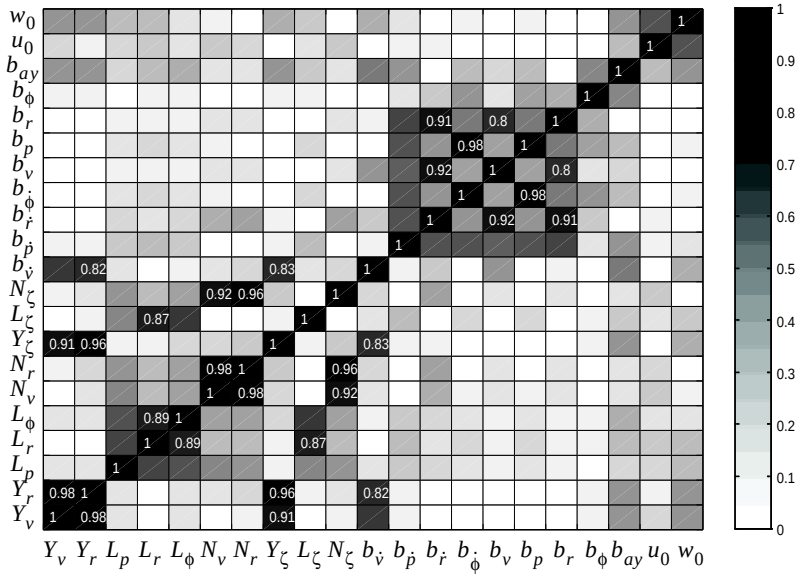

Figure 6.13: Correlation map of lateral-directional parameter estimations

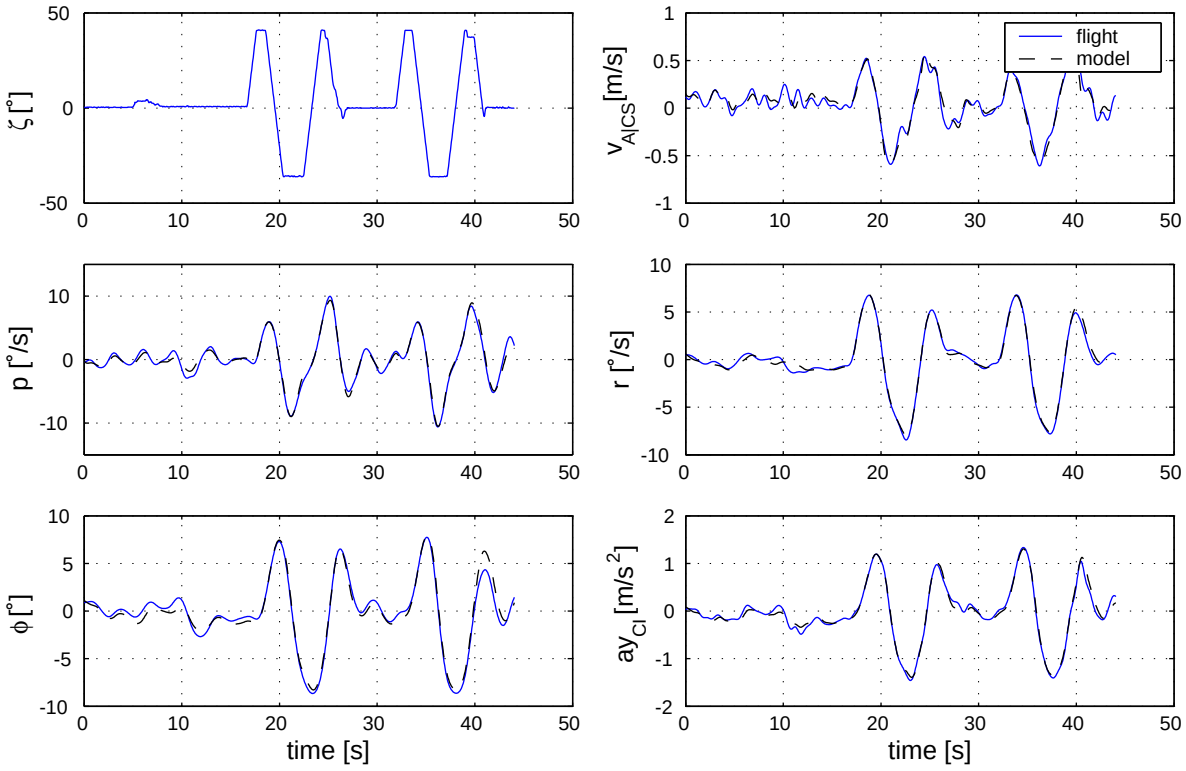

Figure 6.14: Estimations of lateral-directional maneuver using Filter-Error method

6.4 Validation Results

6.4.1 Cross-Validation Tests

To finalize the identification methodology applied for determining the airship dynamics, the cross-validation test, as outlined in section 4.6.4, has been utilized. In this technique, the predictive ability of the estimated model is studied: as already pointed out, the important prerequisite for the cross-validation test is a repeatability of the flight maneuvers. This means that if the model was estimated from a particular flight record, it can be compared with the different record only if the latter is taken under similar trim and configuration conditions as the first one.

Because repeatability of the flight maneuvers for the remotely operated airship has posed serious difficulties for the pilot, each identification maneuver had a slightly different trim condition. In order to overcome this problem, it was decided to use the model structure, where the main stability and control derivatives were held at fixed estimated values, whereas the bias parameters $\boldsymbol{b}_x$ and $\boldsymbol{b}_y$ were freely adjustable. In this approach, “freezing” the main derivatives does not change the essential properties of the model, whereas “freeing” the bias parameters can compensate for the uncertainties of the trim condition. This is allowed only at limited extent, because the stability and control derivatives also vary with the change of the

trim condition. In the current investigation, the cross-validation test has been applied only to “nearly similar” flight records.

Figure 6.15 shows the model responses on the doublet elevator input compared with the corresponding measured quantities of the flight record F4S5e. Numerical values for the stability and control derivatives were taken from estimates obtained from the record F4S1e. using filter error algorithm. The vector comprising of bias parameters

$$\Theta = \left[b_{\dot{w}} \; b_{\dot{q}} \; b_{\dot{\theta}} \; b_{w} \; b_{q} \; b_{az} \; u_0 \right]^T \tag{6.12}$$

has been adjusted in order to account for the different trim condition of the doublet maneuver. The model with parameters estimated by the filter error algorithm provides very good predictions of the flight data. The successful result of the cross-validation test is also owing the fact that both flight records are taken in extremely calm air. It might be therefore concluded, that the model adequately describes the airship motion under examined flight and configuration conditions.

6.4.2 Other Validation Results

The lack of additional lateral-directional flight maneuvers makes the application of the cross-validation test irrelevant for the analysis. In this case, a slightly different validation test can

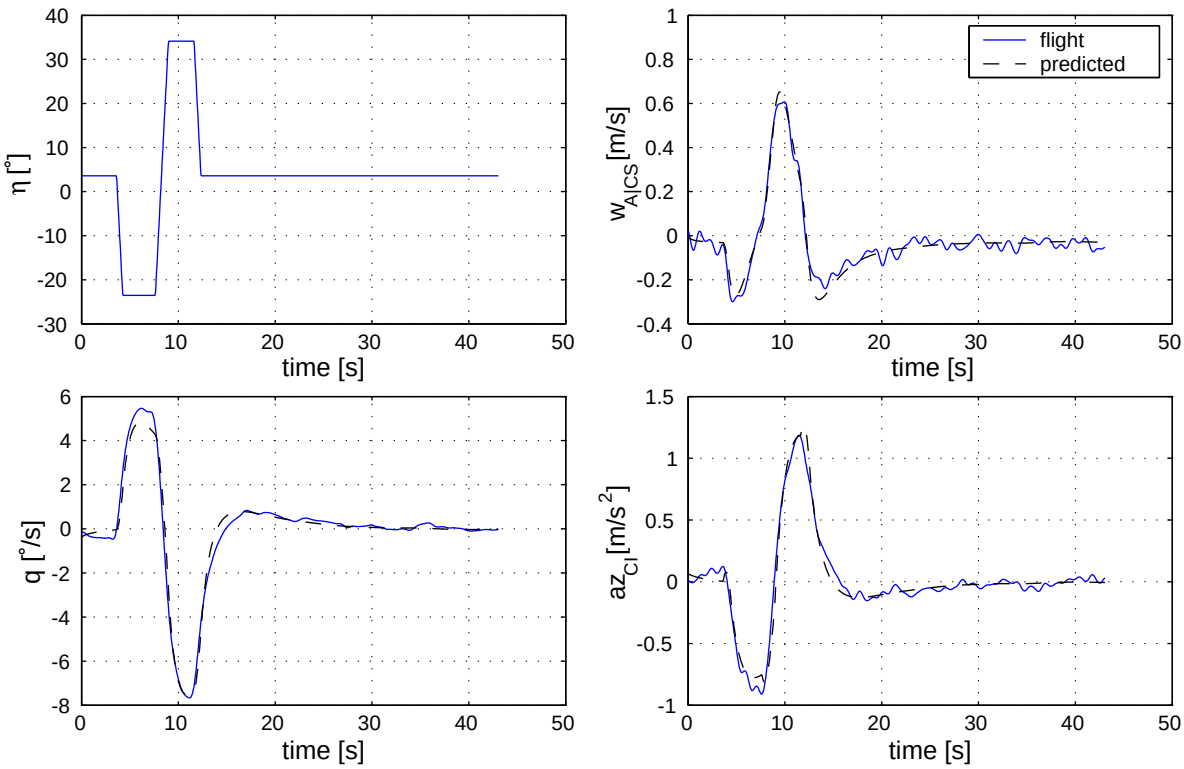

Figure 6.15: Longitudinal model predictive abilities in cross-validation test

be performed, where the model is being estimated on the half interval of the data record, and these results are used to predict the rest of the data [59].

Figure 6.16 shows this validation strategy applied for predicting the lateral-directional dynamics. The model parameters have been estimated based on the first 25 seconds of the data record and then extrapolated to the rest of the record. As can be observed, the predicted model trajectory agrees well with the measured airship responses. There are no visible differences between estimated (Figure 6.12) and predicted (Figure 6.16) model outputs in the last 15 seconds of the flight record. This indicates that a sufficient content of the lateral-directional dynamics could be gained from the first 25 seconds of data used for parameters estimation.

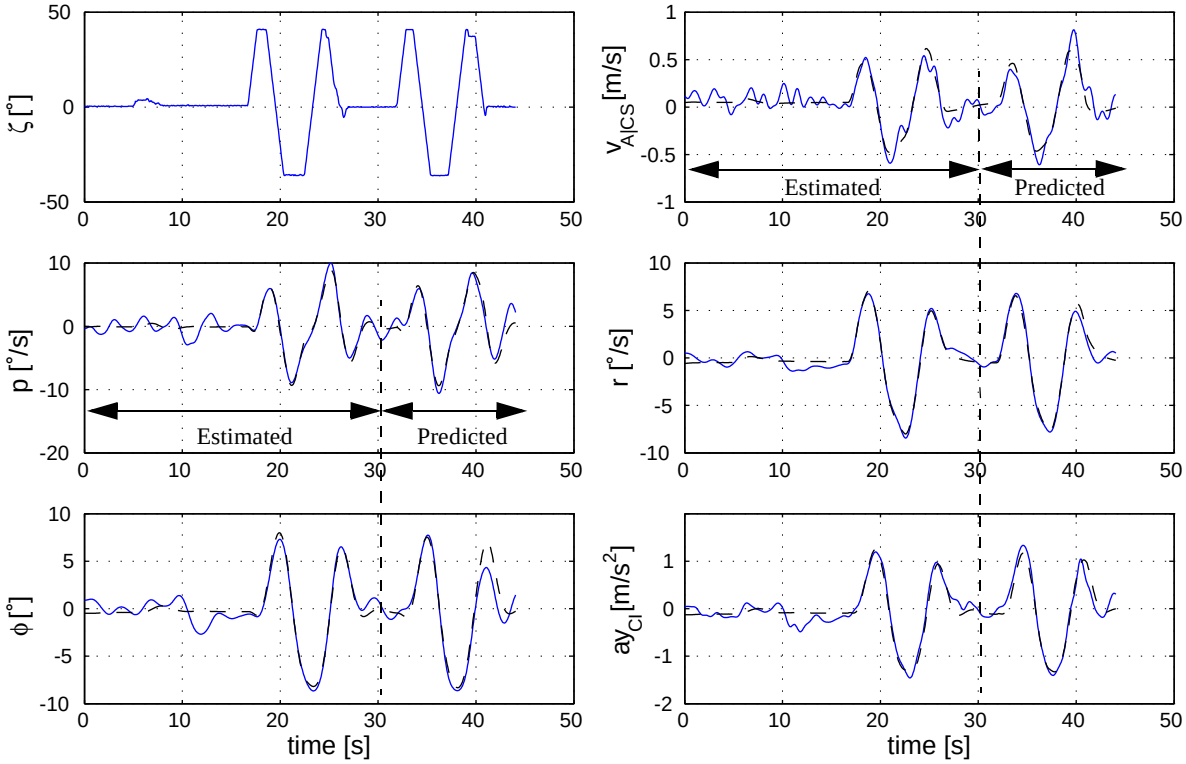

Figure 6.16: Validation result of lateral-directional maneuver

6.5 Estimated Parameters Versus a priori Model Predictions

Sections 6.2-6.4 were mainly focused on system identification issues for estimating and validating dynamical models from the flight data. This section will be devoted to the comparison between the modelled and the flight determined parameters. The eigendynamic properties which are characterized by the stability derivatives will be examined first. Subsequently, the nondimensional aerodynamic coefficients will be extracted from the identified parameters and compared with the wind tunnel data. The nominal configuration data of the Lotte airship outlined in Appendix A has been taken for this analysis.

6.5.1 Examination of Eigendynamic Properties

Longitudinal Dynamics

One of the central issues in estimating the stability derivatives of a linear model is a characterization of its eigendynamics. A summary of pole distribution (heave and longitudinal-pendulum modes) determined from several flight segments with respect to the model predictions is illustrated in Figure 6.17(a). Although each flight record correspond to a slightly different trim condition, the poles tend to concentrate around some definite locations. As can be seen from this distribution, some disagreement between the expected and flight determined pole locations exist.

The damping of the aperiodic heave mode increases with increased trim velocity u_0 as agrees well with the preliminary analysis performed in Chapter 3. However, the estimated time period of the heave mode is shorter than expected, which is predominantly conditioned by large negative values of the estimated pitch damping derivative M_q. The estimated value of M_q is greater then the modelled value by an approximate factor of three. Because the physical interpretation of the heave mode is tightly connected with the stabilizing effect of the fins (see section 3.3), their influence during the flight is greater then expected.

The identified longitudinal-pendulum mode tends to be well dampened as well. The estimated damping ratio of the longitudinal-pendulum mode ranges from 0.83 to 1.0, which is overpredicted comparing to the nominal model. The natural frequency of the oscillatory motion decreases with increased forward velocity u_0 and at certain velocity a mode transition to subsidence aperiodic motion takes place. This well dampened characteristics agrees well with the pilot's opinion, experiencing a very stable motion of the airship even at maximum velocities ($u_{\max} \approx 12[\mathrm{m/s}]$). There are two factors which contribute to this stability. First, the static pitching derivative M_θ has been estimated at values higher than expected. According to equation (6.4) this could be caused either by incorrect specification of the mass properties (metacentric position, mass, moment of inertia) or wrong estimation of the apparent moment of inertia due to potential flow $M_{,\dot{q}}$. Second the large estimated values of M_q explain the transition from oscillatory to aperiodic motion at higher velocities.

Lateral-Directional Dynamics

The strong correlation between lateral parameters detected during estimation, shows that the parameters could be obtained with a relatively small confidence. At the same time, the a priori acquired values of the lateral coefficients also largely deviate from the flight determined ones, as can be seen from Table C.14. Especially the estimated values of damping derivatives L_r and N_r show the largest divergence from the nominal model which confirms the strong influence of the fins also on the lateral-directional stability.

The existence of large differences between the model predicted and determined stability derivatives leads also to a different characterization of eigendynamics of the lateral-directional motion, as shown in Figure 6.17(b). Analogously to the longitudinal case, the eigenfrequency and damping ratio of the roll pendulum mode have been slightly overestimated. A significant difference, however, is that the expected yaw divergence motion has

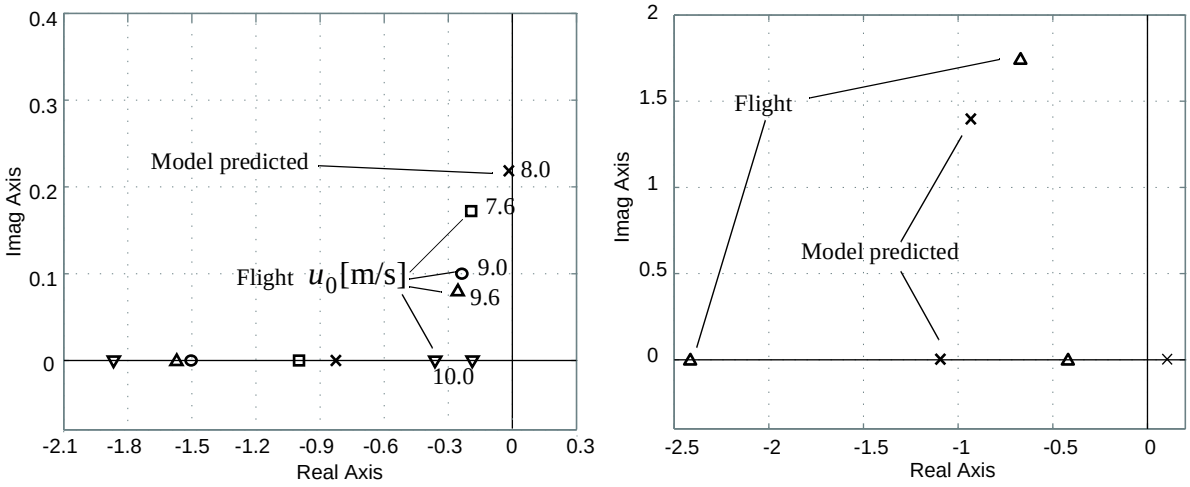

(a) Longitudinal dynamics (b) Lateral-directional dynamics

Figure 6.17: Flight determined pole locations against model predictions

been estimated by a stable aperiodic dynamics. The main contribution to this stability is made by the large negative value of the N_r derivative. Unfortunately, availability of only a single lateral flight maneuver does not allow a more extended examination of this phenomena. More lateral-directional flight maneuvers are required to make a definite statement about the stability of the yaw dynamics.

6.5.2 Extraction of Nondimensional Aerodynamic Coefficients

The relationship between stability and control derivatives and nondimensional aerodynamic coefficients is given in section B.6. Under assumption of correctly specified configuration data (predominantly airship mass, moment of inertia and center mass), it is possible to compute the flight determined aerodynamic parameters and compare them with the wind tunnel database. For this purpose, the coefficients from the wind tunnel database should be first transformed in the body fixed axes as shown in Figure 6.18 using transformation equations (B.51) and (B.52).

For extracting the aerodynamic coefficients from the flight determined derivatives, the reference length and configuration data were taken from the nominal parameter set as outlined in Appendix A. The geometry dependent Munk factors and the derivatives due to instationary flow phenomena have been computed analytically using information about the hull profile of the Lotte airship.

There are two major constraints on comparison between the wind tunnel and flight data should be noticed. First, because the wind tunnel aerodynamic database contains only stationary coefficients, no information about the aerodynamic damping coefficients can be gained. Second constraint arise due to the fact that estimation of the axial derivatives, like X_u, form the flight data was not confident due to the perturbations of only elevator control $\delta\eta$. Therefore, the analysis has been reduced to comparison of the c_{z_α} and c_{m_α} coefficients.

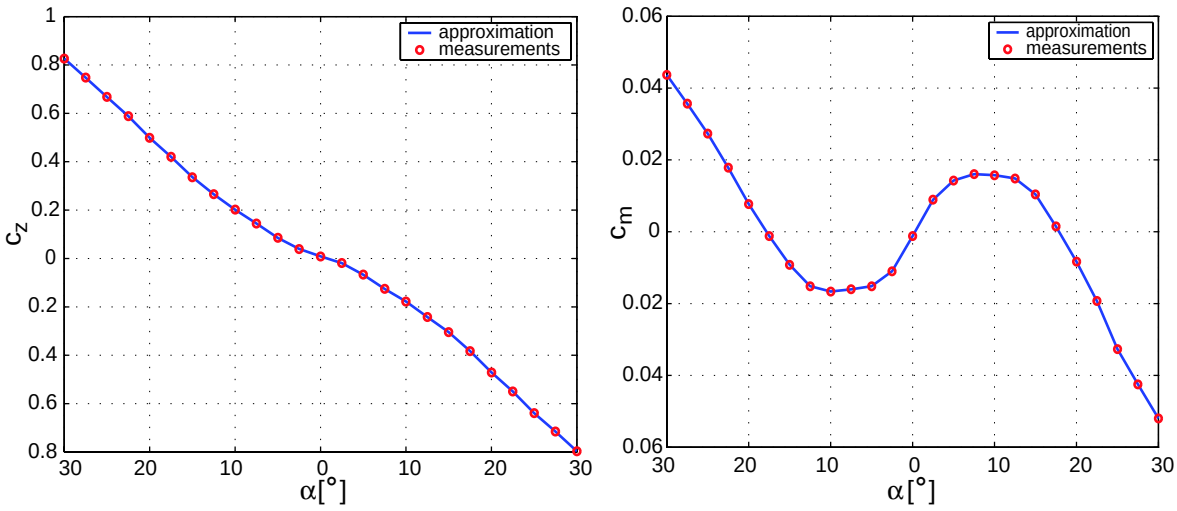

Figure 6.18: Static normal force and pitch coefficients in body fixed axes

The coefficients c_{z_α} and c_{m_α} represent the slopes of the c_z and c_m curves respectively, taken at the nominal α. Using numerical differentiation it is possible to compute the rate of change of the static lift and pitching moment aerodynamic coefficients over the whole range of measured α as illustrated in Figure 6.19. In addition, also displayed are the aerodynamic coefficients evaluated from the flight determined stability derivatives. Due to noticed limitations of the flight test experiments, the achieved trim conditions were at nearly zero angle of attack. This explains a small distribution of the flight determined coefficients over the α range.

Comparing the wind tunnel value of the static c_{z_α} coefficient with its flight determined counterpart (Figure 6.19(a)) it can be said that the normal aerodynamic force of the Lotte airship tends to be more sensitive on variations of α. There are relatively small variations of the identified c_{z_α} derivative with changed trim velocity u_0. One interesting fact is that due to symmetric property of the airship in X-Z and X-Y planes, the curves c_{z_α} and c_{y_β} are identical as follows from equation (B.62). It is therefore possible to verify the flight determined longitudinal aerodynamic derivatives against their lateral counterparts. Thus, the computed non dimensional side force derivative c_{y_α} has less negative value then the longitudinal coefficients. It can be explained by reduced side force derivative due to asymmetric flow as a result of the combined yawing and rolling motion.

Figure 6.19(b) shows the flight determined moment coefficient c_{m_α} versus wind tunnel estimations. As can be seen the resulting aerodynamic pitching moment is less than predicted by the wind tunnel experiments. The reduced destabilizing moment might be caused by a stronger contribution of the fins (under supposition of correct configuration properties of the Lotte airship). Similarly to the static force example the stationary pitching moment coefficient $c_m(\alpha)$ can be effectively comparable with the stationary yawing moment coefficient $c_n(\alpha)$. The same is valid also for the derivatives c_{m_α} and c_{n_β}, which have the same magnitude but the opposite sign as follows from equation (B.63).

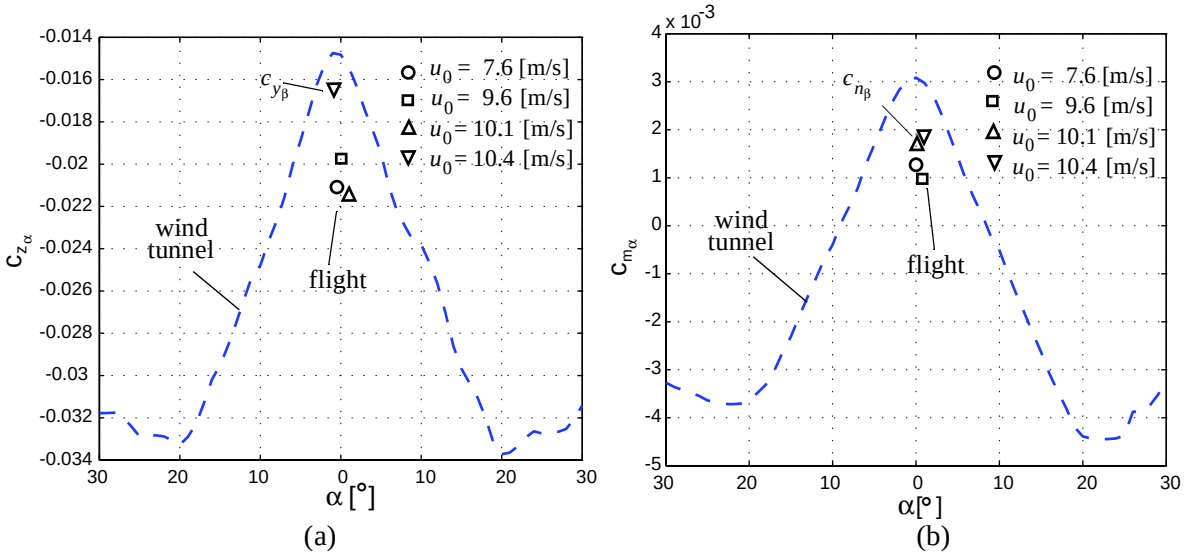

Figure 6.19: Wind tunnel and flight determined aerodynamic coefficients due to α

6.5.3 Variation of Initial Values of Parameters

Because the gradient-like optimization method used in the estimation algorithm do not guarantee the global minima and the start-up algorithm was utilized to acquire the initial parameters, some additional parameter evaluation runs have been performed. Their aim was to ensure that the estimated parameters correspond to the global minima of the likelihood function. In these tests, different initial values of parameters (including the model predicted derivatives) were used. As a consequence, the number of iterations needed to converge has slightly increased, but this did not lead to different values of the final estimations. These results confirm the validity of the obtained parameters.

6.5.4 Cause of Large Deviations

As a consequence of the performed analysis it can be said that although all identified stability and control derivatives were obtained from good fits between the measured and computed data, there are large deviations between the predicted and estimated dynamic characteristics of the Lotte airship. These inconsistencies can be caused by three main factors:

- **Uncertainties of the mass properties:** Because the mass characteristics play a dominant role in overall system dynamics, its primary inaccuracy could lead to a significant difference of results.
- **Aerodynamic phenomena:** It was found that the flight determined aerodynamic coefficients can be different to these derived from the modeling or wind tunnel experiments. This difference can be classified by the scaling problems, i.e geometric differences of the real airship with respect to the scaled model and the incomplete aerodynamic database. Thus, the dynamic characteristics of the real airship was found to be

more stable than predicted. Surely, this well dampened behavior could be explained by incorrect mass properties. From the other side, the lateral directional instability is less sensitive to changes of the mass properties of the airship, being mainly conditioned by the aerodynamic phenomena.

- **Experiments:** The imperfections during the experimental phase cause a negative influence on the final estimation results. As pointed out, the plausible flight data could be only derived at large amplitudes of the control inputs. The most elevator perturbation maneuvers, flown under 3-2-1-1 input shape, resulted in a substantial pitch deviations of the airship, where trigonometric nonlinearities were evident. The large pitch variations also lead to inevitable altitude changes, and thereby additional changes in aerodynamic, buoyancy, mass and thrust properties. Although all these changes are supposed to be insignificant (the computed variation was within 4%), the absolute time invariance of the model parameters can not be guaranteed.

Chapter 7

Conclusions and Perspectives

7.1 Conclusions

The system identification approach for determining a dynamical characteristics of the research airship Lotte, is the central objective of this thesis. The widely utilized identification methodology from the classical aircraft flight mechanics was taken as a basis for the framework. Since the methodology requires a consolidated treatment of several different problems, such as selection of the model structure, appropriate estimation methods, experiment design and evaluation of the flight data, these have been closely investigated in this work.

The model is the fundamental part of the airship identification problem. From the theoretical investigations given in the previous study it was possible to formulate a closed form analytical flight mechanical model, based on physically meaningful parameters. However, for the identification purposes, a linearized form of the airship dynamics was taken and the emphasis was made on estimation of basic stability and control derivatives. Estimating the linearized dynamics was necessary from the limited a priori confidence of the main components of the flight mechanical model. In addition to that, a separate consideration of the longitudinal and lateral-directional dynamics simplifies the model considerably in terms of structure and the number of unknown parameters.

The algorithmic part of this thesis is devoted to the examination of the methods of parameter estimation. Among a large number of estimation algorithms available in aircraft system identification, only two of them have been attentively considered in airship identification. Both algorithms use the time domain representation of the parameterized models and corresponding measured signals. One of them is the Output-error method that is based on the probabilistic likelihood criteria and provides the unbiased estimation of parameters in presence of measurement noise. The second algorithm was based on Filter Error method. It applies to the optimal state estimation using the Kalman filter. Its utilization was preferable for the airship identification, because this method effectively estimates the model parameters in presence of the proces (wind disturbance, modelling errors) and measurement noise sources.

One of the most critical and the most difficult parts of the airship identification project was devoted to the experiment design problem. Designing the flight test maneuvers and find-

ing an adequate measurement setup are the central issues of the experimental part. While evaluating the identification project, both issues had to be designed along with severe practical limitations. Weather condition, remote operation of the airship, small payload, altogether have significantly complicated the acquisition of the flight data.

The acquired flight data have allowed a separate estimation of three low-order approximate models, i.e. the angle-of-attack-pitch, the forward velocity and the lateral-directional models. Based on flown trajectories and estimated parameters of the models, several important conclusions of the Lotte dynamics can be drawn:

- The perturbations of the elevator controls can be widely approximated by the angle-of attack-pitch model without the axial velocity state. Even maximal control elevator deviations do not lead to large perturbations of the axial velocity.
- Due to low center mass location, the rudder controls effectively excites not only the sideslip and subsidence modes, but also the roll oscillation mode. In this case an utilization of the full order lateral-directional model was required.
- The estimated pole locations of the longitudinal dynamics greatly deviate from the predicted ones. The longitudinal-pendulum mode is effectively dampened. The predicted instability of the longitudinal-pendulum mode does not occur even at maximal flight velocities.
- The sideslip subsidence mode does not appear to be unstable in the lateral-directional dynamics. The latter fact, however could not be verified due to a lack of the lateral-directional flight maneuvers.

It is also shown, that a relatively simple form of the linear model can accurately approximate the motion of the airship.

Although the results obtained by utilizing the system identification approach can be treated as satisfactory in describing the dynamics of the airship, they are different to the predictions made out of wind tunnel experiments and from the physical flight mechanical model. This justifies the importance of flight test program and, in particular, system identification in the flight control system design.

7.2 Future research

Although the achieved results can be effectively utilized for the controller design in order to achieve an autonomous operation of the Lotte airship, several unsolved problems still exist which should be examined in future studies.

The main disadvantage of the models used to approximate the airship dynamics is that their parameters describe the system dynamics as a whole, i.e. it is impossible to extract the aerodynamic derivatives and compare them with the wind tunnel data unless the mass model is accurately known. In order to achieve this, an accurate determination of the basic mass model is obligatory.

The obtained results can be effectively utilized for future experiment design. It would be interesting here to examine the unsteady aerodynamic effects. For this purpose, new experiments can be designed including accelerated flight, mass drops and inclusion of thrust vectoring.

There is a great potential in improving the hardware capability in order to track the basic dynamic variables. An effective IMU/GPS integration algorithm should be implemented in order to track the flight path velocity. Utilization of multiple airstream sensors will allow the measurement of the flow distribution along the airship hull, yielding the involvement of the approximated wind/turbulence models. Additionally, the thrust measurements are required for estimation of the axial drag components.

Finally, with improved confidence in the mass model and systematic improvement of the measurement hardware, estimation of the basic components of the nonlinear aerodynamic model will be possible. However, additional research is required in order to obtain a plausible model parametrization, involving an extensive sensitivity analysis.

Bibliography

[1] Batterson, J., Klein, V., “Partitioning of Flight Data for Aerodynamic Modeling of Aircraft at High Angles of Attack”, *Journal of Aircraft*, Vol. 26, No. 4, 1989, pp. 334-339.

[2] Bauer, J., Andrisani, D., “Estimating Short-Period Dynamics Using an Extended Kalman Filter”, NASA Technical Memorandum 101722, 1990.

[3] Betts, J., Practical Methods of Optimal Control using Nonlinear Programming, Society for Industrial and Applied Mathematics, Philadelphia, 2001.

[4] Brockhaus, R., “Flugregelung”, Springer-Verlag, Berlin, 1994.

[5] Brown, R., Hwang, P., “Introduction to Random Signals and Applied Kalman Filtering“, Second Edition, John Wihley & Sons, New York, 1992.

[6] Etkin, B., “Dynamics of Flight, Stability and Control“, Second Edition, John Wihley & Sons, New York, 1982.

[7] Fletcher, R., “Practical Methods of Optimization”, Second Edition, John Wihley & Sons, New York, 1991.

[8] Funk, P., “Kraft- und Momentenmessungen am, 1:20 Windkanalmodell des Solarluftschiffs “Lotte”, Technical Report, Institute of Aerodynamics und Gasdynamics, University of Stuttgart, 1998.

[9] Gelb, A., “Applied Optimal Estimation“, The Academic Sciences Corporation, MIT Press, Boston, 1974.

[10] Gomes, S. B. V., “An Investigation of the Flight Dynamics of Airships with Application to the YEZ-2A”, PhD Thesis, Cranfield Institute of Technology, College of Aeronautics, Cranfield, 1990.

[11] Goodwin, G., Payne, R., “Dynamic System Identification: Experiment Design and Data Analysis“, Academic Press, New York, 1977.

[12] Hamel, P., and Jategaonkar, R., “Evolution of Flight Vehicle System Identification”, *Journal of Aircraft*, Vol. 33, No. 1, 1996, pp. 9-28.

[13] Hess, R., “On the Use of Back Propagation with Feed-Forward Neutral Networks for the Aerodynamic Estimation Problem”, AIAA Paper 93-3638, 1993.

[14] Hobilt, F., “Gust Loads on Aircraft: Concepts and Applications”, AIAA Education Series, AIAA, Washington, D. C., 1988.

[15] Iliff, K., “Identification of Aircraft Stability and Control Derivatives in the Presence of Turbulence, Parameter Estimation Technics and Applications in Flight Testing”, NASA TN D-7647, 1974.

[16] Iliff, K., “Aircraft Parameter Estimation“, AIAA Dryden Lecture in Research, NASA TM-88281, 1987.

[17] Iliff, K., Wang, K-S., “Extraction of Lateral-Directional Stability and Control Derivative for the Basic F-18 Aircraft at High Angles of Attack”, NASA TM-4786, February 1997.

[18] Jategaonkar, R., and Weiss, S., “Flight Vehicle System Identification in Time Domain”, DGLR-DLR Short Course, Hamburg, Germany, September 2001.

[19] Jategaonkar, R., and Plaetschke, E., “Maximum Likelihood Estimation of Parameters in Linear Systems with Process and Measurement Noise“, DFVLR-FB 87-20, Braunschweig, 1987.

[20] Jategaonkar, R., and Plaetschke, E., “Estimation of Aircraft Parameters Using Filter Error Methods and Extended Kalman Filter“, DFVLR-FB 88-15, Braunschweig, 1988.

[21] Jategaonkar, R., Plaetschke, E., “Identification of Moderately Nonlinear Flight Mechanics Systems with Additive Process and Measurement Noise“, *Journal of Guidance, Control, and Dynamics*, Vol. 13, No. 2, 1990, pp. 277-285.

[22] Jategaonkar, R., and Thielecke, F., “Evaluation of Parameter Estimation Methods for Unstable Aircraft”, *Journal of Aircraft*, Vol 31, No. 3, 1994, pp. 510-519.

[23] Jex, H., Magdaleno, R., and Geldhausen, P., “Pre- and Post-flight-Test Models Versus Measured Skyship-500 Control Responses”, AIAA Paper 87-2508-CP, 1987.

[24] Jones, S., DeLaurier, J., “Aerodynamic Estimation Techniques for Aerostats and Airships”, *Journal of Aircraft* Vol. 20, Nr. 2, Feb. 1983, pp. 120-126.

[25] Jonkers, H., “Application of the Kalman Filter to Flight Path Reconstruction from Flight Test Data Including Estimaiton of Instrumental Bias Error Corrections“, Ph. D. Thesis, Delft, 1976.

[26] Kaempf, B., “Flugmechanische Modellbildung von Luftschiffen”, Technical Report IFR-TR-99-02, Institute of Flight Mechanics and Control, University of Stuttgart, 1999.

[27] Kaempf, B., “Configuration File Version 1.0.0, Airship MatrixX™ Model 2.0” Institute of Flight Mechanics and Control, University of Stuttgart, 1996.

[28] Keskar, D., Klein, V., “Determination of Instrumentation Errors from Measured Data using Maximum Likelihood Method”, AIAA Paper 80-1602, 1980.

[29] Khoury, G., and Gillett, D., “Airship Technology”, Cambridge University Press, Cambridge, 1999.

[30] Klein, V., and Morelli, E., “Parameter Estimation of a Highly Augmented Aircraft from Flight Data”, 9-th IFAC Symposium on Identification and System Parameter Estimation, Budapest, 1991.

[31] Kornienko, A., “Recalculation of Aerodynamic Forces on Airships“, IFR-TR-99-008, Institute of Flight Mechanics and Control, University of Stuttgart, 1999.

[32] Kornienko, A., “System Identification of the Airship’s Longitudinal Motion“, IFR-TR-00-003, Institute of Flight Mechanics and Control, University of Stuttgart, 2000.

[33] Kornienko, A., “Test Results by Verifying the MMLE3 Algorithm”, IFR-TR-01-03, Institute of Flight Mechanics and Control, University of Stuttgart, 2001.

[34] Kornienko, A., Well, K., “Estimation of Longitudinal Motion of a Remotely Controlled Airship“, AIAA Paper 03-5697, 2003.

[35] Kungl, P., “Das Solarluftschiff LOTTE”, <http://www.isd.uni-stuttgart.de/forschung/fsforschung.htm>, 2000-2006.

[36] Lamb, H., “Hydrodynamics”, sixth Edition, Dower Publications, New York, 1932

[37] Lebacqz, V., “Application of a Kalman Filter Identification Technique to Flight Data from the X-22A Variable Stability V/STOL Aircraft”, NASA TN D-7647, 1974.

[38] Lutz, T., et al., “Summary of Aerodynamic Studies on the Lotte Airship”, International Airship Convention and Exhibition, Cambridge, England, July 2002.

[39] Ljung, L., “System Identification. Theory for the User“, Prentice-Hall, Inc., New-Jersey 1999.

[40] Maine, R., and Iliff, K., “User’s Manual for MMLE3, a General FORTRAN Program for Maximum Likelihood Parameter Estimation”, NASA TP-1563, 1980.

[41] Maine, R., and Iliff, K., “Formulation and Implementation of a Practical Algorithm for Parameter Estimation with Process and Measurement Noise”, *SIAM Journal of Applied Mathematics*, Vol. 41, Dec. 1981, pp 558-579.

[42] Maine, R., and Iliff, K., “Practical Aspects of using a Maximum Likelihood Estimation Method to extract Stability and Control Derivatives from Flight Data”, NASA TN D-8209, 1976.

[43] Maine, R., and Iliff, K., “The Theory and Practice of Estimating the Accuracy of Dynamic Flight-Determined Coefficients“, NASA Reference Publication 1077, July 1981.

[44] Maine, R., and Iliff, K., “Application fo Parameter Estimation to Aircraft Stability and Control, The Output-Error Approach“, NASA Reference Publication 1168, June 1986.

[45] Maine, R., and Iliff, K., “Identification of Dynamic Systems, Theory and Formulation“, NASA Reference Publication 1138, Dryden Flight Research Facility, California, February 1985.

[46] Marchand, M., “Identifizierbarkeit und Eingangssignale”, Manuskript zum Kurs F1.13, Carl-Cranz-Gesellschaft.

[47] McLean, D., “Automatic Flight Control Systems”, Prentice Hall International, Cambridge, 1990.

[48] Morelli, E., “Flight Test Validation of Optimal Input Design and Comparison to Conventional Inputs”, Paper AIAA-97-3711, 1997.

[49] Morelli, E., “In-Flight System Identification”, Paper AIAA-98-XXXX, 1998.

[50] Morelli, E., “Advances in Experiment Design For High Performance Aircraft”, Paper AIAA-00-XXXX, 2000.

[51] Murray-Smith, D., “Methods for the External Validation of Continious System Simulation Models: A Reveiw”, *Journal of Mathematical and Computer Modeling of Dynamical Systems*, Vol 4, No. 1 pp. 5-31, 1998.

[52] Naghabushan B., Tomilson, N., “Flight Dynamics Simulation of a Heavy Lift Airship” AIAA Paper 79-1593R, 1979.

[53] Norton, J., “An Introduction to Identification”, Academic Press Inc., 1986.

[54] Pafonsky., H., and Dutton., J., “Atmospheric Turbulence, Models and Methods for Engineering Applications”, John Wiley & Sons, Inc, New York, 1984.

[55] Plaetschke, E., “Maximum-Likelihood-Verfahren” Vortragsmanuskript für CCG-Lehrgang F 1.13, Braunschweig, 1985.

[56] Seifert, J., “Identifizierung nichtlinearer aerodynamischer Derivative mit einem Modularen Neuronalen Netzwerk”, dissertation, Universität der Bundeswehr München, 2003.

[57] Schlichting, H., Truckenbrodt, E., “Aerodynamik des Flugzeuges“, Band 2, Springer Verlag, Berlin, 1960.

[58] Shafer, M., “Flight Investigation of Various Control Inputs Intended for Parameter Estimation”, NASA TM-85901, August 1984.

[59] Stepner, D., and Mehra, R., “Maximum Likelihood Identification and Optimal Input Design for Identifying Aircraft Stability and Control Derivatives“, NASA CR-2200, March 1973.

[60] Thomasson, P., “Motion of a rigid body in an unsteady non-uniform heavy fluid, an extension”, Report No. 9610, College of Aeronautics, Cranfield University, Cranfield, June 1996.

[61] Wagner, J., “Zur Simulation und Identifikation der Segelflug-Längsbewegung”, dissertation, University of Stuttgart, 1995.

[62] Wagner, S., “Stroemungslehre I&II”, University of Stuttgart, 1999.

[63] Warner, E., and Norton, F., “Preliminary Report on Free Flight Tests”, NACA Rep., No. 70, 1919.

[64] Yazawa, K., “Identification of Aircraft Stability and Control Derivatives in the Presence of Turbulence”, AIAA Paper 77-1134, 1977.

[65] Zadeh, L., “From Circuit Theory to System Theory”, Proc. IRE, Vol. 50, pp. 856-865.

[66] Zhu, Y., Backx, T., “Identification of Multivariable Industrial Proces for Simulation, Diagnostics and Control“, Springer-Verlag, London, 1993.

Appendix A

LOTTE Airship: Technical Data

Figure A.1: Lotte airship at starting phase of test flight

dimensions:		
	length [m]	15
	max. thickness [m]	4
	hull volume [m^3]	107.42
	span width [m]	4.6
	fin area [m^2]	2.88
estimated mass and elements of I_{CG}:		
	mass (at altitude 200m) [kg]	136.8
	I_{xx} [kgm^2]	213
	I_{yy} [kgm^2]	3310
	I_{zz} [kgm^2]	3211
	I_{xz} [kgm^2]	-88
estimated center of mass wrt. CR:		
	(at altitude 200m)	
	x_{CG} [m]	0
	y_{CG} [m]	0
	z_{CG} [m]	0.45
important reference points wrt. CR:		
	x_{CI} [m]	0.11
	y_{CI} [m]	0
	z_{CI} [m]	1.88
	x_{CS} [m]	8.13
	y_{CS} [m]	0
	z_{CS} [m]	-0.2
electrical engine:		
	max thrust [N]	120
performance:		
	max. velocity [m/s]	12
	max. payload [kg]	12
energy sources:		
	solar panels/rechargeable batteries	

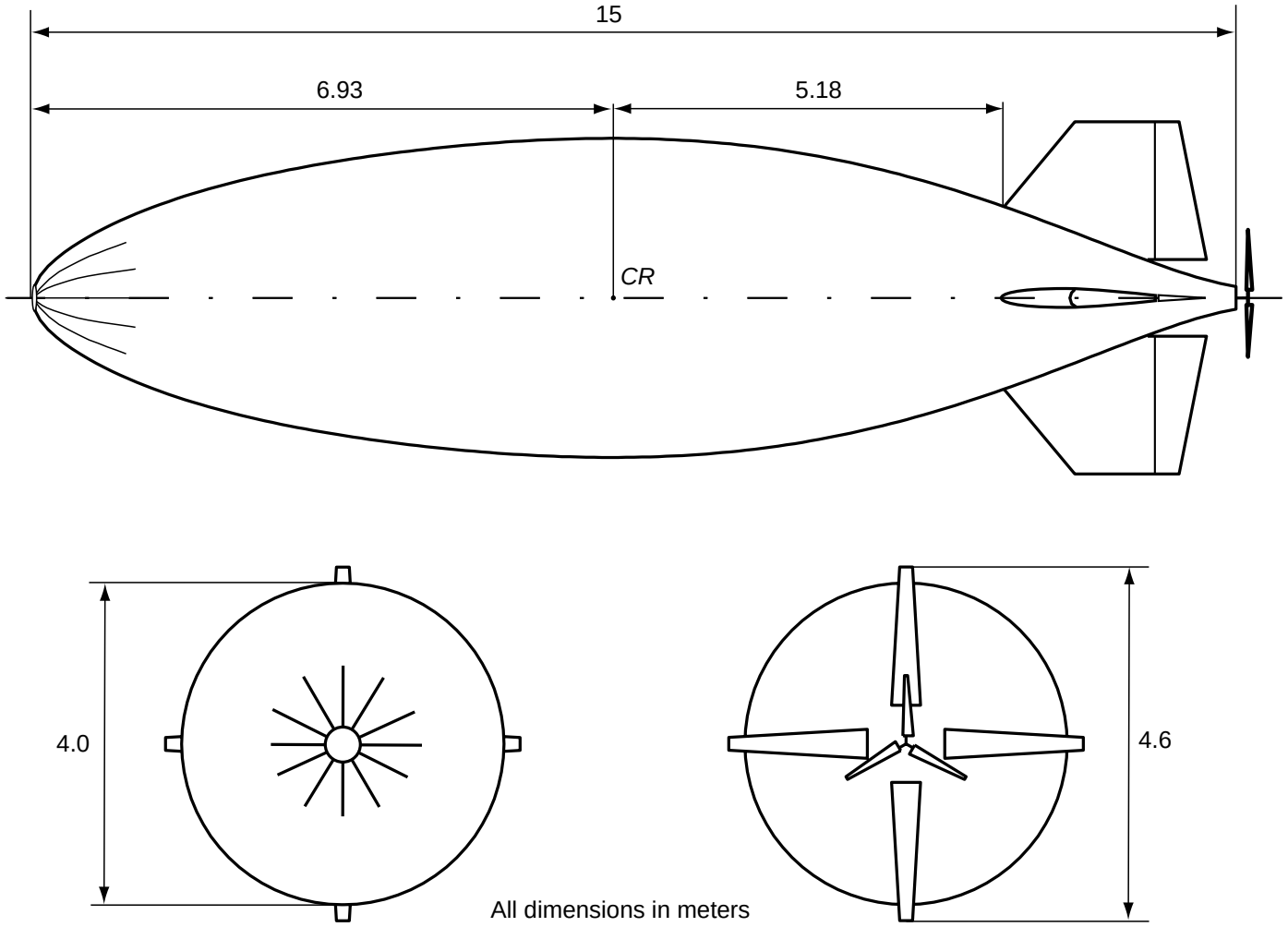

Figure A.2: Three-view of the Lotte airship with major dimensions shown

Appendix B

Annotations to Derivation of Flight Mechanical Model

B.1 Similarity Transformations

The basic force and moment equations of motion established in Chapter 2 are

$$\frac{d}{dt}\{m\boldsymbol{V}_{K|CG}\}_f^g = \{\boldsymbol{F}^{\Sigma}{}_{CG}\}_f \tag{B.1}$$

and

$$\frac{d}{dt}\{\boldsymbol{I}_{CG}\Omega_{CG}\}_f^g = \{\boldsymbol{Q}^{\Sigma}{}_{CG}\}_f \,. \tag{B.2}$$

It is further necessary to apply two similarity transformations on these two equations in order to derive the motion variables with respect to the center of body reference CR. First, the transformation of the time derivative of vector variables given in the body reference (superscript f) is required. For this purpose, a rule of expressing the time derivative of a vector in a rotating reference frame is requested [6]:

$$\frac{d}{dt}\{\boldsymbol{V}\}_f^g = \frac{d}{dt}\{\boldsymbol{V}\}_f^f + \Omega\times\{\boldsymbol{V}\}_f^f \quad . \tag{B.3}$$

Applying this rule to the left hand side of the force equation yields

$$\begin{aligned}\frac{d}{dt}\{m\boldsymbol{V}_{K|CG}\}_f^g &= \frac{d}{dt}\{m\boldsymbol{V}_{K|CG}\}_f^f + \Omega_{CG}\times(m\boldsymbol{V}_{K|CG}) \\ &= m(\dot{\boldsymbol{V}}_{K|CG} + \Omega_{CG}\times\boldsymbol{V}_{K|CG}) + \dot{m}\boldsymbol{V}_{K|CG}\end{aligned} \tag{B.4}$$

and analogously for the moment equation

$$\begin{aligned}\frac{d}{dt}\{\boldsymbol{I}_{CG}\Omega_{CG}\}_f^g &= \frac{d}{dt}\{\boldsymbol{I}_{CG}\Omega_{CG}\}_f^f + \Omega\times(\boldsymbol{I}_{CG}\Omega_{CG}) \\ &= \boldsymbol{I}_{CG}\dot{\Omega}_{CG} + \Omega_{CG}\times(\boldsymbol{I}_{CG}\Omega_{CG}) + \dot{\boldsymbol{I}}_{CG}\Omega_{CG}\,.\end{aligned} \tag{B.5}$$

The second transformation of the equations of motion requires a translation of all its terms from the mass center CG to the center of body reference CR. For this purpose, the velocity at the mass center can be expressed by

$$\boldsymbol{V}_{K|CG} = \boldsymbol{V}_{K|CR} + \Omega_{CR}\times\boldsymbol{r}_{CG},\ \Omega_{CG} = \Omega_{CR}\,. \tag{B.6}$$

Henceforward, the subscripts of all variables that related to the center of reference will be omitted ($\Omega_{CR} = \Omega$, $\boldsymbol{V}_{K|CR} = \boldsymbol{V}_K$, etc.). Moreover, the rates of change of the airship mass $\dot{m}$ in equation (B.4), moment of inertia $\dot{\boldsymbol{I}}_{CG}$ in equation (B.5) are insignificantly small with regard to other motion variables and can be therefore neglected:

$$\dot{m} \cong 0,\ \dot{\boldsymbol{I}}_{CG} \cong \boldsymbol{0}. \tag{B.7}$$

Substituting transformed velocity from equation (B.6) into equation (B.4) and equating the latter with (B.1), one obtains:

$$m(\dot{\boldsymbol{V}}_K + \dot{\Omega}\times\boldsymbol{r}_{CG} + \Omega\times(\boldsymbol{V}_K + \Omega\times\boldsymbol{r}_{CG})) = \boldsymbol{F}^{\Sigma}. \tag{B.8}$$

The translation of the net force from the CG point to the CR is done straightforwardly, since for the force valid $\boldsymbol{F}_{CG} = \boldsymbol{F}$.

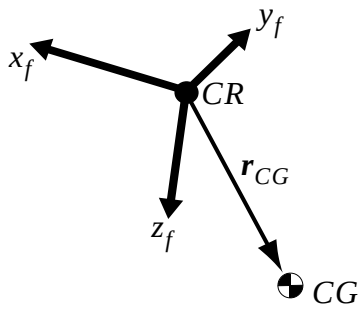

Figure B.1: Definition of reference vector $\boldsymbol{r}_{CG}$ in transformation $\boldsymbol{Q}_{CG}^{\Sigma} \rightarrow \boldsymbol{Q}^{\Sigma}$

The derivation of the moment equation with respect to the center of body requires a simultaneous transformation of both sides of the equation (B.2), because the tensor of inertia

and the summary moment are expressed in center mass point. The transformation of the moment to the CR point can be obtained using common relation (See Figure B.1):

$$\boldsymbol{Q}^{\Sigma} = \boldsymbol{Q}^{\Sigma}_{CG} + \boldsymbol{r}_{CG} \times \boldsymbol{F}^{\Sigma}_{CG}. \tag{B.9}$$

Then the expanded moment equation yields

$$\boldsymbol{I}_{CG}\dot{\Omega}_{CG} + \Omega_{CG} \times (\boldsymbol{I}_{CG}\Omega_{CG}) + \dot{\boldsymbol{I}}_{CG}\Omega_{CG} = \boldsymbol{Q}^{\Sigma} - \boldsymbol{r}_{CG} \times \boldsymbol{F}^{\Sigma} \tag{B.10}$$

or equivalently

$$\boldsymbol{I}_{CG}\dot{\Omega}_{CG} + \Omega_{CG} \times (\boldsymbol{I}_{CG}\Omega_{CG}) + \dot{\boldsymbol{I}}_{CG}\Omega_{CG} + \boldsymbol{r}_{CG} \times \boldsymbol{F}^{\Sigma} = \boldsymbol{Q}^{\Sigma}. \tag{B.11}$$

If the externally acting net force $\boldsymbol{F}^{\Sigma}$ in the latter equation will be substituted by the equation (B.8), then the moment equation with some rearrangements appears as follows:

$$\begin{aligned} &\boldsymbol{I}_{CG}\dot{\Omega} + m\boldsymbol{r}_{CG} \times (\dot{\Omega} \times \boldsymbol{r}_{CG}) \\ &+ \Omega \times (\boldsymbol{I}_{CG}\Omega) + m\boldsymbol{r}_{CG} \times \Omega \times (\Omega \times \boldsymbol{r}_{CG}) \\ &+ m\boldsymbol{r}_{CG} \times (\dot{\boldsymbol{V}}_K + \Omega \times \boldsymbol{V}_K) = \boldsymbol{Q}^{\Sigma}. \end{aligned} \tag{B.12}$$

This equation can be further simplified, if an inertia matrix transformation from the mass center CG to the center of reference CR is applied according to formula

$$\boldsymbol{I}_{CG} = \boldsymbol{I} + m(\boldsymbol{r}_{CG}\boldsymbol{r}^{T}_{CG} - \boldsymbol{r}^{T}_{CG}\boldsymbol{r}_{CG}\boldsymbol{E}), \tag{B.13}$$

with the $\boldsymbol{E}$ multiplier representing the identity matrix. Using (B.13) and properties of a vector product, the first two rows in (B.12) may be simplified by

$$\begin{aligned} \boldsymbol{I}_{CG}\dot{\Omega} + m\boldsymbol{r}_{CG} \times (\dot{\Omega} \times \boldsymbol{r}_{CG}) &\equiv \boldsymbol{I}\dot{\Omega} \\ \Omega \times (\boldsymbol{I}_{CG}\Omega) + m\boldsymbol{r}_{CG} \times \Omega \times (\Omega \times \boldsymbol{r}_{CG}) &\equiv \Omega \times (\boldsymbol{I}\Omega). \end{aligned} \tag{B.14}$$

Finally, after all substitutions done, the moment equation becomes:

$$\boldsymbol{I}\dot{\Omega} + \Omega \times (\boldsymbol{I}\Omega) + m\boldsymbol{r}_{CG} \times (\dot{\boldsymbol{V}}_K + \Omega \times \boldsymbol{V}_K) = \boldsymbol{Q}^{\Sigma}. \tag{B.15}$$

It should be noticed, that the moment of inertia matrix $\boldsymbol{I}$ is now expressed with respect to the center of body reference CR and not with respect to the mass center CG.

B.2 Mass Matrix

The mass matrix in equation (2.12) includes the definition of airship's total mass m and tensor of moments of inertia $\boldsymbol{I}$. In the expanded form, the matrix is

$$\boldsymbol{M} = \begin{bmatrix} m & 0 & 0 & 0 & mz_{CG} & 0 \\ 0 & m & 0 & -mz_{CG} & 0 & mx_{CG} \\ 0 & 0 & m & 0 & -mx_{CG} & 0 \\ 0 & -mz_{CG} & 0 & I_{xx} & 0 & I_{xz} \\ mz_{CG} & 0 & -mx_{CG} & 0 & I_{yy} & 0 \\ 0 & mx_{CG} & 0 & I_{xz} & 0 & I_{zz} \end{bmatrix}. \tag{B.16}$$

Airships are generally symmetrical with respect to the vertical plane. Therefore, the mass matrix in the equation (B.16) is expressed for the cases where this symmetry is valid $y_{CG} = 0$ and $I_{xy} = I_{yz} = 0$.

B.3 Dynamics Vector

The dynamics vector in the right hand side of equation (2.12) appears due to kinematical transformations of the system coordinates. It contains only stationary (non-accelerated) terms of the flight path and the rotational velocities

$$\boldsymbol{K} = \begin{bmatrix} -\Omega\times\ (\boldsymbol{V}_K + \Omega\times\ \boldsymbol{r}_{CG})m \\ -\Omega\times\ (\boldsymbol{I}\Omega) - (m\cdot\boldsymbol{r}_{CG}\ \times\ (\Omega\times\ \boldsymbol{V}_K)) \end{bmatrix}. \tag{B.17}$$

Along with linear and rotational velocities, the dynamic matrix also comprises of the total mass of the airship, position of the mass center and moment of inertia. The dynamic vector equation (B.17) in its expanded form yields

$$\boldsymbol{K} = \begin{bmatrix} m(rv - qw + (q^2 + r^2)x_{CG} - prz_{CG}) \\ -m(ru - pw + pqx_{CG} + qrz_{CG}) \\ m(qu - pv - prx_{CG} + (p^2 + q^2)z_{CG}) \\ -pqI_{xz} + qrI_{yy} - qrI_{zz} + m(ruz_{CG} - pwz_{CG}) \\ -prI_{xx} + (p^2 - r^2)I_{xz} + prI_{zz} - m(qux_{CG} - pvx_{CG} - rvz_{CG} + qwz_{CG}) \\ pqI_{xx} + qrI_{xz} - pqI_{yy} - m(rux_{CG} - pwx_{CG}) \end{bmatrix}. \tag{B.18}$$

B.4 Aerodynamic Model

This section summarizes the generic aerodynamic model of a conventional airship developed in [26]. The analysis of the original model was performed by the author in [31]. The model utilizes the structure shown in Figure B.2.

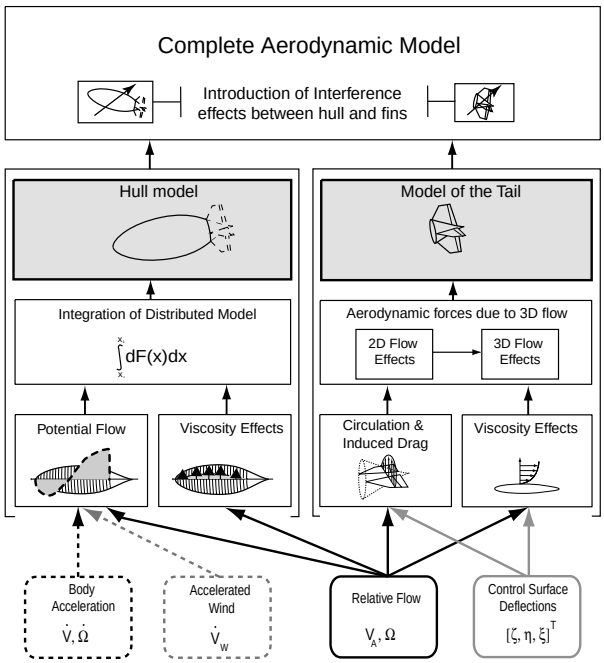

Figure B.2: Topology of the aerodynamical model [26]

The derivation of the aerodynamic model is divided onto two main parts. The first part describes the aerodynamics of the bare hull of the airship and defined as hull model, whereas the second part deals with description of aerodynamics of the tail area.

Approaches describing the model are based on formulation of the potential flow around the hull area, and a classical profile theory for the tail area. Separation and friction effects, which are usually to expect are modelled through viscosity and cross-flow terms for both the hull and the fin areas.

B.4.1 Hull Aerodynamics from Potential Flow Theory

For modelling the hull aerodynamics from the theory of potential flow, an assumption is made that the shape of the bare hull can be approximated by an ellipsoidal body. This allows to apply a closed analytical form of the velocity potential [36]

$$\Phi(x,\ y,\ z)\ =\ -k_1 xu - k_2 yv - k_2 zw + k_3 xzq - k_3 xyr\,, \tag{B.19}$$

where k_1, k_2 and k_3 are the geometry dependant Munk-factors of the potential of the disturbance of the flow around the ellipsoidal body.

For computing the net forces and moments, it is advantageous to consider the bare hull as a combination of infinitely thin segments, as illustrated in Figure B.3. The force and the moment are first determined for the entire segment and then integrated along the length of the body.

The study of hull aerodynamics due to potential flow should cover three basic operational cases. These are the accelerated motion of airship, the steady motion and the case where the airship operates in the unsteady atmosphere.

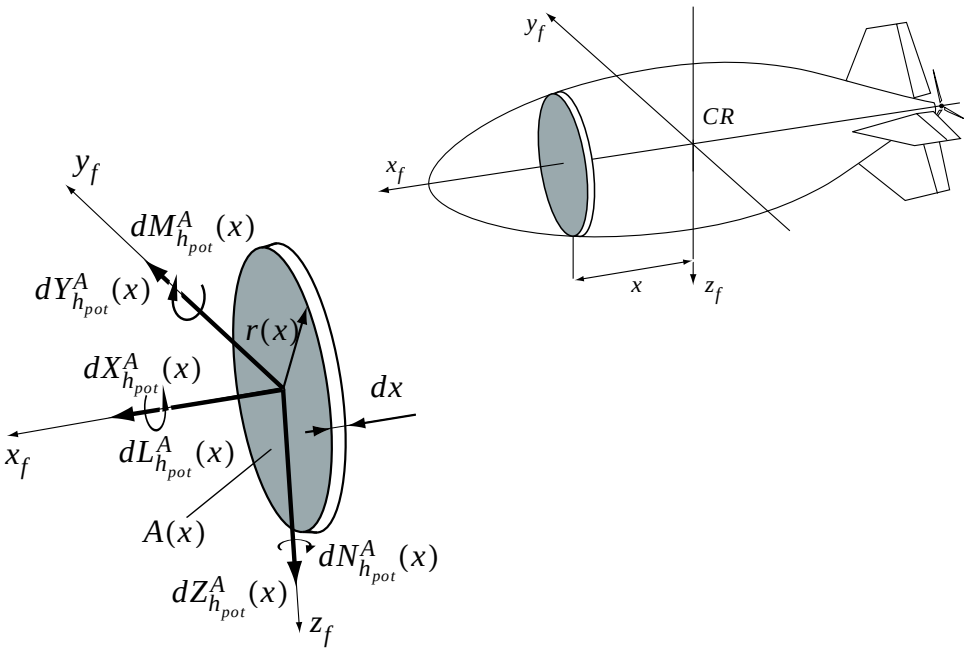

Figure B.3: Representation of the hull segment

Potential Flow due to Accelerated Motion

The flow distribution due to the accelerated motion incorporates the time differential of the velocity potential:

$$\frac{d}{dt}\Phi(x,\ y,\ z) = -k_1 x\dot{u} - k_2 y\dot{v} - k_2 z\dot{w} + k_3 xz\dot{q} - k_3 xy\dot{r}\,. \tag{B.20}$$

Applying (B.20) in the unsteady Bernoulli equation the forces acting on the segment of hull can be computed. This leads to the following relations:

$$d\boldsymbol{F}^A_{h_{pot-acc}}(x) = \begin{bmatrix} dX^A_{h_{pot-acc}}(x) \\ dY^A_{h_{pot-acc}}(x) \\ dZ^A_{h_{pot-acc}}(x) \end{bmatrix} = \rho \begin{bmatrix} -k_1 \dfrac{dA(x)}{dx} x\dot{u}_K \\ k_2 A(x)\dot{v}_K + k_3 A(x) x\dot{r} \\ k_2 A(x)\dot{w}_K - k_3 A(x) x\dot{q} \end{bmatrix} dx \tag{B.21}$$

and

$$d\boldsymbol{M}^A_{h_{pot-acc}}(x) = \begin{bmatrix} dL^A_{h_{pot-acc}}(x) \\ dM^A_{h_{pot-acc}}(x) \\ dN^A_{h_{pot-acc}}(x) \end{bmatrix} = \rho \begin{bmatrix} 0 \\ -\frac{k_2}{2}\frac{dA(x)}{dx} r(x)^2 \dot{w}_K + \frac{k_3}{2}\frac{dA(x)}{dx} r(x)^2 x\dot{q} \\ \frac{k_2}{2}\frac{dA(x)}{dx} r(x)^2 \dot{v}_K + \frac{k_3}{2}\frac{dA(x)}{dx} r(x)^2 x\dot{r} \end{bmatrix} dx \ . \quad \text{(B.22)}$$

Potential Flow due to Steady Motion

In the steady motion, the forces due to potential flow can be calculated using the pressure distribution around the segment calculated from the steady Bernoulli equation. The velocity distribution required for evaluating the Bernoulli equation can derived from the velocity potential introduced in (B.19). This gives the distributed force and moment in the form

$$d\boldsymbol{F}^A_{h_{pot}}(x) = \begin{bmatrix} dX^A_{h_{pot}} \\ dY^A_{h_{pot}} \\ dZ^A_{h_{pot}} \end{bmatrix} = \rho \begin{bmatrix} (u_K^2 + v_K^2 + w_K^2)a_1(x) - u_K^2 a_2 + (v_K^2 + w_K^2)a_3(x) \\ uva_6(x) - ura_7(x) \\ uwa_6(x) - uqa_7(x) \end{bmatrix} \cdots$$

$$\cdots \begin{bmatrix} + w_K q a_4(x) + q^2 a_5(x) - v_K r a_4(x) + r^2 a_5(x) \\ - \\ - \end{bmatrix} dx$$

$$d\boldsymbol{M}^A_{h_{pot}}(x) = \begin{bmatrix} dL^A_{h_{pot}} \\ dM^A_{h_{pot}} \\ dN^A_{h_{pot}} \end{bmatrix} = \rho \begin{bmatrix} 0 \\ -u_K w_K a_8(x) + u_K q a_9(x) \\ u_K v_K a_8(x) + u_K r a_9(x) \end{bmatrix} dx, \quad \text{(B.23)}$$

with the $a_i(x)$ defined as geometry dependant variables:

$$
\begin{aligned}
a_1(x) &= \frac{1}{2}\cdot \frac{dA(x)}{dx}\\
a_2(x) &= \frac{k_1^2}{2}\cdot \cos^2\theta(x)\cdot \frac{dA(x)}{dx}\\
a_3(x) &= \frac{1}{4}\cdot k_2^2\cdot \left(\cos^2\theta(x)\cdot \frac{dA(x)}{dx} - 2\frac{dA(x)}{dx}\right)\\
a_4(x) &= -x\cdot \frac{dA(x)}{dx} + \frac{1}{2}k_2(k_3-1)r(x)\cos\theta(x)\sin\theta(x)\frac{dA(x)}{dx} - \frac{1}{2}k_2(k_3+1)r(x)\left(\cos^2\theta(x)x\frac{dA(x)}{dx} - 2x\frac{dA(x)}{dx}\right)\\
a_5(x) &= -\frac{1}{2}(k_3^2-1)xr(x)\cos\theta(x)\sin\theta(x)\frac{dA(x)}{dx} + \frac{1}{4}r(x)^2\sin^2\theta(x)\frac{dA(x)}{dx} + \frac{1}{4}(2k_3-k_3^2)r(x)^2\cos^2\theta(x)\frac{dA(x)}{dx}\\
&\quad \ldots + \frac{1}{4}x^2\cos\theta(x)\frac{dA(x)}{dx} + (2k_3+k_3^2)\cdot \left(\frac{1}{4}x^2\cos^2\theta(x)\frac{dA(x)}{dx} - \frac{1}{2}x^2\frac{dA(x)}{dx}\right)\\
a_6(x) &= \frac{k_1k_2}{2}\cos^2\theta(x)\frac{dA(x)}{dx}\\
a_7(x) &= A(x) + k_1(k_3-1)\cos^2\theta(x)A(x) + \frac{1}{2}k_1(k_3+1)\cos^2\theta(x)x\frac{dA(x)}{dx}\\
a_8(x) &= \frac{k_1k_2}{2}\sin\theta(x)\cos\theta(x)r(x)\frac{dA(x)}{dx}\\
a_9(x) &= \frac{1}{2}r(x)^2\frac{dA(x)}{dx} + \frac{1}{2}k_1(k_3-k_1)\cos^2\theta(x)r(x)^2\frac{dA(x)}{dx} + \frac{1}{2}k_1(k_3+k_1)\sin\theta(x)\cos\theta(x)xr(x)\frac{dA(x)}{dx},
\end{aligned}
\tag{B.24}
$$

with $\theta(x)$ indicating the inclination of the hull's surface at x point with respect to the x_f direction

$$
\theta(x) = \operatorname{atan}\frac{dr(x)}{dx}. \tag{B.25}
$$

In the steady but rolling motion, the lateral and vertical components of the velocity vector are in permanent change due to the roll rate. In order that this change is not recognized as accelerated motion, the roll induced change in lateral and vertical velocities needs to be compensated. For the unaccelerated rolling motion the induced accelerations are expressed:

$$
\begin{bmatrix}\dot{u}_{ind}\\ \dot{v}_{ind}\\ \dot{w}_{ind}\end{bmatrix} = -\begin{bmatrix}p\\0\\0\end{bmatrix}\times\begin{bmatrix}u_K\\v_K\\w_K\end{bmatrix} = \begin{bmatrix}0\\pw_K\\-rv_K\end{bmatrix} \qquad \text{and} \qquad \begin{bmatrix}\dot{p}_{ind}\\ \dot{q}_{ind}\\ \dot{r}_{ind}\end{bmatrix} = \begin{bmatrix}p\\0\\0\end{bmatrix}\times\begin{bmatrix}p\\q\\r\end{bmatrix} = \begin{bmatrix}0\\pr\\-pq\end{bmatrix}. \tag{B.26}
$$

Applying these induced accelerations directly into equations (B.21) and (B.22) yields

$$d\boldsymbol{F}^{A}_{h_{pot-ind}}(x) = \begin{bmatrix} dX^{A}_{h_{pot-ind}}(x) \\ dY^{A}_{h_{pot-ind}}(x) \\ dZ^{A}_{h_{pot-ind}}(x) \end{bmatrix} = -\rho \begin{bmatrix} 0 \\ -k_2 \cdot \dfrac{dA(x)}{dx} \cdot pw_K + k_3 \dfrac{dA(x)}{dx} xpq \\ k_2 \cdot \dfrac{dA(x)}{dx} \cdot rv_K - k_3 \dfrac{dA(x)}{dx} xpr \end{bmatrix} dx \qquad (B.27)$$

$$d\boldsymbol{M}^{A}_{h_{pot-ind}}(x) = \begin{bmatrix} dL^{A}_{h_{pot-ind}}(x) \\ dM^{A}_{h_{pot-ind}}(x) \\ dN^{A}_{h_{pot-ind}}(x) \end{bmatrix} = -\rho \begin{bmatrix} 0 \\ -k_2 \dfrac{dA(x)}{dx} r(x)^2 rv_K + k_3 \dfrac{dA(x)}{dx} r(x)^2 xpr \\ k_2 \dfrac{dA(x)}{dx} r(x)^2 pw_K + k_3 \dfrac{dA(x)}{dx} r(x)^2 xpq \end{bmatrix} dx \; . \qquad (B.28)$$

Aerodynamics of Airship in Unsteady Atmosphere

For expressing the aerodynamic forces and moments in the unsteady atmosphere, a formulation introduced in [60] can be applied. Its main principle is based on expanding the accelerated flow $\dot{\boldsymbol{V}}_A(x)$ through the flight path and wind accelerations, i.e. $\dot{\boldsymbol{V}}_A(x) = \dot{\boldsymbol{V}}_K(x) - \dot{\boldsymbol{V}}_W(x)$. According to his formulation, it is sufficient to distinguish the effects caused by the flight path acceleration $\dot{\boldsymbol{V}}_K(x)$ together with the rotational acceleration Ω of the body, the stationary flow with $\boldsymbol{V}_A(x)$ and Ω, and the accelerated wind $\dot{\boldsymbol{V}}_W(x)$. In the latter statement, the wind acceleration is translated from the earth fixed into the body fixed coordinates using approximation [26]

$$\dot{\boldsymbol{V}}_W(x) = \begin{bmatrix} \dot{u}_W(x) \\ \dot{v}_W(x) \\ \dot{w}_W(x) \end{bmatrix}_f = \boldsymbol{T}_{fg}\left(\frac{D}{Dt}\{\boldsymbol{V}_W(x)\}^g_g\right) - \Omega \times \boldsymbol{V}_W(x), \qquad (B.29)$$

where the operator D/Dt denotes the substantial derivative of the wind velocity field derived and expressed in the earth fixed frame. In (B.29) the rotational motion of the wind velocity is included in the wind acceleration vector, therefore the Ω_W term is omitted.

In expressing the hull aerodynamics in the unsteady atmosphere, the equations related to the steady state motion (equations (B.22), (B.23), (B.27) and (B.28)) should appear with the relative velocity-$\boldsymbol{V}_A$ variables. The terms responsible for the accelerated motion (equations (B.21), (B.22)) appear twice to account for the airship and the wind accelerations respectively, although in the latter case they appear with negative sign and without the rotational acceleration (see equation (B.29)).

There is a difference in treating the airship that accelerates in the air from the case where the airship moves in the accelerated wind. The accelerated wind is always associated with a pressure gradient. The gradient itself produces an aerostatic buoyancy force in direc-

tion of the acceleration of the air. This phenomena is usually known as the *horizontal buoyancy* effect. It can be computed from the Bernoulli equation under a condition where the local pressure gradient is constant over the circumference of the segment of the hull

$$d\boldsymbol{F}^{A}_{h_{stat-W}}(x) = \begin{bmatrix} dX^{A}_{h_{stat-W}}(x) \\ dY^{A}_{h_{stat-W}}(x) \\ dZ^{A}_{h_{stat-W}}(x) \end{bmatrix} = \begin{bmatrix} \Delta p_W(x) \cdot \dfrac{dA(x)}{dx} \\ 0 \\ 0 \end{bmatrix} dx - \begin{bmatrix} 0 & 0 & 0 \\ 0 & 1 & 0 \\ 0 & 0 & 1 \end{bmatrix} \cdot (\nabla_f p_W) A(x) dx, \quad \text{(B.30)}$$

$$d\boldsymbol{Q}^{A}_{h_{stat-W}}(x) = \begin{bmatrix} dL^{A}_{h_{stat-W}}(x) \\ dM^{A}_{h_{stat-W}}(x) \\ dN^{A}_{h_{stat-W}}(x) \end{bmatrix} = \begin{bmatrix} 0 & 0 & 0 \\ 0 & -1 & 0 \\ 0 & 0 & -1 \end{bmatrix} \cdot (\nabla_f p_W) r(x)^2 \frac{dA(x)}{dx} dx. \quad \text{(B.31)}$$

An important consequence of the analysis given in [26] is that the flow effects from accelerated body motion, accelerated wind and the steady aerodynamics can be treated independently as a sum of their respective contributions to the airship aerodynamics.

Integration of Distributed Forces due to Potential Flow

The net force and moment due to potential flow is determined through integration of the segment forces and moments along the axial length of the hull. Studying the hull aerodynamics in Equations (B.21) through (B.31), one can observe that the forces and moments acting on the segment are proportional to the geometrical characteristics concentrated in the $a_i(x)$ terms. For simplicity, this property can be expressed in the following general form:

$$d \bullet^{A}_{h}(x) = f(\boldsymbol{V}_K, \ \Omega, \ \boldsymbol{V}_A, \ \dot{\boldsymbol{V}}_W) \cdot a_i(x) dx. \quad \text{(B.32)}$$

Therefore, for determination of the net force and moment the motion variables can be taken out of the integration delimiter.

In deriving the integral of the moment one has to take into account an offset of the segment from the center of reference CR (see Figure B.3). The contribution of one segment to the total moment is given by

$$d\boldsymbol{Q}^{A}_{h|CR}(x) = d\boldsymbol{Q}^{A}_{h} + \begin{bmatrix} x \\ 0 \\ 0 \end{bmatrix} \times d\boldsymbol{F}^{A}_{h}(x). \quad \text{(B.33)}$$

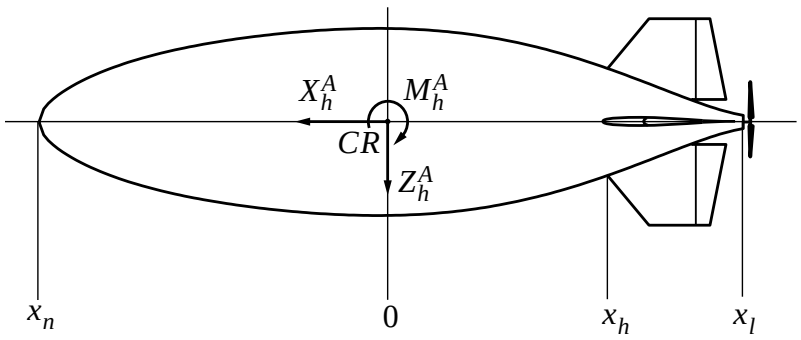

Figure B.4: Definition of integration limits for the distributed hull forces due to potential flow

There are two principal limits selected for the integration of the distributed hull forces and moments. Their definition follows from the discussion of validity regions of the potential flow theory and can be found in the related work [24]. It is decided, that all normal forces and moments of the hull due to steady flow should be integrated along the region from the leading edge of the fins x_h to the nose of the airship x_n (see Figure B.4). From the other hand, the axial force and moment, as well as all apparent mass and horizontal buoyancy forces and moments can be integrated along the total length of the hull ($x_l \rightarrow x_n$).

Table B.1 summarizes the analytical form of the geometrical integrals. Note, equation (B.37) was taken into account for derivation of the moment integrals $I_{m_{pot}}$.

Table B.1: Time invariant integrals as functions of geometrical properties of the hull

Integrals along the whole airship length ($x_l \rightarrow x_n$)

$$I^{\dot{u}}_{x_{pot}} = \int_{x_l}^{x_n} k_1 \cdot \frac{dA(x)}{dx} x dx \;,\; I^{\dot{w}}_{z_{pot}} = \int_{x_l}^{x_n} k_2 \cdot A(x) dx \;,\; I^{\dot{q}}_{z_{pot}} = \int_{x_l}^{x_n} k_3 \cdot A(x) x dx$$

$$I^{\dot{w}}_{m_{pot}} = \int_{x_l}^{x_n} k_2 \left(\frac{1}{2} \cdot \frac{dA(x)}{dx} r(x)^2 + A(x) x \right) dx \,,\; I^{\dot{q}}_{m_{pot}} = \int_{x_l}^{x_n} k_3 \left(\frac{1}{2} \cdot \frac{dA(x)}{dx} r(x)^2 x + x^2 A(x) \right) dx$$

$$I^{uvw}_{x_{pot}} = \int_{x_l}^{x_n} a_1(x) dx, \quad I^{u}_{x_{pot}} = \int_{x_l}^{x_n} a_2(x) dx$$

$$I^{vw}_{x_{pot}} = \int_{x_l}^{x_n} a_3(x) dx, \quad I^{wq}_{x_{pot}} = \int_{x_l}^{x_n} a_4(x) dx, \quad I^{q}_{x_{pot}} = \int_{x_l}^{x_n} a_5(x) dx$$

Integrals from the leading edge of the fins to the nose ($x_h \rightarrow x_n$)

$$I^{uw}_{z_{pot}} = \int_{x_h}^{x_n} a_6(x) dx \;,\; I^{uq}_{z_{pot}} = \int_{x_h}^{x_n} a_7(x) dx$$

$$I^{uw}_{m_{pot}} = \int_{x_h}^{x_n} (a_8(x) + x a_6(x)) dx \;,\; I^{uq}_{m_{pot}} = \int_{x_h}^{x_n} (a_9(x) + x a_7(x)) dx$$

Hence, the integrated aerodynamic force due to potential flow theory appears as

$$\boldsymbol{F}^{A}_{h_{pot}\Sigma} = -\rho \begin{bmatrix} -I^{\dot{u}}_{x_{pot}} \dot{u}_K \\ I^{\dot{w}}_{z_{pot}} \dot{v}_K + I^{\dot{q}}_{z_{pot}} \dot{r} \\ I^{\dot{w}}_{z_{pot}} \dot{w}_K + I^{\dot{q}}_{z_{pot}} \dot{q} \end{bmatrix} + \ldots$$

$$\ldots + \rho \begin{bmatrix} (u_A^2 + v_A^2 + w_A^2) I^{uvw}_{x_{pot}} - u_A^2 I^{u}_{x_{pot}} + (v_A^2 + w_A^2) I^{vw}_{x_{pot}} + (w_A q - v_A) I^{wq}_{x_{pot}} + (q^2 + r^2) I^{q}_{x_{pot}} \\ u_A v_A I^{uw}_{z_{pot}} + u_A r I^{uq}_{z_{pot}} + p w_A I^{\dot{w}}_{z_{pot}} - pq I^{\dot{q}}_{z_{pot}} \\ u_A w_A I^{uw}_{z_{pot}} + u_A q I^{uq}_{z_{pot}} + p v_A I^{\dot{w}}_{z_{pot}} - pr I^{\dot{q}}_{z_{pot}} \end{bmatrix} \tag{B.34}$$

$$\ldots + \rho \begin{bmatrix} -I^{\dot{u}}_{x_{pot}} \dot{u}_W \\ I^{\dot{w}}_{z_{pot}} \dot{v}_W \\ I^{\dot{w}}_{z_{pot}} \dot{w}_W \end{bmatrix} + \rho V \boldsymbol{T}_{bg} \frac{D \boldsymbol{V}_{W_g|CR}}{Dt}$$

and the net moment

$$\boldsymbol{Q}^{A}_{h_{pot}\Sigma} = -\rho \begin{bmatrix} 0 \\ -I^{\dot{w}}_{m_{pot}} \dot{w}_K + I^{\dot{q}}_{m_{pot}} \dot{q} \\ I^{\dot{w}}_{m_{pot}} \dot{v}_K + I^{\dot{q}}_{m_{pot}} \dot{r} \end{bmatrix} + \ldots$$

$$\ldots + \rho \begin{bmatrix} 0 \\ -u_A w_A I^{uw}_{m_{pot}} + u_A q I^{uq}_{m_{pot}} + v_A p I^{\dot{w}}_{m_{pot}} + pr I^{\dot{q}}_{m_{pot}} \\ u_A v_A I^{uw}_{m_{pot}} + u_A r I^{uq}_{m_{pot}} + w_A p I^{\dot{w}}_{m_{pot}} - pq I^{\dot{q}}_{m_{pot}} \end{bmatrix} \tag{B.35}$$

$$\ldots + \rho \begin{bmatrix} 0 \\ -I^{\dot{w}}_{m_{pot}} \dot{w}_W \\ I^{\dot{w}}_{m_{pot}} \dot{v}_W \end{bmatrix} + \begin{bmatrix} 0 \\ 0 \\ 0 \end{bmatrix}.$$

B.4.2 Hull Aerodynamics due to Viscous Effects

Along with the potential flow effects, the viscous effects are important for a correct estimation of the drag of the airship. Because of the complexity of the boundary layer of the skin friction, only semi-empirical models can be applied for describing it. The parameters for these models are partly determined from experimental data (wind-tunnel tests) or the CFD simulations.

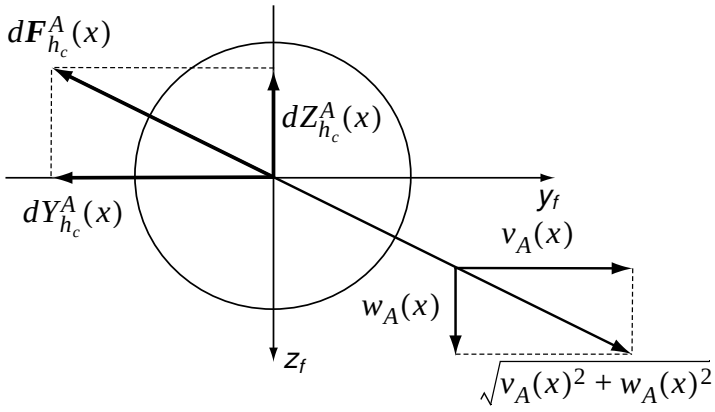

Figure B.5: Definition of vertical and side flow velocity for modeling the cross-flow force

The viscous effects are commonly modelled by examination of axial and cross flow effects. Classical formulation of the axial drag is expressed by

$$X^A_{h_0} = -\frac{\rho}{2} u_A |u_A| c_{d_0,\ h} V^{2/3} \ . \tag{B.36}$$

For computing the cross flow drag, the theory of flow around a slender body of revolution is used [57]. Its principle is based on examination of the forces and moments acting on the infinitesimally thin segment of the hull, analogously to that used for the potential flow.

According to Figure B.5, the lateral and vertical moments of the segment can be approximated by

$$\begin{aligned} dY^A_{h_c}(x) &= -\rho\, v_A(x) \sqrt{v_A^2(x) + w_A^2(x)}\, c_{d_c,\ h} \cdot r(x) dx \\ dZ^A_{h_c}(x) &= -\rho\, w_A(x) \sqrt{v_A^2(x) + w_A^2(x)}\, c_{d_c,\ h} \cdot r(x) dx \end{aligned} \tag{B.37}$$

and the pitch and yaw moments expressed with respect to center of reference are respectively:

$$\begin{aligned} dM^A_{h_c}(x) &= -x \cdot dZ^A_{h_c}(x) \\ dN^A_{h_c}(x) &= x \cdot dY^A_{h_c}(x). \end{aligned} \tag{B.38}$$

Integrating equations (B.37) and (B.38), the cross flow terms of forces and moments due to viscous effects can be obtained. The integration limit for this case constitutes the interval from the nose of the hull till the attachment of the fins.

B.4.3 Model of the Tail Area

The fins of the airship can modeled in a classical way by using the lifting line theory [57]. For this purpose the flow phenomena can be first modelled for the two dimensional flow for rudders and elevators and then consequently expanded into three dimensional flow. For the 2D aerodynamics, the reference area includes not only fins, but also a rear part of the hull.

A classical profile theory includes a description of the following aerodynamic phenomena: the circulation, the induced, the profile and the cross-flow drag [62]. The last two effects appear due to viscous effects and separation and are similar to the viscous effects discussed for the hull. They are expressed by an axial $c_{d_{0,\,f}}$ and cross-flow drag $c_{d_{c},f}$ coefficients respectively.

According to classical lifting body theory [57], the lift $c_{l,\,f}(\alpha_f)$ and induced drag $c_{d_{ind},f}(\alpha_f)$ coefficients for a profile of the finite length can be approximated by the following formula

$$\begin{aligned} c_{l,\,f}(\alpha_f) &= \left.\frac{dc_l}{d\alpha_f}\right|_{\alpha_f = 0} \sin\alpha_f = c_{l\alpha_0,f}\sin\alpha_f \\ c_{d_{ind},\,f}(\alpha_f) &= \frac{c_{l,\,f}^2(\alpha_f)}{\pi\Lambda_f} = \frac{c_{l\alpha_0,\,f}^2}{\pi\Lambda_f}\sin^2\alpha_f = c_{d_{ind}\alpha_0,\,f}\sin^2\alpha_f\,, \end{aligned} \tag{B.39}$$

where Λ_f represents the aspect ratio of the tail area. The variable α_f denotes the effective local flow angle of the fin and is defined below in equation (B.48).

Both, the circulation and the induced drag terms can be classified by the attached flow effects and appear with index f_a. Terms due to viscous effects and separation have index f_c. Hence, applying the coefficients from equation (B.39) and the effects due to the profile and the cross flow drag, the fin forces in two dimensional flow for small angles α_f appear:

$$\begin{aligned} X_f^A &= X_{f_a}^A + X_{f_c}^A \\ &= q\cdot(c_{l\alpha_0,f} - c_{d_{ind}\alpha_0,f}\cos\alpha_f)\sin^2\alpha_f S_f - q\cdot c_{d_{0,f}} U_f^2 S_f \\ Z_f^A &= Z_{f_a}^A + Z_{f_c}^A \\ &= -q\cdot(c_{l\alpha_0,f}\cos\alpha_f + c_{d_{ind}\alpha_0,f}\sin^2\alpha_f)\sin\alpha_f S_f - q\cdot(c_{d_c,f}\left|\sin\alpha_f\right| + c_{d_{0,f}}\cos\alpha_f)\sin\alpha_f S_f\,. \end{aligned} \tag{B.40}$$

Based on these forces the resulting moment of the tail about the reference point CR is calculated as

$$M_f^A = -x_{f_a} Z_{f_a} - x_{f_c} Z_{f_c}\,. \tag{B.41}$$

To notice is the lever arms x_{f_a} and x_{f_c} having different distance from the center of reference because of the different attachment point of the attached and cross-flow forces.

Expanding the fin forces and moments into the three-dimensional flow, it is necessary to describe the flow in terms of the local angles of attack and sideslip for the horizontal and vertical fins respectively. They are expressed together with their corresponding dynamic pressures:

$$\alpha_f = \alpha_f(x_f) = \operatorname{atan}\frac{w_{A_f}}{u_{A_f}}, \qquad q_{\alpha f} = \frac{\rho}{2}(u_{A_f}^2 + w_{A_f}^2), \tag{B.42}$$

$$\beta_f = \beta_f(x_f) = \operatorname{atan}\frac{v_{A_f}}{u_{A_f}}, \qquad q_{\beta f} = \frac{\rho}{2}(u_{A_f}^2 + v_{A_f}^2). \tag{B.43}$$

Applying these developments into 2D flow equations () and accounting for the similarity of the Y_f^A and Z_f^A flow the fin forces due to 3D flow can be calculated.

Additional factor in calculating aerodynamics of the fin area arise due to rolling motion. The rolling motion induces local angle of attack at the fin edges

$$\alpha_{p,\,f} = \operatorname{atan}\left(\frac{pb}{2u_{A_f}}\right) \tag{B.44}$$

and the local dynamic pressure

$$q_{p,\,f} = \frac{\rho}{2}\left(u_{A_f}^2 + p\frac{b}{2}\right), \tag{B.45}$$

where b is the span of the fins. The computed induced angle of attack and the local dynamic pressure are used for determination of the roll moment of the fins

$$L_{p,f}^A = -\eta_{L_p} 2bq_{p,f}((c_{l\alpha_0,f} + c_{d_0,f})\sin 2\alpha_{p,f} + c_{d_c,f}\sin\alpha_{p,f}\left|\sin\alpha_{p,\,f}\right|)S_f\ . \tag{B.46}$$

The first term η_{L_p} indicates the aerodynamic roll efficiency factor of the fins and is usually derived from corresponding reference tables given, for example, in reference [6].

There are additional aerodynamic effects that lead to the roll induced moment. They appear due to the asymmetrical flow around the fins and modeled by using aerodynamic moment coefficients $c_{L\alpha}$ for the horizontal fins and $c_{L\beta}$ for the vertical fins:

$$L_{\alpha\beta,\,f}^A = q_{\alpha f}(c_{L\alpha}\alpha_f + c_{L\beta}\beta_f)S_f. \tag{B.47}$$

The detailed treatment of the roll moment due to asymmetrical flow of the fins can be also found in reference [6].

For closing the aerodynamics of the tail area, the changes of the aerodynamic properties of the fins against the control surfaces of the horizontal and vertical fins are modelled. The control of the airship is achieved by change of the effective local flow angles of the fins

$$\begin{aligned} \alpha_f &= \alpha(x_f) + \eta_\eta(\eta) \cdot \eta \\ \beta_f &= \beta(x_f) + \eta_\zeta(\zeta) \cdot \zeta \\ \alpha_{p,f} &= \alpha_{p,f} + \eta_\xi(\xi) \cdot \xi . \end{aligned} \tag{B.48}$$

The surface efficiency factors $\eta_\eta(\eta)$, $\eta_\zeta(\zeta)$, $\eta_\xi(\xi)$ and their numerical approximations are referenced in [6], [57].

B.4.4 Integrated Aerodynamic Model

Since the model of the hull and the model of the fins are derived separately, an extra enhancement of the complete model has been performed based on the proposition given in reference [24]. It is known, that at rear part of the hull there are aerodynamic interference effects between the hull and the fins. The aerodynamic components of the hull are influenced by fins and vice versa. Introducing an additional scaling factor η_k helps to account the influence of the fins on the flow around the hull and is appeared as a multiplicative term in describing the potential force and moment respectively. The influence of the fins on the hull aerodynamics in the instationary flow is negligible and therefore η_k appears only with the stationary force and moment terms. The opposite interaction of the hull aerodynamics on the fin aerodynamics is described by η_f term and appear as multiplicative coefficient of the fins forces and moments.

At present, there is no analytical approach for describing η_k and η_f is available. They are therefore determined in [24] from static wind tunnel experiments for a number of typical airships. Similar approach for the accounting the mutual interconnections is adopted for building the current aerodynamic model. The numerical values for these coefficients are also provided through the aerodynamic model fit against curves generated by wind tunnel experiments.

B.4.5 Aerodynamic Coefficients

As noticed in section 2.4.5 (aerodynamic part of the flight mechanical model) the parameters of the analytical aerodynamic model were adjusted by means of nondimensional aerodynamic coefficients determined from the wind tunnel experiments. The aerodynamic coefficients have been extracted at different values of free-stream velocity and flow angles α and

β. For a conventional airship they are defined as non dimensional force and moment coefficients:

$$\begin{aligned} c_x &= \frac{2X^A}{\rho U_\infty^2 V^{2/3}} & c_l &= \frac{2L^A}{\rho U_\infty^2 V^{2/3} b_R} \\ c_y &= \frac{2Y^A}{\rho U_\infty^2 V^{2/3}} \quad \text{and} & c_m &= \frac{2M^A}{\rho U_\infty^2 V^{2/3} l_R} \quad , \\ c_z &= \frac{2Z^A}{\rho U_\infty^2 V^{2/3}} & c_n &= \frac{2N^A}{\rho U_\infty^2 V^{2/3} l_R} \end{aligned} \tag{B.49}$$

with U_∞ denoting the free-stream velocity, ρ -air density and V-volume of the hull. b_R is the span of the fins and l_R is the reference length of the airship.

The aerodynamic coefficients determined by the wind tunnel are usually given in the wind tunnel axes (e.g. drag-c_D and lift-c_L coefficients) and additional transformation is needed for transforming them into the airship body fixed frame. It can be performed using directional cosine transformation matrix $\boldsymbol{T}_{fa}$ with arguments of longitudinal-α and lateral-β incidence angles:

$$\boldsymbol{T}_{fa} = \begin{bmatrix} \cos\alpha\cos\beta & -\cos\alpha\sin\beta & -\sin\alpha \\ \sin\beta & \cos\beta & 0 \\ \sin\alpha\cos\beta & -\sin\alpha\sin\beta & \cos\alpha \end{bmatrix}, \tag{B.50}$$

The transformed aerodynamic forces yield

$$\begin{bmatrix} X^A \\ Y^A \\ Z^A \end{bmatrix}_f = \boldsymbol{T}_{fa} \begin{bmatrix} -D \\ Y \\ -L \end{bmatrix}_a = \boldsymbol{T}_{fa} \frac{\rho}{2} U_\infty^2 V^{2/3} \begin{bmatrix} -c_D \\ c_Y \\ -c_L \end{bmatrix}_a \tag{B.51}$$

and the moments

$$\begin{bmatrix} L^A \\ M^A \\ N^A \end{bmatrix}_f = \boldsymbol{T}_{fa} \begin{bmatrix} L^A \\ M^A \\ N^A \end{bmatrix}_a = \boldsymbol{T}_{fa} \frac{\rho}{2} U_\infty^2 V^{2/3} \begin{bmatrix} c_l b_R \\ c_m l_R \\ c_n l_R \end{bmatrix}_a . \tag{B.52}$$

The subscripts $[\ ]_f$ and $[\ ]_a$ denote the body fixed and wind tunnel axis respectively. D and L are the aerodynamic drag and lift forces respectively. Using equations (B.51) and (B.52) it is possible to perform the forward and back transformation from the wind tunnel to the body coordinates.

B.5 Force and Moment Derivatives

B.5.1 Approximated Form

The force and moment derivatives represent the coefficients of the Taylor row expansion when linearization of external forces and moments takes place. Using analytical representation of the gravity, buoyancy and aerodynamic forces and moments, it is possible to perform the linearization analytically in terms of physically meaningful parameters. The obtained force and moment derivatives are summarized in equations (B.53)-(B.58):

$$
\begin{aligned}
X_{,u} &= \rho u_0(-c_{d_0,\,h}V^{2/3} - c_{d_0,f}S_f - 2\eta_k I^u_{x_{\text{pot}}} + 2\eta_k I^{uvw}_{x_{\text{pot}}}) \\
X_{,w} &= \rho w_0(2\eta_k I^{uvw}_{x_{\text{pot}}} + 2\eta_k I^{vw}_{x_{\text{pot}}} + \eta_f(c_{l_{\alpha_0},f} - \eta_f c_{d_{\text{ind}},\,f})S_f) \\
X_{,q} &= \rho w_0(\eta_k I^q_{x_{\text{pot}}} + \eta_f(c_{l_{\alpha_0},f} - \eta_f c_{d_{\text{ind}},\,f})S_f x_{f_a}) \\
X_{,\theta} &= (B-G)\cos\theta_0 \\
X_{,\eta} &= \rho u_0 w_0 \eta_f(c_{l_{\alpha_0},f} - \eta_f c_{d_{\text{ind}},\,f})S_f \eta_\eta \\
X_{,\delta_T} &= X_{\delta_T}(x_0),
\end{aligned}
\tag{B.53}
$$

$$
\begin{aligned}
Y_{,v} &= Z_{,w} = \rho u_0\left(\eta_k I^{uw}_{z_{\text{pot}}} - \frac{1}{2}\eta_f c_{l_{\alpha_0},f} S_f\right) \\
Y_{,p} &= \rho k_2 V w_0 \\
Y_{,r} &= \rho u_0\left(\eta_k I^{uq}_{z_{\text{pot}}} - \frac{1}{2}\eta_f c_{l_{\alpha_0},f} S_f x_{f_a}\right) \\
Y_{,\phi} &= (G-B)\cos\theta_0 \approx 0 \\
Y_{,\zeta} &= -\rho\frac{1}{2}u_0^2 \eta_f c_{l_{\alpha_0},f} S_f \eta_\zeta,
\end{aligned}
\tag{B.54}
$$

$$
\begin{aligned}
Z_{,u} &= \rho w_0\left(\eta_k I^{uw}_{z_{\text{pot}}} - \frac{1}{2}\eta_f c_{l_{\alpha_0},f} S_f\right) \\
Z_{,w} &= Y_{,v} = \rho u_0\left(\eta_k I^{uw}_{z_{\text{pot}}} - \frac{1}{2}\eta_f c_{l_{\alpha_0},f} S_f\right) \\
Z_{,q} &= \rho u_0\left(-\eta_k I^{uq}_{z_{\text{pot}}} + \frac{1}{2}\eta_f c_{l_{\alpha_0},f} S_f x_{f_a}\right) \\
Z_{,\theta} &= (B-G)\sin\theta_0 \approx 0 \\
Z_{,\eta} &= -\rho\frac{1}{2}u_0^2 \eta_f c_{l_{\alpha_0},f} S_f \eta_\eta,
\end{aligned}
\tag{B.55}
$$

$$
\begin{aligned}
L_{,p} &= -\frac{1}{2}\rho u_0 \eta_f c_{l_{\alpha_0,f}} S_f \eta_{L_p} b_f^2 \\
L_{,\phi} &= (Bz_{CB} - Gz_{CG})\cos\theta_0 \\
L_{,\xi} &= -\rho\frac{1}{2}u_0^2 \eta_f c_{l_{\alpha_0,f}} S_f \eta_{L_p} b_f \eta_\xi,
\end{aligned}
\tag{B.56}
$$

$$
\begin{aligned}
M_{,u} &= \rho w_0\left(-\eta_k I^{uw}_{m_{\text{pot}}} + \frac{1}{2}c_{l_{\alpha_0,f}} \eta_f S_f x_{f_a}\right) \\
M_{,w} &= -N_{,v} = \rho u_0\left(-\eta_k I^{uw}_{m_{\text{pot}}} + \frac{1}{2}c_{l_{\alpha_0,f}} \eta_f S_f x_{f_a}\right) \\
M_{,q} &= N_{,r} = \rho u_0\left(\eta_k I^{uq}_{m_{\text{pot}}} - \frac{1}{2}c_{l_{\alpha_0,f}} \eta_f S_f x_{f_a}^2\right) \\
M_{,\theta} &= (Bz_{CB} - Gz_{CG})\cos(\theta_0) + (Gx_{CG} - Bx_{CB})\sin\theta_0 \\
M_{,\eta} &= \frac{1}{2}\rho u_0^2 c_{l_{\alpha_0,f}} \eta_f S_f x_{f_a} \eta_\eta \\
M_{,\delta_T} &= X_{\delta_T}(x_0) z_{CT},
\end{aligned}
\tag{B.57}
$$

$$
\begin{aligned}
N_{,v} &= -M_{,w} = \rho u_0\left(\eta_k I^{uw}_{m_{\text{pot}}} - \frac{1}{2}c_{l_{\alpha_0,f}} \eta_f S_f x_{f_a}\right) \\
N_{,r} &= M_{,q} = \rho u_0\left(\eta_k I^{uq}_{m_{\text{pot}}} - \frac{1}{2}c_{l_{\alpha_0,f}} \eta_f S_f x_{f_a}^2\right) \\
N_{,\phi} &= (Gx_{CG} - Bx_{CB})\cos\theta_0 \approx 0 \\
N_{,\zeta} &= -\frac{1}{2}\rho u_0^2 c_{l_{\alpha_0,f}} \eta_f S_f x_{f_a} \eta_\zeta \\
N_{,\delta_T} &= -X_{\delta_T}(x_0) y_{CT} \approx 0.
\end{aligned}
\tag{B.58}
$$

B.5.2 Dominant Force and Moment Derivatives

By studying the equilibrium point condition and numerical order of some individual parts of the aerodynamic derivatives, it is also possible to make some simplifications of the derivatives, by neglecting the smallest of them. Thus, all derivatives, that have the multiplier ρw_0 can be neglected from the analysis because of negligibly small value of the trimmed vertical velocity w_0. Moreover, numerical values of the geometry dependant integrals: $I^{uvw}_{x_{pot}}$, $I^{u}_{x_{pot}}$, $I^{vw}_{x_{pot}}$, $I^{uw}_{z_{pot}}$, were found to be negligibly small and can be therefore neglected. For the rectilinear flight, the dominant derivatives are presented in Table B.2.

Table B.2 Significant force and moment derivatives

Component	Dominant Derivatives	
Axial force X	$X_{,\dot{u}}$, $X_{,u}$	$X_{,\delta T}$
Side force Y	$Y_{,\dot{v}}$, $Y_{,v}$, $Y_{,r}$	$Y_{,\zeta}$
Vertical force Z	$Z_{,\dot{w}}$, $Z_{,w}$, $Z_{,q}$	$Z_{,\eta}$
Rolling moment L	$L_{,\dot{p}}$, $L_{,p}$, $L_{,\phi}$	$L_{,\xi}$
Pitching moment M	$M_{,\dot{q}}$, $M_{,w}$, $M_{,q}$, $M_{,\theta}$	$M_{,\eta}$
Yawing moment N	$N_{,\dot{r}}$, $N_{,v}$, $N_{,r}$	$N_{,\zeta}$

B.5.3 Relationship Between Force and Moment Derivatives and Aerodynamic Coefficients

It is easy to establish the analytical relationship between major aerodynamic derivatives and their non dimensional coefficients. All important aerodynamic coefficients can be computed from the corresponding force and moment derivatives under assumption of small steady angle of attack ($\alpha_0 \ll 1$). Under this condition the following approximations are valid:

$$\alpha_0 \cong \frac{w_0}{u_0} \text{ and } \delta\alpha \cong \frac{\delta w}{u_0},\ \delta\beta \cong \frac{\delta v}{u_0}. \tag{B.59}$$

Using this approximation the aerodynamic coefficients are related to the force and moment derivatives as follows:

$$\begin{aligned}
Y_{,v}\delta v &= Y_{,v}u_0\delta\beta = \frac{\rho}{2}u_0^2 c_{y_\beta} V^{2/3}\delta\beta, & M_{,w}\delta w &= \frac{\rho}{2}u_0^2 c_{m_\alpha} V^{2/3} l_R \delta\alpha,\\
Y_{,r}\delta r &= \frac{\rho}{2}u_0^2 c_{y_r} V^{2/3}\frac{\delta r l_R}{u_0}, & M_{,q}\delta q &= \frac{\rho}{2}u_0^2 c_{m_q} V^{2/3} l_R \frac{\delta q l_R}{u_0},\\
Z_{,w}\delta w &= Z_{,w}u_0\delta\alpha = \frac{\rho}{2}u_0^2 c_{z_\alpha} V^{2/3}\delta\alpha, & N_{,v}\delta v &= \frac{\rho}{2}u_0^2 c_{n_\beta} V^{2/3} l_R \delta\beta,\\
Z_{,q}\delta q &= \frac{\rho}{2}u_0^2 c_{z_q} V^{2/3}\frac{\delta q l_R}{u_0}, & N_{,r}\delta r &= \frac{\rho}{2}u_0^2 c_{n_r} V^{2/3} l_R \frac{\delta r l_R}{u_0}.
\end{aligned} \quad \text{and} \tag{B.60}$$

Note that the rotational variables in equation (B.60) are expressed in nondimensionalized form:

$$\begin{aligned} \delta q &\rightarrow \delta q l_R / u_0 \\ \delta r &\rightarrow \delta p l_R / u_0 . \end{aligned} \tag{B.61}$$

The aerodynamic coefficients yield

$$\begin{aligned} c_{y_\beta} &= \frac{2Y_{,v}}{\rho u_0 V^{2/3}} = \frac{2\eta_k I_{z_{\text{pot}}}^{uw} - \eta_f c_{l_{\alpha_0},f} S_f}{V^{2/3}} \\ c_{y_r} &= \frac{2Y_{,r}}{\rho u_0 V^{2/3} l_R} = \frac{2\eta_k I_{z_{\text{pot}}}^{qu} - \eta_f c_{l_{\alpha_0},f} S_f x_{f_a}}{V^{2/3} l_R} \\ c_{z_\alpha} &= \frac{2Z_{,w}}{\rho u_0 V^{2/3}} = \frac{2\eta_k I_{z_{\text{pot}}}^{uw} - \eta_f c_{l_{\alpha_0},f} S_f}{V^{2/3}} = c_{y_\beta} \\ c_{z_q} &= \frac{2Z_{,q}}{\rho u_0 V^{2/3} l_R} = \frac{-2\eta_k I_{z_{\text{pot}}}^{qu} + \eta_f c_{l_{\alpha_0},f} S_f x_{f_a}}{V^{2/3} l_R} = -c_{y_r} \end{aligned} \tag{B.62}$$

and the moment coefficients are given by

$$\begin{aligned} c_{m_\alpha} &= \frac{2M_{,w}}{\rho u_0 V^{2/3} l_R} = \frac{-2\eta_k I_{m_{\text{pot}}}^{uw} + \eta_f S_f c_{l_{\alpha_0},f} x_{f_a}}{V^{2/3} l_R} \\ c_{m_q} &= \frac{2M_{,q}}{\rho u_0 V^{2/3} l_R^2} = \frac{2\eta_k I_{m_{\text{pot}}}^{qu} - \eta_f S_f c_{l_{\alpha_0},f} x_{f_a}^2}{V^{2/3} l_R} \\ c_{n_\beta} &= \frac{2N_{,v}}{\rho l_R u_0 V^{2/3}} = \frac{2\eta_k I_{m_{\text{pot}}}^{uw} - \eta_f S_f c_{l_{\alpha_0},f} x_{f_a}}{V^{2/3} l_R} = -c_{m_\alpha} \\ c_{n_r} &= \frac{2N_{,r}}{\rho l_R^2 u_0 V^{2/3}} = \frac{2\eta_k I_{m_{\text{pot}}}^{qu} - \eta_f S_f c_{l_{\alpha_0},f} x_{f_a}^2}{l_R^2 V^{2/3}} = c_{m_q}. \end{aligned} \tag{B.63}$$

B.6 Stability and Control Derivatives

B.6.1 Extraction of Aerodynamic Coefficients

In order to extract the aerodynamic relevant data from the flight determined parameters, it is first necessary to transform the identified stability and control derivatives into force and moment derivatives. Subsequently, the calculated derivatives are used for derivation of aerodynamic coefficients.

The baseline for evaluation of the force and moment derivatives from the flight determined stability and control derivatives is introduced in Chapter 3. Using back transformation of equations, it is possible to compute the force and moment derivatives from the estimated stability and control derivatives. Thus in examining the longitudinal and lateral-directional dynamics, the matrices $\boldsymbol{A}'_{lon}$, $\boldsymbol{B}'_{lon}$, $\boldsymbol{A}'_{lat}$, $\boldsymbol{B}'_{lat}$ contain dimensional force and moment derivatives, computed by:

$$\boldsymbol{A}'_{lon} = \boldsymbol{M}'_{lon} \cdot \boldsymbol{A}_{lon}, \qquad \boldsymbol{B}'_{lon} = \boldsymbol{M}'_{lon} \cdot \boldsymbol{B}_{lon} \tag{B.64}$$

and

$$\boldsymbol{A}'_{lat} = \boldsymbol{M}'_{lat} \cdot \boldsymbol{A}_{lat}, \qquad \boldsymbol{B}'_{lat} = \boldsymbol{M}'_{lat} \cdot \boldsymbol{B}_{lat}, \tag{B.65}$$

with $\boldsymbol{M}'_{lon}$ and $\boldsymbol{M}'_{lat}$ denoting the mass matrices together with apparent mass terms of the instationary aerodynamics (Munk factors). The dynamic $\boldsymbol{A}_{lon}$, $\boldsymbol{A}_{lat}$ and control $\boldsymbol{B}_{lon}$, $\boldsymbol{B}_{lat}$ matrices contain the estimated stability and control derivatives respectively. The expanded form of the system matrices is summarized in Table B.3 separately for the longitudinal and lateral-directional dynamics. It is easy to observe the importance of configuration properties (i.e. the mass m, mass center CG, the moment of inertia matrix $\boldsymbol{I}$) of an airship on computation of the aerodynamic coefficients. Moreover the derivatives which are related to the apparent mass effects ($X_{,\dot{u}}$, $Y_{,\dot{v}}$, etc.) are also required for accurate determination of the major aerodynamic coefficients.

Table B.3 System matrices of Longitudinal and Lateral-directional dynamics

Longitudinal Dynamics	**Lateral-Directional Dynamics**
$\boldsymbol{M}'_{lon} = \begin{bmatrix} m - X_{,\dot{u}} & 0 & mz_{CG} & 0 \\ 0 & m - Z_{,\dot{w}} & \sim 0 & 0 \\ mz_{CG} & \sim 0 & I_{yy} - M_{,\dot{q}} & 0 \\ 0 & 0 & 0 & 1 \end{bmatrix}$	$\boldsymbol{M}'_{lat} = \begin{bmatrix} m - Y_{,\dot{v}} & -mz_{CG} & \sim 0 & 0 \\ -mz_{CG} & I_{xx} & I_{xz} & 0 \\ \sim 0 & I_{xz} & I_{zz} - N_{,\dot{r}} & 0 \\ 0 & 0 & 0 & 1 \end{bmatrix}$
$\boldsymbol{A}'_{lon} = \begin{bmatrix} X_{,u} & \sim 0 & -mw_0 & X_{,\theta} \\ \sim 0 & Z_{,w} & Z_{,q} + mu_0 & \sim 0 \\ \sim 0 & M_{,w} & (M_{,\bar{q}} - mz_{CG} w_0) & M_{,\theta} \\ 0 & 0 & 1 & 0 \end{bmatrix}$	$\boldsymbol{A}'_{lat} = \begin{bmatrix} Y_{,v} & mw_0 & Y_{,r} - mu_0 & \sim 0 \\ \sim 0 & (L_{,p} - mz_{CG} w_0) & (L_{,r} + mz_{CG} u_0) & L_{,\phi} \\ N_{,v} & \sim 0 & N_{,r} & \sim 0 \\ 0 & 1 & \sim 0 & 0 \end{bmatrix}$
$\boldsymbol{B}'_{lon} = \begin{bmatrix} \sim 0 & X_{,T} \\ Z_{,\eta} & \sim 0 \\ M_{,\eta} & \sim 0 \\ 0 & 0 \end{bmatrix}$	$\boldsymbol{B}'_{lat} = \begin{bmatrix} Y_{,\zeta} & 0 \\ 0 & L_{,\xi} \\ N_{,\zeta} & \sim 0 \\ 0 & 0 \end{bmatrix}$
$\boldsymbol{A}_{lon} = \begin{bmatrix} X_u & X_w & X_q & X_\theta \\ \sim 0 & Z_w & Z_q & \sim 0 \\ M_u & M_w & M_q & M_\theta \\ 0 & 0 & 1 & 0 \end{bmatrix}$	$\boldsymbol{A}_{lat} = \begin{bmatrix} Y_v & Y_p & Y_r & Y_\phi \\ L_v & L_p & L_r & L_\phi \\ N_v & N_p & N_r & N_\phi \\ 0 & 1 & \sim 0 & 0 \end{bmatrix}$
$\boldsymbol{B}_{lon} = \begin{bmatrix} X_\eta & X_\delta \\ Z_\eta & 0 \\ M_\eta & M_\delta \\ 0 & 0 \end{bmatrix}$	$\boldsymbol{B}_{lat} = \begin{bmatrix} Y_\zeta & 0 \\ 0 & L_\xi \\ N_\zeta & 0 \\ 0 & 0 \end{bmatrix}$

Substituting the corresponding matrices from Table B.4 in transformation equations (B.64) and (B.65), one obtains the expanded form of the force and moment derivatives. The dominant derivatives are summarized in Table B.4.

Table B.4 Relationship between force and moment derivatives and flight determined parameters

Force/Moment Derivative	**Derivation using stability and control derivatives**
$X_{,u}$	$(m - X_{,\dot{u}})X_u + (I_{yy} - M_{,\dot{q}})z_{CG}M_u \approx (m - X_{,\dot{u}})X_u$
$X_{,\delta_T}$	$(m - X_{,\dot{u}})X_\delta$
$Z_{,w}$	$(m - Z_{,\dot{w}})Z_w$
$Z_{,q}$	$(m - Z_{,\dot{w}})Z_q - mu_0$
$Z_{,\theta}$	$(m - Z_{,\dot{w}})Z_\theta$

Force/Moment Derivative	Derivation using stability and control derivatives
$Z_{,\eta}$	$(m - Z_{,\dot{w}})Z_{\eta}$
$M_{,w}$	$(I_{yy} - M_{,\dot{q}})M_{w} + mz_{CG}X_{w} \approx (I_{yy} - M_{,\dot{q}})M_{w}$
$M_{,q}$	$(I_{yy} - M_{,\dot{q}})M_{q} + mz_{CG}X_{q} + mz_{CG}w_{0} \approx (I_{yy} - M_{,\dot{q}})M_{q} + mz_{CG}w_{0}$
$M_{,\theta}$	$(I_{yy} - M_{,\dot{q}})M_{\theta} + mz_{CG}X_{\theta} \approx (I_{yy} - M_{,\dot{q}})M_{\theta}$
$M_{,\eta}$	$(I_{yy} - M_{,\dot{q}})M_{\eta} + mz_{CG}X_{\eta} \approx (I_{yy} - M_{,\dot{q}})M_{\eta}$
$Y_{,v}$	$(m - Y_{,\dot{v}})Y_{v} - mz_{CG}L_{v}$
$Y_{,p}$	$(m - Y_{,\dot{v}})Y_{p} - mz_{CG}L_{p} - mw_{0}$
$Y_{,r}$	$(m - Y_{,\dot{v}})Y_{r} - mz_{CG}L_{r} + mu_{0}$
$Y_{,\phi}$	$(m - Y_{,\dot{v}})Y_{\phi} - mz_{CG}L_{\phi}$
$Y_{,\zeta}$	$(m - Y_{,\dot{v}})Y_{\zeta} - mz_{CG}L_{\zeta}$
$L_{,p}$	$I_{xx}L_{p} - mz_{CG}Y_{p} + I_{xz}N_{p} + mz_{CG}w_{0}$
$L_{,r}$	$I_{xx}L_{r} - mz_{CG}Y_{r} + I_{xz}N_{r} - mz_{CG}u_{0}$
$L_{,\phi}$	$I_{xx}L_{\phi} - mz_{CG}Y_{\phi} + I_{xz}N_{\phi}$
$L_{,\xi}$	$I_{xx}L_{\xi} - mz_{CG}Y_{\xi} + I_{xz}N_{\xi}$
$N_{,v}$	$(I_{zz} - N_{\dot{r}})N_{v} + I_{xz}L_{v}$
$N_{,r}$	$(I_{zz} - N_{\dot{r}})N_{r} + I_{xz}L_{r}$
$N_{,\phi}$	$(I_{zz} - N_{\dot{r}})N_{\phi} + I_{xz}L_{\phi}$
$N_{,\zeta}$	$(I_{zz} - N_{\dot{r}})N_{\zeta} + I_{xz}L_{\phi}$

Appendix C

Flight Data Evaluation Results

C.1 Summary of Flight Maneuvers

The maneuvers presented in Table C.1 have been taken for the parameter estimation of the postulated dynamical models. In order to perform the maneuver, the pilot has manually acquired a steady flight condition. Its indication was a directional flight of the airship with unchanged control inputs. Instantaneously after acquisition of the trimmed condition, a perturbed motion was initiated by the controls. The control perturbations were partly performed by the pilot and partly generated by the onboard computer. The flight maneuvers have been performed under limitations discussed in section 5.2.4.

Table C.1: Summary of identification flight records

Flight record Acronym	Flight date	Duration [s]	Used controls type/shape/mode
F4S1e	15.08.2002	55	elevator 3-2-1-1 automatic
F4S2e	15.08.2002	53	elevator 3-2-1-1automatic
F4S3e	15.08.2002	53	elevator 3-2-1-1automatic
F4S4e	15.08.2002	43	elevator doublet automatic
F4S5e	15.08.2002	38	elevator doublet automatic
F4S6e	15.08.2002	57	elevator 3-2-1-1 automatic
F4S7e	15.08.2002	80	elevator sin manual
F5S9e	14.08.2002	51	elevator sweep manual
F5S12e	14.08.2002	60	elevator 3-2-1-1 manual
F3S2e	15.08.2006	52	elevator 3-2-1-1 automatic
F7S6r	15.08.2002	45	rudder 2x doublet

C.2 Flight Data Analysis

C.2.1 Data Prefiltering

Figure C.1 illustrates the raw measurements from a typical longitudinal maneuver. Applying the power spectral density function to the measured data, the vibration disturbances can be effectively observed in the frequency domain, as shown in Figure C.2. One noticeable peak can be detected near $5.3[\mathrm{Hz}]$ for the acceleration and angular rate measurements. The effect causing this peak are vibrations induced by the stern propeller rotating at approximately $360[\mathrm{rpm}]$.

Since the indicated measurement disturbances have nonwhite nature, they cannot be directly utilized in the estimation algorithm based on likelihood criteria for parameter determination (see discussion in 4.2.2). Formally, if the disturbance model were known, it would be easy to design a prefilter based on the inverted noise model. Although this approach is favored and does not invalidate the likelihood function, its practical utilization is very restricted. It is in general very difficult to model all disturbance factors which appear in the flight vehicle during the flight. Even if it is possible to derive a parameterized disturbance model, its determination requires significant evaluation efforts and is often conflicting with the plant model [39].

In the practical applications, the high frequency disturbances in the flight data are remedied by a low pass filtering [12]. It is based on supposition, that the eigendynamic characteristics of the flight vehicle are concentrated at lower frequencies than the structural oscillations. This assumption is also valid in the current analysis of the airship dynamics.

For evaluation of the airship flight data, a digital FIR (Finite Impulse Response) filter, based on linear combination of input values was used. The filter equation yields

$$\begin{aligned} y_i = \frac{1}{b}(&- a_5 u_{i-5} - a_4 u_{i-4} - a_3 u_{i-3} - a_2 u_{i-2} - a_1 u_{i-1} + a_0 u_i + \dots \\ &+ a_1 u_{i+1} + a_2 u_{i+2} + a_3 u_{i+3} + a_4 u_{i+4} + a_5 u_{i+5}), \end{aligned} \tag{C.1}$$

with

$$a_0 = 74,\ a_1 = 67,\ a_2 = 46,\ a_3 = 21,\ a_4 = 3,\ a_5 = -5,\ b = 216.$$

The filter incorporates a low pass characteristics with the cutoff frequency designed to be at $f_c = 1[\mathrm{Hz}]$. The advantage in utilizing this symmetrical filter is that it does not introduce any lag in the filtered values. The filtering has been applied to all measurements, except the GPS and the control indications of the pilot commands. The time histories of the filtered signals are shown in Figure C.3.

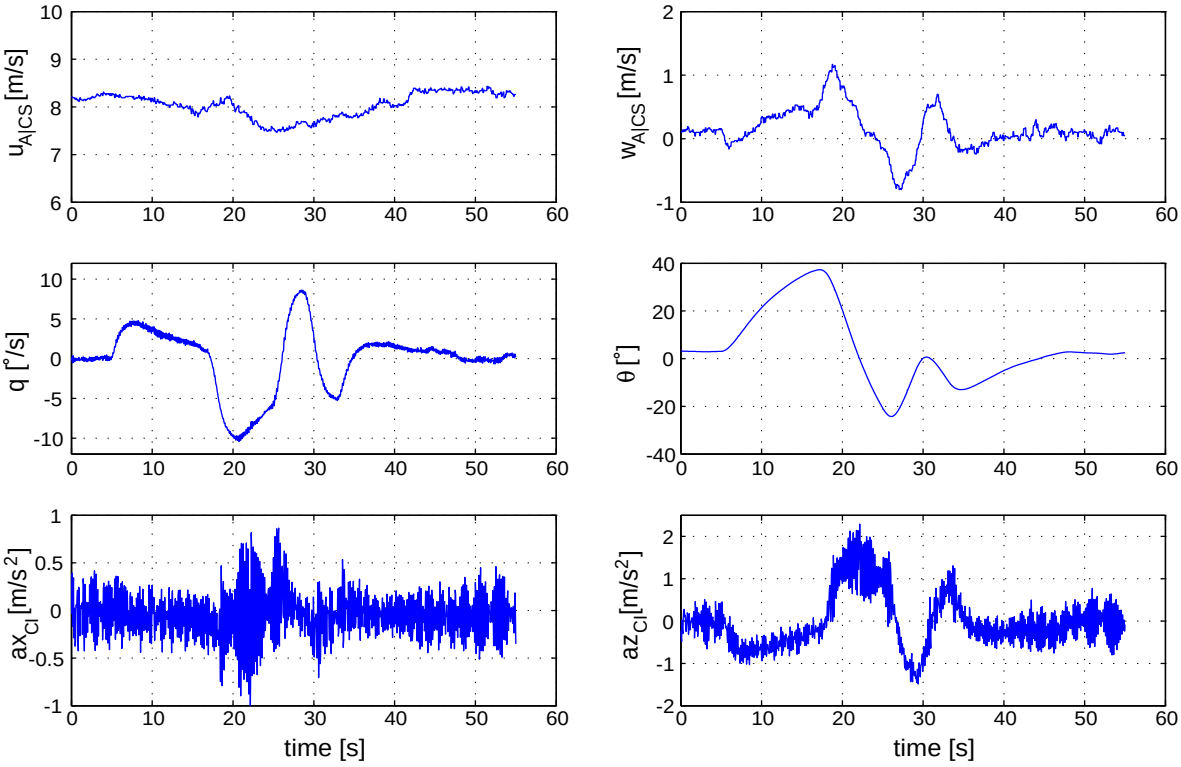

Figure C.1: Raw measurements of airstream and inertial components (acceleration due to gravity is removed)

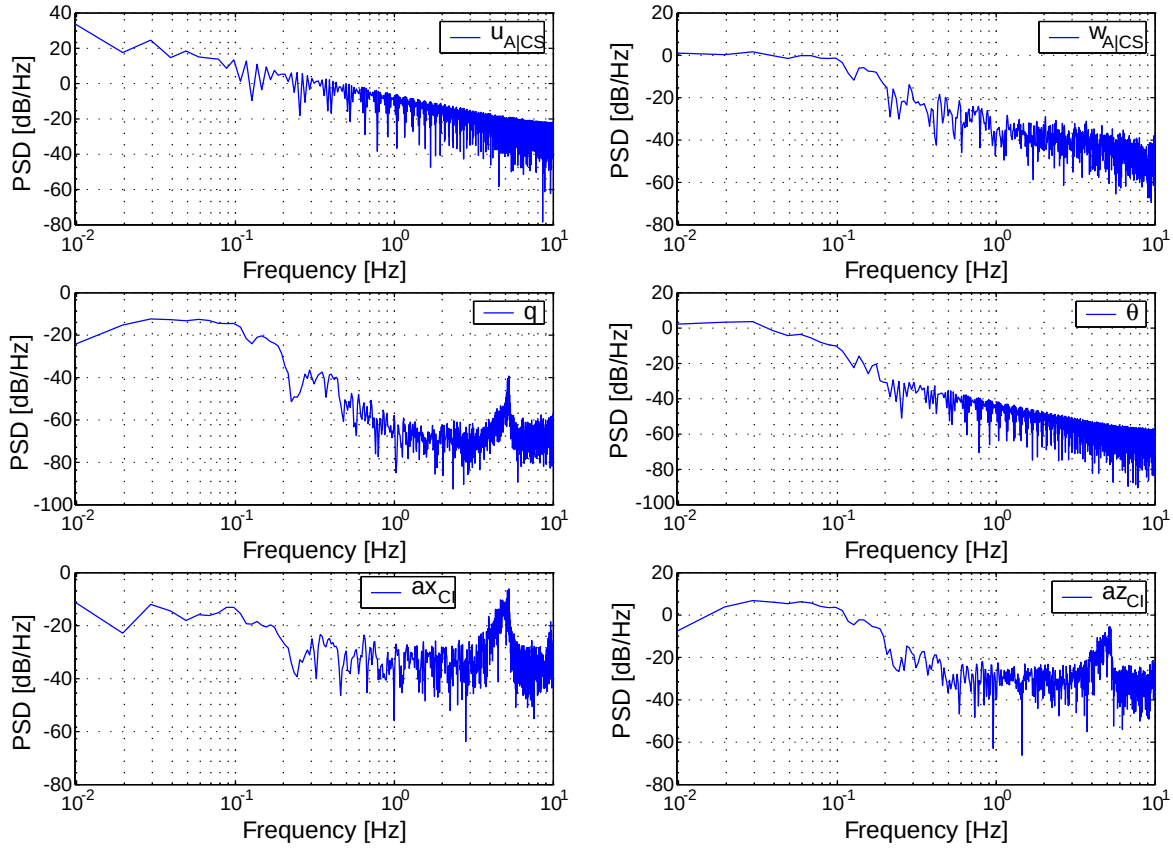

Figure C.2: Power Spectral Density (PSD) function of the raw measurements

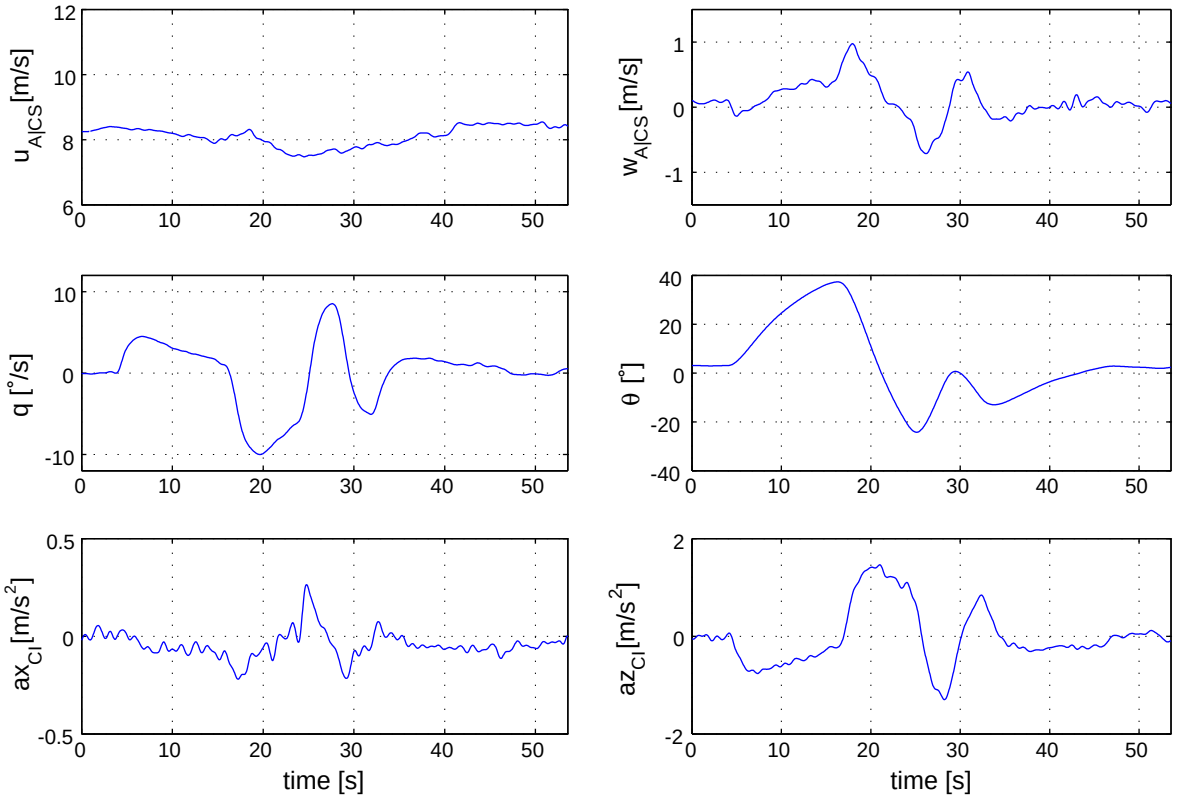

Figure C.3: Filtered IMU and airstream measurements

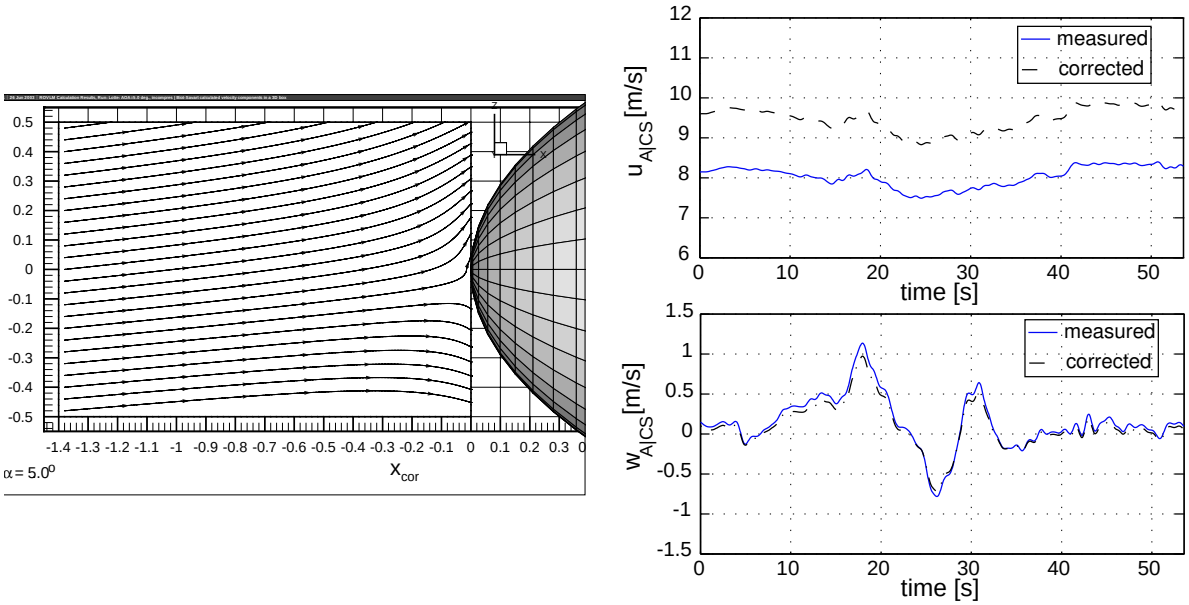

Figure C.4: Computation of interference effects of the hull in the *CS* location and correction of the airstream measurements.

C.2.2 Airdata Correction

In addition to the data prefiltering, the airstream measurements were corrected for the free-stream conditions in order to eliminate the interference effects caused by the hull of the airship. The interference effects were computed at different flow angles using CFD computations, as shown in Figure C.4. As can be seen, the applied corrections lead to increase of the axial airstream velocity $u_{A|CS}$ of about 20%. The corrected airstream velocities are then utilized for the subsequent processing.

C.2.3 Checking for Compatibility

The data compatibility procedure is based on the flight path reconstruction algorithm, where signals from different sensors are compared using kinematic relations. The detailed overview of this approach can be found in references [25], [28].

The flight path reconstruction algorithm involves a set of two state and two observation equations. The first state equation represents the attitude of the airship in terms of rotational variables and was already introduced in the equation (2.14)

$$\begin{bmatrix} \dot{\phi} \\ \dot{\theta} \\ \dot{\psi} \end{bmatrix} = \begin{bmatrix} 1 & \sin\phi\tan\theta & \cos\phi\tan\theta \\ 0 & \cos\phi & -\sin\phi \\ 0 & \dfrac{\sin\phi}{\cos\theta} & \dfrac{\cos\phi}{\cos\theta} \end{bmatrix} \begin{bmatrix} p - b_p \\ q - b_q \\ r - b_r \end{bmatrix}. \tag{C.2}$$

The measured p, q and r signals are assumed to be corrupted by systematic bias constants b_p, b_q and b_r respectively.

The second reconstruction equation utilizes the measured linear accelerations ax_{CI}, ay_{CI}, az_{CI}, measured angular rates p, q, r, and in equation (C.2) reconstructed Euler angles ϕ and θ

$$\begin{bmatrix} \dot{u}_{K|CI} \\ \dot{v}_{K|CI} \\ \dot{w}_{K|CI} \end{bmatrix} = \begin{bmatrix} 0 & r - b_r & -(q - b_q) \\ -(r - b_r) & 0 & p - b_p \\ q - b_q & -(p - b_p) & 0 \end{bmatrix} \begin{bmatrix} u_{K|CI} \\ v_{K|CI} \\ w_{K|CI} \end{bmatrix} + \begin{bmatrix} -g\sin\theta \\ g\cos\theta\sin\phi \\ g\cos\theta\cos\phi \end{bmatrix} + \begin{bmatrix} ax_{CI} - b_{ax} \\ ay_{CI} - b_{ay} \\ az_{CI} - b_{az} \end{bmatrix}, \tag{C.3}$$

with $u_{K,\ r|CI}$, $v_{K,\ r|CI}$ and $w_{K,\ r|CI}$ indicating the flight path velocity components at center of inertial measurements CI. The unknowns b_{ax}, b_{ay}, b_{az} are the respective bias components of the acceleration measurement signals ax_{CI}, ay_{CI} and az_{CI}. It is advantageous to formulate equation (C.3) using flight path velocity in CI location because it avoids the unmeasured rotational accelerations.

The output equations relate the reconstructed trajectories with the measured ones

$$\begin{aligned} \tilde{\phi} &= \phi + b_{\phi} \\ \tilde{\theta} &= \theta + b_{\theta} \\ \tilde{\psi} &= \psi + b_{\psi} \end{aligned} \tag{C.4}$$

and

$$\begin{bmatrix} u_{K|CS} \\ v_{K|CS} \\ w_{K|CS} \end{bmatrix} = \begin{bmatrix} u_{K|CI} \\ v_{K|CI} \\ w_{K|CI} \end{bmatrix} - \begin{bmatrix} 0 & r - b_r & -(q - b_q) \\ -(r - b_r) & 0 & p - b_p \\ q - b_q & -(p - b_p) & 0 \end{bmatrix} \begin{bmatrix} x_{CI} - x_{CS} \\ y_{CI} - y_{CS} \\ z_{CI} - z_{CS} \end{bmatrix}. \tag{C.5}$$

By means of the state and observation equations given in equations (C.2)-(C.5), the data consistency procedure can be reformulated to a standard identification problem. Minimizing the error between the measured and reconstructed trajectories, the unknown bias b_p, b_q, b_r, b_{ax}, b_{ay}, b_{az}, b_{ϕ}, b_{θ}, b_{ψ} and initial state parameters $u_{K0|CI}$, $v_{K0|CI}$, $w_{K0|CI}$ can be estimated. As a criteria, the maximum-likelihood function can be utilized

$$J(\Theta) = \sum_{i=1}^{N} \boldsymbol{e}_i^T \boldsymbol{R}^{-1} \boldsymbol{e}_i \,, \tag{C.6}$$

where elements of the error vector $\boldsymbol{e}_i$ are

$$\boldsymbol{e}_i = \begin{bmatrix} \phi_m - \tilde{\phi} \\ \theta_m - \tilde{\theta} \\ \psi_m - \tilde{\psi} \\ u_{A|CS} - u_{K|CS} \\ v_{A|CS} - v_{K|CS} \\ w_{A|CS} - w_{K|CS} \end{bmatrix} \tag{C.7}$$

and the elements of the covariance matrix $\boldsymbol{R}$ were taken from the specifications of the measurement components. In this formulation, the identification problem requires an extensive computational effort, involving an extended Kalman filter to account for the unknown forcing functions caused by wind and the sensor noise.

For the practical use, however, it is recommended to admit several simplifications. One of them is to neglect the process noise and to make an open loop integration of the state equa-

tions. In this approximation, a reasonable fit between the measured and the reconstructed trajectories can be achieved only if the wind and other unknown disturbances (predominantly sensor noise) have only a minor presence, i.e. do not distort greatly the effectively measured signals. Therefore, the goodness of the fit between the measured and reconstructed velocities can be taken as the plausibility criteria for selecting the flown maneuvers for the subsequent estimation purposes.

Since the sensor errors also appear as bias parameters $\boldsymbol{b}_x$, $\boldsymbol{b}_y$ within the estimation model (Equations (3.37) and (3.39)), their determination from the data consistency procedure is not of the primary importance. Important here is to show that throughout the selection of the appropriate bias constants, a compatibility of measured quantities can be achieved. Equation (C.4) does not consider any drift errors of the measured Euler angles. It can be neglected due to the fact, that duration of the identification record is normally does not exceed 60 seconds. Within this interval, the drift effects in the measured Euler angles can be neglected. Moreover, because of relatively small outer dimensions of the Lotte airship, it is assumed that all sensor positions could be accurately determined and not changing during the flight. The time delays between signal acquisition of the IMU platform and the ultrasonic anemometer are assumed to be negligibly small and neglected.

For the longitudinal maneuvers, it is preferable to perform the data compatibility check using only longitudinal variables:

$$\boldsymbol{x} = \left[u \; w \; \theta\right]^T, \boldsymbol{u} = \left[ax_{CI} \; az_{CI} \; q\right]^T, \quad \boldsymbol{y} = \left[u_{A|CS} \; w_{A|CS} \; \theta\right]^T . \tag{C.8}$$

This reduced formulation is used to ensure that not only the wind, but also unavoidable cross-coupling effects, altogether have only insignificant influence on the longitudinal motion.

In the next, several results of application of the data compatibility check to three different longitudinal maneuvers will be presented. In the first example illustrated in Figure C.5, a very poor fit between the measured and reconstructed velocities is achieved. The large velocity magnitudes can be explained by the existence of a strong turbulence field. Although at the beginning of record, all control inputs were held constant, the airstream velocity measurements indicate a large deviations from their mean/trimmed values. The same behavior is observed during and at the end of the record.

The second example, shown in Figure C.6, illustrates a trajectory reconstruction for the flight record with relatively smooth airspeed measurements. In this case, the trajectory fit is still unsatisfactory. Not only the linear velocities $u_{K|CS}$, $w_{K|CS}$, but also the reconstructed pitch angle θ does not match the corresponding measured quantities. The reason for such a large discrepancies arise from the dominance of the cross-coupling effects. Because of relatively small aerodynamic rolling moment of the fins, in some flight instances the induced roll oscillations (due to $CG \neq CB$) could not be effectively dampened. This leads to the noticed poor matching in trajectories.

Finally, the last example demonstrates a case, where a good agreement between the measured and reconstructed quantities is achieved. As can be seen from Figure C.7, the dis-

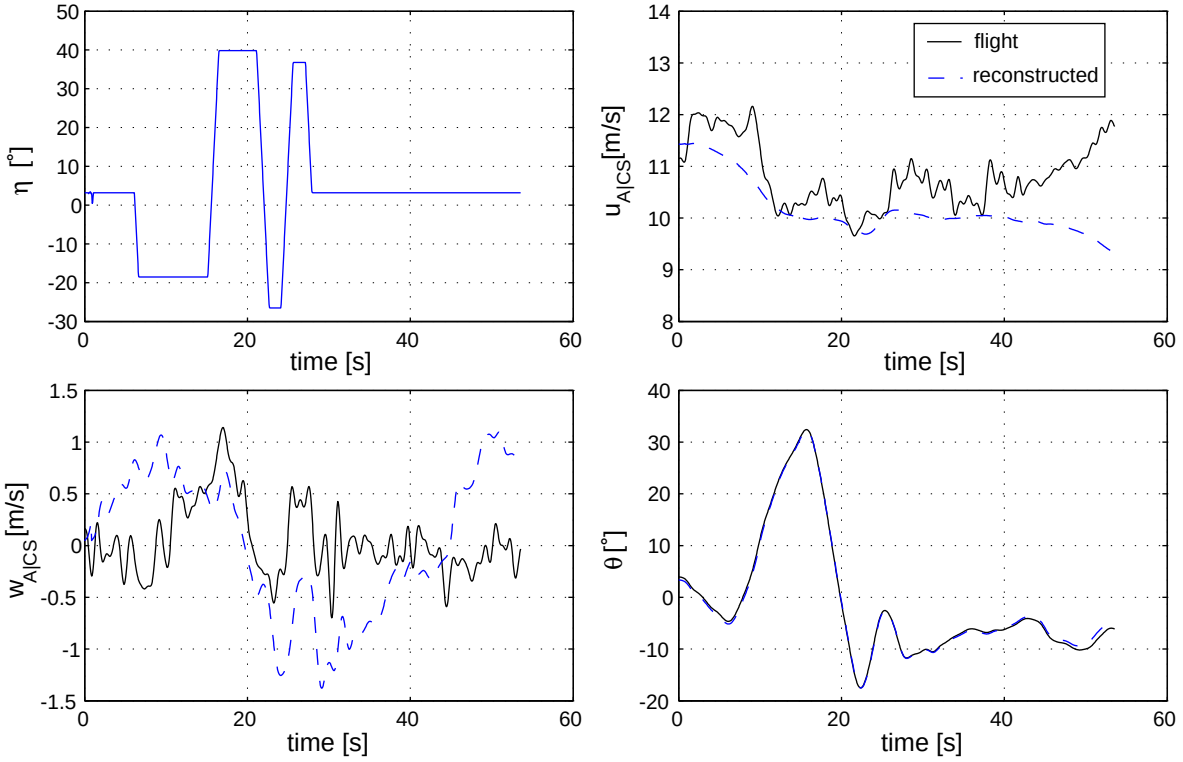

Figure C.5: Compatibility results for identification maneuver taken at severe turbulence conditions

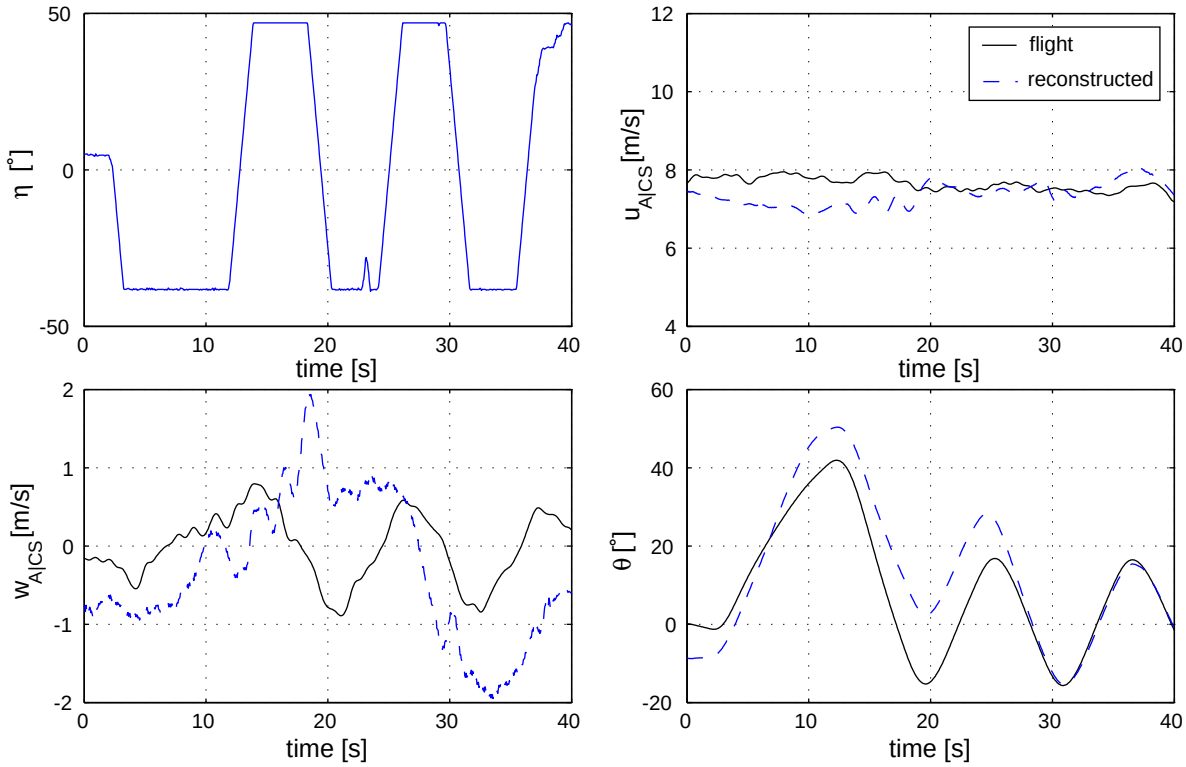

Figure C.6: Compatibility results for identification maneuver with high cross-coupling effects

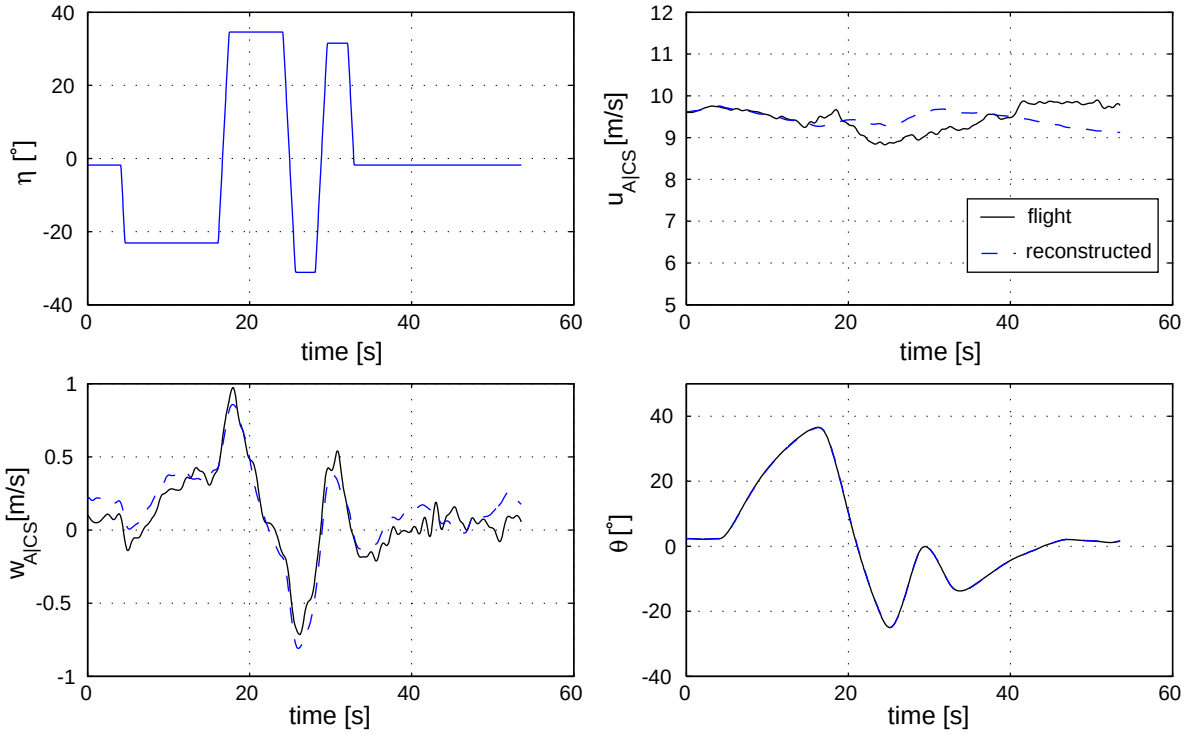

Figure C.7: Compatibility results for identification maneuver utilized for estimation purposes

tortions of the wind, as well as cross-coupling and other unwanted effects were at minimum level. It can be also concluded from the measurements itself, i.e relatively smooth trajectories and from the fact that the airship shows an ability to return to a nearly the same trim condition it held before the perturbation maneuver has began. Some errors in matching the velocity components are acceptable because of unavoidable atmospheric disturbances.

Obviously, only these flight records, where the data compatibility analysis was successful, have been further utilized for estimation of the model parameters.

Although it seems to be advantageous to utilize also the GPS measurements in the flight path reconstruction procedure, in the current evaluations the velocity estimations from the GPS receiver were not used directly in the data reconstruction. There were two reasons for not doing it. First, the reconstruction using GPS velocity can not be performed using longitudinal variables only, because it requires the transformation from the geodetic to the body frame of reference (equations (2.4) and (2.33)). Second, the velocity estimations provided by GPS receiver have apparent, but unknown time delay $\tau_{GPS} > 1[s]$, which should be accounted properly in the data processing. All these factors lead to increase of the number of unknown parameters. In fact, by trying out this setup, serious convergence problems of the numerical optimization algorithm have been encountered. Moreover, no repeatability of the obtained parameter values was acquired. It should be also noticed that although the GPS data were not used directly in the data consistency procedure, its absolute values of the estimated velocity vector $|\boldsymbol{V}_{GPS}|$ were used for comparison with the absolute value of the airsream velocity $|\boldsymbol{V}_A|$ in order to provide a raw estimation of the wind intensity.

C.3 Estimation Results of Elevator Input Maneuvers

C.3.1 Flight Record F4S1e

Table C.2: Estimated parameters of the full state longitudinal model

Parameter	Model Value (B/G=0.98)	Fully parametrized (C-R bounds[a])	Reduced parametrization (C-R bounds)
X_u	-0.099	-0.009 (0.235)	-0.0006 (0.120)
X_w	-0.419	0.108 (0.37)	-[b]
X_q	-0.023	-0.002 (2.67)	-
X_θ	-0.249	-0.140 (0.330)	-
Z_u		-0.005 (0.023)	
Z_w	-0.390	-0.805 (0.353)	-0.88 (0.042)
Z_q	3.937	4.212 (4.372)	4.507 (0.37)
Z_θ	0.015	0.147 (0.629)	-
M_u	-0.004	0.0073 (0.029)	-
M_w	0.108	0.076 (0.76)	0.068 (0.016)
M_q	-0.620	-1.209 (0.48)	-1.313 (0.092)
M_θ	-0.137	-0.201 (0.066)	-0.198 (0.009)
X_η	0.172	-0.10 (0.148)	-0.15 (0.038)
Z_η	-1.242	-0.498 (0.233)	-0.513 (0.057)
M_η	-0.430	-0.183 (0.108)	-0.188 (0.08)
$b_{\dot{u}}$	-	-0.075 (0.033)	0.012 (0.007)
$b_{\dot{w}}$	-	-0.009 (0.140)	0.017 (0.072)
$b_{\dot{q}}$	-	0.0006 (0.012)	0.0001 (0.006)
b_u	-	9.519 (0.1055)	9.509 (0.09)
b_w	-	0.134 (0.059)	0.057 (0.126)
b_q	-	-0.006 (0.009)	-0.006 (0.012)
b_θ	-	0.035 (0.010)	0.04 (0.010)
b_{ax}	-	-0.050 (0.016)	-0.037 (0.016)
b_{az}	-	0.047 (0.194)	0.056 (0.011)
u_0	9.5	9.531	9.284 (0.26)
w_0	-	-0.06 (0.35)	0.0376 (0.48)
Iterations		100[c]	21

Parameter	**Model Value (B/G=0.98)**	**Fully parametrized (C-R bounds[a])**	**Reduced parametrization (C-R bounds)**
Eigenvalue	-0.07 -1.15 0.042 +/- 0.2i	-0.015 -1.491 -0.258 +/- 0.173i	-0.0006 -1.590 -0.317 +/- 0.083i
Taylor Inequality Coefficient (TIC):			
u		0.23	0.52
w		0.08	0.08
q		0.048	0.032
θ		0.017	0.020
ax_{CI}		0.29	0.23
az_{CI}		0.056	0.056

a. Multiplied with a correction factor specified in Equation (4.38)

b. Not estimated

c. Manually stopped

Table C.3: Summary of longitudinal parameter values estimated with reduced state model

Parameter	Model Value	Output Error (C-R bound) M_θ estimated	Output Error (C-R bound) M_θ fixed
Z_w	-0.390	-0.572 (0.041)	-0.581 (0.041)
Z_q	3.937	2.602 (0.356)	2.650 (0.368)
M_w	-0.108	0.073 (0.023)	0.680 (0.002)
M_q	-0.620	-1.41 (0.113)	-1.42 (0.016)
M_θ	-0.137	-0.184 (0.011)	-0.18[a]
Z_η	-1.24	-0.498 (0.056)	-0.504 (0.056)
M_η	-0.430	-0.242 (0.009)	-0.242 (0.003)
$b_{\dot{w}}$	-	0.0008 (0.073)	-0.001 (0.072)
$b_{\dot{q}}$	-	-0.002 (0.006)	-0.002 (0.005)
$b_{\dot{\theta}}$	-	-0.003 (0.010)	-0.003 (0.010)
b_w	-	0.064 (0.128)	0.078 (0.125)
b_q	-	-0.001 (0.013)	-0.002 (0.005)
b_θ	-	0.030 (0.015)	0.029 (0.015)
b_{az}	-	-0.016 (0.145)	-0.015 (0.143)
u_0	9.5	9.640 (0.253)	9.642 (0.253)
Iterations		18	6
Eigenvalue	-1.15 0.042 +/- 0.2i	-1.48 -0.23 +/- 0.121i	-1.5 -0.25 +/- 0.08i
TIC: w q θ az_{CI}		 0.088 0.046 0.019 0.069	 0.088 0.046 0.019 0.069

a. Fixed value

Table C.4: Summary of longitudinal parameter values estimated with extended model

Parameter	Model Value	Output Error	Filter Error
Z_w	-0.390	-0.615 (0.044)	-0.703 (0.060)
Z_q	3.937	2.54 (0.393)	3.101 (0.240)
M_w	-0.108	0.079 (0.018)	0.072 (0.03)
M_q	-0.620	-1.41 (0.151)	-1.39 (0.051)
M_θ	-0.137	-0.182 (0.016)	-0.18 (0.037)
Z_η	-1.24	-0.570 (0.061)	-0.552 (0.073)
M_η	-0.430	-0.236 (0.011)	-0.205 (0.014)
$b_{\dot{w}}$	-	0.0005 (0.073)	-0.001 (0.048)
$b_{\dot{q}}$	-	0.007 (0.008)	0.002 (0.010)
b_w	-	0.064 (0.128)	0.103 (0.025)
b_q	-	-0.001 (0.013)	-0.0004 (0.012)
b_{az}	-	-0.016 (0.145)	-0.020 (0.125)
u_0	9.5	9.375 (0.279)	9.608 (0.23)
$\sigma_{\dot{w}}$	-	-	0.030 (0.007)
σ_q	-	-	0.003 (0.0008)
Iterations		15	8
Eigenvalue	-1.15 0.042 +/- 0.2i	-1.51 -0.25 +/- 0.09i	-1.54 -0.27 +/- 0.08i
TIC: w q az_{CI}		 0.088 0.046 0.069	 0.026 0.025 0.006

C.3.2 Fight Record F4S2e

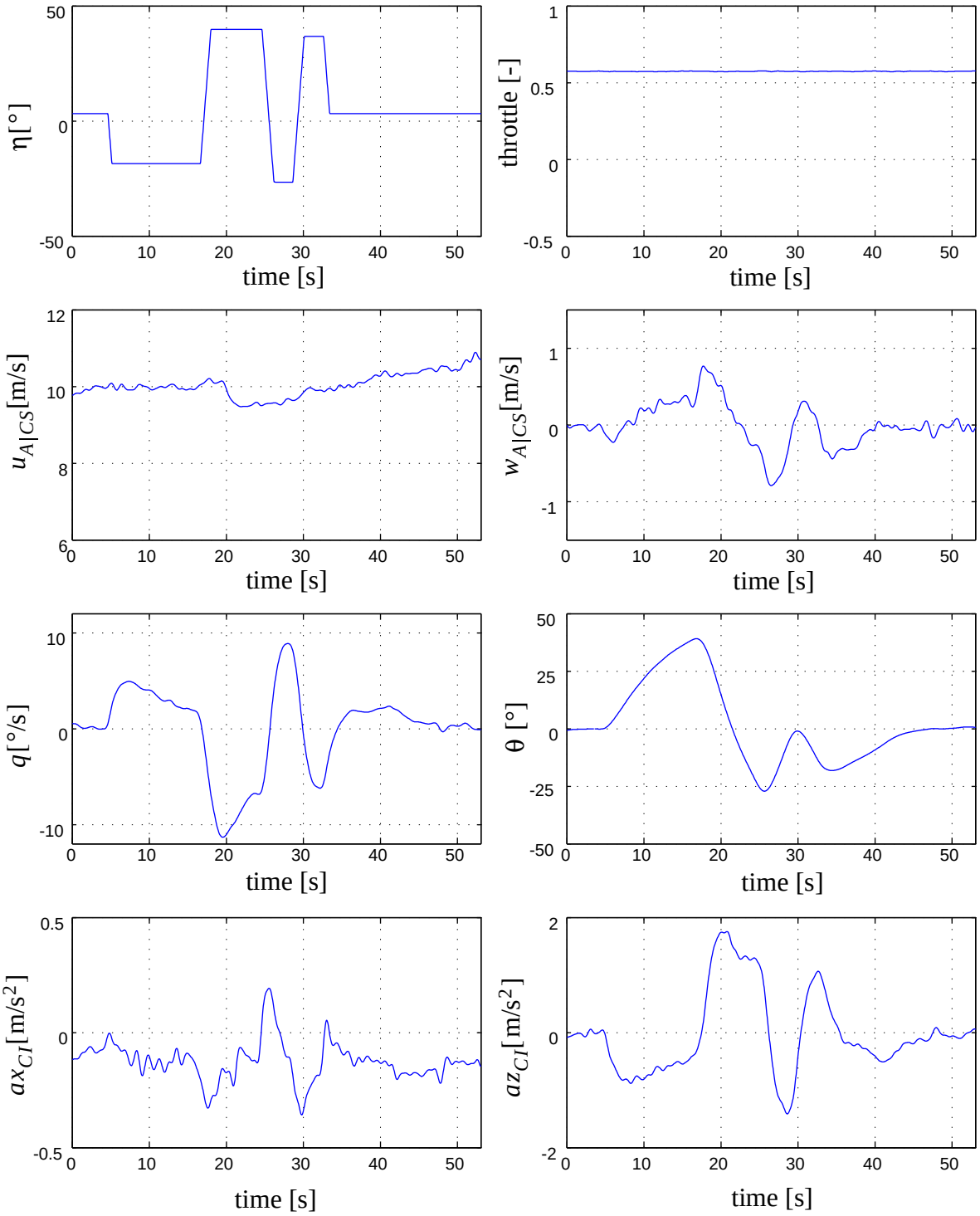

Figure C.8: Filtered measurements during F4S2e flight maneuver

Table C.5: Summary of longitudinal parameter values estimated with extended model

Parameter	Model Value	Output Error	Filter Error
Z_w	-0.404	-0.728 (0.049)	-0.825 (0.058)
Z_q	4.118	3.147 (0.483)	3.960 (0.619)
M_w	0.114	0.091 (0.018)	0.081 (0.016)
M_q	-0.641	-1.623 (0.072)	-1.634 (0.144)
M_θ	-0.016	-0.192 (0.021)	-0.28
Z_η	-0.135	-0.714 (0.079)	-0.652 (0.076)
M_η	-0.468	-0.271 (0.015)	-0.229 (0.023)
$b_{\dot{w}}$	-	0.016 (0.011)	0.011 (0.030)
$b_{\dot{q}}$	-	0.005 (0.013)	0.006 (0.005)
b_w	-	-0.011 (0.14)	-0.011 (0.009)
b_q	-	0.005 (0.020)	0.003 (0.017)
b_{az}	-	-0.049 (0.269)	-0.033 (0.263)
u_0	10.0	10.091 (0.338)	10.107 (0.22)
$\sigma_{\dot{w}}$	-	-	0.022 (0.008)
σ_q	-	-	0.002 (0.001)
Iterations	-	21	14
Eigenvalue	-1.15 0.052+/-0.16i	-1.78 -0.18 -0.32	-1.85 -0.19 -0.41
TIC: w q az_{CI}		 0.122 0.058 0.083	 0.012 0.003 0.021

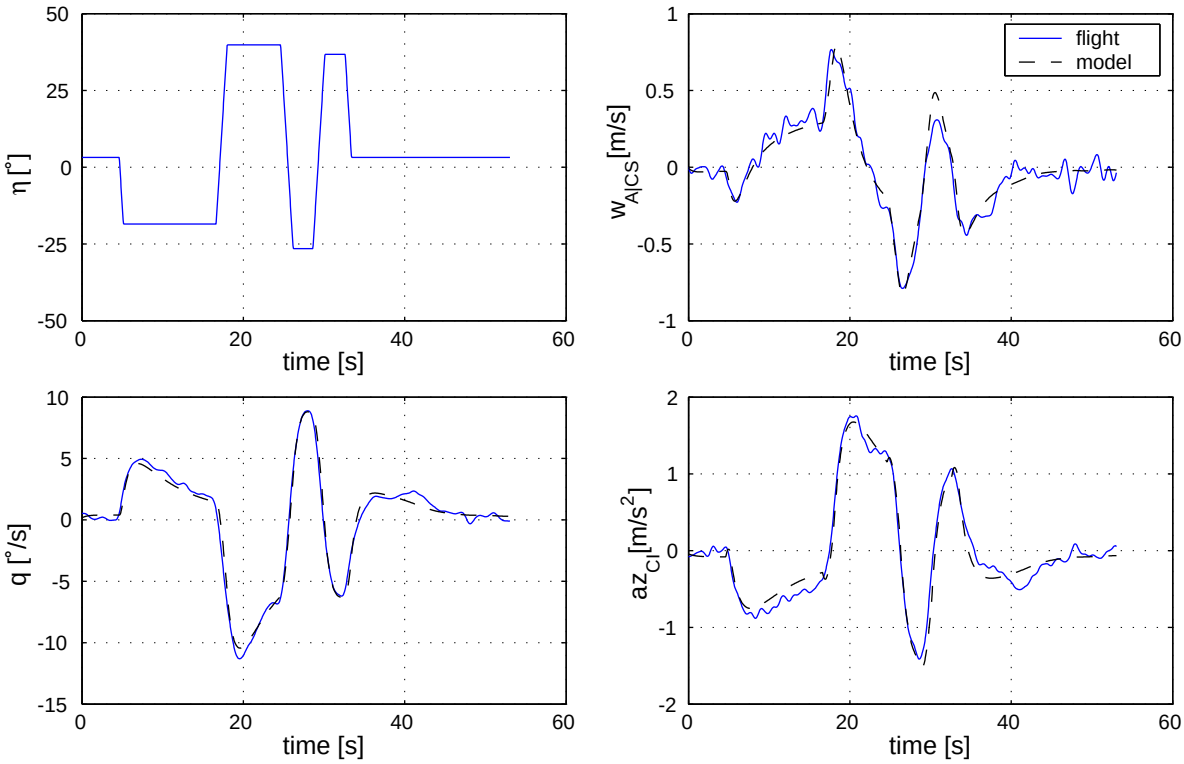

Figure C.9: Estimation results of F4S2e maneuver (Output-Error algorithm)

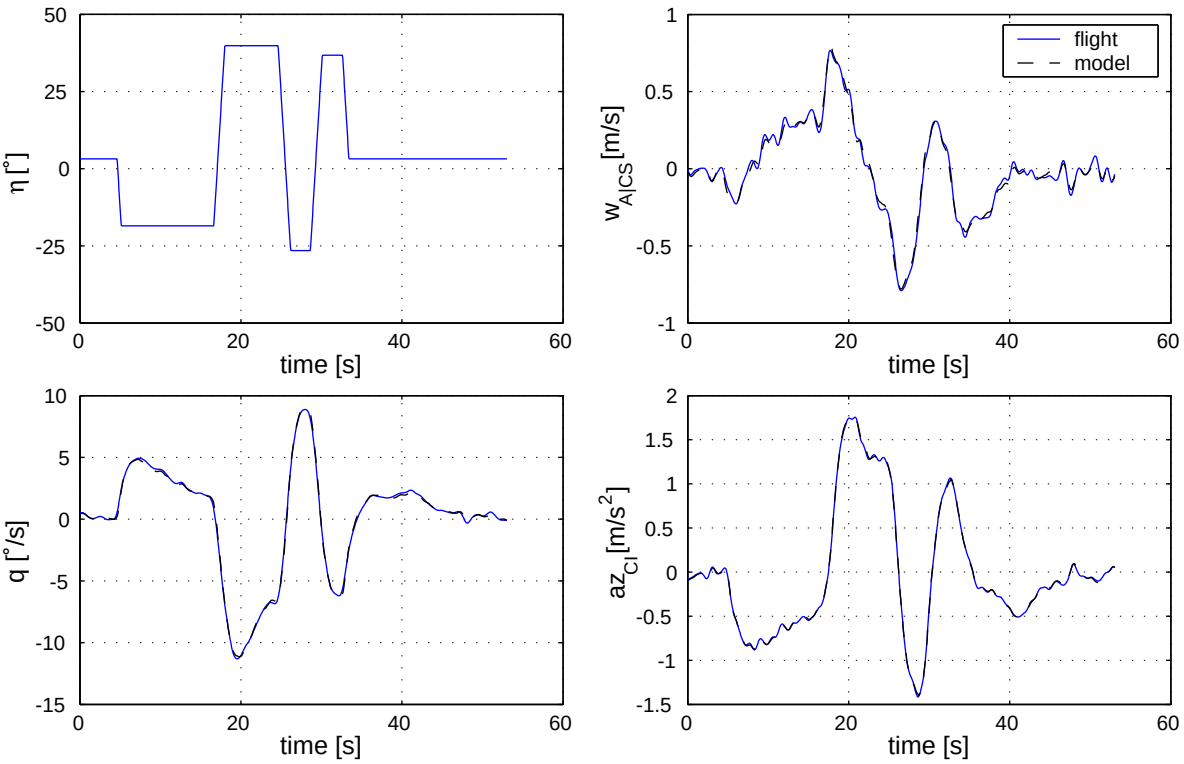

Figure C.10: Estimation results of F4S2e maneuver (Filter-Error algorithm)

C.3.3 Fight Record F4S3e

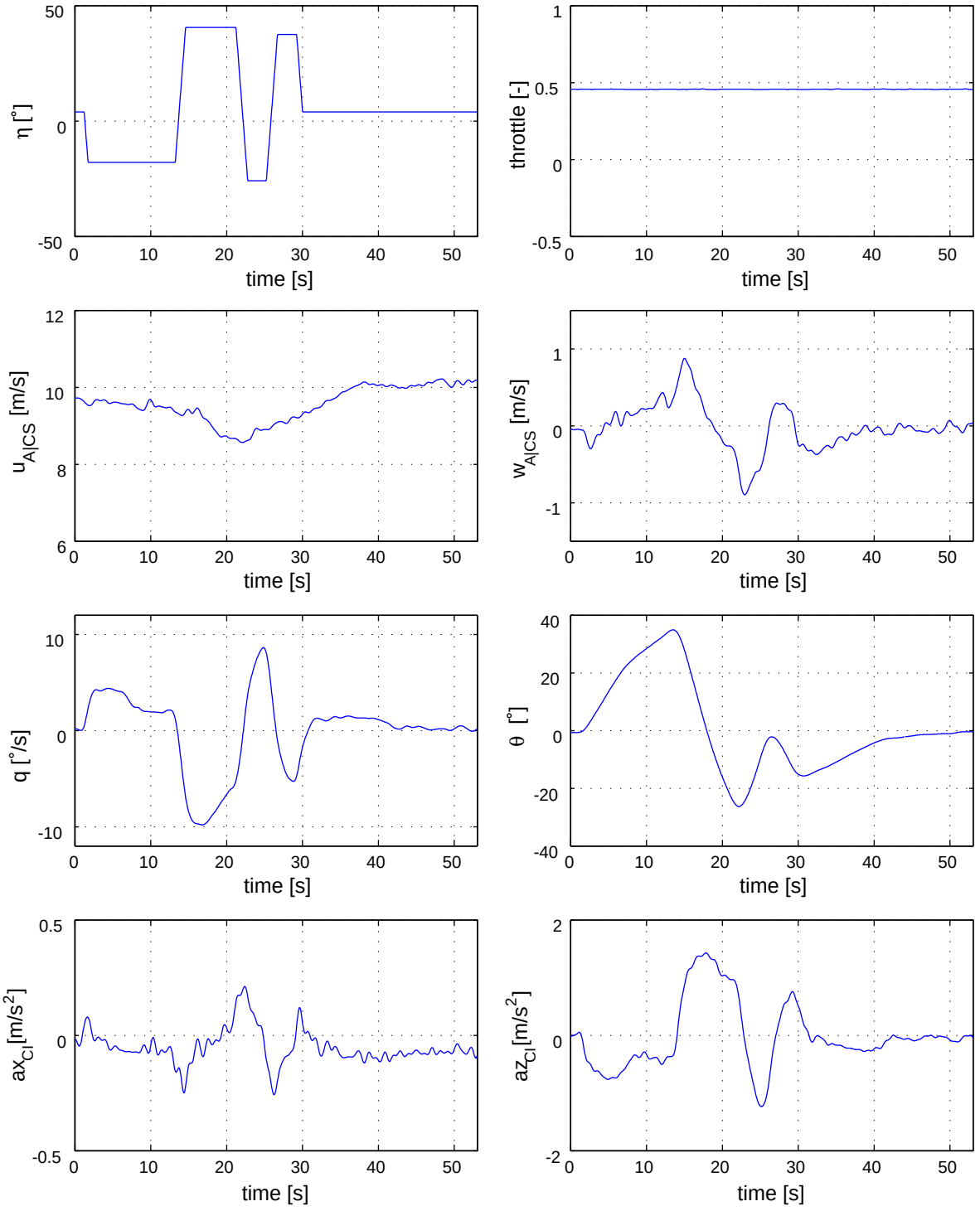

Figure C.11: Filtered measurements during F4S3e flight maneuver

Table C.6: Parameter values estimated from F4S3e record with extended longitudinal model

Parameter	Model Value	Output Error	Filter Error
Z_w	-0.376	-0.608 (0.038)	-0.672 (0.022)
Z_q	3.742	2.252 (0.37)	2.702 (0.313)
M_w	0.102	0.080 (0.006)	0.075 (0.007)
M_q	-0.599	-1.45 (0.049)	-1.41 (0.07)
M_θ	-0.137	-0.176 (0.018)	-0.18
Z_η	-1.128	-0.617 (0.052)	-0.582 (0.021)
M_η	-0.391	-0.244 (0.013)	-0.219 (0.010)
$b_{\dot{w}}$	-	-0.021 (0.076)	0.031 (0.025)
$b_{\dot{q}}$	-	0.006 (0.009)	0.008 (0.008)
b_w	-	-0.021 (0.144)	-0.029 (0.034)
b_q	-	0.003 (0.014)	0.0004 (0.011)
b_{az}	-	-0.027 (0.15)	0.011 (0.136)
u_0	9.20	9.16 (0.26)	9.09 (0.25)
$\sigma_{\dot{w}}$	-	-	0.036 (0.008)
σ_q	-	-	0.002 (0.001)
Iterations		14	10
Eigenvalue	-1.04 0.021 +/- 0.208i	-1.53 -0.24 +/- 0.017i	-1.52 -0.25 +/- 0.08i
TIC: w q az_{CI}		 0.117 0.040 0.066	 0.012 0.003 0.021

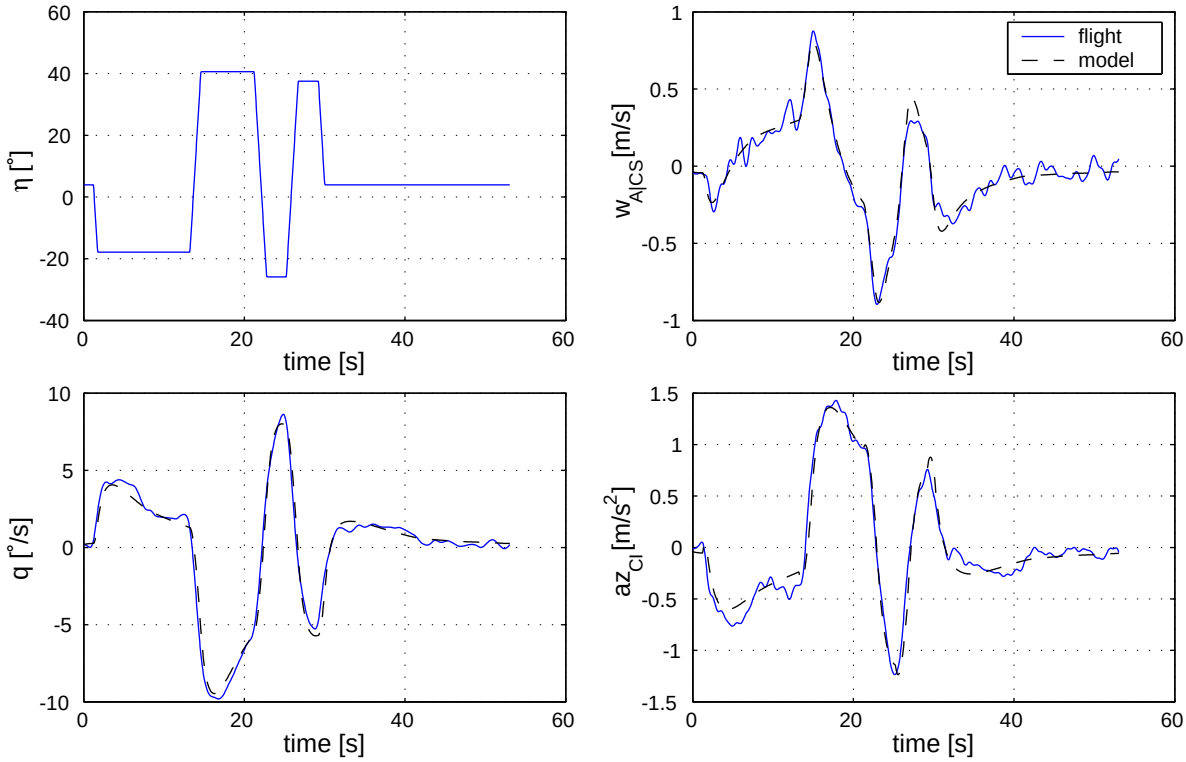

Figure C.12: Estimation results of F4S3e maneuver (Output-Error algorithm)

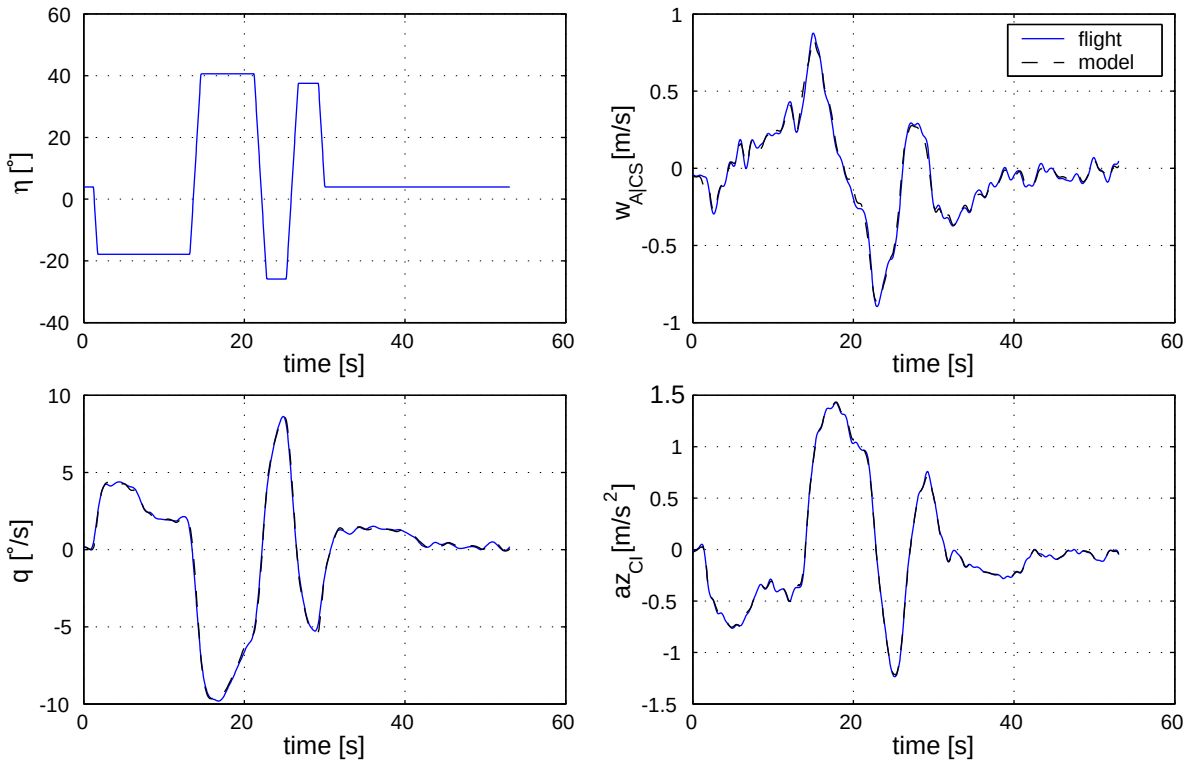

Figure C.13: Estimation results of F4S3e maneuver (Filter-Error algorithm)

C.3.4 Flight Record F4S4e

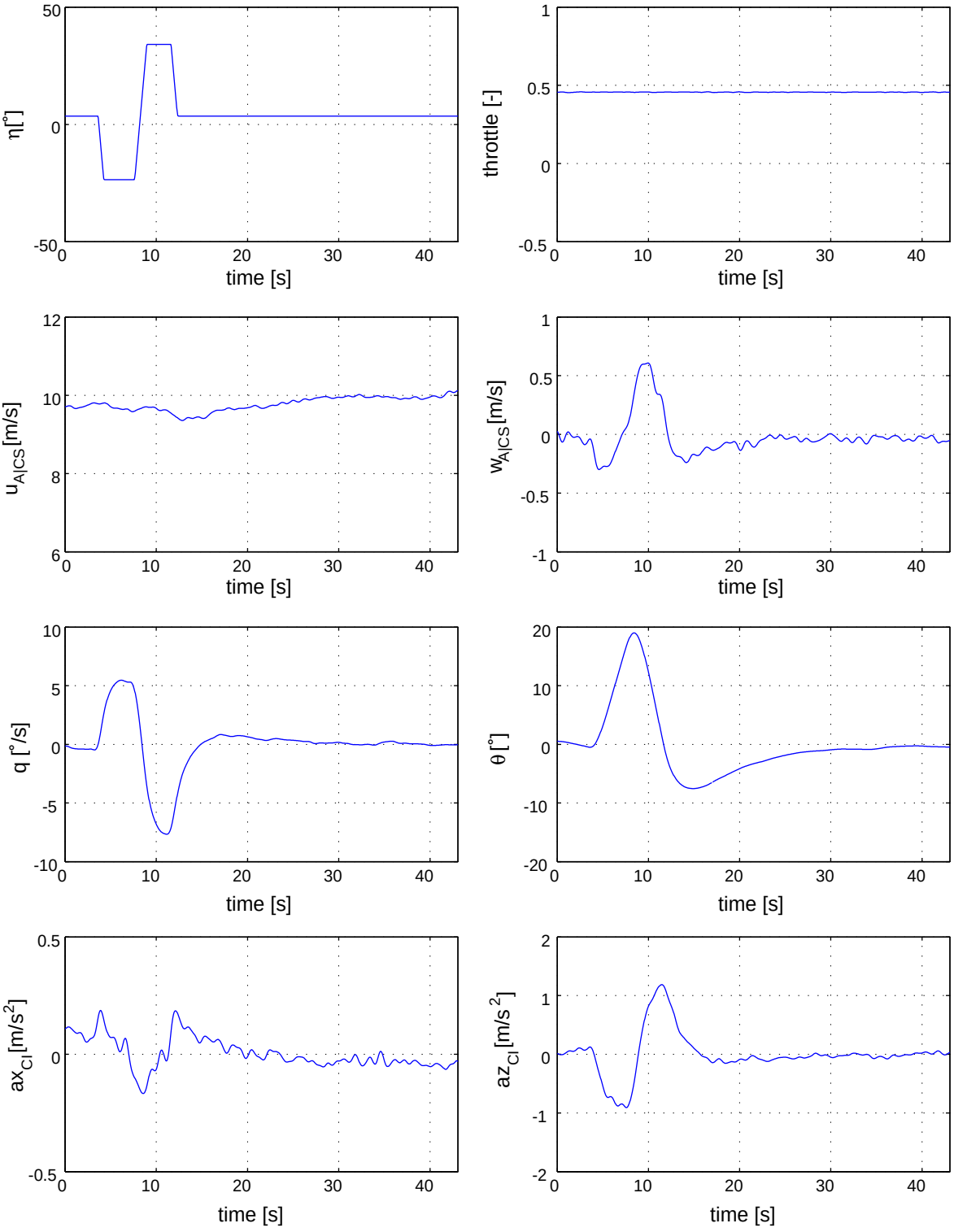

Figure C.14: Filtered measurements of F4S4e flight maneuver

Table C.7: Parameter values estimated from F4S4e record with extended longitudinal model

Parameter	Model Value	Output Error	Filter Error
Z_w	-0.3916	-0.659 (0.061)	-0.721 (0.088)
Z_q	3.95	2.757 (0.524)	3.256 (0.474)
M_w	0.109	0.069 (0.005)	0.067 (0.033)
M_q	-0.622	-1.379 (0.053)	-1.299 (0.274)
M_θ	-0.137	-0.184 (0.021)	-0.18
Z_η	-1.25	-0.597 (0.069)	-0.547 (0.082)
M_η	-0.433	-0.225 (0.007)	-0.205 (0.033)
$b_{\dot{w}}$	-	-0.007 (0.050)	-0.010 (0.029)
$b_{\dot{q}}$	-	0.012 (0.004)	0.008 (0.003)
b_w	-	0.020 (0.078)	0.032 (0.025)
b_q	-	-0.008 (0.007)	-0.005 (0.008)
b_{az}	-	0.078 (0.084)	0.034 (0.087)
u_0	9.67	9.693 (0.276)	9.572 (0.314)
$\sigma_{\dot{w}}$	-	-	0.015 (0.005)
σ_q	-	-	0.002 (0.008)
Iterations	-	15	12
Eigenvalue	-1.10 0.035 +/- 0.204i	-1.48 -0.27 +/- 0.08i	-1.46 -0.28 +/- 0.1i
TIC: w q az_{CI}		 0.090 0.025 0.049	 0.012 0.003 0.021

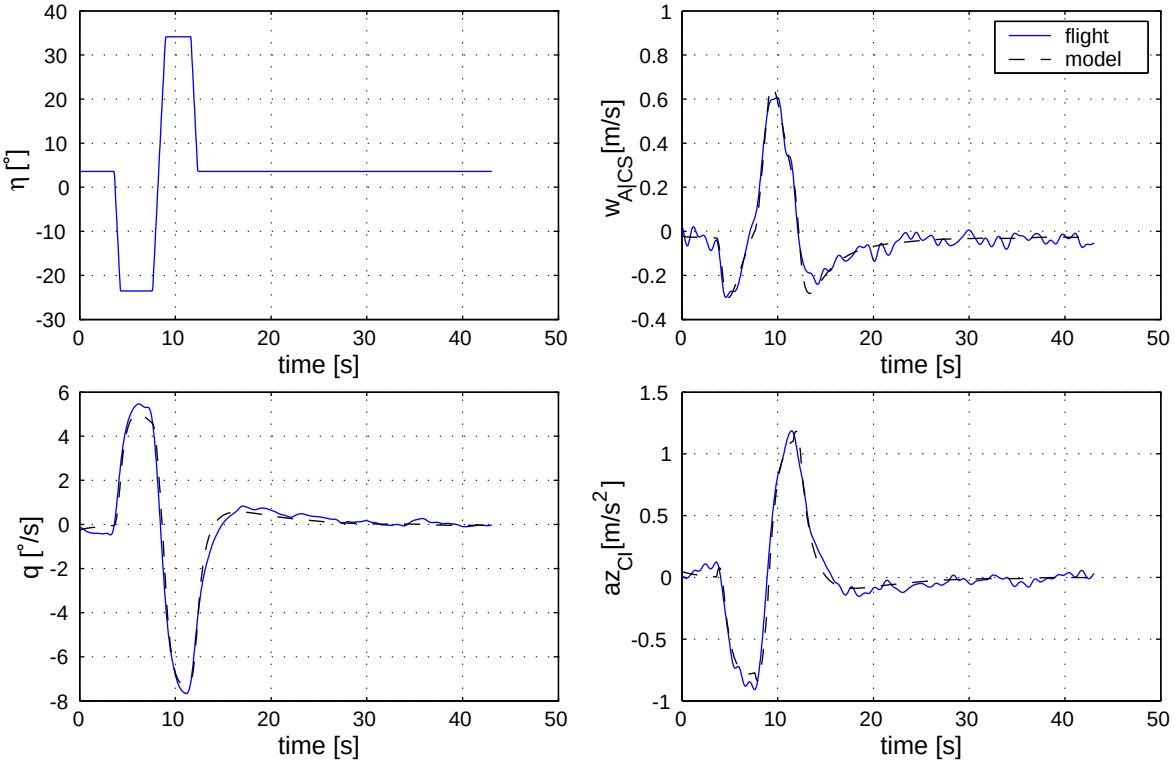

Figure C.15: Estimation results of F4S4e maneuver (Output-Error algorithm)

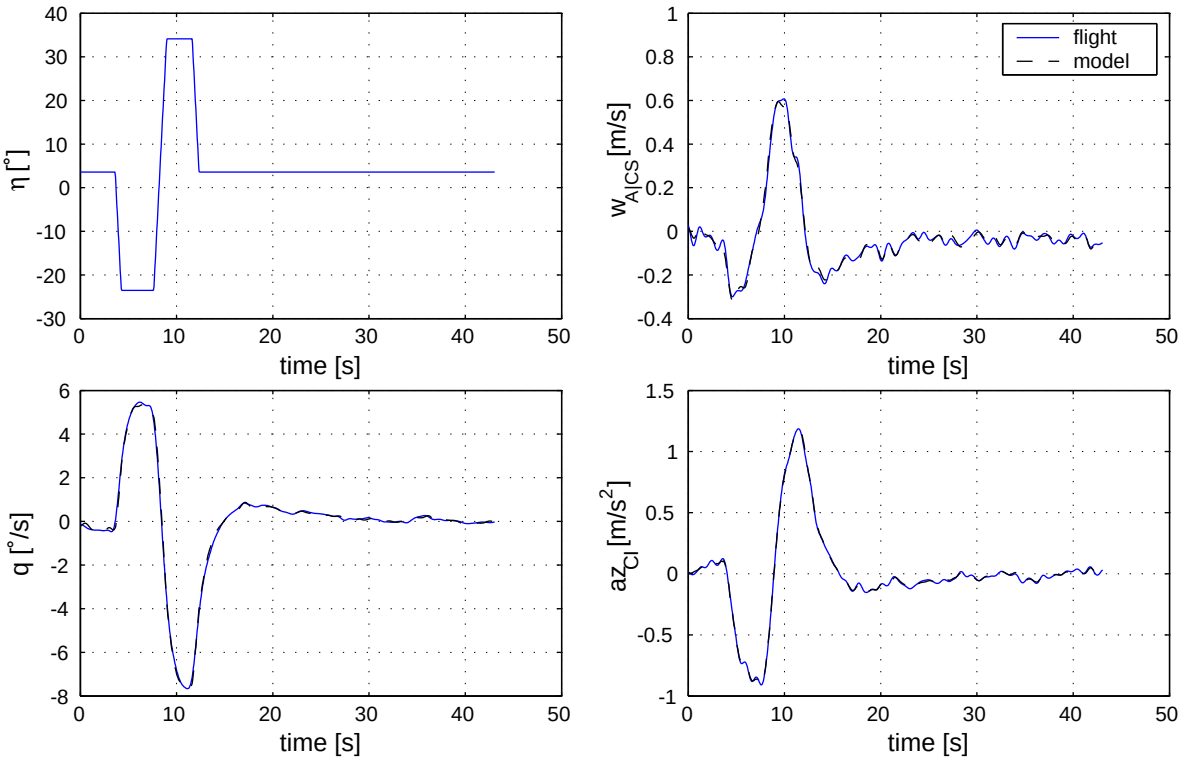

Figure C.16: Estimation results of F4S4e maneuver (Filter-Error algorithm)

C.3.5 Flight Record F4S5e

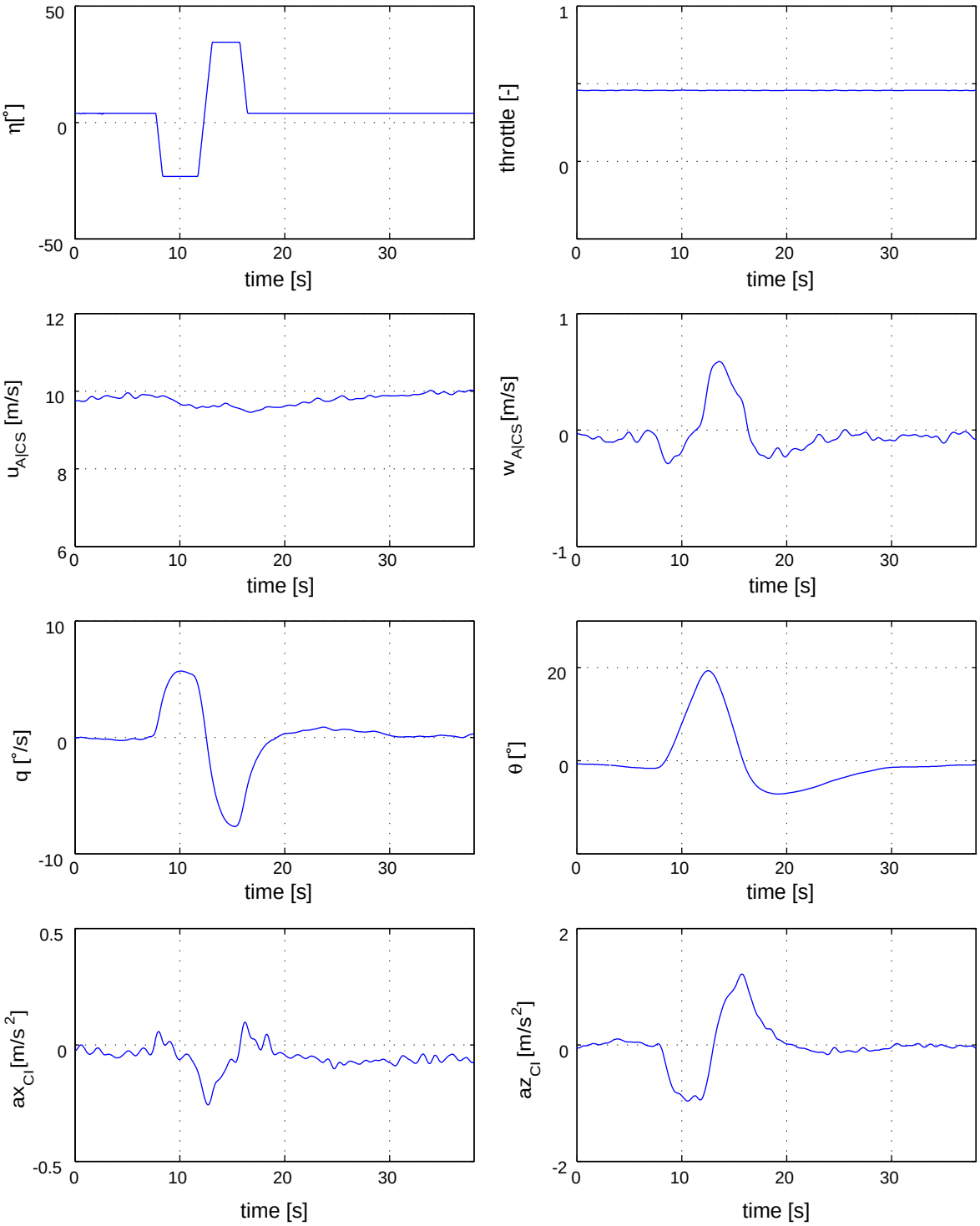

Figure C.17: Filtered measurements during F4S5e flight maneuver

Table C.8: Parameter values estimated from F4S5e record with extended longitudinal model

Parameter	Model Value	Output Error	Filter Error
Z_w	-0.393	-0.692 (0.072)	-0.833 (0.089)
Z_q	3.977	2.939 (0.648)	3.065 (0.639)
M_w	0.11	0.069 (0.006)	0.067 (0.022)
M_q	-0.625	-1.402 (0.065)	-1.492 (0.130)
M_θ	-0.137	-0.186 (0.021)	-0.18
Z_η	-1.266	-0.641 (0.087)	-0.530 (0.091)
M_η	-0.438	-0.240 (0.008)	-0.219 (0.021)
$b_{\dot{w}}$	-	0.043 (0.061)	0.024 (0.033)
$b_{\dot{q}}$	-	0.011 (0.004)	0.008 (0.005)
b_w	-	-0.047 (0.089)	-0.035 (0.019)
b_q	-	-0.003 (0.007)	0.001 (0.008)
b_{az}	-	0.066 (0.089)	0.073 (0.121)
u_0	9.7	9.74 (0.318)	9.712 (0.29)
$\sigma_{\dot{w}}$	-	-	0.015 (0.005)
σ_q	-	-	0.001 (0.0006)
Iterations	-	14	8
Eigenvalue	-1.11 0.035+/-0.203i	-1.52 -0.26+/-0.05i	-1.57 -0.16 -0.60
TIC: w q az_{CI}		 0.098 0.026 0.061	 0.012 0.003 0.021

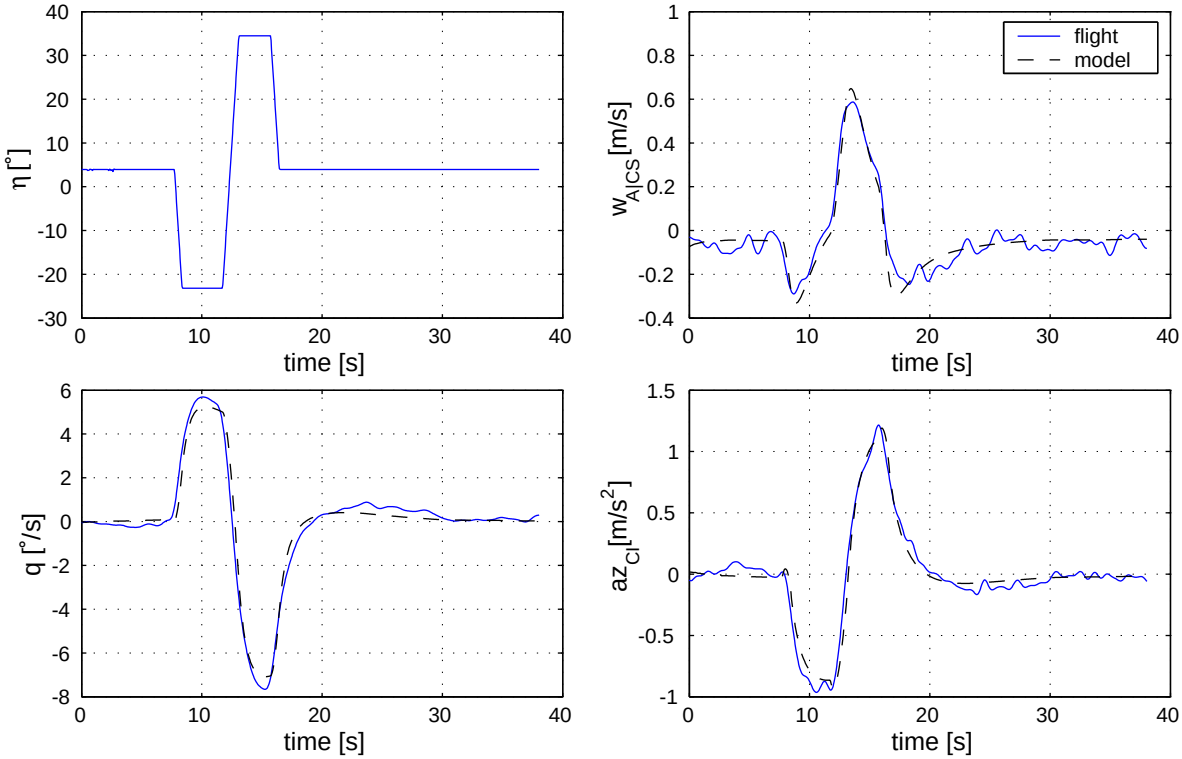

Figure C.18: Estimation results of F4S5e maneuver (Output-Error algorithm)

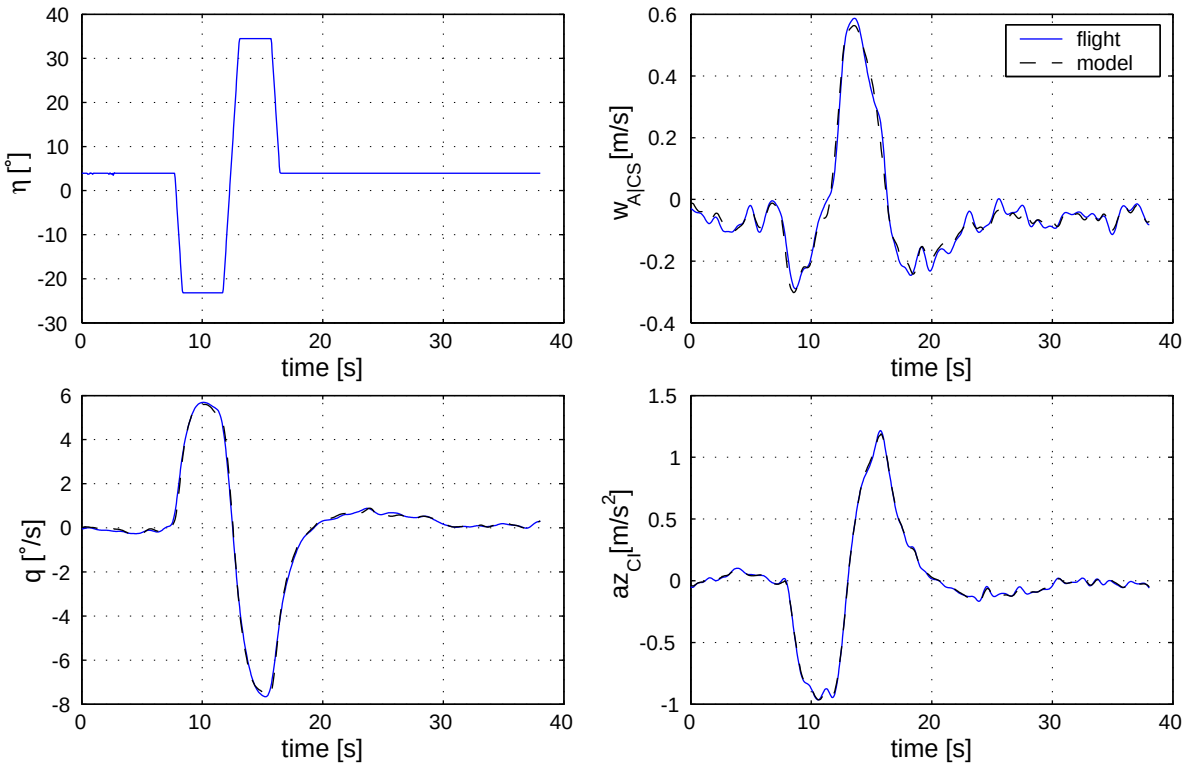

Figure C.19: Estimation results of F4S5e maneuver (Filter-Error algorithm)

C.3.6 Flight Record F4S6e

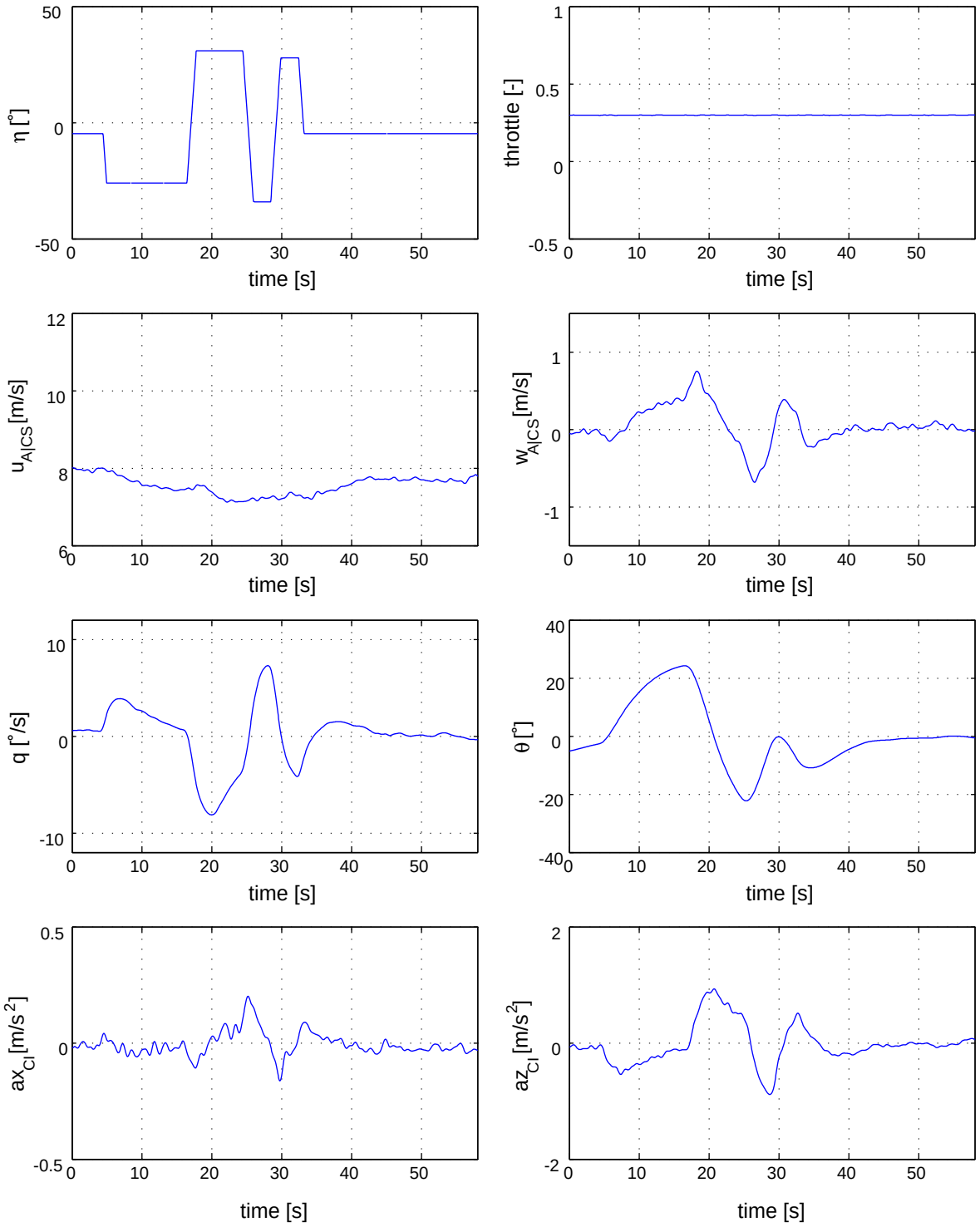

Figure C.20: Filtered measurements of F4S6e flight maneuver

Table C.9: Parameter values estimated from F4S6e record with extended longitudinal model

Parameter	Model Value	Output Error	Filter Error
Z_w	-0.321	-0.52 (0.031)	-0.448 (0.039)
Z_q	2.931	1.519 (0.231)	1.997 (0.220)
M_w	0.076	0.054 (0.004)	0.057 (0.011)
M_q	-0.517	-1.117 (0.028)	-1.028 (0.093)
M_θ	-0.137	-0.187 (0.015)	-0.18
Z_η	-0.674	-0.505 (0.047)	-0.418 (0.041)
M_η	-0.233	-0.162 (0.006)	-0.145 (0.012)
$b_{\dot{w}}$	-	-0.059 (0.038)	-0.013 (0.012)
$b_{\dot{q}}$	-	-0.011 (0.014)	-0.008 (0.006)
b_w	-	-0.034 (0.135)	-0.054 (0.012)
b_q	-	0.007 (0.009)	0.009 (0.009)
b_{az}	-	-0.076 (0.087)	-0.092 (0.089)
u_0	7.4	7.385 (0.197)	7.504 (0.374)
$\sigma_{\dot{w}}$	-	-	0.013 (0.004)
σ_q	-	-	0.001 (0.0005)
Iterations	-	33	12
Eigenvalue	-0.807 -0.031+/-0.224i	-1.08 -0.27+/-0.12i	-1.04 0.21 +/- 0.18i
TIC: w q az_{CI}		 0.074 0.044 0.074	 0.012 0.003 0.021

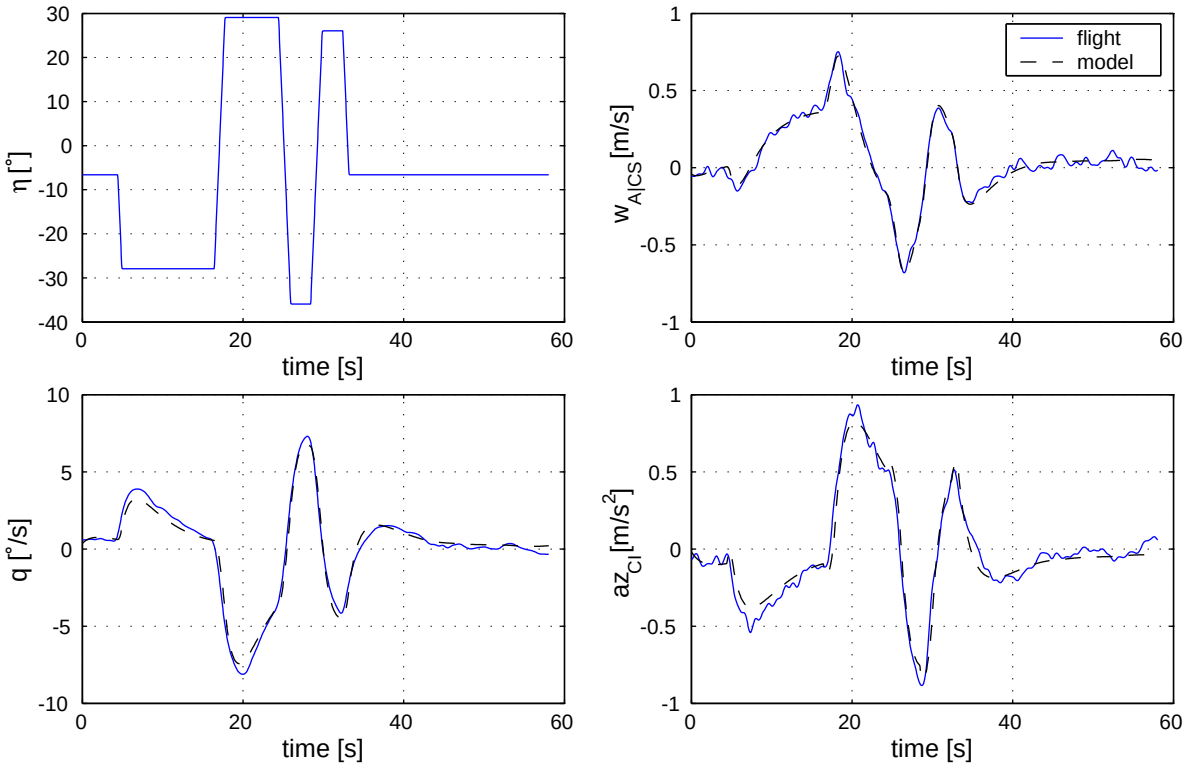

Figure C.21: Estimation results of F4S6e maneuver (Output-Error algorithm)

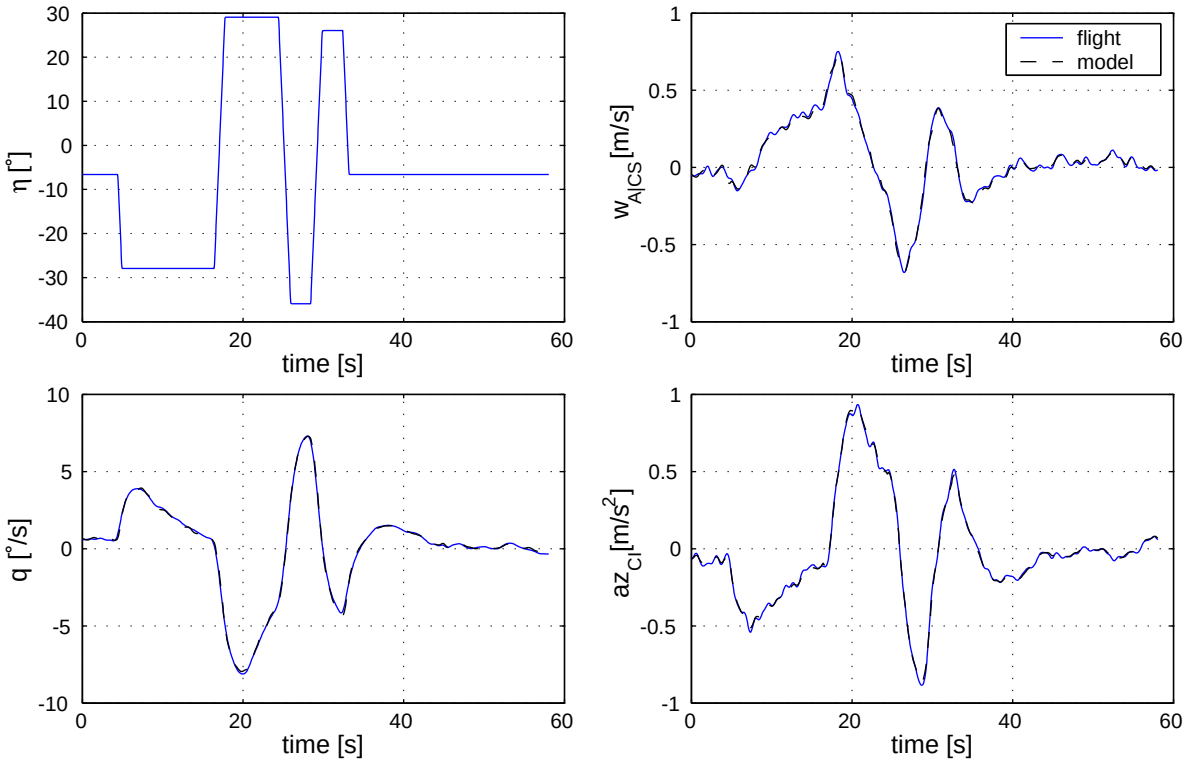

Figure C.22: Estimation results of F4S6e maneuver (Filter-Error algorithm)

C.3.7 Flight Record F4S7e

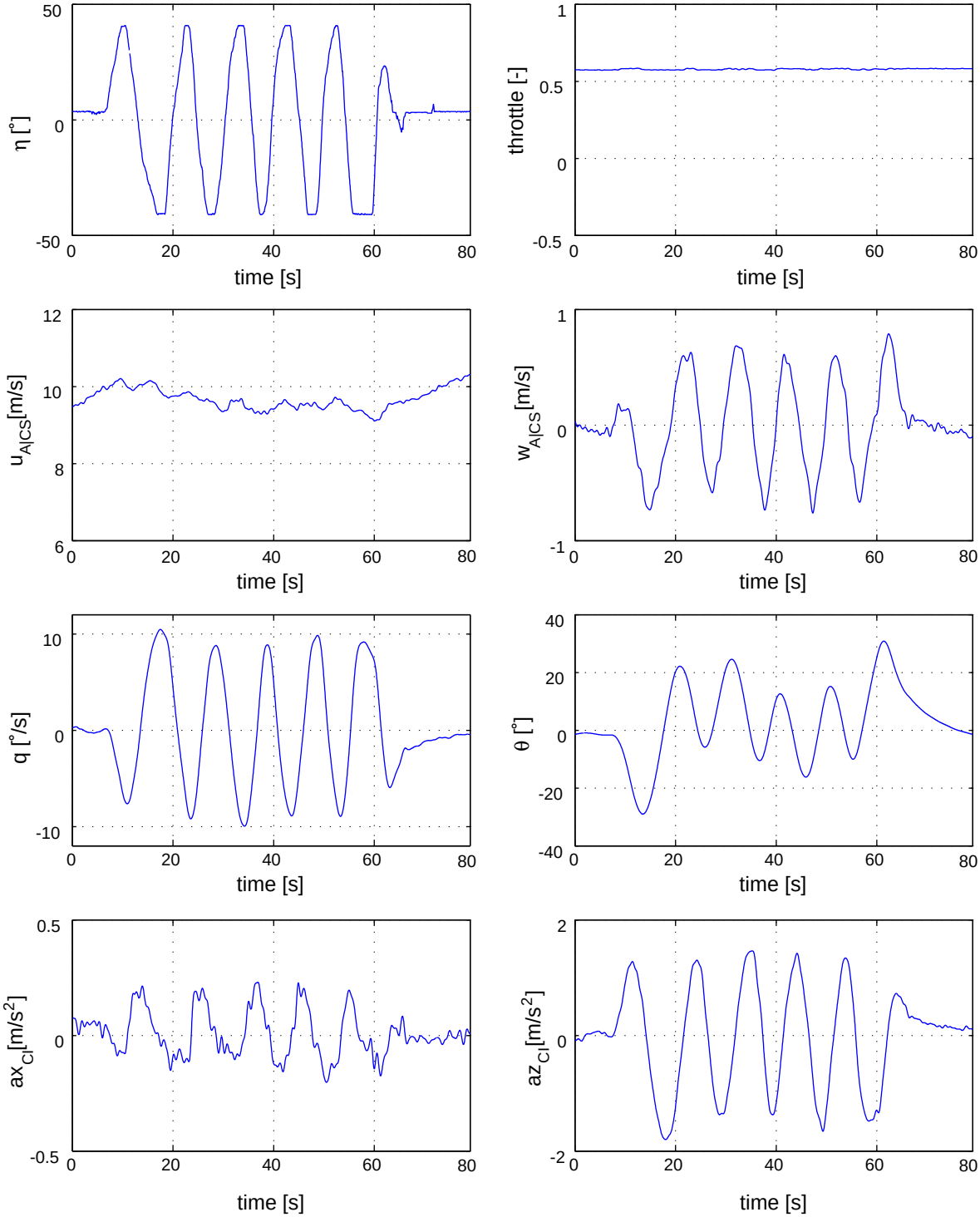

Figure C.23: Filtered measurements of F4S7e flight maneuver

Table C.10: Parameter values estimated from F4S7e record with extended longitudinal model

Parameter	Model Value	Output Error	Filter Error
Z_w	-0.402	-0.702 (0.033)	-0.775 (0.044)
Z_q	4.096	2.84 (0.360)	3.59 (0.238)
M_w	0.113	0.074 (0.007)	0.081 (0.012)
M_q	-0.638	-1.622 (0.077)	-1.683 (0.117)
M_θ	-0.137	-0.181 (0.139)	-0.18
Z_η	-1.338	-0.67 (0.048)	-0.580 (0.023)
M_η	-0.464	-0.262 (0.009)	-0.226 (0.014)
$b_{\dot{w}}$	-	0.004 (0.063)	0.004 (0.131)
$b_{\dot{q}}$	-	0.003 (0.009)	0.004 (0.006)
b_w	-	-0.016 (0.103)	-0.045 (0.026)
b_q	-	0.005 (0.013)	0.002 (0.008)
b_{az}	-	-0.072 (0.162)	-0.076 (0.110)
u_0	10.0	10.028 (0.155)	9.997 (0.256)
$\sigma_{\dot{w}}$	-	-	0.020 (0.004)
σ_q	-	-	0.002 (0.0008)
Iterations	-	20	14
Eigenvalue	-1.14 0.0417+/-0.201i	-1.72 -0.43 -0.17	-1.85 -0.43 -0.18
TIC: w q az_{CI}		 0.067 0.037 0.052	 0.012 0.003 0.021

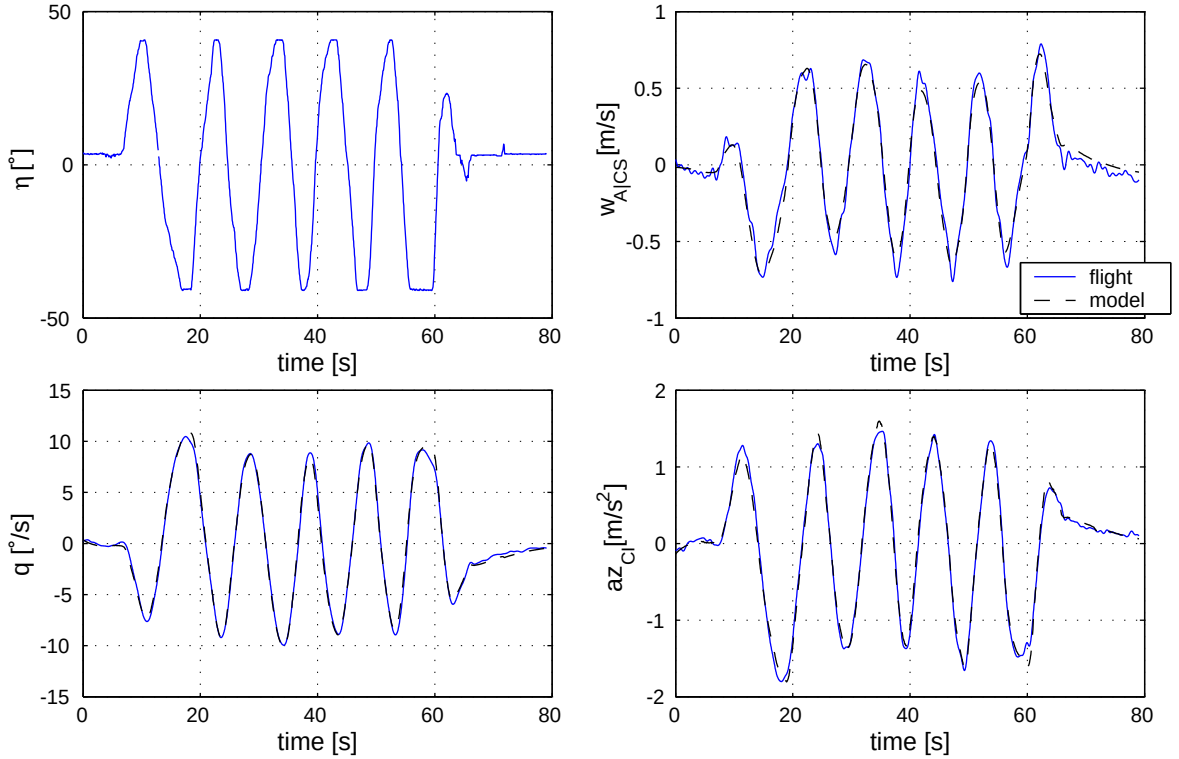

Figure C.24: Estimation results of F4S7e maneuver (Output-Error algorithm)

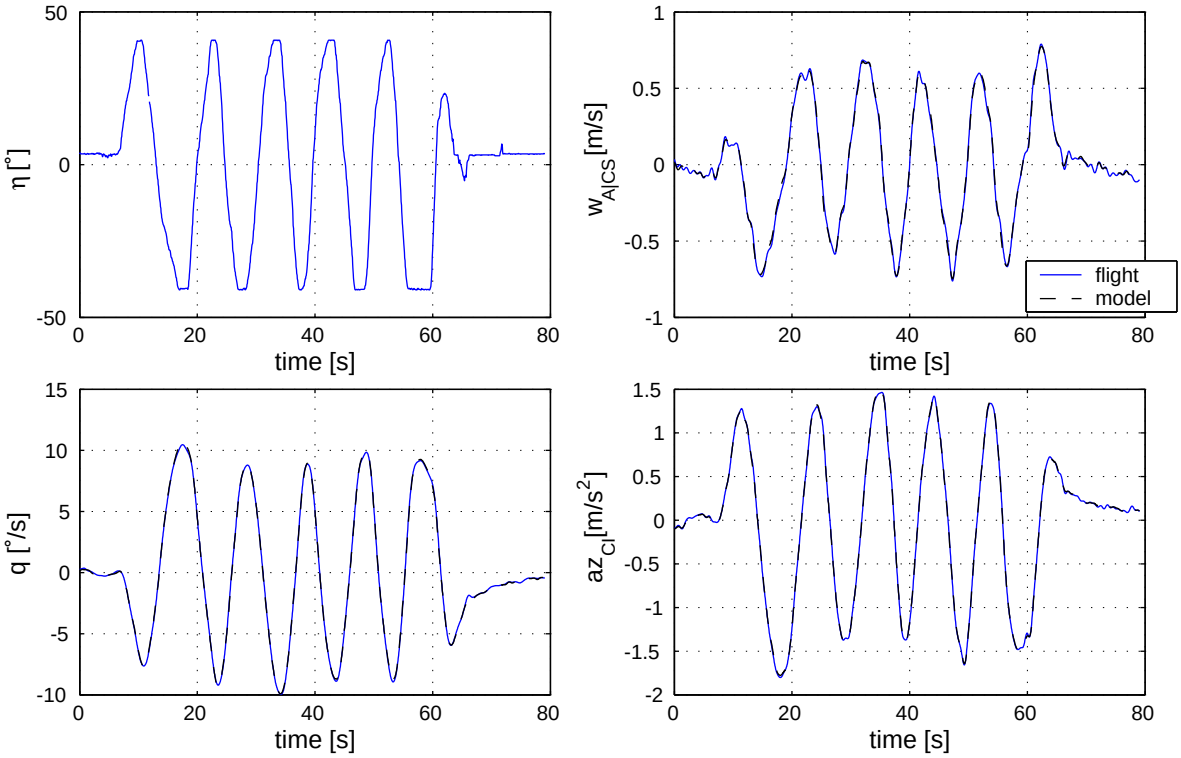

Figure C.25: Estimation results of F4S7e maneuver (Filter-Error algorithm)

C.3.8 Flight Record F5S9e

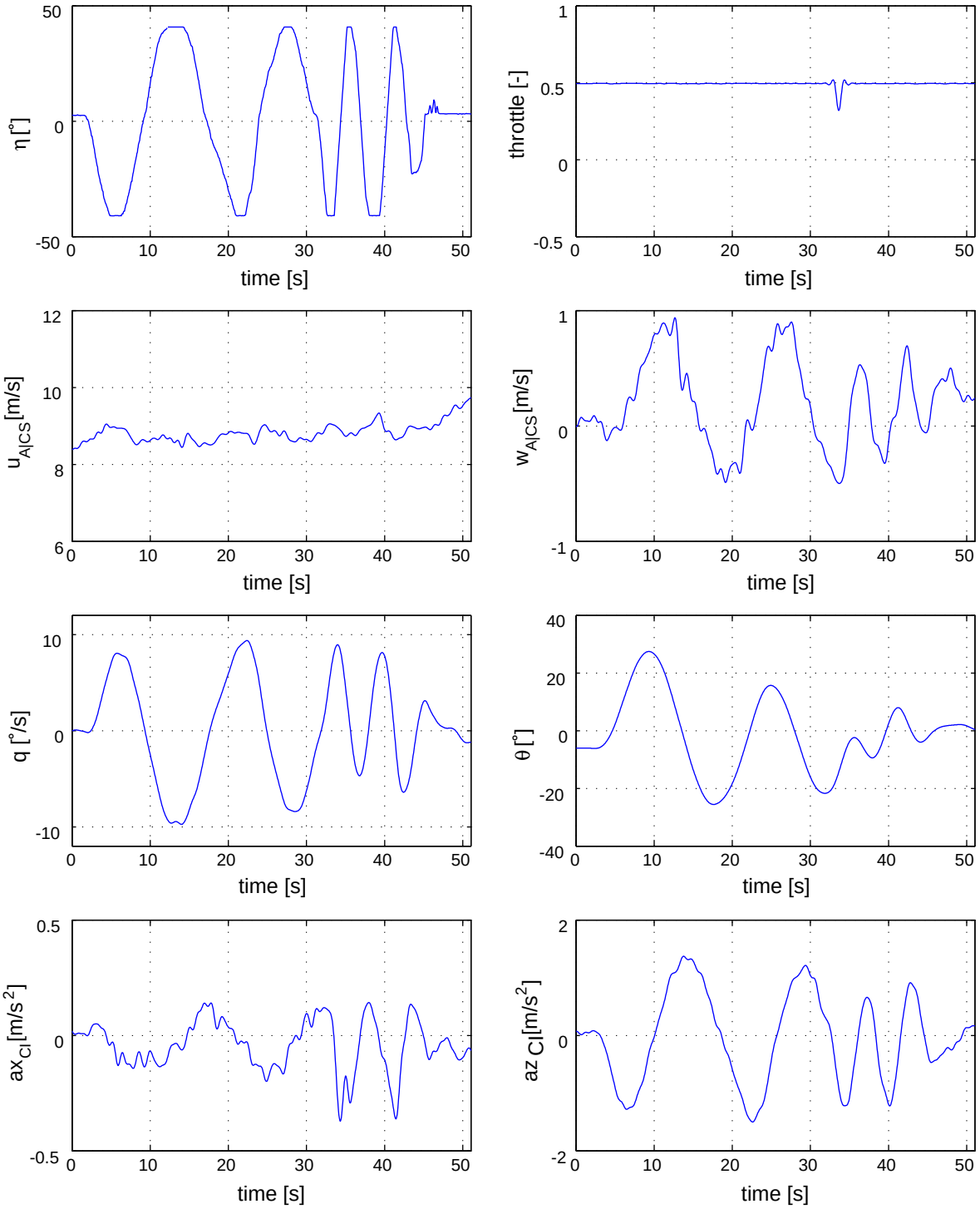

Figure C.26: Filtered measurements of F5S9e flight maneuver

Table C.11: Parameter values estimated from F5S9e record with extended longitudinal model

Parameter	Model Value	Output Error	Filter Error
Z_w	-0.368	-0.664 (0.062)	-0.737 (0.052)
Z_q	3.63	2.187 (0.621)	3.116 (0.728)
M_w	0.099	0.060 (0.008)	0.060 (0.012)
M_q	-0.587	-1.237 (0.083)	-1.299 (0.113)
M_θ	-0.016	-0.192 (0.021)	-0.18
Z_η	-1.065	-0.629 (0.063)	-0.540 (0.059)
M_η	-0.369	-0.223 (0.014)	-0.174 (0.012)
$b_{\dot{w}}$	-	0.124 (0.105)	0.132 (0.084)
$b_{\dot{q}}$	-	0.018 (0.017)	0.012 (0.018)
b_w	-	0.047 (0.144)	0.011 (0.044)
b_q	-	-0.005 (0.023)	-0.001 (0.037)
b_{az}	-	0.137 (0.26)	0.100 (0.28)
u_0	9.0	8.881 (0.275)	8.941 (0.549)
$\sigma_{\dot{w}}$	-	-	0.035 (0.11)
σ_q	-	-	0.003 (0.001)
Iterations	-	16	14
Eigenvalue	-1.01 0.014 +/- 0.210i	-1.29 -0.30 +/- 0.09i	-1.43 -0.30 +/- 0.07i
TIC: w q az_{CI}		 0.134 0.058 0.081	 0.012 0.003 0.021

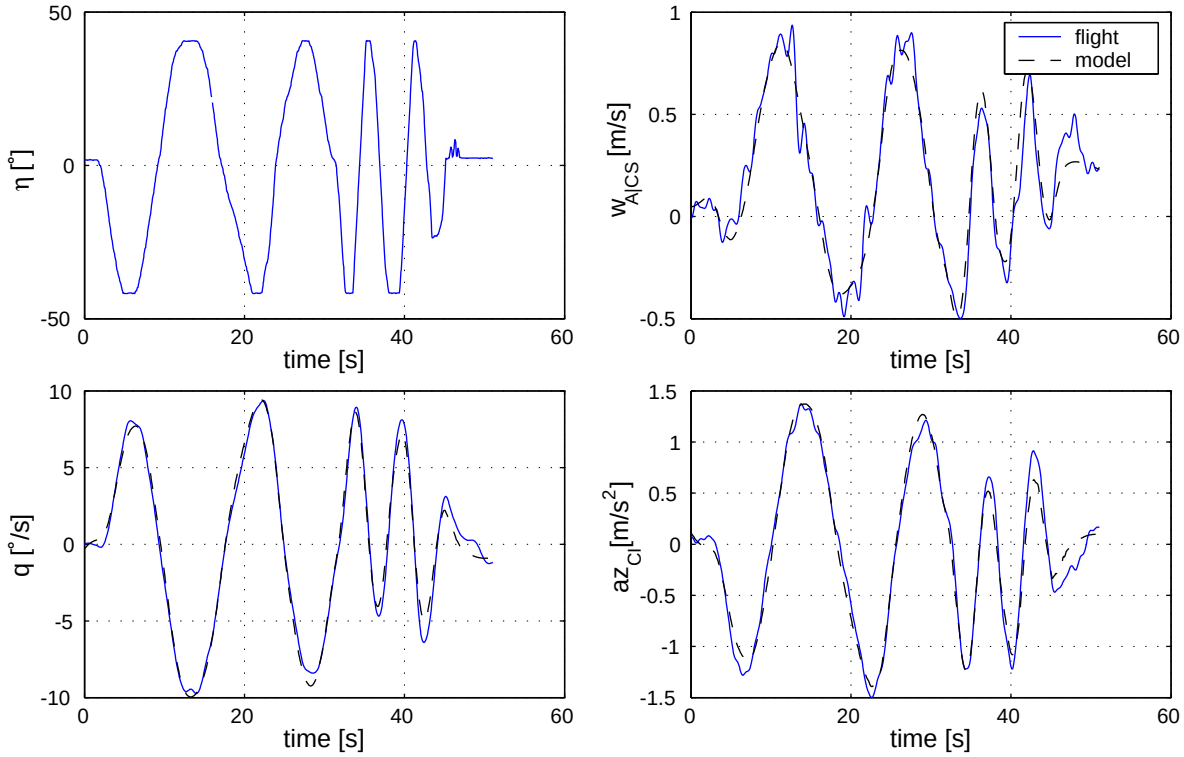

Figure C.27: Estimation results of F5S9e maneuver (Output-Error algorithm)

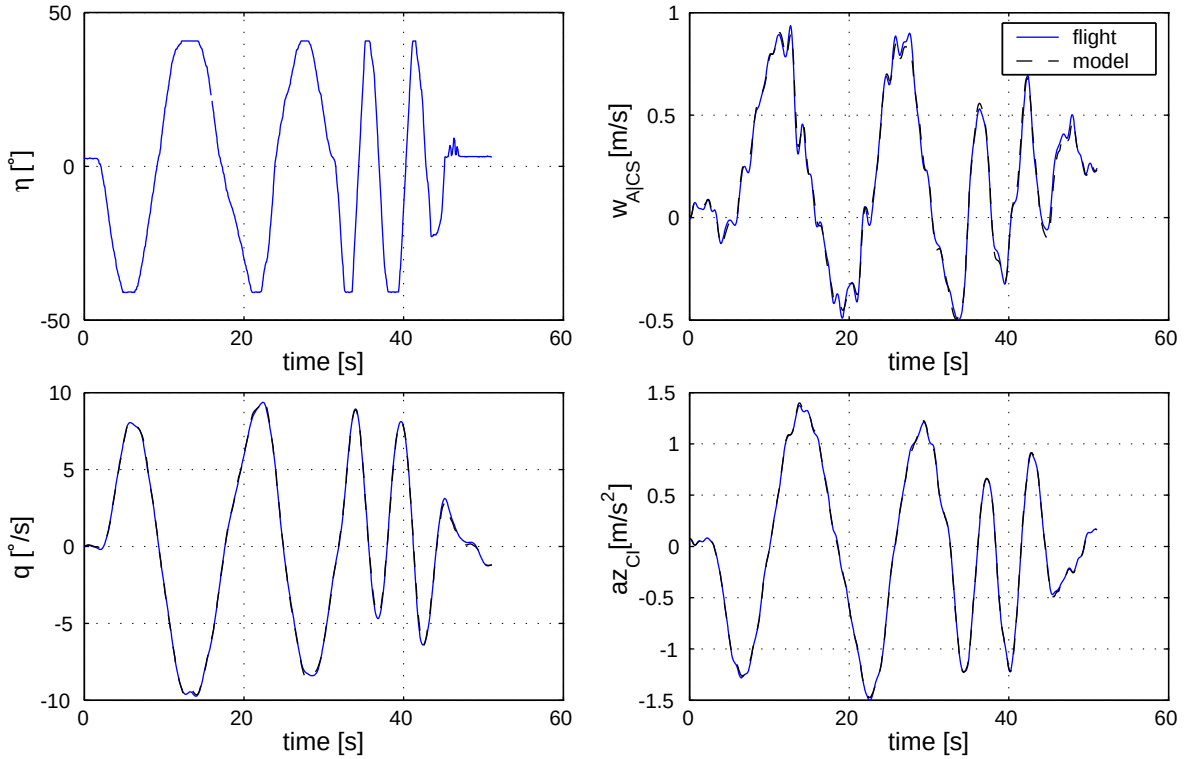

Figure C.28: Estimation results of F5S9e maneuver (Filter-Error algorithm)

C.3.9 Flight Record F5S12e

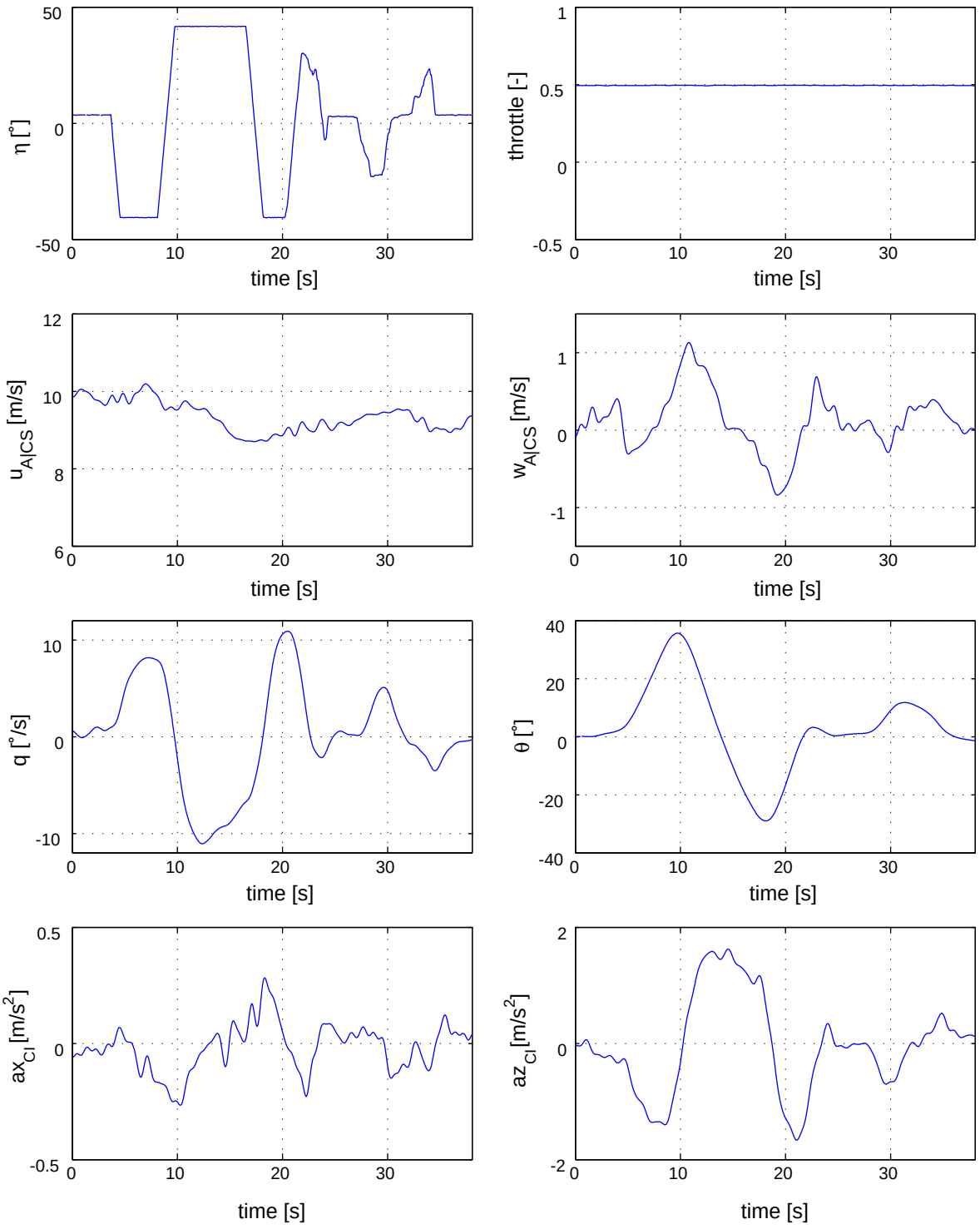

Figure C.29: Filtered measurements of F5S12e flight maneuver

Table C.12: Parameter values estimated from F5S12e record with extended longitudinal model

Parameter	Model Value	Output Error	Filter Error
Z_w	-0.389	-0.667 (0.074)	-0.710 (0.068)
Z_q	3.919	3.107 (0.781)	3.327 (1.031)
M_w	0.108	0.072 (0.013)	0.078 (0.021)
M_q	-0.618	-1.413 (0.138)	-1.493 (0.206)
M_θ	-0.137	-0.193 (0.031)	-0.18
Z_η	-1.23	-0.489 (0.094)	-0.479 (0.085)
M_η	-0.426	-0.231 (0.020)	-0.189 (0.026)
$b_{\dot{w}}$	-	0.042 (0.143)	0.124 (0.105)
$b_{\dot{q}}$	-	-0.004 (0.013)	-0.004 (0.015)
b_w	-	0.030 (0.216)	0.08 (0.055)
b_q	-	0.014 (0.018)	0.010 (0.020)
b_{az}	-	-0.115 (0.227)	0.093 (0.138)
u_0	9.6	9.559 (0.282)	9.536 (0.21)
$\sigma_{\dot{w}}$	-	-	0.047 (0.119)
σ_q	-	-	0.003 (0.001)
Iterations	-	13	9
Eigenvalue	-1.09 0.031+/-0.020i	-1.54 -0.27 +/- 0.1i	-1.66 -0.27 +/- 0.04i
TIC: w q az_{CI}		 0.141 0.043 0.065	 0.012 0.003 0.021

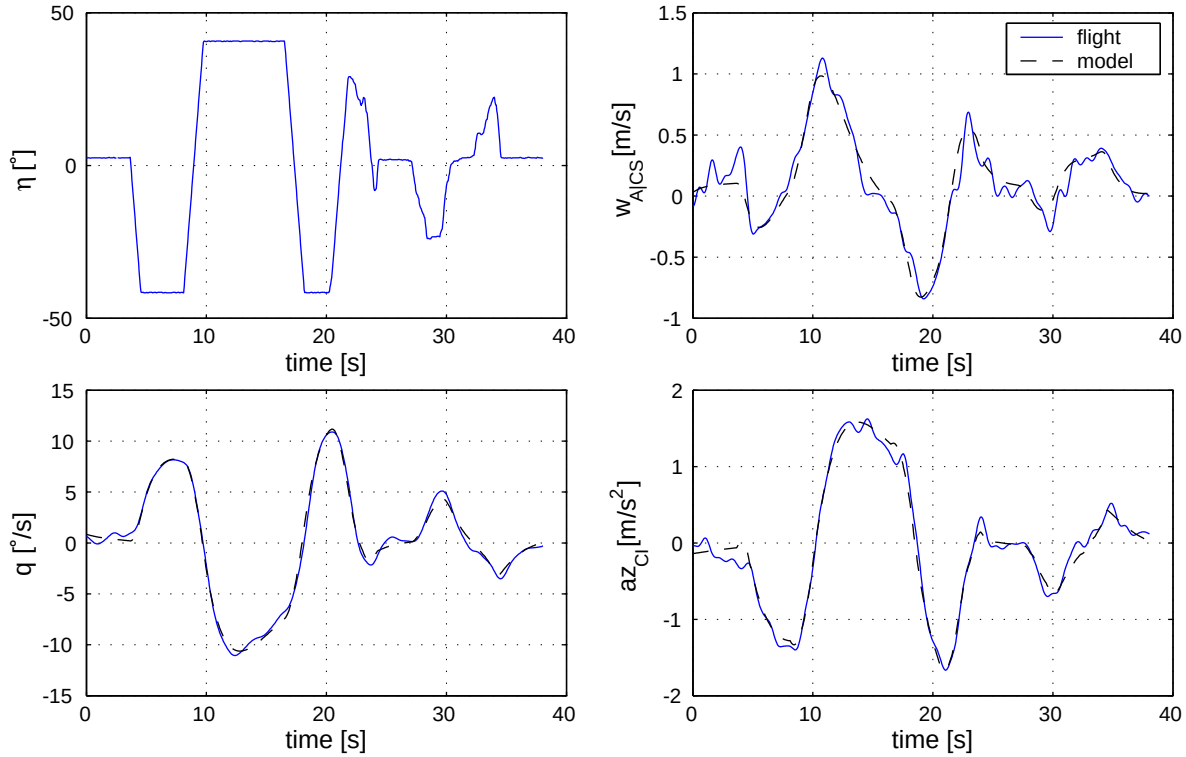

Figure C.30: Estimation results of F5S12e maneuver (Output-Error algorithm)

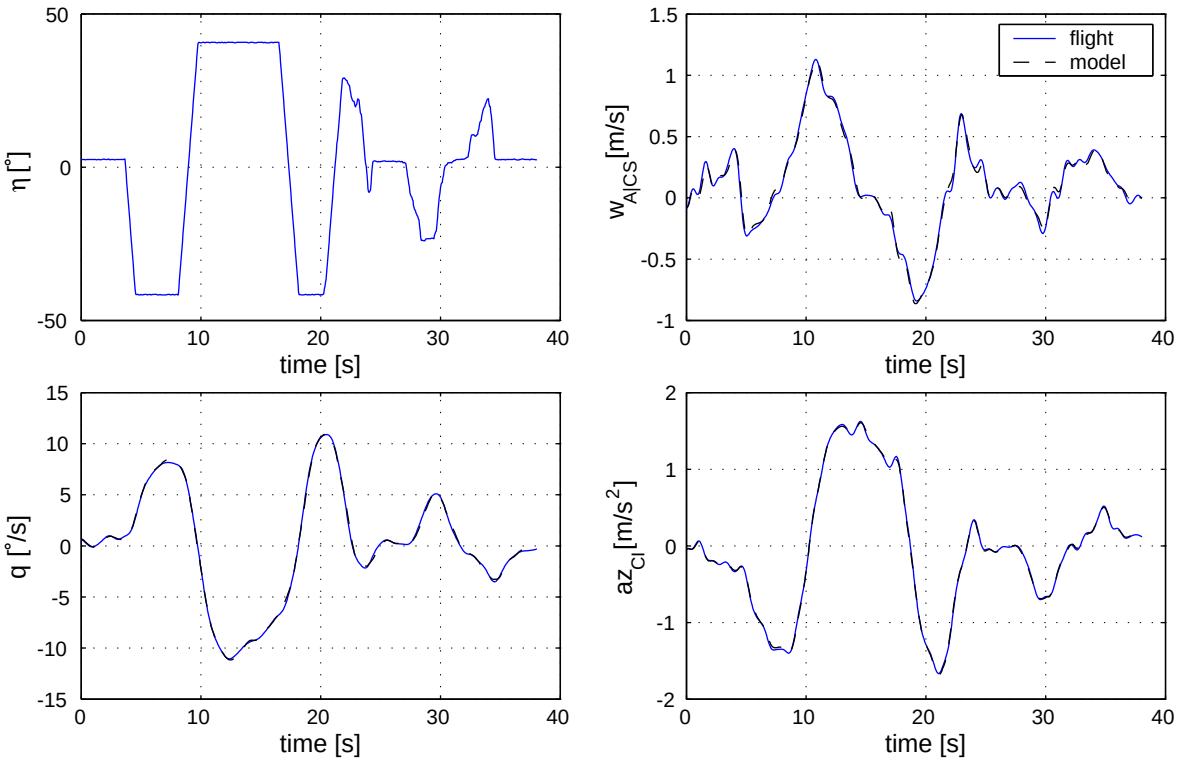

Figure C.31: Estimation results of F5S12e maneuver (Filter-Error algorithm)

C.3.10 Flight Record F3S2: High Turbulence

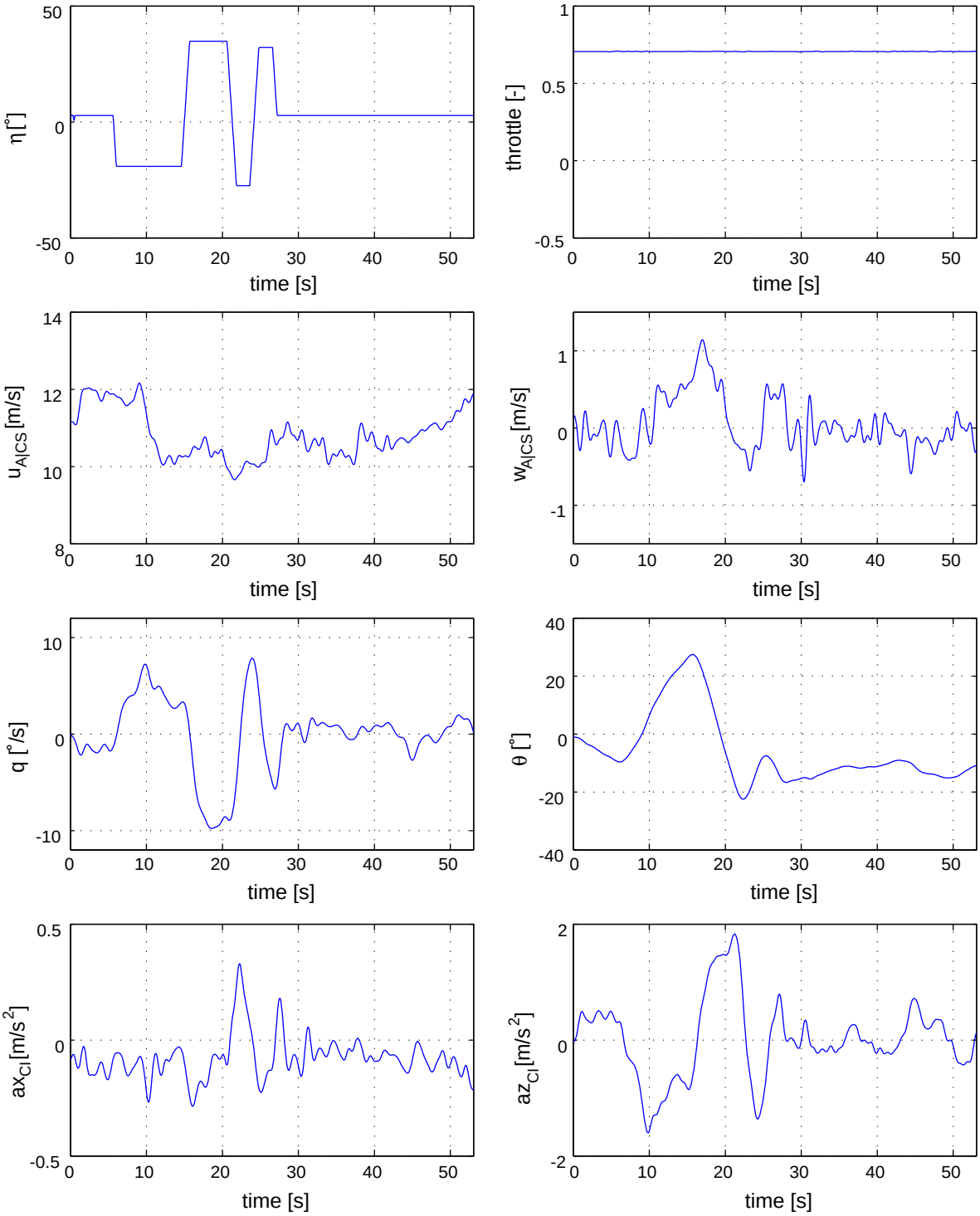

Figure C.32: Filtered measurements of F3S2e flight maneuver

Table C.13: Parameter values estimated from F3S2e record with extended longitudinal model

Parameter	Model Value	Output Error	Filter Error
Z_w	-0.422	-1.34 (0.156)	-0.851 (0.075)
Z_q	4.361	8.645 (1.291)	3.145 (0.934)
M_w	0.121	0.096 (0.007)	0.090 (0.041)
M_q	-0.668	-0.916 (0.200)	-1.693 (0.026)
M_θ	-0.137	-0.031 (0.023)	-0.18
Z_η	-1.507	-0.481 (0.257)	-0.455 (0.085)
M_η	-0.522	-0.503 (0.164)	-0.191 (0.026)
$b_{\dot{w}}$	-	0.042 (0.143)	0.124 (0.105)
$b_{\dot{q}}$	-	-0.004 (0.013)	-0.004 (0.015)
b_w	-	0.030 (0.216)	0.08 (0.055)
b_q	-	0.014 (0.018)	0.010 (0.020)
b_{az}	-	-0.115 (0.227)	0.093 (0.138)
u_0	10.6	10.608 (1.34)	10.53 (1.21)
$\sigma_{\dot{w}}$	-	-	0.047 (0.119)
σ_q	-	-	0.003 (0.001)
Iterations	-	38	9
Eigenvalue	-1.22 0.056+/-0.195i	-0.028 -1.11+/-0.412i	-1.87 -0.16 -0.51
TIC: w q az_{CI}		 0.088 0.046 0.069	 0.012 0.003 0.021

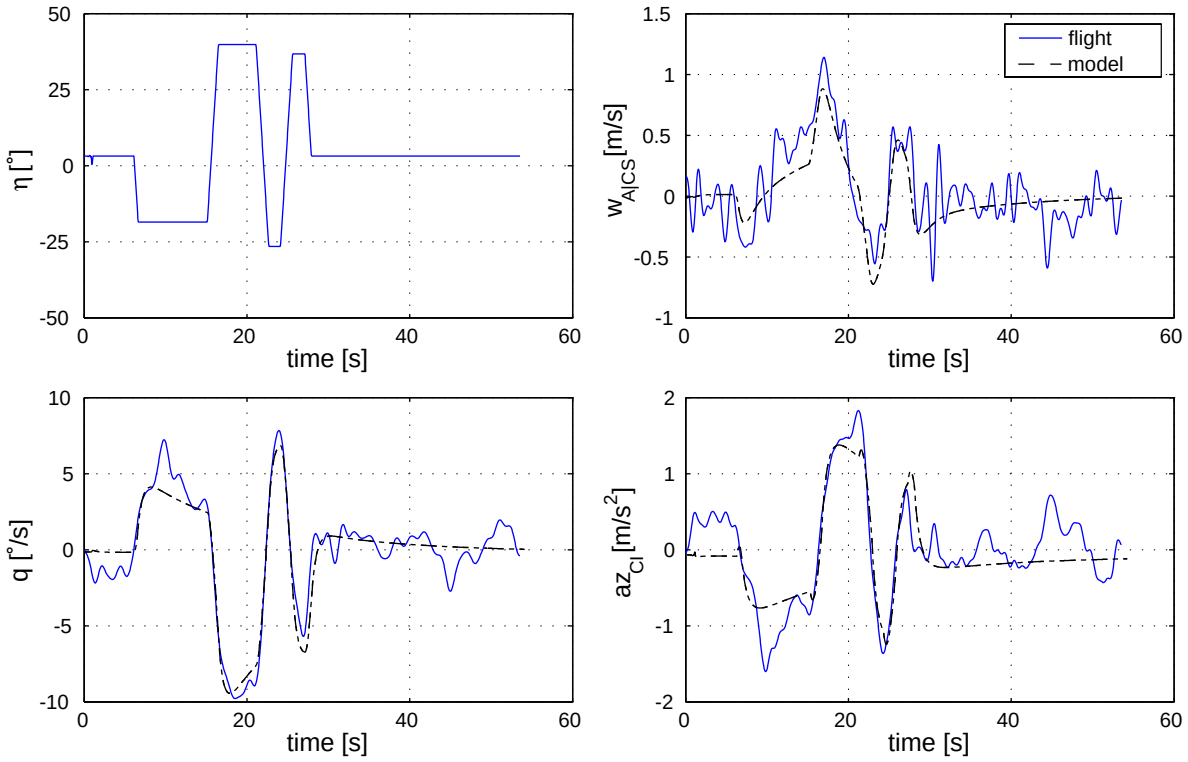

Figure C.33: Estimation results of F3S2e maneuver (Output-Error algorithm)

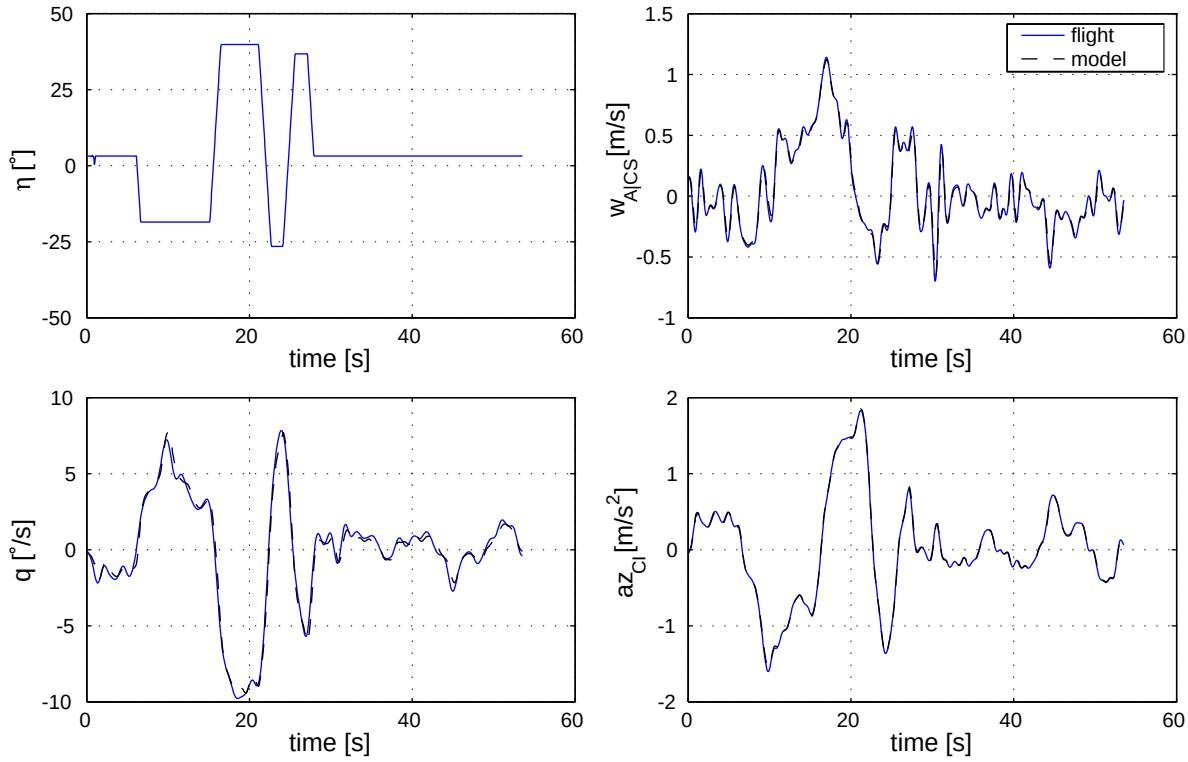

Figure C.34: Estimation results of F3S2e maneuver (Filter-Error algorithm)

C.4 Estimation Results of Lateral-Directional Maneuver

Table C.14: Estimated parameters of the lateral-directional model

Parameter	Model value	Output Error (C-R bounds)	Filter-Error (C-R bounds)
Y_v	-0.416	-0.429 (0.356)	-0.525 (0.431)
Y_r	-3.985	-1.059 (2.877)	-1.076 (1.77)
L_p	-1.493	-1.483 (0.264)	-1.492 (0.156)
L_r	1.36	4.503 (0.835)	4.602 (0.832)
L_ϕ	-2.545	-3.436 (0.467)	-3.496 (0.443)
N_v	-0.131	-0.059 (0.052)	-0.06 (0.031)
N_r	-0.584	-1.522 (0.411)	-1.541 (0.425)
Y_ζ	1.455	0.738 (0.243)	0.711 (0.245)
L_ζ	0.213	0.361 (0.092)	0.372 (0.104)
N_ζ	-0.495	-0.282 (0.038)	-0.282 (0.025)
$b_{\dot{v}}$	-	-0.017 (0.118)	-0.021 (0.100)
$b_{\dot{p}}$	-	0.002 (0.091)	0.001 (0.121)
$b_{\dot{r}}$	-	-0.004 (0.030)	0.002 (0.028)
$b_{\dot{\phi}}$	-	0.005 (0.041)	0.002 (0.067)
b_v	-	-0.094 (0.207)	-0.082 (0.204)
b_p	-	-0.005 (0.041)(	-0.001 (0.053)
b_r	-	0.015 (0.018)	0.021 (0.024)
b_ϕ	-	0.044 (0.027)	0.038 (0.011)
b_{ay}	-	0.077 (0.245)	0.079 (0.210)
u_0	-	10.26 (0.835)	10.46 (0.791)
w_0	-	0.194 (0.750)	0.205 (0.643)
$\sigma_{\dot{v}}$	-	-	0.023 (0.032)
$\sigma_{\dot{p}}$	-	-	0.002 (0.0002)
$\sigma_{\dot{r}}$	-	-	0.001 (0.0001)
Iterations	-	38	12
Eigenvalue	0.234 -1.24 -0.744+/-1.42i	-0.037 -1.60 -0.740+/-1.69i	-0.046 -1.61 -0.746+/-0.172i
TIC: v p r ϕ ay_{CI}		 0.17 0.13 0.07 0.12 0.11	 0.012 0.003 0.021 0.017 0.004